

OCRWM	MODEL COVER SHEET	1. QA: CA Page 1 of 230
--------------	--------------------------	----------------------------

2. Type of Mathematical Model
☒ Process Model ☐ Abstraction Model ☐ System Model

Description Intended Use of Model
 The purpose of this Model Report is to document the unsaturated zone (UZ) fluid flow and solute transport models and submodels as well as the flow fields generated utilizing the UZ Flow and Transport Model of Yucca Mountain (UZ Model), Nevada.

3. Title
 UZ Flow Models and Submodels

4. DI (including Rev. No. and Change No., if applicable):
 MDL-NBS-HS-000006 REV01

5. Total Attachments 6	6. Attachment Numbers - No. of Pages in Each I-12, II-2, III-20, IV-2, V-4
---------------------------	---

	Printed Name	Signature	Date
7. Originator	Y-S. Wu	<i>Y-S. Wu</i>	8/5/03
8. CSO	M. Zhu	<i>M. Zhu</i>	8/5/03
9. Checker	P. Percoff	<i>P. Percoff</i>	8/5/03
10. QER	S. Martin	<i>S. Martin</i>	8/5/03
11. Responsible Manager/Lead	J.S.Y. Wang	<i>J.S.Y. Wang</i>	8/5/03
12. Responsible Manager	P. Dixon	<i>P. Dixon</i>	8/5/03

13. Remarks
 Block 6. One CD-ROM, "Title of Attachment III for Model Report, MDL-NBS-HS-000006 REV01." is included with this attachment and submitted with this report.
 Block 7. Additional contributors to this report are G. Lu, K. Zhang, G. Zhang, H.H. Liu, T. Xu, and E.L. Spruntthal.
 Block 8. S. Altman contributed to the CSO reviews.

Technical Error Report (TER) log number addressed in this Model Report
 TER-02-0081

OFFICE OF CIVILIAN RADIOACTIVE WASTE MANAGEMENT

MODEL REVISION RECORD

1. Page: 2 of 230

2. Model Title:
UZ Flow Models and Submodels

3. DI (including Rev. No. and Change No., if applicable):

MDL-NBS-HS-000006 REV01

4. Revision/Change No.	5. Description of Revision/Change
REV00	Initial Issue
REV00/ICN01	<p>This ICN updates data tracking number (DTN) status and usage and makes minor editorial changes. "To-be-verified" (TBV) designations were removed, and verified and qualified DTNs were identified that contain the same data. No input or output values to this technical product were affected by this activity.</p> <p>TBV-4755 was addressed by replacing unqualified DTN GS000399991221.004 with qualified and verified DTN MO0109HYMXP.001. TBV-3608 was addressed by deleting Section 6.4.4.3 associated with unqualified DTN GS010908315214.003. TBV-0536 was addressed by replacing unqualified DTN GS960208312261.001 with qualified, superseding DTN GS981008312313.003 with qualified and verified DTN GS980508312313.001. TBV-3999, formerly identified with LBNL software code infil2grid V. 1.6, was removed because the associated software is now qualified. The input status of DTNs GS960908312231.004, GS980408312232.001, and GS980908312242.036 was corrected to N/A - Corroborative Information to reflect actual use of data in the report. Reference to input transmittals MOL.19991027.0149, MOL.19991014.0102, MOL.20000118.0092 and MOL.19991213.0041 was removed and replaced with DTN citations MO0109HYMXP.001, GS000399991221.003, GS950308312231.002 and GS960808312231.004, respectively.</p> <p>Table 3-1 was changed to identify the correct operational systems used in preparing the AMR. Section 6.4.3.3 was determined to be unnecessary and was deleted along with the associated Figure 6-32. Seven DTNs (LB991121233129.001 through LB991121233129.007) were removed from Table 4-1 and Section 8.3 and inserted into Section 8.4 because they are actually technical product outputs of this AMR. Incomplete reference citations in Section 8.1, 8.3, and 8.4 were updated.</p> <p>A printout of the Document Input Reference System (DIRS) sheets for this AMR, formerly presented in Attachment I, has been replaced with a reference to the YMP electronic DIRS database.</p> <p>Attachment III of this technical product contains documentation of single use software routines that were qualified under procedure AP-SI.1Q, Software Management, prior to the release of Rev. 3 of said procedure. As the scope of the ICN did not involve a change to the routine codes, and they have not been used to develop additional quality affecting information in this technical product, these single use software routines will remain documented herein, in accordance with AP-SI.1Q prior to release of Rev. 3.</p> <p>These changes made in this ICN are identified by change bars. This ICN affects Sections 1, 2, 3, 4, 6, 8, and Attachment I. Only the footer was changed in Attachment II and a footer with page numbers was added to Attachment III. This ICN affects pages 17, 19, 21, 24-27, 41, 45, 53, 54-55, 68, 73, 75, 77, 81, 83, 85, 88, 90, 102, 104-405, 125, 128-129, 142-144, 149, 152, 159, 160-164, 166-170, I-1.</p>
REV01	<p>The entire model documentation was revised. Side bars are not used because the changes were too extensive to use Step 5.9d)1) per AP-SIII.10Q, Rev. 1/ICN 2.</p>

TABLE OF CONTENTS

ACRONYMS	15
1. PURPOSE	17
2. QUALITY ASSURANCE.....	19
3. USE OF SOFTWARE.....	21
4. INPUTS	23
4.1 DATA AND PARAMETERS	23
4.2 CRITERIA	25
4.3 CODES AND STANDARDS.....	28
5. ASSUMPTIONS	29
6. MODEL DISCUSSION	31
6.1 MODEL DESCRIPTION	33
6.1.1 Geological Model and Numerical Grids	33
6.1.2 Numerical Codes and Modeling Approach	37
6.1.3 Model Boundary Conditions	40
6.1.4 Infiltration Scenarios	41
6.1.5 Model Parameters and Rock Properties	46
6.2 3-D UZ FLOW MODEL CALIBRATION	46
6.2.1 Calibration Data	47
6.2.2 Conceptual Models of UZ Flow	47
6.2.3 Parameter Adjustment	50
6.2.4 Numerical Treatment and Solution Convergence	54
6.2.5 Simulation Scenarios, Results, and Analyses.....	55
6.2.6 Features, Events, and Processes	61
6.3 TEMPERATURE CALIBRATION	71
6.3.1 3-D Thermal Model Grid	71
6.3.2 Top Boundary Temperature	72
6.3.3 Bottom Boundary Temperature.....	73
6.3.4 Calibration of Ambient Temperatures.....	73
6.4 PNEUMATIC CALIBRATION	79
6.4.1 Model Parameters and Boundary Conditions.....	79
6.4.2 Modeling Approach and Calibration.....	79
6.4.3 Analysis of Results.....	80
6.5 ANALYSIS AND MODELING OF PORE WATER CHEMICAL DATA	82
6.5.1 Available Data.....	83
6.5.2 Three-Dimensional Simulations.....	87
6.6 FLOW PATTERN ANALYSIS OF TSPA-LA 3-D FLOW FIELDS	92
6.6.1 Simulation Scenarios	92

TABLE OF CONTENTS (Continued)

6.6.2	UZ Alternative Flow Model Results	93
6.6.3	Flow Fields and Analyses.....	94
6.7	TRACER TRANSPORT TIMES	122
6.7.1	Methodology and Transport Parameters	122
6.7.2	Simulation Scenarios.....	123
6.7.3	Simulation Results and Analyses	125
6.8	SENSITIVITY ANALYSES OF ACTIVE FRACTURE PARAMETER AND FRACTURE POROSITY	138
6.8.1	Sensitivity Analyses of Flow Field with Respect to the Active Fracture Parameter (γ)	138
6.8.2	Sensitivity Analyses of Transport	141
6.9	UNCERTAINTIES AND ALTERNATIVE MODELS	144
7.	VALIDATION	149
7.1	THE VALIDATION CRITERIA	149
7.2	VALIDATION USING ECRB WATER-POTENTIAL MEASUREMENTS	151
7.3	VALIDATION USING PERCHED-WATER DATA AT WT-24	153
7.4	3-D PNEUMATIC MODEL PREDICTION	155
7.5	MODEL VALIDATION WITH CARBON-14 DATA	157
7.6	MODELING ANALYSIS OF ALCOVE 8/NICHE 3 FAULT TESTS	161
7.6.1	Field Observations.....	161
7.6.2	Numerical Model.....	165
7.6.3	Model Simulations and Discussions.....	167
7.7	AMBIENT THERMAL MODEL.....	178
7.8	VALIDATION USING CHLORIDE MEASUREMENTS ALONG ESF	181
7.9	CALCITE RESULTS	182
7.9.1	Introduction	182
7.9.2	Calcite Precipitation Mechanisms	183
7.9.3	Reactive-Transport Model.....	184
7.9.4	Hydrogeological and Geochemical Conditions.....	185
7.9.5	Results and Discussion.....	190
7.9.6	Concluding Remarks	194
7.10	MODEL VALIDATION USING STRONTIUM GEOCHEMISTRY AND ISOTOPIC RATIOS	195
7.10.1	Background	195
7.10.2	Validation of Conceptual and Numerical Models of UZ Transport Based on Corroborative Information from Published Works	196
7.10.3	Model for 3-D Sr Concentrations	197
8.	CONCLUSIONS	201
8.1	UZ FLOW MODEL CALIBRATION.....	203
8.2	GEOHERMAL MODEL CALIBRATION.....	203
8.3	GAS FLOW MODEL	204
8.4	CHLORIDE SUBMODEL	204
8.5	CALCITE SUBMODEL.....	204

TABLE OF CONTENTS (Continued)

8.6	TSPA FLOW FIELDS	205
8.7	TRACER TRANSPORT TIMES	205
8.8	SENSITIVITY ANALYSIS OF ACTIVE-FRACTURE-MODEL PARAMETER	206
8.9	MODEL VALIDATION	206
8.10	BARRIER CAPABILITY OF THE UZ	206
8.11	LIMITATIONS	208
8.12	SATISFACTION OF ACCEPTANCE CRITERIA	209
9.	INPUTS AND REFERENCES	211
9.2	CODES, STANDARDS, REGULATIONS, AND PROCEDURES	222
9.3	SOURCE DATA, LISTED BY DATA TRACKING NUMBER.....	223
9.4	OUTPUT DATA, LISTED BY DATA TRACKING NUMBER.....	223
ATTACHMENT I—CALIBRATED PARAMETER SETS, COMBINING ONE- DIMENSIONAL INVERSIONS AND THREE-DIMENSIONAL PERCHED-WATER AND CHLORIDE-TRANSPORT MODELING, USED IN GENERATING THE NINE FLOW FIELDS, AND TRACER TRANSPORT TIMES		I-1
ATTACHMENT II—LOCATION COORDINATES AND SURFACE ELEVATIONS OF SELECTED BOREHOLES USED IN MODEL CALIBRATION AND STUDIES		II-1
ATTACHMENT III—COMPUTATIONS IN INPUT DATA PREPARATIONS AND SIMULATION RESULT ANALYSES.....		III-1
ATTACHMENT IV—PTN/TSW FLUX AND FLOW FIELD CONVERSION		IV-1
ATTACHMENT V—MATHEMATICAL EQUATIONS		V-1

INTENTIONALLY LEFT BLANK

LIST OF FIGURES

6.1-1.	Plan View of the 3-D UZ TSPA-LA Model Grid, Showing the Model Domain, Faults Incorporated, Repository Layout, and Several Borehole Locations	36
6.1-2.	Plan View of Net Infiltration Distributed over the 3-D UZ TSPA-LA Model Grid for the Present-Day (Base-Case) Mean Infiltration Scenario	43
6.1-3.	Plan View of Net Infiltration Distributed over the 3-D UZ TSPA-LA Model Grid for the Monsoon Mean Infiltration Scenario	44
6.1-4.	Plan View of Net Infiltration Distributed over the 3-D UZ TSPA-LA Model Grid for the Glacial Transition Mean Infiltration Scenario	45
6.2-1.	Schematic Showing the Conceptualized Flow Processes and Effects of Capillary Barriers, Major Faults, and Perched-Water Zones within a Typical Cross Section of the UZ Flow Model Domain in the East-West Direction	48
6.2-2.	Comparison to the Simulated and Observed Matrix Liquid Saturations and Perched-Water Elevations for Borehole UZ-14, Using the Results of the Simulations with Three Mean Infiltration Rates.....	58
6.2-3.	Comparison to the Simulated and Observed Matrix Liquid Saturations and Perched-Water Elevations for Borehole SD-12, Using the Results of the Simulations with Three Mean Infiltration Rates.....	59
6.2-4.	Comparison to the Simulated and Averaged Observed Water Potentials and Perched-Water Elevations for Borehole SD-12, Using the Results of the Simulations with Three Mean Infiltration Rates.....	60
6.3-1.	Plan View of the 3-D Thermal Model Grid, Showing the Model Domain, Faults Incorporated, Several Borehole Locations, and TH Model Boundaries.....	72
6.3-2.	Comparisons between Measured and Modeled Ambient Temperature Profiles for the Five Boreholes under the Present-Day Mean Infiltration Rate.....	75
6.3-3.	Ambient Temperature Distributions at the Water Table for the Present-Day Mean Infiltration Scenario	77
6.3-4.	Temperature Distributions at the Mountain Surface, the Top Model Boundary, for the Present-Day Mean Infiltration Scenario.....	78
6.4-1.	Comparison of Simulated and Observed Gas Pressure at Borehole SD-7 during a 60-Day Period	81
6.4-2.	Comparison of Simulated and Observed Gas Pressure at Borehole SD-12 during the First 30-Day Period.....	82
6.5-1.	Chloride Concentration (mg/L) Profiles at Borehole USW NRG-6 for Present Recharge with Mean, Upper, and Lower Bounds and Glacial Recharge	88
6.5-2.	Chloride Concentration (mg/L) Profiles at Borehole USW UZ-14 for Present Recharge with Mean, Upper, and Lower Bounds and Glacial Recharges.....	89
6.5-3.	Chloride Concentration (mg/L) Profiles at Borehole USW SD-9 for Present Recharge with Mean, Upper, and Lower Bounds and Glacial Recharge	90
6.5-4.	Chloride Concentration (mg/L) Profiles at the ECRB for Present Recharge with Mean, Upper, and Lower Bounds	91
6.6-1.	Simulated Percolation Fluxes at the Repository Horizon under the Present-Day, Mean Infiltration Scenario Using the Results of Simulation preq_mA.....	96
6.6-2.	Simulated Percolation Fluxes at the Repository Horizon under the Monsoon, Mean Infiltration Scenario Using the Results of Simulation monq_mA.....	97

LIST OF FIGURES (Continued)

6.6-3.	Simulated Percolation Fluxes at the Repository Horizon under the Glacial Transition Mean Infiltration Scenario Using the Results of Simulation glaq_mA.....	98
6.6-4.	Simulated Percolation Fluxes at the Water Table under the Present-Day, Lower-Bound Infiltration Scenario Using the Results of Simulating the Base-Case Model: preq_1A.....	100
6.6-5.	Simulated Percolation Fluxes at the Water Table under the Present-Day, Lower-Bound Infiltration Scenario Using the Results of Simulating the Alternative Model: preq_1B.....	101
6.6-6.	Simulated Percolation Fluxes at the Water Table under the Present-Day, Mean Infiltration Scenario Using the Results of Simulating the Base-Case Model: preq_mA.....	102
6.6-7.	Simulated Percolation Fluxes at the Water Table under the Present-Day, Mean Infiltration Scenario Using the Results of Simulating the Alternative Model: preq_mB.....	103
6.6-8.	Simulated Percolation Fluxes at the Water Table under the Present-Day, Upper-Bound Infiltration Scenario Using the Results of Simulating the Base-Case Model: preq_uA.....	104
6.6-9.	Simulated Percolation Fluxes at the Water Table under the Present-Day, Upper-Bound Infiltration Scenario Using the Results of Simulating the Alternative Model: preq_uB.....	105
6.6-10.	Simulated Percolation Fluxes at the Water Table under the Monsoon, Lower-Bound Infiltration Scenario Using the Results of Simulating the Base-Case Model: monq_1A.....	106
6.6-11.	Simulated Percolation Fluxes at the Water Table under the Monsoon, Lower-Bound Infiltration Scenario Using the Results of Simulating the Alternative Model: monq_1B.....	107
6.6-12.	Simulated Percolation Fluxes at the Water Table under the Monsoon, Mean Infiltration Scenario Using the Results of Simulating the Base-Case Model: monq_mA.....	108
6.6-13.	Simulated Percolation Fluxes at the Water Table under the Monsoon, Mean Infiltration Scenario Using the Results of Simulating the Alternative Model: monq_mB.....	109
6.6-14.	Simulated Percolation Fluxes at the Water Table under the Monsoon, Upper-Bound Infiltration Scenario Using the Results of Simulating the Base-Case Model: monq_uA.....	110
6.6-15.	Simulated Percolation Fluxes at the Water Table under the Monsoon, Upper-Bound Infiltration Scenario Using the Results of Simulating the Alternative Model: monq_uB.....	111
6.6-16.	Simulated Percolation Fluxes at the Water Table under the Glacial Transition, Lower-Bound Infiltration Scenario Using the Results of Simulating the Base-Case Model: glaq_1A.....	112
6.6-17.	Simulated Percolation Fluxes at the Water Table under the Glacial Transition, Lower-Bound Infiltration Scenario Using the Results of Simulating the Alternative Model: glaq_1B.....	113

LIST OF FIGURES (Continued)

6.6-18.	Simulated Percolation Fluxes at the Water Table under the Glacial Transition, Mean Infiltration Scenario Using the Results of Simulating the Base-Case Model: glaq_mA	114
6.6-19.	Simulated Percolation Fluxes at the Water Table under the Glacial Transition, Mean Infiltration Scenario Using the Results of Simulating the Alternative Model: glaq_mB	115
6.6-20.	Simulated Percolation Fluxes at the Water Table under the Glacial Transition, Upper-Bound Infiltration Scenario Using the Results of Simulating the Base-Case Model: glaq_uA	116
6.6-21.	Simulated Percolation Fluxes at the Water Table under the Glacial Transition, Upper-Bound Infiltration Scenario Using the Results of Simulating the Alternative Model: glaq_uB	117
6.6-22.	Areal Frequency and Distribution of Simulated Percolation Fluxes within the Repository Domain Normalized to the Three Mean Infiltration Rates: (a) Present Day, (b) Monsoon, and (c) Glacial Transition	120
6.6-23.	Cumulative Flux Distribution and Range as Functions of Normalized Percolation Flux within the Repository from the 18 Flow Fields	121
6.7-1.	Simulated Breakthrough Curves of Cumulative Tracer Mass Arriving at the Water Table, after Release from Fractures in the Repository, Using the Base-Case Flow Fields with the Nine Infiltration Scenarios for Nonadsorbing and Adsorbing Tracers	127
6.7-2.	Simulated Breakthrough Curves of Cumulative Tracer Mass Arriving at the Water Table, after Release from Fractures in the Repository, Using the Alternative Flow Fields with the Nine Infiltration Scenarios for Nonadsorbing and Adsorbing Tracers	128
6.7-3.	Comparison of Simulated Breakthrough Curves of Cumulative Tracer Mass Arriving at the Water Table, after Release from Fractures and Matrix Blocks in the Repository, Using the Base-Case and Alternative Flow Fields under the Present-Day Mean Infiltration Flow Fields with the Nine Infiltration Scenarios for Nonadsorbing and Adsorbing Tracers	129
6.7-4.	Correlation of Average Infiltration Rates and Tracer Transport Times at 50% Mass Breakthrough for the 36 Tracer-Fracture-Release Simulation Scenarios	132
6.7-5.	Simulated Cumulative, Normalized Mass Arrival Contours of a Conservative Tracer at the Water Table after 1,000 Years, Indicating Potential Breakthrough Locations at the Time, Using the Present- Day, Mean Infiltration Scenario	134
6.7-6.	Simulated Cumulative, Normalized Mass Arrival Contours of a Reactive Tracer at the Water Table after 1,000 Years, Indicating Potential Breakthrough Locations at the Time, Using the Present-Day, Mean Infiltration Scenario	135
6.7-7.	Simulated Cumulative, Normalized Mass Arrival Contours of a Conservative Tracer at the Water Table after 1,000,000 Years, Indicating Potential Breakthrough Locations at the Time, Using the Present-Day, Mean Infiltration Scenario	136
6.7-8.	Simulated Cumulative, Normalized Mass Arrival Contours of a Reactive Tracer at the Water Table after 1,000,000 Years, Indicating Potential Breakthrough Locations at the Time, Using the Present-Day, Mean Infiltration Scenario	137

LIST OF FIGURES (Continued)

6.8-1.	Comparison of (a) Simulated Matrix Liquid Saturation and (b) Water Potential Using Calibrated Hydraulic Properties (Solid Line) with That Obtained Using Smaller (Half) γ of TSw Units (Dashed Line) for Borehole USW SD-6	140
6.8-2.	Comparison of (a) Simulated Matrix Liquid Saturation and (b) Water Potentials Using Calibrated Hydraulic Properties (Solid Line) with That Obtained Using Smaller (Half) γ of Under Repository Units (Dashed Line) for Borehole USW SD-6	140
6.8-3.	Comparison of a Simulated Breakthrough Curve of Relative Tracer Mass at the Groundwater Table Obtained for the Base Case (Using Calibrated Rock Hydraulic Properties, Red Solid Line), a Case Using the Smaller γ of TSw Units (Blue Dash Line), and Another Case Using the Smaller γ of All Units below the Repository (Green Solid Line).....	143
6.8-4.	Comparison of Simulated Breakthrough Curve of Relative Tracer Mass at the Groundwater Table Obtained for the Base Case (Using Calibrated Rock Hydraulic Properties, Red Solid Line), and a Case Using a Smaller (1/10) Fracture Porosity (Green Solid Line).....	144
7.3-1.	Comparison of Predicted and Measured Matrix Water Potentials and Perched-Water Elevations at Borehole WT-24 Using the Present-Day Mean Infiltration Rate (preq_mA)	154
7.4-1.	Comparison of 3-D Pneumatic Prediction to Observation Data from Borehole UZ-7a	156
7.4-2.	Comparison of 3-D Pneumatic Prediction to Observation Data from Borehole SD-12	156
7.5-1.	Simulated Groundwater Age for UZ-1 Borehole Compared to the Measured ^{14}C Age.....	159
7.5-2.	Simulated Groundwater Age for SD-12 Borehole Compared to the Measured ^{14}C Age.....	160
7.6-1.	Infiltration Rate as a Function of Time.....	162
7.6-2.	Total Seepage Rate as a Function of Time	163
7.6-3.	Water Travel Velocity Data for Boreholes 9 and 10	164
7.6-4.	Observed Flux-Average Breakthrough Curve	165
7.6-5.	Cross Sectional Schematic of the 3-D Numerical Grid Used for Modeling Studies of Alcove 8/Niche 3	166
7.6-6.	A Comparison between Simulated Seepage Rates as a Function of Time (Run #1) and Field Observations	170
7.6-7.	A Comparison among Calculated Water Travel Velocities from Two Calibration Runs and the Velocity Data Observed from the Fault Test	171
7.6-8.	A Comparison between Simulated Seepage Rates as a Function of Time (Run #2) and Field Observations	173
7.6-9.	Comparisons between Simulated Breakthrough Curves at the Niche for Two Different Fault-Matrix Interface Areas and the Observed Data	174
7.6-10.	Comparisons between Simulated Breakthrough Curves (Considering Dispersion) at the Niche for the Increased Fault-Matrix Interface Areas and the Observed Data.....	176

LIST OF FIGURES (Continued)

7.7-1.	Comparison of Simulated and Observed Temperature Profiles for Borehole H-5	179
7.7-2.	Comparison of Simulated and Observed Temperature Profiles for Borehole H-4	180
7.7-3.	Comparison of Simulated and Observed Temperature Profiles for Borehole WT-18	181
7.8-1.	Comparison of Chloride Concentration (mg/L) Profiles under Present-Day Recharges with Mean, Upper, and Lower Bounds and Glacial Transition Recharge at the ESF	182
7.9-1.	Modeled Steady-State Water Saturations for the WT-24 Column Using Infiltration Rates: 2, 5.92, and 20 mm/yr	189
7.9-2.	Modeled Temperature Profiles in Borehole WT-24 as a Function of Depth for Three Infiltration Rates	189
7.9-3.	Simulated Total (Fracture plus Matrix) Calcite Abundances (in ppmV or 10^{-6} Volume Fraction) in the WT-24 Column for Different Infiltration Rates after 10 Million Years: (a) Extended-Case Geochemical System, (b) Base-Case Geochemical System	190
7.9-4.	Modeled Calcite Abundances (in ppmV or 10^{-6} Volume Fraction) in Fractures and in the Matrix after 10 Million Years for Differing Infiltration Rates Using the Extended-Case Geochemical System	191
7.9-5.	Modeled Calcite Abundances (in ppmV or 10^{-6} Volume Fraction) in Fractures and in the Matrix for (a) the Extended-Case and (b) Base-Case Geochemical Systems	192
7.9-6.	Changes in Calcite Volume Fraction (ppmV) vs. Infiltration Rates for TSw4 Layer (at an Elevation of 1,126 m) for (a) the Extended-Case and (b) Base-Case Geochemical Systems	193
7.9-7.	Calcite Abundances (in ppmV or 10^{-6} Volume Fraction) with Depth in Boreholes WT-24 and SD-6	194
7.9-8.	Geometric Means of Calcite Abundances with Depth for Boreholes WT-24 and SD-6	194
7.10-1.	Comparison of Measured and Modeled Sr Concentrations as a Function of Elevation for the Surface-Based Boreholes (a) SD-9 and (b) SD-12	199
7.10-2.	Measured and Modeled Sr Concentrations in Pore Waters Extracted from Cores Taken in the ECRB	200

INTENTIONALLY LEFT BLANK

LIST OF TABLES

3-1.	Qualified Software Used in This Report.....	21
4.1-1.	Input Data Source and Data Tracking Numbers.....	24
4.2-1.	Project Requirements and YMRP Acceptance Criteria Applicable to This Model Report.....	26
6-1.	Scientific Notebooks Used in Model-Development Documentation	32
6.1-1.	GFM2000 Lithostratigraphy, UZ Model Layer, and Hydrogeologic Unit Correlation Used in the UZ Flow Model and Submodels	34
6.1-2.	Infiltration Rates (mm/year) Averaged over the UZ Model Domain	42
6.2-1.	Borehole Data Used for 3-D Flow Model Calibration	47
6.2-2.	Calibrated PTn Fracture-Matrix Parameters for the Present-Day, Mean Infiltration Scenario	51
6.2-3.	Calibrated PTn Fracture-Matrix Parameters for the Present-Day, Upper-Bound Mean Infiltration Scenario	51
6.2-4.	Calibrated PTn Fracture-Matrix Parameters for the Present-Day, Lower-Bound Mean Infiltration Scenario	52
6.2-5.	Calibrated Parameters of Perched-Water Conceptual Model for the Present-Day, Base-Case Infiltration Scenario	53
6.2-6.	Calibrated Parameters of Perched-Water Conceptual Model for the Present-Day, Upper-Bound Infiltration Scenario	53
6.2-7.	Calibrated Parameters of Perched-Water Conceptual Model for the Present-Day, Lower-Bound Infiltration Scenario.....	53
6.2-8.	Calibrated TSw Fracture Permeability for the Present-Day, Mean Infiltration Scenario	54
6.2-9.	Nine UZ Flow Simulation Scenarios: Data Files, Parameter Sets, and Infiltration Maps for the UZ Model Calibrations.....	56
6.2-10.	Mass-Balance Results for Nine Flow Simulations	56
6.2-11.	FEPs Addressed in This Model Report.....	62
6.3-1.	Temperature Boreholes and Corresponding Element Columns of the Thermal Model Grid.....	74
6.4-1.	Observation Data and Corresponding Grid Columns of Boreholes SD-7 and SD-12, Used in the Pneumatic Calibration	80
6.5-1.	Chloride Data Sources	84
6.5-2.	Present-Day and Glacial Infiltration Fluxes at Different Scenarios (Averaged over Model Domain, mm/year).....	86
6.6-1.	Nine Simulation Scenarios of Alternative UZ Flow: Data Files, Parameter Sets, and Infiltration Maps for the UZ Flow Fields.....	92
6.6-2.	Mass-Balance Results for Nine Simulations of Alternative Flow Model	93
6.6-3.	Comparison of the Water Flux through Matrix, Fractures, and Faults as a Percentage of the Total Flux at Two Different Horizons (1) at the Repository and (2) at the Water Table for the Nine Base-Case Flow Fields.....	118
6.6-4.	Comparison of the Water Flux through Matrix, Fractures, and Faults as a Percentage of the Total Flux at Two Different Horizons, at the Repository and at the Water Table, for the Nine Alternative Flow Fields	119
6.7-1.	K _d Values Used for Reactive Tracer Transport in Different Hydrogeologic Units.....	123

LIST OF TABLES (Continued)

6.7-2.	Transport Simulation Scenarios: Data Files and Corresponding Nine Base-Case Flow Fields with Nine Infiltration Rates	124
6.7-3.	Transport Simulation Scenarios: Data Files and Corresponding Nine Alternative Fields with Nine Infiltration Rates.....	125
6.7-4.	Tracer Transport Times at 10% and 50% Mass Breakthrough Times for 18 Transport Simulation Scenarios, Corresponding to the Nine Base-Case Flow Fields with Nine Infiltration Rates.....	130
6.7-5.	Tracer Transport Times at 10% and 50% Mass Breakthrough Times for 14 Transport Simulation Scenarios, Corresponding to the Nine Alternative Flow Fields with Nine Infiltration Rates.....	131
6.8-1.	The γ Values Used in Flow Simulations for Sensitivity Analyses	138
6.8-2.	Relative Changes of Fracture Flux in Response to the Changes in γ	141
6.9-1.	Comparison between the Two Timing Estimates of Future Climate States for the Next ~50,000 Years	146
7.4-1	Observation Sensors in Borehole USW UZ-7a	155
7.6-1.	Uncalibrated Rock Properties	169
7.6.2.	Rock Properties Calibrated from Seepage Rate Data (Run #1).....	171
7.6.3.	Rock Properties Calibrated from Both Seepage Rate and Water Travel Velocity Data (Run #2).....	172
7.9-1.	Hydrogeologic Units, Model Layers, and Hydrogeological Properties for the Yucca Mountain Unsaturated Zone Flow and Transport Model, as Given by the Calibrated Property Model.....	186
7.9-2.	Water and Gas Chemistry Used for Initial and Boundary Conditions of the Reaction-Transport Simulations	188
8-1.	Output Data and Data Tracking Numbers	202
8-2.	Percentage of Net Infiltration over Net Recharge after Evapotranspiration for Present-Day/Modern Climates over the Model Domain).....	207

ACRONYMS

1-D	one-dimensional
2-D	two-dimensional
3-D	three-dimensional
ACC	Accession Number
AFM	Active Fracture Model
AMR	Analysis/Model Report
AP	Administrative Procedure (DOE)
BSC	Bechtel SAIC Company
CFu	Crater Flat undifferentiated hydrogeologic unit
CH	Calico Hills
CHn	Calico Hills nonwelded hydrogeologic unit
CRWMS	Civilian Radioactive Waste Management System
DIRS	Document Input Reference System
DOE	Department of Energy
DRI	Desert Research Institute
DTN	Data Tracking Number
ECM	Effective Continuum Model (or Method)
ECRB	Enhanced Characterization of Repository Block
ESF	Exploratory Studies Facility
FY	Fiscal Year
GFM	Geologic Framework Model
HGU	hydrogeologic unit
ISM	Integrated Site Model
ITN	Input Transmittal Number
LA	License Application
LBNL	Lawrence Berkeley National Laboratory
masl	meters above sea level
MINC	multiple interacting continua
M&O	Management and Operating Contractor
non-Q	non-Qualified
NRC	Nuclear Regulatory Commission
NSP	Nevada State Plane

ACRONYMS (Continued)

OCRWM	Office of Civilian Radioactive Waste Management
PA	Performance Assessment
PMR	Process Model Report
PTn	Paintbrush nonwelded hydrogeologic unit
PFBA	pentafluorobenzoic acid
Q	Qualified
QA	Quality Assurance
QAP	Quality Administrative Procedure (M&O)
QARD	Quality Assurance Requirements and Description
QIP	Quality Implementing Procedure
RIB	Reference Information Base
RIS	Records Information System
SR	Site Recommendation
STN	Software Tracking Number
TBD	to be determined
TBV	to be verified
TCw	Tiva Canyon welded hydrogeologic unit
TDMS	Technical Data Management System
TSPA	Total System Performance Assessment
TSw	Topopah Spring welded hydrogeologic unit
TWP	Technical Work Plan
USGS	United States Geological Survey
UZ	unsaturated zone
UZ Model	Unsaturated Zone Flow and Transport Model
YMP	Yucca Mountain Project
YMRP	<i>Yucca Mountain Review Plan, Final Report</i>

1. PURPOSE

The purpose of this Model Report is to document the unsaturated zone (UZ) fluid flow and tracer transport models and submodels as well as the flow fields generated utilizing the UZ Flow and Transport Model of Yucca Mountain (UZ Model), Nevada. This work was planned in *Technical Work Plan (TWP) for: Performance Assessment Unsaturated Zone* (BSC 2002 [160819], Section 1.10, Work Package AUZM06). The UZ Model has revised, updated, and enhanced the previous UZ Flow Model REV 00 ICN 01 (BSC 2001 [158726]) by incorporation of the conceptual repository design with new grids, recalibration of property sets, and more comprehensive validation effort. The flow fields describe fracture-fracture, matrix-matrix, and fracture-matrix liquid flow rates and their spatial distributions as well as moisture conditions in the UZ system. These 3-D UZ flow fields are used directly by Performance Assessment (PA). The model and submodels evaluate important hydrogeologic processes in the UZ as well as geochemistry and geothermal conditions. These provide the necessary framework to test conceptual hypotheses of flow and transport at different scales and predict flow and transport behavior under a variety of climatic conditions. In addition, this Model Report supports several PA activities, including abstractions, particle-tracking transport simulations, and the UZ Radionuclide Transport Model.

The base-case 3-D flow fields are generated using the UZ Model, with input parameters based on the calibrated property sets documented in *Calibrated Properties Model* (BSC 2003 [160240]) and in this Model Report. The flow fields are developed for spatially varying maps representing the mean, lower, and upper bounds of estimated net infiltration for the current climate and two projected future climates (monsoon and glacial transition), resulting in a total of 9 base-case flow fields. Nine alternative flow fields were also generated to assess the importance of lateral diversion in the PTn. These flow fields have been submitted to the Technical Data Management System (TDMS) for use by PA and for Total System Performance Assessment (TSPA) activities.

The UZ Flow Models and submodels documented in this Model Report include the UZ Flow Model, Ambient Thermal Submodel, Chloride Submodel, Calcite Submodel, and Strontium Submodel. The Flow Model is used for generating 3-D UZ flow fields, estimating current and future UZ conditions, and studying tracer-transport behavior. The ambient thermal or temperature submodels characterize ambient geothermal conditions with temperature data for use in the UZ Model. The pneumatic data are used for additional calibration of the 3-D UZ Flow Model. The chloride submodel represents the conceptual model for the spatial and temporal variations in chloride chemistry and is compared with pore-water concentrations measured in samples from boreholes, the Exploratory Studies Facility (ESF), and the Enhanced Characterization of Repository Block (ECRB) Cross Drift. Modeling calcite deposition can be used to constrain hydrological parameters such as the infiltration-percolation flux. The calcite modeling also provides additional evidence for validation of the UZ Model. In addition, the Strontium Submodel incorporates the effects of rate-limited dissolution and precipitation on the concentration of a solute, in addition to dispersion, radioactive decay, and linear equilibrium adsorption.

The primary objectives of developing the UZ Flow Model and its submodels are:

- To integrate all the available field data and conceptual knowledge of the UZ system into a single, comprehensive, and calibrated 3-D model for simulating the ambient hydrological, thermal, and geochemical conditions, and for predicting system responses to future climate conditions.
- To quantify the flow of moisture, heat, and gas through the UZ, under present-day and predicted future climate scenarios.
- To perform detailed studies of perched water, percolation through the Paintbrush non-welded (PTn) unit, flow patterns through Calico Hills nonwelded (CHn) zeolitic units, and pore-water chemical and calcite analyses.
- To predict the migration of potential radionuclide releases after waste emplacement.
- To contribute model parameters and boundary conditions for drift seepage and other modeling studies.
- To provide Performance Assessment and Repository Design with a scientifically defensible and credible model of all relevant UZ flow processes.

2. QUALITY ASSURANCE

Development of this Model Report and the supporting modeling activities have been determined to be subject to the Yucca Mountain Project's quality assurance (QA) program as indicated in *Technical Work Plan for: Performance Assessment Unsaturated Zone* (BSC 2002 [160819], Section 8.2, Work Package (WP) AUZM06). Approved QA procedures identified in the TWP (BSC 2002 [160819], Section 4) have been used to conduct and document the activities described in this model report. The TWP also identifies the methods used to control the electronic management of data (BSC 2002 [160819], Section 8.4, WP AUZM06) without variations during the modeling and documentation activities.

This Model Report provides information pertaining to unsaturated zone (UZ) flow and transport through natural barriers (hydrogeologic units of the UZ) important to the demonstration of compliance with the postclosure performance objectives prescribed in 10 CFR 63.113 [156605]. Therefore, it is classified as "Quality Level-1" with regard to importance to waste isolation, as defined in AP-2.22Q, *Classification Criteria and Maintenance of the Monitored Geologic Repository Q-List*. The report contributes to the analysis and modeling data used to support performance assessment; the conclusions do not directly impact engineered features important to safety, as defined in AP-2.22Q.

INTENTIONALLY LEFT BLANK

3. USE OF SOFTWARE

The software and routines used in this study are listed in Table 3-1. These are appropriate for the intended application and were used only within the range of validation. These codes were obtained from software configuration management in accordance with AP-SI.1Q, *Software Management*. All qualified software used in this model report have been run on the OS Platform Version Numbers consistent with those listed in the Software Baseline Report readily available through the Software Configuration Management.

Table 3-1. Qualified Software Used in This Report

Software Name, Codes	Version	Software Tracking Number (STN)	DIRS Reference Number
TOUGH2	1.4	10007-1.4-01	146496
T2R3D	1.4	10006-1.4-00	146654
TOUGHREACT	3.0	10396-3.0-00	161256
TOUGH2	1.6	10007-1.6-01	161491
infil2grid	1.7	10077-1.7-00	154793
2kgrid8.for	1.0	10503-1.0-00	154787
bot_sum.f	1.0	10349-1.0-00	153471
vf_con.for	1.0	10466-1.0-00	154345
WINGRIDDER	2.0	10024-2.0-00	154785
TOPTMP_V0.f	1.0	10224-1.0-00	147030
GET_TEMP_V0.f	1.0	10222-1.0-00	147027
GEN-INCON-V0.f	1.0	10220-1.0-00	147023
TBgas3D	2.0	10882-2.0-00	160107
iTOUGH2	4.0	10003-4.0-00	139918
Bkread.f	1.0	10894-1.0-00	162143
Smesh.f	1.0	10896-1.0-00	162142
flow-con	1.0	10993-1.0-00	163162
T2FEHM	4.0	10997-4.0-00	163161

The use of the codes listed in Table 3-1 is documented in Section 6 and in the supporting scientific notebooks identified in Table 6-1. These codes and routines were qualified under AP-SI.1Q, *Software Management*. The software code TOUGH2 V1.4 (LBNL 2000 [146496]) was used to generate flow fields (Section 6) and to conduct model calibrations (Sections 6.2 and 6.3). Also, TOUGH2 V1.4 (LBNL 2000 [146496]) was also used to simulate 3-D gas flow (Section 6) and for geothermal calibrations. T2R3D V1.4 (LBNL 1999 [146654]) was used for tracer transport simulations, tracer transport travel-time estimates (Section 6.8), and modeling pore-water chemistry (Section 6.5). The infil2grid V1.7 software (LBNL 2002 [154793]) was used to apply infiltration maps onto the grids used for simulating flow and transport (Section 6).

Standard spreadsheet (Microsoft Excel 97 and Microsoft Excel 2002) and plotting programs (Tecplot v 9.0) were also used but are exempt from software qualification requirements of AP-SI.1Q. Details and procedures for calculations using Excel and its standard functions in post-processing and flow field extraction are provided in Attachment III*. The infil2grid V1.7 software (LBNL 2002 [154793]) was used, not V1.6 (LBNL 1999 [134754]) as planned in the TWP (BSC [160819], Table II-2). This is because infil2grid V1.7 (LBNL 2002 [154793]) can handle eight-character grid element names, while infil2grid V1.6 (LBNL 1999 [134754]) cannot. For the same reason, 2kgrid8.for V1.0 (LBNL 2002 [154787]) also was used although not planned in the TWP (BSC 2002 [160819], Table II-2).

The 3-D unsaturated zone flow fields are generated using a dual-permeability model with extra global fracture-matrix connections, which cannot be directly used by the FEHM code in TSPA calculations. Therefore, the TOUGH2 flow fields are converted using the routine: flow-con V1.0 (LBNL 2003 [163162]) into flow fields on the dual-permeability mesh that does not have the extra fracture-matrix connections. These output flow field files of flow-con v1.0 are then used as input files to the routine: T2FEHM V4.0 (LBNL 2003 [163161]), which converts TOUGH2 files in format of "flow9.dat" into files readable to FEHM.

The software WTRISE V2.0 (LBNL 2003 [163453]) is mentioned in Section 6.6.3, but is not used in this report.

* Attachments I, II, IV, and V are referred to elsewhere in this Model Report.

4. INPUTS

This section provides documentation for data (Table 4.1-1) used as inputs to this Model Report. The Q-status of all input and a description of the data are shown in the Document Input Reference System (DIRS) database. The inputs to the modeling activities described in this Model Report are obtained from the Technical Data Management Systems (TDMS) and include the following:

- Stratigraphy data from borehole logs
- Infiltration maps
- Calibrated fracture and matrix properties
- Geochemistry data from the ESF, the ECRB, and boreholes
- Unsaturated Zone Flow and Transport Model (UZ Model) grids
- Temperature data for boreholes
- Pneumatic-pressure data
- Locations and elevations of perched water in boreholes
- Uncalibrated fracture properties
- Water-potential data
- Matrix liquid-saturation data.

4.1 DATA AND PARAMETERS

The key input data used in the UZ Model and its submodel development include the following (See Table 4.1-1):

- Fracture properties (frequency, permeability, van Genuchten α and m parameters, porosity, and interface area per unit volume rock) for each UZ Model layer
- Matrix properties (porosity, permeability, and the van Genuchten α and m parameters) for each UZ Model layer
- Thermal and transport properties (grain density, wet and dry thermal conductivity, grain specific heat, and tortuosity coefficients) for each UZ Model layer
- Fault properties (matrix and fracture parameters) for each major hydrogeologic unit as defined by Table 6.1-1.

The calibrated parameter sets also include an estimate for each model layer of the active-fracture parameter, γ (Liu et al. 1998 [105729]), that accounts for the reduction in interaction between matrix and fracture flow resulting from flow fingering and channelization. Uncertainty in the input data and parameters are addressed in Section 6. Specific input data sets and associated Data Tracking Numbers (DTNs) are listed in Table 4.1-1.

Table 4.1-1. Input Data Source and Data Tracking Numbers*

Current DTN	Location in this report			Description/Remarks
	Text	Figure	Table	
LB03023DKMGRID.001 [162354]		Figure 6.1-1		3-D TSPA-LA model grid
GS000308311221.005 [147613]	6.1.4, 6.5, 6.5.1.2, 6.8.1, 7.2	Figures 6.1-2, 6.1-3, 6.1-4	Tables 6.1-2, 6.2-9, 6.5-2, 6.6-1, 6.7-2, 6.7-3	Net infiltration maps
LB02091DSSCP3I.002 [161433]	6.1.5, 6.2, 6.4.1			1-D Site scale calibrated properties
LB02092DSSCFPR.002 [162128]	6.1.5, 6.2, 6.3.4, 6.4.1, 7.2			2-D site scale calibrated fault properties
LB0205REVUZPRP.001 [159525]	6.2.3			Fracture properties
LB991121233129.001 [147328]	6.2		Tables 6.2-2	PTn fracture-matrix parameters (for present-day, mean infiltration)
LB991121233129.003 [147335]	6.2		Tables 6.2-3	PTn fracture-matrix parameters (for present-day, upper-bound infiltration)
LB991121233129.005 [147346]	6.2		Tables 6.2-4	PTn fracture-matrix parameters (for present-day, lower-bound infiltration)
GS950208312232.003 [105572]	6.3.2, 6.3.3			Surface temperature for boreholes NRG-6 and NRG-7a
GS970808312232.005 [105978] GS971108312232.007 [105980]	6.3.3	Figure 6.3-2		Temperature data in boreholes NRG-7a, SD-12 UZ#4, UZ#5 and UZ-7a
GS960808312232.004 [105974] GS970108312232.002 [105975] GS980408312232.001 [105982]	6.3.3	Figure 6.3-2		Temperature data in boreholes NRG-6, NRG-7a, SD-12 UZ#4, UZ#5 and UZ-7a

Table 4.1-1. Input Data Source and Data Tracking Numbers (Continued)

Current DTN	Location in this report			Description/Remarks
	Text	Figure	Table	
LB0210THRMLPRP.001 [160799]	6.3.4, 6.4.1, 6.7.1			Thermal properties
LB0302AMRU0035.001 [162378]	6.4.1			Measured atmospheric barometric pressure
LB991091233129.001 [125868]	6.4.2	Figures 6.2-4, 6.4-1, 6.4-2, 7.4-2	Table 6.4-1	Pneumatic pressure data used for calibration
LB02092DSSCFPR.001 [162422]	6.4.1, 6.4.2	Figure 7.4-1	Table 7.4-1	Pneumatic pressure data used for calibration
LA0003JC831362.001 [149557]	6.7.1, 6.8.2.1			Diffusion coefficients for conservative and active components
LA0010JC831341.001 [162476] LA0010JC831341.002 [153321] LA0010JC831341.003 [153322] LA0010JC831341.004 [153323] LA0010JC831341.005 [153320] LA0010JC831341.006 [153318] LA0010JC831341.007 [153319]	6.7.1		Table 6.7-1	Sorption coefficients

Note: *DTN LB03013DSSCP3I.001 and DTN LB0303THERMESH.001 are the output DTNs. They are source DTNs for DTN LB0303THERMSIM.001 and DTN LB0303GASFLW3D.001 as well.

This Model Report documents the flow models and submodels in the UZ Flow and Transport Model. It utilizes properties from the Calibrated Properties Model (BSC 2003 [160240]). The input and output files for the model runs presented in this Model Report are listed in Tables 6.2-9, 6.6-1, 6.7-2, and 6.7-3, and some of the model input fracture and matrix parameters are given in Attachment I. The data used as direct input for the UZ flow model and UZ flow fields are all qualified in accordance with the requirements of QARD. The model input data are available, qualified data except some borehole temperature data used as corroborative for thermal model validation (Section 7.7) and sorption coefficient (K_d) data used for Sr model validation (Section 7.10). The qualified data are appropriate for this study because they represent fracture and matrix properties calibrated for the UZ at Yucca Mountain,. The appropriateness of the data is also discussed in Sections 6 and 7 when they are used for modeling and validation efforts.

4.2 CRITERIA

Technical requirements to be satisfied by performance assessment (PA) are based on 10 CFR 63.114 [156605] (*Requirements for Performance Assessment*) and 10 CFR 63.115 [156605] (*Requirements for Multiple Barriers*). They are identified in the *Yucca Mountain Project Requirements Document* (Canori and Leitner 2003 [161770]). The acceptance criteria that will be used by the Nuclear Regulatory Commission (NRC) to determine whether the technical requirements have been met are identified in the *Yucca Mountain Review Plan, Final Report*. (YMRP; NRC 2003 [163274]). The pertinent requirements and acceptance criteria for this Model Report are summarized in Table 4.2-1.

Table 4.2-1. Project Requirements and YMRP Acceptance Criteria Applicable to This Model Report

Requirement Number ^a	Requirement Title ^a	10 CFR 63 Link	YMRP Acceptance Criteria
PRD-002/T-016	Requirements for Performance Assessment	10 CFR 63.114(a-c)	Criteria 1 to 4 for <i>Flow Paths in the Unsaturated Zone</i> ^b
PRD-002/T-015	Requirements for Multiple Barriers	10 CFR 63.115(a-c)	Criteria 1 to 3 for <i>Demonstration of Multiple Barriers</i> ^c

NOTES: ^a from Canori and Leitner 2003 [161770])

^b from NRC (2003 [163274], Section 2.2.1.3.6.3)

^c from NRC (2003 [163274], Section 2.2.1.1.3)

The acceptance criteria applicable to this Model Report identified in Section 2.2.1.3.6.3 of the YMRP (NRC 2003 [163274]) relating to flow paths in the UZ are given below, followed by a short description of their applicability to this Model Report:

- Acceptance Criterion 1, *System Description and Model Integration Are Adequate:*

The aspects of geology, hydrology, geochemistry, and physical phenomena that may affect flow paths in the UZ are adequately considered. Conditions and assumptions in the abstraction of flow paths in the UZ are readily identified and consistent with the body of data presented in the description. The system and model are described in Section 6.1.

The process-level model of flow in the UZ uses assumptions, technical bases, data, and models that are appropriate and consistent with other related U.S. Department of Energy abstractions. The descriptions and technical bases are transparent and traceable to site and design data.

Sufficient data and technical bases to assess the degree to which features, events, and processes have been included in this process-level model are provided.

Adequate spatial variability of model parameters and boundary conditions are employed in process-level models to estimate flow paths in the UZ, percolation flux, and seepage flux. The infiltration boundary condition is output from an approved model that considers future changes in climate. Average parameter estimates used in process-level models are representative of the temporal and spatial discretizations considered in the model.

- Acceptance Criterion 2, *Data Are Sufficient for Model Justification:*

Hydrological values used in the safety case are adequately justified. Adequate descriptions of how data were used, interpreted, and appropriately synthesized into the parameters are provided.

Estimates of deep-percolation flux rates are based on a technically defensible UZ flow model that reasonably represents the physical system. The flow model is calibrated using site-specific hydrological, geological, and geochemical data. Deep-percolation flux is estimated, using the appropriate spatial and temporal variability of model parameters, and

boundary conditions that consider climate-induced change in infiltration. Flow fields are computed for all relevant future climate states.

Sensitivity or uncertainty analyses are performed to assess data sufficiency and determine the possible need for additional data.

Accepted and well-documented procedures are used to construct and calibrate numerical models.

Process-level conceptual and mathematical models are used in the analyses. Mathematical models are provided that are consistent with conceptual models and site characteristics, and the robustness of results from different mathematical models is compared. Input data used to develop this model are summarized in Section 4.

- Acceptance Criterion 3, *Data Uncertainty Is Characterized and Propagated through the Model Abstraction*:

Models use parameter values, assumed ranges, probability distributions, and/or bounding assumptions that are technically defensible, and reasonably account for uncertainties and variabilities. The multiple flow fields generated by the UZ Model capture the uncertainty in the parameter values and boundary conditions, as summarized in Section 8.1.1.

The initial conditions, boundary conditions, and computational domain used in sensitivity analyses and/or similar analyses are consistent with available data and output from approved models. Parameter values are consistent with the initial and boundary conditions and the assumptions of the conceptual models for the Yucca Mountain site.

Uncertainties in the characteristics of the natural system are considered.

- Acceptance Criterion 4, *Model Uncertainty Is Characterized and Propagated through the Model Abstraction*:

Alternative modeling approaches of features, events, and processes consistent with available data and current scientific understanding are investigated. The results and limitations are appropriately considered in the abstraction. Model uncertainty is captured by alternative parameter sets as discussed in Section 6.9.

This includes all the criteria identified in the TWP (BSC 2002 [160819], Table 3.1) except Acceptance Criterion 5 for UZ flow paths. This one has been omitted because the flow fields are used directly in the TSPA, rather than being abstracted for use in TSPA. Therefore, there is no need to show that the abstractions match the results of process-level models.

The acceptance criteria identified in Section 2.2.1.1.3 of the YMRP (NRC 2003 [163274]) are given below, followed by a short description of their applicability to this Model Report:

- Acceptance Criterion 1, *Identification of Barriers Is Adequate*:

The surficial soils and topography, unsaturated rock layers above the repository (and below surficial soils), and the unsaturated rock layers below the repository (and above the

water table) are natural barriers important to waste isolation. These barriers function by diverting and substantially reducing the movement of percolating groundwater. The capabilities of these barriers are determined by their hydrological properties and the hydrological environment as implemented in this and other models for infiltration and flow in the UZ. The barriers are identified and analyzed in Section 6.

- Acceptance Criterion 2, Description of Barrier Capability to Isolate Waste Is Acceptable:

The capability of the identified barriers to prevent or substantially delay the movement of water is adequately identified and described. The uncertainty associated with barrier capabilities is adequately described. Section 8.10 describes the barrier capability.

- Acceptance Criterion 3, Technical Basis for Barrier Capability Is Adequately Presented:

The technical bases are consistent with the technical basis for the performance assessment. The technical basis for assertions of barrier capability is commensurate with the importance of each barrier's capability and the associated uncertainties. The technical basis for the barrier capability is presented throughout Section 6.

4.3 CODES AND STANDARDS

No specific formally established standards have been identified as applying to this analysis and modeling activity.

5. ASSUMPTIONS

There is no need to assume numerical values for lack of information in the development of the UZ flow model and its submodels. Several approximations and idealizations were used for model development, such as selection of hydrogeological conceptual models, use of numerical modeling approaches, and specification of model boundary conditions. These are discussed and justified as appropriate in Section 6. The methodological premises used for specific modeling studies are more appropriately discussed in the context of the modeling methodologies in Section 6.

INTENTIONALLY LEFT BLANK

6. MODEL DISCUSSION

As outlined in Section 1, this Model Report documents the development and results of the Unsaturated Zone Flow and Transport Model (UZ Model) and the temperature and geochemistry submodels. This section consists of the following:

- Model description (Section 6.1)
- 3-D (three-dimensional) UZ flow model calibrations (Section 6.2)
- Ambient geothermal model (Section 6.3)
- Gas flow analysis and pneumatic calibration (Section 6.4)
- Geochemical submodel for chloride (Section 6.5)
- Flow patterns and analysis of 3-D flow fields (Section 6.6)
- Tracer transport (Section 6.7)
- Sensitivity analysis of active-fracture-model parameters (Section 6.8)
- Uncertainty and alternative models (Section 6.9)

The UZ Flow Model, temperature model, and geochemistry submodels have all been developed to simulate past, present, and future hydrological, geothermal, and geochemical conditions in the UZ of Yucca Mountain. In the last decade, Yucca Mountain has been studied extensively, and many types of data have been collected. These data have been used in developing conceptual and numerical models for investigating the hydrological, geothermal, and geochemical behavior of the site. These models simulate ambient conditions and perform predictive studies of changes in the mountain caused by climatic, thermal, and geochemical perturbations. The comprehensive model that integrates all pertinent data from the UZ at Yucca Mountain is the 3-D site-scale UZ Model, developed over the past decade (as documented e.g., in Bodvarsson et al. 1999 [120055]; Wu et al. 1999 [117161]; 2002 [160195]). Model development described in this Model Report results from the continued modeling investigations and field studies of flow and transport behavior in the UZ system of Yucca Mountain.

The UZ Model is a process model developed according to the *Technical Work Plan for: Performance Assessment Unsaturated Zone* (BSC 2002 [160819]) and for support of the License Application (LA). The Total System Performance Assessment for License Application (TSPA-LA) will use the UZ flow simulations to provide input to other models such as ambient and thermal drift-scale models, the mountain-scale thermal-hydrological model, and the radionuclide transport model. The UZ Model and its submodels evaluate features and processes that are important to the performance of the repository, all of which contribute to the TSPA-LA, such as:

- The spatially distributed values of the percolation flux at the repository horizon
- The components of fracture and matrix flow at and below the repository horizon

- The flow diversion in the PTn unit
- The perched-water zones and associated flow barriers
- The probable flow paths from the repository to the water table
- Tracer transport times and paths from the repository to the water table, and breakthrough curves and areas at the water table for tracers.

In developing the UZ Model, the main objective has been placed on preparing a defensible and credible UZ Model for Yucca Mountain to evaluate it as an underground radioactive waste repository. Major activities, as reported in this Model Report, include updated model calibration studies of 3-D UZ flow, PTn and perched water, geochemistry, geothermal conditions, estimates of tracer transport times and radionuclide transport, and intensive model validation efforts.

Other activities involved generating 18 3-D flow fields (Sections 6.2 and 6.7) to evaluate the uncertainties and sensitivity of the UZ Model relative to fracture-matrix parameters and infiltration rates over the mountain, by using six sets of model parameters and nine infiltration scenarios. A total of 18 flow fields (nine base cases and nine alternatives) have been submitted to the TDMS as output DTNs. The nine base case flow fields are provided for use in TSPA calculations of radionuclide transport through the UZ system, and for other activities such as drift seepage abstraction. The other nine alternatives show the results of using an alternative conceptual model (Sections 6.5, 6.6, and 6.7).

The scientific notebooks (with relevant page numbers) used for modeling and validation activities described in this Model Report are listed in Table 6-1.

Table 6-1. Scientific Notebooks Used in Model-Development Documentation

LBL Scientific Notebook ID	M&O Scientific Notebook ID	Relevant Pages	Citation
YMP-LBNL-YSW-3	SN-LBNL-SCI-199-V1	pp. 65–70, 81–278	Wang 2003 [162417]
YMP-LBNL-YSW-KZ-1	SN-LBNL-SCI-202-V1	pp. 68–97, 105–111	Wang 2003 [162417]
YMP-LBNL-ELS-GL-1	SN-LBNL-SCI-219-V1	pp. 74–83, 120–150	Wang 2003 [162417]
YMP-LBNL-HHL-GZ-1	SN-LBNL-SCI-227-V1	pp. 87, 89–119	Wang 2003 [162417]
YMP-LBNL-GSB-TX-1	SN-LBNL-SCI-160-V1	pp. 89–92	Wang 2003 [162417]
YMP-LBNL-GSB-LHH-3	SN-LBNL-SCI-215-V1	pp. 107–119	Wang 2003 [162417]
YMP-LBNL-UZ-ELS-1	SN-LBNL-SCI-170-V1	pp. 42–44	Wang 2003 [162417]
YMP-LBNL-YSW-3.1	SN-LBNL-SCI-199-V2	pp. 7-26	Wang 2003 [162417]

6.1 MODEL DESCRIPTION

The conceptual and numerical models used for the modeling studies are documented in this Model Report as well as in the AMR, *Conceptual and Numerical Models for Flow and Transport* (CRWMS M&O 2000 [141187]). The conceptual and numerical models are presented in this section so that a complete discussion of the model can be made.

6.1.1 Geological Model and Numerical Grids

The geological model used for developing the UZ Model and its submodels is the Geological Framework Model (GFM2000; MO0012MWDGFM02.002 [153777]). The development and features of the 3-D model grids are documented in the report entitled *Development of Numerical Grids for UZ Flow and Transport Modeling* (BSC 2003 [160109]). Table 6.1-1 lists the geological units/layers for different hydrogeologic units and the associated UZ Model numerical grid-layer information. These geologic formations have been organized into layered hydrogeologic units based primarily on the degree of welding (Montazer and Wilson 1984 [100161]). These are the Tiva Canyon welded (TCw) hydrogeologic unit, the Paintbrush nonwelded unit (PTn), the Topopah Spring welded (TSw) unit, the Calico Hills nonwelded (CHn), and the Crater Flat undifferentiated (CFu) units.

Table 6.1-1. GFM2000 Lithostratigraphy, UZ Model Layer, and Hydrogeologic Unit Correlation Used in the UZ Flow Model and Submodels

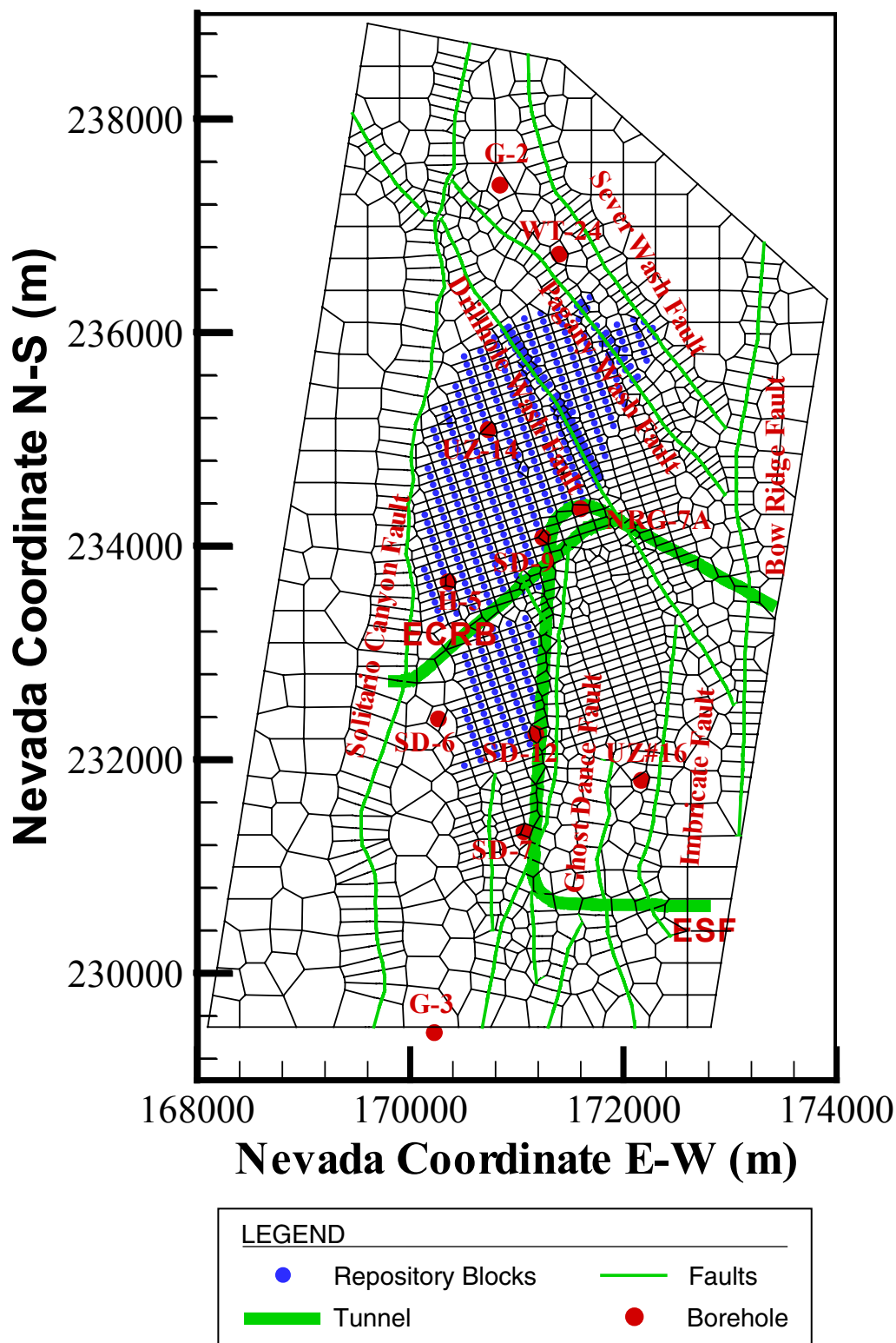
Major Unit (Modified from Montazer and Wilson 1984 [100161])	Lithostratigraphic Nomenclature (BSC 2002 [159124])	UZ Model Grid Layer* (BSC 2003 [160109])	Hydrogeologic Unit (Flint 1998 [100033])
Tiva Canyon welded (TCw)	Tpcr	tcw11	CCR, CUC
	Tpcp	tcw12	CUL, CW
	TpcLD		
	Tpcpv3	tcw13	CMW
	Tpcpv2		
Paintbrush nonwelded (PTn)	Tpcpv1	ptn21	CNW
	Tpbt4	ptn22	BT4
	Tpy (Yucca)	ptn23	TPY
		ptn24	BT3
	Tpbt3		
	Tpp (Pah)	ptn25	TPP
	Tpbt2	ptn26	BT2
	Tptrv3		
	Tptrv2		
Topopah Spring welded (TSw)	Tptrv1	tsw31	TC
	Tptrn	tsw32	TR
	Tptrl, Tptf	tsw33	TUL
	Tptpul, RHHtop		
	Tptpmn	tsw34	TMN
	Tptpll	tsw35	TLL
	Tptpln	tsw36	TM2 (upper 2/3 of Tptpln)
		tsw37	TM1 (lower 1/3 of Tptpln)
	Tptpv3	tsw38	PV3
	Tptpv2	tsw39 (vit, zeo)	PV2

Table 6.1-1. GFM2000 Lithostratigraphy, UZ Model Layer, and Hydrogeologic Unit Correlation Used in the UZ Flow Model and Submodels (Continued)

Major Unit (Modified from Montazer and Wilson 1984 [100161])	Lithostratigraphic Nomenclature (BSC 2002 [159124])	UZ Model Grid Layer* (BSC 2003 [160109])	Hydrogeologic Unit (Flint 1998 [100033])
Calico Hills nonwelded (CHn)	Tptpv1	ch1 (vit, zeo)	BT1 or BT1a (altered)
	Tpbt1		
	Tac (Calico)	ch2 (vit, zeo)	CHV (vitric) or CHZ (zeolitic)
		ch3 (vit, zeo)	
		ch4 (vit, zeo)	
		ch5 (vit, zeo)	
	Tacbt (Calicobt)	ch6 (vit, zeo)	BT
	Tcpuv (Prowuv)	pp4	PP4 (zeolitic)
	Tcpuc (Prowuc)	pp3	PP3 (devitrified)
	Tcpmd (Prowmd)	pp2	PP2 (devitrified)
	Tcplc (Prowlc)		
	Tcplv (Prowlv)	pp1	PP1 (zeolitic)
	Tcpbt (Prowbt)		
	Tcbuv (Bullfroguv)		
Crater Flat undifferentiated (CFu)	Tcbuc (Bullfroguc)	bf3	BF3 (welded)
	Tcbmd (Bullfrogmd)		
	Tcbic (Bullfrogic)		
	Tcbiv (Bullfrogiv)	bf2	BF2 (nonwelded)
	Tcbbt (Bullfrogbt)		
	Tctuv (Tramuv)		
	Tctuc (Tramuc)	tr3	Not Available
	Tctmd (Trammd)		
	Tctlc (Tramlc)		
	Tctiv (Tramiv)	tr2	Not Available
	Tctbt (Trambt) and below		

NOTE: * Defined as a rock material type, represented by the code name, for grid blocks belonging to the rock unit.

The 3-D UZ Model domain, as well as the numerical grid for this study, is shown in plan view in Figure 6.1-1, encompassing approximately 40 km² of the area over the mountain. The UZ Model grid, shown in Figure 6.1-1, is referred to as the TSPA-LA grid. It is primarily designed for model calibration and simulations of 3-D flow fields delivered for use in TSPA-LA calculations. This 3-D model grid uses a refined mesh in the vicinity of the repository, located near the center of the model domain, covering the region from the Solitario Canyon fault to Ghost Dance fault in the west-east direction, and from borehole G-3 in the south to beyond Sever Wash fault in the north. Also shown in Figure 6.1-1 are the locations of several boreholes used in model calibrations and analyses. The model domain is selected to focus on the study area of the repository area and to investigate the effects of different infiltration scenarios and major faults on moisture flow around and below the repository. In the model grid, faults are represented in the model by vertical or inclined 30-m-wide zones.



DTN: LB03023DKMGRID.001 [162354]

Figure 6.1-1. Plan View of the 3-D UZ TSPA-LA Model Grid, Showing the Model Domain, Faults Incorporated, Repository Layout, and Several Borehole Locations

The model grid, as shown in Figure 6.1-1, has 2,042 mesh columns of both fracture and matrix continua and an average of 59 computational grid layers in the vertical direction, resulting in 245,506 gridblocks and 989,375 connections in a dual-permeability grid.

6.1.2 Numerical Codes and Modeling Approach

The model calibration and simulation results presented in this Model Report were carried out mainly using TOUGH2 V1.4 (LBNL 2000 [146496]), and T2R3D V1.4 (LBNL 1999 [146654]), as summarized in Section 3. The single active liquid-phase flow module (EOS9) of the TOUGH2 code was used to calibrate the UZ Flow Model and several submodels and to generate 3-D TSPA-LA flow fields. For gas flow simulation and temperature calibration, the TOUGH2 V1.4 (LBNL 2000 [146496]) EOS3 module was used. Tracer transport and chloride studies were performed using the decoupled module of T2R3D V1.4 (LBNL 1999 [146654]) with flow fields generated by the EOS9 module. TOUGH2 V1.4 (LBNL 2000 [146496]) and T2R3D V1.4 (LBNL 1999 [146654]) were selected because they have been baselined through YMP QA procedure AP-SI.1Q for modeling flow and transport in heterogeneous fractured rock (e.g., BSC 2001 [158726]; Wu et al. 2002 [160195]). No other numerical codes could be used for this work, either because they were not qualified and baselined for use at the time of preparing this report, or because they did not have the generalized capability of handling global fracture-matrix interaction, which was needed in modeling studies of this report.

To model flow and transport processes in the UZ system at Yucca Mountain, mathematical models or governing equations are needed to describe the physical processes quantitatively. The physical processes associated with flow and transport in porous media are governed by the fundamental conservation laws (i.e., conservation of mass, momentum, and energy), which govern the behavior of fluid flow, chemical migration, and heat transfer through fractured porous media. The macroscopic continuum approach has been most commonly used in practical applications (Bear 1972 [156269]). In this approach, the physical laws governing flow of several fluids, transport of multicomponents, and heat transfer in porous media are represented mathematically on the macroscopic level by a set of partial differential or integral equations. Fluid and heat flow and chemical-transport processes in fracture and matrix systems in the UZ are described using a macroscopic, dual-permeability continuum approach.

In addition to the conservation or continuity equations of mass and thermal energy in fracture and matrix systems, specific relationships or *mechanisms* are needed that describe how fluid flow, solute/tracer transport, and heat transfer occur in porous and fractured media. The following specific constitutive laws act as such mechanisms by governing local fluid flow, component transport, and heat-transfer processes in porous and fractured media:

1. Under unsaturated conditions, liquid pressure is negative from the capillary suction. In the UZ Flow Model we also call capillary pressure as water potential (by changing the negative sign to "+"). The governing equation for isothermal, unsaturated liquid flow is the Richards' equation (Richards 1931 [104252]; Pruess et al. 1999 [160778], Equation A-17, p. 146), based on the conservation of mass (volumetric water content) and Darcy's law (Bear 1972 [156269]) with flux driven by gravity and capillary pressure gradient. The unsaturated flux is equal to unsaturated hydraulic conductivity times the driving gradient. The hydraulic conductivity is proportional to permeability and fluid density, and inversely proportional to fluid viscosity. The fluid properties are treated as constants under isothermal conditions. The unsaturated permeability (relative

permeability times formation permeability or saturated permeability) is related to both water content (saturation times porosity) and capillary pressure, as described by the model of van Genuchten (1980 [100610]). The governing equations for unsaturated flow under isothermal conditions are given in Attachment V.

The UZ Flow Model adopts the dual-continuum approach for flows through both the fractures and matrix. Richards' equation is applied to both fracture continuum and the matrix continuum. The fluid exchange between fracture continuum and matrix continuum is the fracture-matrix interaction, which is simulated by active fracture model in the UZ Flow Model (Liu et al. 1998 [105729]).

The active fracture model was developed within the context of the dual-continuum approach (Liu et al. 1998 [105729]). It is based on the reasoning that, because of the fingering flow, only a portion of fractures in a connected, unsaturated fracture network contribute to liquid water flow, while other fractures are simply bypassed. The portion of the connected fractures that actively conduct water are called active fractures. In other words, the active fracture model uses a combination of the continuum approach and a simple filtering concept to model fracture flow. Inactive fractures are filtered out in modeling fracture-matrix interaction and flow in the fracture continuum.

The Richards' equation, Darcy's law, and van Genuchten's model can be generalized for multi-phase flows under nonisothermal conditions. The governing equations for both gas-and liquid-flows and temperature are based on conservation of mass of fluid phases, and on conservation of energy for conductive and convective heat transfer processes, respectively. The full set of equations of nonisothermal, two-phase flows of gas and water in both fractures and matrix are presented in Pruess et al. (1999 [160778], Appendix A).

In solving the above equations, a number of variables are known and given as input to the UZ Flow Model. Some of those variables are treated as constants, for example, fluid density and viscosity under isothermal conditions. Others are provided as known parameters measured either in the laboratory or in field tests, and/or further calibrated. Examples of known parameters are rock density, porosity, and permeability. The input parameters are discussed Section 6.1.5. In addition, boundary conditions are needed to solve the equation (Section 6.1.3). The top boundary for the UZ Flow Model is net infiltration from the land surface (Section 6.1.4). With these input parameters and boundary conditions, the solving of the full set of equations (Pruess et al. 1999 [160778]) in the UZ Flow Model provides outputs for variables such as saturation, capillary pressure, and flux, in addition to temperature in the thermal model.

2. The migration of dissolved mass components or chemical species within a fluid in the two-phase, fractured porous media system is governed by advective, diffusive, and dispersive processes. It may also be subject to other processes such as radioactive decay, adsorption, mass exchange or partition between phases, and other chemical reactions under local thermodynamic equilibration or kinetic reactions.
3. The generalized Fick's law (Wu and Pruess 2000 [153972], Equations 3.1.5–3.1.7, pp. 705), including hydrodynamic dispersion effects in a multiphase system, is used to evaluate diffusive and dispersive flux of chemical transport.

In both research and application, the multiphase extension of Darcy's law (Pruess et al. 1999 [160778], Equation A-5, pp. 145), Richards' equation (Richards 1931 [104252]), and the generalized Fick's law (Wu and Pruess 2000 [153972], pp. 704–707) have been used as fundamental laws that govern multiphase flow and transport processes within porous-medium and fractured rocks. These fundamental laws or correlations, based on theory, experiment, and field studies, reflect our current understanding of porous-medium physics. Note that Richards' equation is extended for use in both fracture and matrix flow, as well as interflow.

A key issue for simulating fluid and heat flow and chemical transport in the fractured porous rock of Yucca Mountain is how to handle fracture and matrix flow and interaction under multiphase, multicomponent, and isothermal or nonisothermal conditions. The available methods for treating fluid flow in fractures and the rock matrix using a numerical approach include: (1) an explicit discrete-fracture and matrix representation; (2) the dual-continuum method, including double- and multi-porosity, dual-permeability, or the more general “multiple interacting continua” (MINC) method (Pruess and Narasimhan 1985 [101707]); and (3) the generalized effective continuum method (ECM). For the work documented in this Model Report, the dual-permeability conceptual model is applied to evaluate fluid flow and transport in the fracture-matrix system of the UZ system of Yucca Mountain, in which the active fracture model is adopted to modify fracture-matrix interface areas for flow and transport between fracture and matrix systems.

The dual-continuum conceptualization provides an appropriate representation of flow and transport processes within the UZ at Yucca Mountain (Doughty 1999 [135997]; CRWMS M&O 2000 [141187]). It is much less demanding in computational effort or in data requirements than the discrete-fracture-modeling approach. Therefore, the dual-continuum method has become the main approach used in the modeling studies of the Yucca Mountain Project (Wu et al. 1999 [117161]; 2002 [160195]). The dual-permeability methodology for handling fluid flow, tracer transport, and heat transfer through fractured rocks treats fracture and rock matrix flow and interaction with a multicontinuum numerical approach. It considers global flow occurring not only between fractures but also between matrix gridblocks. In this approach, each gridblock of the primary mesh is divided into two gridblocks, one for fracture and the other for matrix, connected to each other. Because of the one-block representation of fracture or matrix, the interflow between fractures and matrix has to be handled using a quasi-steady-state flow approximation, and this may limit its application in estimating the gradients of pressures, temperatures, and concentrations within the matrix. Note that the UZ Flow Model of this Model Report has been developed to simulate steady-state UZ flow conditions at Yucca Mountain. Under steady-state flow conditions, however, such gradients near the matrix surfaces become minimal, and the one-block matrix-fracture model is expected to produce accurate solutions (Doughty 1999 [135997]).

As applied in this Model Report, the traditional dual-permeability concept is first modified using an active fracture model (Liu et al. 1998 [105729]) to represent fingering effects of liquid flow through fractures and to limit flow into the matrix system. The active fracture concept has been evaluated in the *Analysis of Hydrologic Properties Data Report* (BSC 2003 [161773]) and further sensitivity analyses are provided in Section 6.8 of this Model Report. The dual-permeability model is also modified by adding additional global fracture-matrix connections at interfaces of TCw-PTn, PTn-TSw, and vitric-nonvitric units to better simulate fracture-matrix flow at these transitions. These additional global fracture-matrix connections do not exist in the

original dual-permeability model. Specifically, TCw fractures are vertically connected to the PTn matrix, PTn matrix to TSw fractures, and vitric matrix to nonvitric fractures, respectively, along these interfaces. Note that vitric units in the CHn are handled as single-porosity matrix only (i.e., the effect of fractures on flow and transport within Calico Hills vitric zones is neglected). This conceptual model is supported by observation from the tracer tests (BSC 2001 [160828]; BSC 2001 [156609], p. 136).

As an alternative modeling approach, the discrete fracture or weeps type model face extremely high uncertainties in fracture distribution data within the mountain and an extensive computational burden that cannot be solved in the near future. On the other hand, the ECM approach, although the most computationally efficient, may not capture important, non-equilibrium interaction in flow and transport between fractures and matrix.

In model calibration of moisture flow and tracer transport, ambient variably saturated flow in the UZ underlying Yucca Mountain is approximated as an isothermal, steady-state flow system. This is considered to be a good approximation within the UZ below the PTn unit, because the relatively unfractured nonwelded PTn unit is expected to damp and homogenize downward-moving transient pulses arising from episodic surface infiltration events, and geothermal temperature or gradients have little effect on ambient percolation (Wu et al. 2000 [154918]; Wu et al. 2002 [161058]; Flint et al. 2003 [163967]). Therefore, estimated surface net infiltration rates are described as steady-state water recharge (Section 6.1.4).

In the development of the UZ flow model and its submodels over the past decade, the steady-state nature of the flow fields and the damping of transient pulses were evaluated in different studies. Wu et al. (1999 [117161], p. 186) referred to the early work of Wang and Narasimhan (1985 [108835]; 1993 [106793], Figure 7.4.7) which suggested that effects of infiltration pulses at the surface are damped by the underlying tuff units, especially the PTn. The welded tuff of the potential repository horizon exhibited only small changes in saturations, pressures, and potentials from steady-state values in response to the transient pulses. Pan et al. (1997 [164181]) investigated transient flow behavior for downward water flow through sloping layers in the vadose zone, with upslope flow developed during heavy rain likely enhancing the downward flow. Wu et al. (2002 [161058], p. 35-11) analyzed the capillary barrier capacities in unsaturated units and indicated that, on average, it took several thousands years for water to travel through the PTn. Both Wu et al. (2000 [154918]; 2002 [161058]) and Flint et al. (2003 [163967]) analyzed the implications of capillary barrier development in subunits of the PTn for lateral diversion of flow in the PTn. Along sloping layers, strong capillary barrier capacities promote lateral diversions. The degree of lateral diversion can be further evaluated by comparative sensitivity studies, by detailed analysis of field data including geochemical evidences, and by long-term controlled field tests.

6.1.3 Model Boundary Conditions

The ground surface of the mountain (or the tuff-alluvium contact in areas of significant alluvial cover) is taken as the top model boundary; the water table is treated as the bottom model boundary. Both the top and bottom boundaries of the model are treated as Dirichlet-type conditions with specified constant but spatially varying temperature and gas pressure. A constant liquid saturation value of 0.99 was set for the bottom boundary. For flow simulations using the EOS9 module, only pressure or saturation values are needed along the top and bottom model boundaries. Surface infiltration, as discussed below in Section 6.1.4, is applied using a source

term in the fracture gridblocks within the second grid layer from the top. This method was adopted because the first layer is treated as a Dirichlet-type boundary with constant pressure, saturation, and temperature to represent average atmospheric conditions at the mountain.

The water table is used as the bottom model boundary, a surface where the water pressure is a fixed, single value. Within the numerical models, only one single set of model primary variables for solving Richards' equations is specified for the bottom boundary, and this is equivalent to specifying a constant saturation. For gas and heat flow simulations, the bottom model boundary representing the water table is subject to fixed gas pressure, equal to the atmospheric pressure at the elevation (Sections 6.3.3 and 6.4.1). All lateral boundaries, as shown in Figure 6.1-1, are treated as no-flow (closed) boundaries, which allow flow only along the vertical plane. This treatment is reasonable for the eastern boundary, which is along or near the Bow Ridge fault, because high vertical permeability and lower capillary forces are expected within the faults (see fault properties estimated in BSC (2003 [160240])). For the western and northern lateral boundaries, no-lateral-flow boundaries would have little effect on moisture flow within and near the repository areas because these boundaries are separated from the repository by faults. For the southern lateral boundary, this is also true because it is far from the repository (Figure 6.1-1).

The spatially distributed values of temperatures along the top and bottom boundaries are based on field observation. This treatment is corroborated by data reported by Sass et al. (1988 [100644]) and the calibrated temperature distribution along the water table (BSC 2001 [158726]), and further confirmed by matching qualified temperature profiles from a number of boreholes as described in Section 6.3.

Pressure conditions at the bottom boundary of the model are based on observed gas-pressure values. The water table, which is the bottom boundary of the UZ Model, is shown to be a relatively flat, stable surface in most of the model domain, increasing its elevation only in the north (BSC 2003 [160109]). The rise in the north has little effect on flow simulation results within the vertical model domain, because the flow is essentially determined by upstream, not downstream (water table) conditions in the UZ. In the eastern part of the site to the Solitario Canyon fault, the water table elevation of the flat portion is about 730 m above sea level (masl) (BSC 2003 [160109]). In specifying water boundary conditions at the water table, capillary rise is not included. This is because borehole measurements of matrix saturation and water potential show small capillary fringes (e.g., Figure 6.2-3) at the water table, which can be ignored by the large-scale UZ model. The gas pressures are estimated using a pressure value of 92 kPa at an elevation of 730 m. Surface gas pressures are determined by running the TOUGH2 code, EOS3 module to steady-state under given temperature, bottom pressure, and surface-infiltration conditions. This is necessary to generate a steady state, equilibrated gas-pressure boundary to avoid artificial airflow or circulation, which may occur if nonequilibrated pressures are imposed on the ground surface boundaries.

6.1.4 Infiltration Scenarios

Water entering the UZ as net infiltration from precipitation at land surface is the major control on overall hydrological and thermal-hydrological conditions within the UZ at Yucca Mountain. Net infiltration is the ultimate source of percolation through the UZ. Water percolating downward through the UZ will be the principal means by which radionuclides may be transported from the repository to the water table.

The UZ Model uses net infiltration rates as surface water recharge boundary conditions. The net infiltration rates consist of present-day and future scenarios, determined by studies of modern and future climates (USGS 2001 [158378] and USGS 2001 [160355]). A total of nine net infiltration maps (DTN: GS000308311221.005 [147613]) are implemented with the UZ Model and its submodels. These infiltration maps are documented in two AMRs: *Future Climate Analysis* (USGS 2001 [158378]); *Simulation of Net Infiltration for Modern and Potential Future Climates* (USGS 2001 [160355]) for infiltration and climate models. They include present-day (modern), monsoon, and glacial transition—three climatic scenarios, each of which consists of lower-bound, mean, and upper-bound rates. The nine infiltration rates are summarized in Table 6.1-2 for average values over the model domain. Note that the UZ Model is concerned primarily with steady-state flow under each infiltration scenario, while in the climate models reference to future climates means climates are expected to act sequentially over the modeled period: present-day, monsoon, and then glacial transition for specific periods.

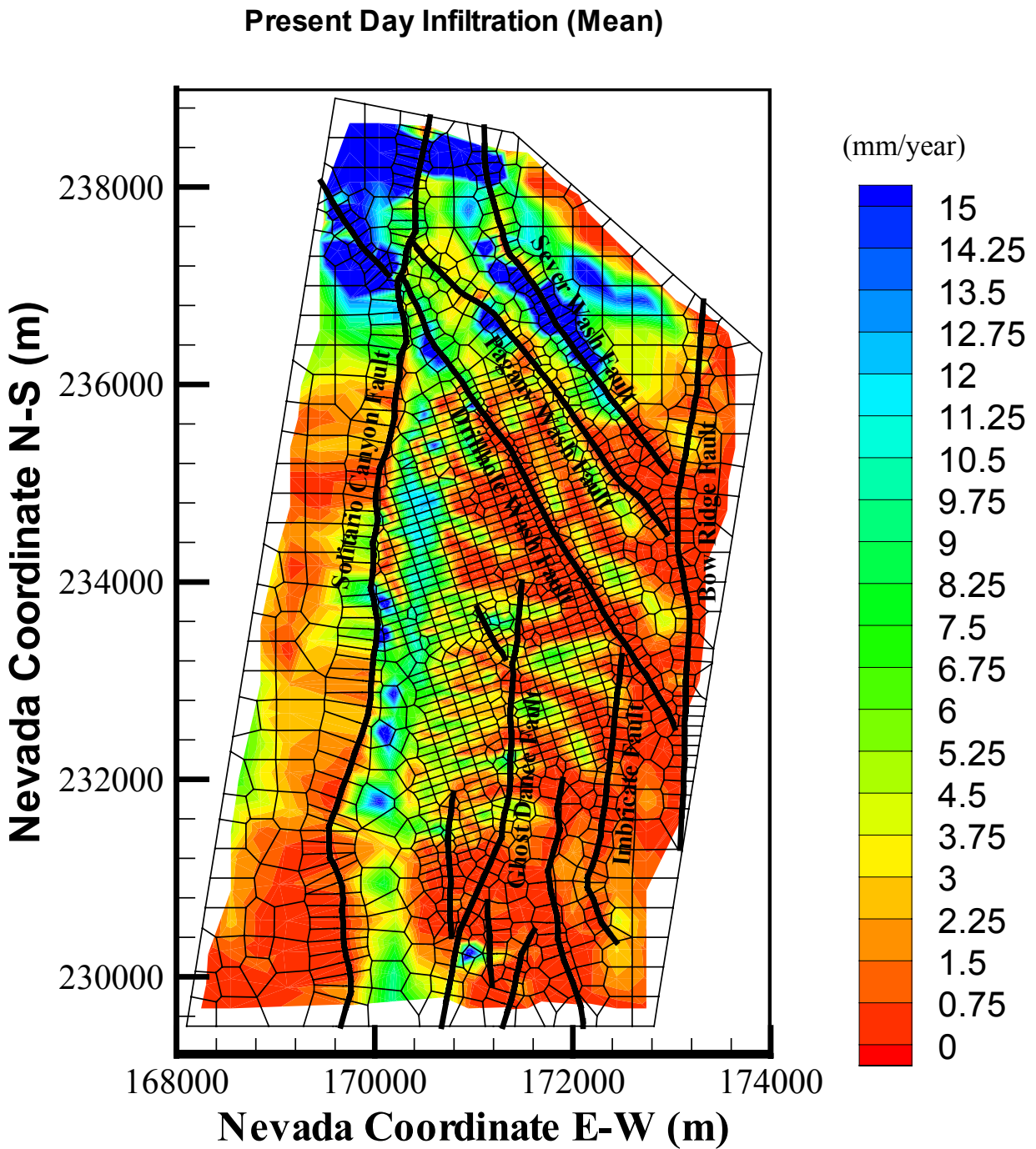
Table 6.1-2. Infiltration Rates (mm/year) Averaged over the UZ Model Domain

Scenario	Lower-Bound Infiltration	Mean Infiltration	Upper-Bound Infiltration
Present-Day/Modern	1.25	4.43	10.74
Monsoon	4.43	11.83	19.23
Glacial Transition	2.35	17.02	31.69

Values averaged from DTN: GS000308311221.005 [147613]

As shown in Table 6.1-2, the average rate over the model domain for the present-day mean infiltration with the UZ Model grid is 4.43 mm/yr (Wang 2003 [162417], SN-LBNL-SCI-199-V1, pp. 99–101), which is considered as a base-case infiltration scenario. The use of the lower- and upper-bound infiltration values is intended to cover the uncertainties associated with the infiltration for each climate. The two future climatic scenarios, the monsoon and glacial transition periods, are used to account for possible climate-induced changes in precipitation and net infiltration. Note that the glacial transition has higher infiltration rates except for the lower-bound case. The average values in Table 6.1-2 are estimated using the TSPA-LA grid, shown in Figure 6.1-1 for infiltration maps (DTN: GS000308311221.005 [147613]), and the software routine infil2grid V1.7 (LBNL 2002 [154793]). Net infiltration is handled in a consistent manner in this report, i.e., mapping the USGS infiltration maps to model grids.

A plan view of the spatial distribution in the three mean infiltration maps, as interpolated onto the TSPA-LA grid, is shown in Figures 6.1-2, 6.1-3 and 6.1-4 respectively, for the present-day, monsoon, and glacial transition mean infiltration scenarios. The figures show similar patterns of flux distributions with the three infiltration rates, with higher infiltration rates in the northern part of the model domain and along the mountain ridge east of the Solitario Canyon fault.



DTN: GS000308311221.005 [147613]

Figure 6.1-2. Plan View of Net Infiltration Distributed over the 3-D UZ TSPA-LA Model Grid for the Present-Day (Base-Case) Mean Infiltration Scenario

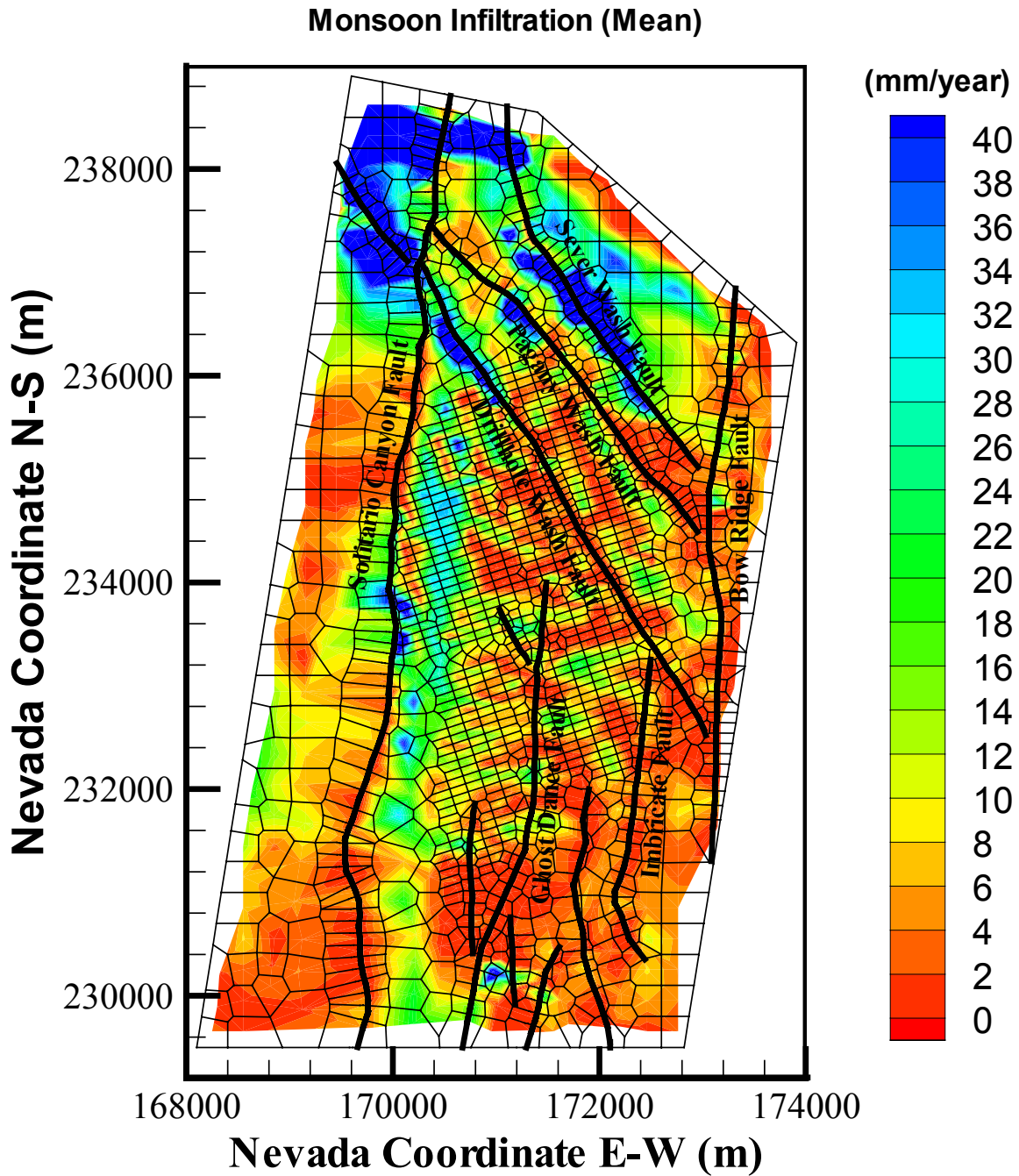
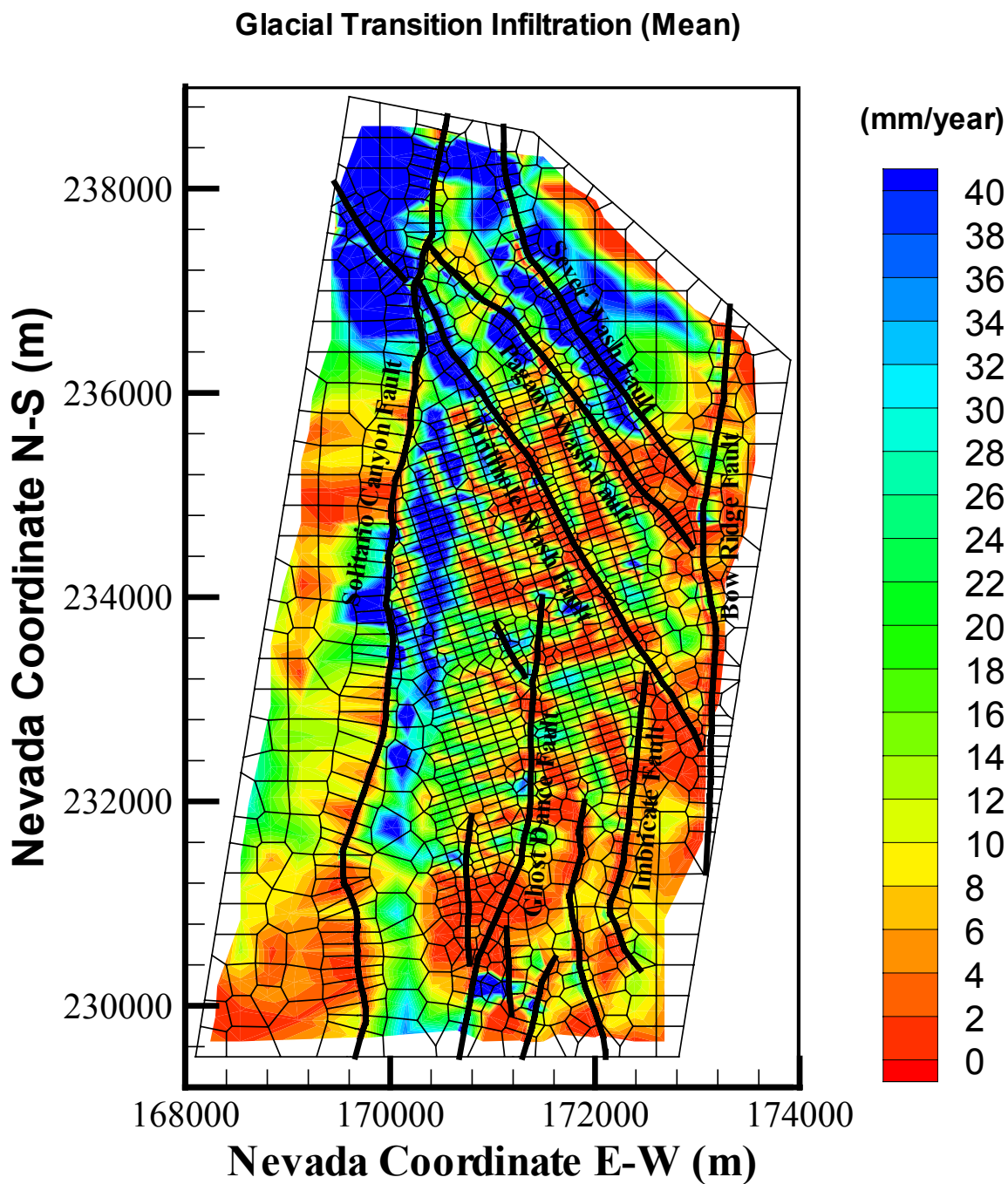


Figure 6.1-3. Plan View of Net Infiltration Distributed over the 3-D UZ TSPA-LA Model Grid for the Monsoon Mean Infiltration Scenario



DTN: GS000308311221.005 [147613]

Figure 6.1-4. Plan View of Net Infiltration Distributed over the 3-D UZ TSPA-LA Model Grid for the Glacial Transition Mean Infiltration Scenario

6.1.5 Model Parameters and Rock Properties

The key input rock and fluid-flow parameters used in UZ Model development are summarized in Section 4. They include (1) fracture properties (frequency, permeability, van Genuchten α and m parameters, porosity, fracture-matrix interface area, and residual and saturated saturations) for each UZ Model layer; (2) matrix properties (porosity, permeability, the van Genuchten α and m parameters, and residual and saturated saturations) for each UZ Model layer; (3) thermal and transport properties (grain density, wet and dry thermal conductivity, grain specific heat, and tortuosity coefficients) for each UZ Model layer; and (4) fault properties (fracture parameters, DTN: LB02092DSSCFPR.002 [162128]) for each of the major hydrogeologic units (Table 6.1-1). The development and estimation of these parameters are presented in the report, *Calibrated Properties Model* (BSC 2003 [160240]) (DTN: LB02091DSSCP3I.002 [161433]), as well as the calibration results of this Model Report.

The rock-parameter specification in the 3-D UZ Model and its submodels is, in general, layer-wise uniform (BSC 2003 [160109]). However, certain portions of grid layers representing the CHn unit are partly altered from vitric to zeolitic. In these altered layers, different rock properties are specified for vitric or zeolitic zones. The UZ model treats all of the geological units, including those representing fault zones, as fracture-matrix systems using a dual-permeability approach, except the CHn vitric zones, which are treated as single-porosity matrix. Global fracture-matrix connections are added to those across interfaces between TCw-PTn, PTn-TSw, and vitric-nonvitric units to model transition between fracture- and matrix-dominated flow at these interfaces. In addition, the van Genuchten relative permeability and capillary pressure functions (van Genuchten 1980 [100610]) are used to describe flow in both fractures and matrix.

6.2 3-D UZ FLOW MODEL CALIBRATION

A critical step in developing the 3-D UZ flow model was to use field-measured liquid saturation, water potential, perched-water, pneumatic, and isotopic tracer data for calibrations of the 3-D model. This is part of the important iterative processes of model calibration and verification, which increase confidence in model predictions for the site conditions. A detailed modeling investigation is reported in BSC (2003 [160240]) using one-dimensional (1-D) models for estimating model parameters with water potential, saturation, and other types of data. However, these 1-D models cannot predict whether lateral flow or perched water occurs in several hydrogeological units below the repository level. This section documents a further model calibration effort, focusing on the 3-D flow patterns: perched-water calibrations using the 3-D model grid (Figure 6.1-1).

The 3-D flow model calibration is conducted using the three sets of parameters of 1-D site-scale calibrated properties (BSC 2003 [160240]; DTN: LB02091DSSCP3I.002 [161433]), 2-D site-scale calibrated fault properties (DTN: LB02092DSSCFPR.002 [162128]), three present-day infiltration rates (See Table 6.1-2), and the geological model and numerical grid for calibration (BSC 2003 [160109]). In addition, previously developed 3-D properties for the PTn unit (BSC 2001 [158726]; DTNs: LB991121233129.001 [147328]; LB991121233129.003 [147335]; LB991121233129.005 [147346]) are adopted for the PTn properties in this Model Report. A permeability-barrier water-perching model is developed. In this model, rock properties are locally adjusted in several grid layers of the lower basal vitrophyre in the TSw unit and upper zeolites in the CHn unit. The objective of perched-water calibrations is (1) to match perched-

water occurrences as observed at the site and (2) to investigate the effects of flow-through and bypassing of perched bodies on tracer transport.

6.2.1 Calibration Data

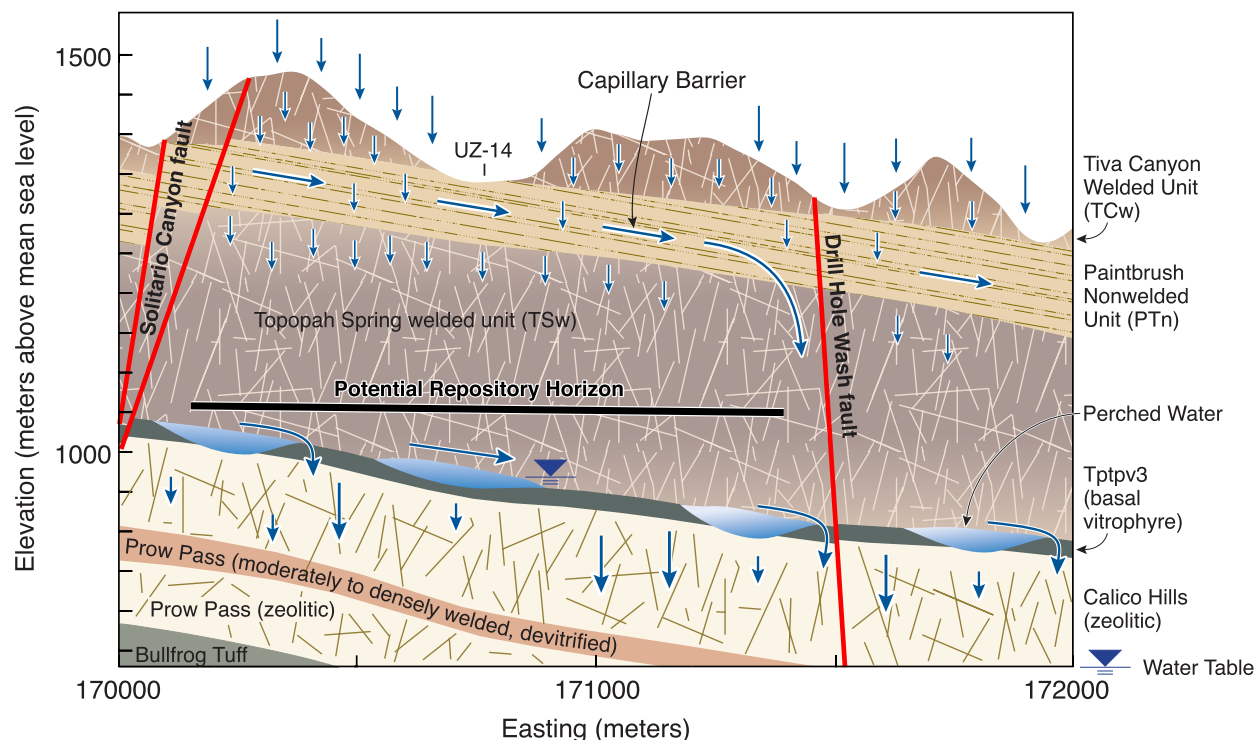
The field data used in the 3-D UZ flow model calibration are matrix liquid saturations, matrix water potentials, and perched-water elevations, as observed from boreholes. Table 6.2-1 shows the types of data from boreholes used in the calibration, and Figure 6.1-1 shows the locations of the boreholes and the tunnel at Yucca Mountain.

Table 6.2-1. Borehole Data Used for 3-D Flow Model Calibration

Borehole	Matrix Liquid Saturation (core)	Matrix Liquid Water Potential	Perched Water Elevation (masl)
USW NRG-7a	MO0109HYMXPROP.001 [155989]		Rousseau et al. 1997 [100178]
USW SD-6	GS980808312242.014 [106748]	GS980808312242.014 [106748]	
USW SD-7	MO0109HYMXPROP.001 [155989]		SNT02110894001.002 [105067]
USW SD-9	MO0109HYMXPROP.001 [155989]		Rousseau et al. 1999 [102097]
USW SD-12	MO0109HYMXPROP.001 [155989]	GS980408312232.001 [105982] (<i>in situ</i> measurement) (organized in LB0208UZDSCPMI.001 [161285] and MO0109HYMXPROP.001 [155989])	Rousseau et al. 1997 [100178]
USW UZ-14	MO0109HYMXPROP.001 [155989]		GS960308312312.005 [107230]
UE-25 UZ#16	MO0109HYMXPROP.001 [155989]		
USW WT-24		GS980708312242.010 [106752]	GS980508312313.001 [109746]
USW G-2			GS980508312313.001 [109746]

6.2.2 Conceptual Models of UZ Flow

Subsurface flow and transport processes in the UZ occur in a heterogeneous system of layered, anisotropic, fractured volcanic rocks. Greater understanding of such processes has been provided by a continuous effort of data collection and analysis as well as modeling studies (BSC 2001 [158726]). The AMR entitled *Conceptual and Numerical Model for the Unsaturated Zone Flow and Transport* (CRWMS M&O 2000 [141187]) presents a discussion of these conceptual models used in the study of UZ flow processes within this Model Report. Figure 6.2-1 illustrates a typical geological profile along a vertical east-west transect as well as the conceptual model that characterizes potential lateral flow in the PTn unit, and the effects of faults and perched water on the UZ system.



UZ03-002

Figure 6.2-1. Schematic Showing the Conceptualized Flow Processes and Effects of Capillary Barriers, Major Faults, and Perched-Water Zones within a Typical Cross Section of the UZ Flow Model Domain in the East-West Direction

The PTn unit, as described by the current geological model, consists primarily of non- to partially welded tuffs. The dip of these layers is generally less than 10° to the east or southeast. The combined thickness of the PTn layers ranges from 150 m in the north end of the model area to 30 m in the south end. The PTn unit as a whole exhibits very different hydrogeologic properties from the TCw and TSw units that bound it above and below. Both the TCw and the TSw have low porosity and intense fracturing typical of the densely welded tuffs at Yucca Mountain. In contrast, the PTn has high porosity and low fracture intensity, and its matrix system has a large capacity for storing groundwater. It has been shown to effectively damp spatial and temporal variations in percolation flux (Wu et al. 2000 [154918], pp. 30–32, 39–41). Therefore, water flow through the UZ is modeled to occur under steady-state conditions. Transient “fast-pathway” flow is considered to contribute insignificantly to the total flow below the PTn through the UZ (BSC 2001 [158726], pp. 137–139).

6.2.2.1 Capillary Barriers

Capillary barriers were speculated to exist within the PTn unit, because of the large contrast in rock properties across the interfaces of the unit (Montazer and Wilson 1984 [100161], pp. 26–30). In addition, rock-property contrasts between sublayers within the PTn unit may potentially produce capillary barriers. Characterization of groundwater flow behavior within the PTn is critically dependent on detailed knowledge of rock properties and the heterogeneity within the PTn unit. Considerable amounts of field data, obtained from tens of boreholes and hundreds of outcrop samples at the site, constrain the distribution of rock properties within the PTn unit. In

general, field data indicate that the Yucca Mountain formation is more heterogeneous vertically than horizontally, so that layer-wise representations provide reasonable approximation of the complex geologic system. Calibration using this conceptual model matches different types of observation data, as further demonstrated in the following sections. However, characterizing general flow behavior within the UZ system is complicated by the presence of faults, which interrupt the lateral continuity of rock matrix properties.

The key conceptualizations made in the conceptual model concerning lateral flow above the repository horizon are as follows: (1) the hydrogeological units/layers are internally homogeneous, and the material properties of each unit are continuous throughout each layer (Table 6.1-1) unless interrupted by faults; (2) ambient water flow in the system is at a steady-state condition; and (3) faults are represented by vertical or inclined columns of gridblocks having finite or small width. The flow patterns associated with capillary barriers within the PTn are studied in the following sections using this conceptual model and alternative parameters.

6.2.2.2 Perched Water

Conceptual models of perched water occurrence are of particular interest in assessing the system performance of the repository and UZ flow patterns below the repository. Waste-isolation strategies and UZ natural barrier capability depend in part on sorption within the zeolitic portions of the CHn and on tracer transport times between the repository horizon and the water table. Several conceptual models have been proposed for the genesis of perched water at Yucca Mountain (e.g., Wu et al. 1999 [117167]).

Perched water may occur where percolation flux exceeds the capacity of the geologic media to transmit vertical flux in the UZ. Perched water has been encountered in a number of boreholes at Yucca Mountain, including UZ-14, SD-7, SD-9, SD-12, NRG-7a, G-2, and WT-24. These perched-water occurrences are found to be associated with low-permeability zeolites in the CHn or the densely welded basal vitrophyre (Ttpv3, Table 6.1-1) of the TSw unit. Possible mechanisms of water-perching in the UZ of Yucca Mountain may be permeability or capillary barrier effects at faults, or a combination of both.

A permeability-barrier conceptual model for perched water occurrence has been used in UZ flow modeling studies since 1996, as summarized in Wu et al. (1999 [117167]). In this model, perched-water bodies in the vicinity of the ESF North Ramp (near boreholes UZ- 14, SD-9, NRG-7a, G-2 and WT-24) are observed to occur above the base of the TSw, underlain by a zone of low-permeability zeolitized rock. The perched-water bodies in this northern area of the repository may be interconnected. However, the perched-water zones at boreholes SD-7 and SD-12 are considered here as local, isolated bodies. In this conceptual model, both vertical and lateral water movement in the vicinity of the perched zones is considered to be controlled mainly by the fracture and matrix permeability distribution in these areas. The major aspects of the permeability-barrier conceptual model are: (1) no large-scale vertically connected potentially fluid-conducting fractures transect the underlying low-permeability units, (2) both vertical and horizontal permeabilities within and below the perched-water zone are small compared with permeabilities outside perching zones, and (3) sufficient percolation flux (>1 mm/yr) exists locally.

Perched-water occurrence caused by permeability barrier effects is consistent with the conceptual model that ambient conditions reflect long-term, steady-state or transient flow through the UZ, and that perched water under steady-state flow conditions may only result from a permeability barrier. Previous modeling studies (BSC 2001 [158726]) concluded that this conceptual water-perching model is able to match the observation data of perched water in the Yucca Mountain UZ. In the present numerical studies, the occurrence of perched water is assumed to follow the conceptual models of a permeability barrier. In other words, perched-water bodies are formed as a result of permeability barrier effects.

6.2.3 Parameter Adjustment

The Model Report entitled *Calibrated Properties Model* (BSC 2003 [160240]) provides basic input parameter sets of fractures and matrix rocks for modeling efforts in this Model Report. However, these properties were estimated through a series of 1-D model inversions, in which lateral flow, perched water, and capillary barrier effects cannot be simulated by the 1-D model. Use of a 3-D model allows further parameter adjustment to match field observation data. This section presents calibrated parameters after adjustment through a series of 3-D model calibrations. The adjusted parameters include fracture-matrix properties of the top TSw layer, PTn unit, and perched water zones, and fracture permeabilities in the upper TSw layers.

In addition to estimating model parameters, these calibration studies can also be used to examine the adequacy of discretization for the 3-D model grid. The 3-D UZ TSPA-LA grid (Figure 6.1-1 for its plan view) uses finer vertical discretization than those used in the TSPA-SR model by BSC (2001 [158726]), particularly, for the PTn unit and the potential perched-water layers. For example, the PTn unit consists in general of six hydrogeological units vertically (namely, ptn21, ptn22, ptn23, ptn24, ptn25, and ptn26; Table 6.1-1), each of which is discretized into one or several vertical grid layers with maximum thickness of 2 or 5 m, respectively. The details of discretization are described in the *Development of Numerical Grids for UZ Flow and Transport Modeling* (BSC 2003 [160109], Section 6.6).

The 3-D model calibration efforts were performed by starting with the three sets of calibrated parameters from 1-D inversions of the Model Report (BSC 2003 [160240] in forward 3-D simulations). Then, model results were compared with the field-observed data of matrix liquid, along with water-potential data, perched-water elevations, and gas pressures. In general, some model parameters from 1-D calibrations are found to need adjustment in order to capture 3-D flow behavior or match observations at the mountain. The following modifications made to the 1-D rock properties were found necessary: modifying the fracture α of the tsw31 unit, using fracture-matrix properties from the previous 3-D calibration, locally adjusting fracture-matrix properties for the model layers associated with perched-water occurrence, and adjusting fracture permeability for the TSw units.

When the 1-D calibrated fracture-matrix properties (BSC 2003 [160240]) were used directly without any modifications as input to the 3-D model, significant lateral flow was predicted to occur along the top layer (tsw31) of the TSw unit under the present-day, mean infiltration scenario. This results from the limitation of a 1-D model; there is no evidence to support lateral flow within this layer. The 3-D simulation results indicated that a strong capillary barrier is formed between this tsw31 layer and the layer below. Examination of the calibrated fracture parameters for this layer showed that such large lateral flow was artificially created by the small

value of fracture α in tsw31, estimated by the 1-D inversion. The 1-D inverted fracture $\alpha = 1.597 \times 10^{-5} \text{ Pa}^{-1}$, which was even smaller than matrix $\alpha (= 8.702 \times 10^{-5} \text{ Pa}^{-1})$ for the same layer. This was an artifact of the 1-D inversion model, because the top unit of the TSw was used as a transitional layer for flow from matrix-dominated flow in the PTn to fracture-dominated flow in the TSw, for which a strong capillary suction is needed within the fractures. Physically, there are many larger fractures along the top layer of the TSw unit (DTN: LB0205REVUZPRP.001 [159525]); therefore, a larger fracture $\alpha (= 1.000 \times 10^{-4} \text{ Pa}^{-1})$ is used instead, leading to a good match between observed data (as discussed in Section 6.2.5) and 3-D models and indicating little lateral flow in the tsw31 layer.

The second modification to the three 1-D inverted property sets is to replace the PTn fracture-matrix properties by those presented in Tables 6.2-2, 6.2-3, and 6.2-4, which are the corresponding parameter sets developed in previous UZ flow modeling studies (BSC 2001 [158726], Tables II-1, II-3, and II-5). The PTn properties of Tables 6.2-2, 6.2-3, and 6.2-4 are used because these parameters provide a better match of not only liquid saturation and water-potential data, but also of observed chloride data, as discussed in the following sections.

Table 6.2-2. Calibrated PTn Fracture-Matrix Parameters for the Present-Day, Mean Infiltration Scenario

Model Layer	K_M (m ²)	α_M (1/Pa)	m_M (-)	K_F (m ²)	α_F (1/Pa)	m_F (-)	γ (-)
ptn21	9.90E-13	1.01E-5	0.176	1.86E-12	1.68E-3	0.580	0.09
ptn22	2.65E-12	1.60E-4	0.326	2.00E-11	7.68E-4	0.580	0.09
ptn23	1.23E-13	5.58E-6	0.397	2.60E-13	9.23E-4	0.610	0.09
ptn24	7.86E-14	1.53E-4	0.225	4.67E-13	3.37E-3	0.623	0.09
ptn25	7.00E-14	5.27E-5	0.323	7.03E-13	6.33E-4	0.644	0.09
ptn26	2.21E-13	2.49E-4	0.285	4.44E-13	2.79E-4	0.552	0.09

DTN: LB991121233129.001 [147328]

Table 6.2-3. Calibrated PTn Fracture-Matrix Parameters for the Present-Day, Upper-Bound Mean Infiltration Scenario

Model Layer	K_M (m ²)	α_M (1/Pa)	m_M (-)	K_F (m ²)	α_F (1/Pa)	m_F (-)	γ (-)
ptn21	1.26E-13	1.84E-4	0.199	1.00E-11	2.38E-3	0.611	0.08
ptn22	5.98E-12	2.42E-5	0.473	1.00E-11	1.26E-3	0.665	0.08
ptn23	3.43E-13	4.06E-6	0.407	1.96E-13	1.25E-3	0.627	0.08
ptn24	3.93E-13	5.27E-5	0.271	4.38E-13	2.25E-3	0.631	0.08
ptn25	1.85E-13	2.95E-5	0.378	6.14E-13	1.00E-3	0.637	0.08
ptn26	6.39E-13	3.54E-4	0.265	3.48E-13	3.98E-4	0.367	0.08

DTN: LB991121233129.003 [147335]

Table 6.2-4. Calibrated PTn Fracture-Matrix Parameters for the Present-Day, Lower-Bound Mean Infiltration Scenario

Model Layer	K_M (m ²)	α_M (1/Pa)	M_M (-)	K_F (m ²)	α_F (1/Pa)	m_F (-)	γ (-)
ptn21	1.86E-13	6.13E-5	0.165	1.00E-11	1.66E-3	0.503	0.01
ptn22	3.27E-12	1.51E-5	0.390	1.00E-11	9.39E-4	0.651	0.01
ptn23	4.20E-13	2.04E-6	0.387*	1.84E-13	1.28E-3	0.518	0.01
ptn24	3.94E-13	2.32E-5	0.210	4.31E-13	2.02E-3	0.594	0.01
ptn25	2.22E-13	2.04E-5	0.296	7.12E-13	7.42E-4	0.555	0.01
ptn26	5.43E-13	1.82E-4	0.264	3.08E-13	2.00E-4	0.401	0.01

DTN: LB991121233129.005 [147346]

NOTE: * In output DTN, this value is 0.388 due to round off.

For perched-water calibration, calibrated parameters of fracture and matrix permeabilities within perched zones are determined from many modeling studies with 3-D simulations. The perched-water conceptual model with respect to water-perching scenarios is realized and carried out by modifying the 3-D UZ model grid file as follows:

- The grid-layer properties of tsw38 (tswF8/tswM8), tsw39 (tswF9/tswM9), chlz (chlFz/chlMz) and ch2z (ch2Fz/ch2Mz) are replaced by (pcF38/pcM38), (pcF39/pcM39), (pcF1z/pcM1z), and (pcF2z/pcM2z), respectively, where the basal vitrophyre of the TSw is underlain by zeolitic units.
- Near borehole SD-7, properties for the gridblocks in grid columns q45, i80, i81, i84, i87, o92, and o95, over grid layers of ch5z (ch5Fz/ch5Mz), ch6z (ch6Fz/ch6Mz) and pp4 (pp4Fz/pp4Mz) are replaced by (pcF5z/pcM5z), (pcF6z/pcM6z), and (pcF4p/pcM4p), respectively.
- Near borehole SD-12, properties for the gridblocks in grid columns q47, b93, b99, k61, k62 and k67, over grid layers of tsw38 (tswF8/tswM8), tsw39 (tswF9/tswM9), and chl1v (chl1Fv/chl1Mv) are replaced by (pcF38/pcM38), (pcF39/pcM39), and (pcF1z/pcM1z), respectively.

Fracture and matrix permeabilities of potential perched layers/zones, as identified above, are calibrated based on the 3-D model calibrated values (BSC 2001 [158726]), and shown in Tables 6.2-5, 6.2-6, and 6.2-7. All properties except intrinsic permeabilities, van Genuchten's α and m parameters, and residual saturations for matrix blocks within perched zones are identical to parameters estimated from the current 1-D inversions of the report by BSC (2003 [160240]). The active-fracture parameter, γ , is set to zero for all the perched zones, causing the fracture-matrix interface-area factor to be equivalent to liquid saturation (Liu et al. 1998 [105729]). Tables 6.2-5, 6.2-6, and 6.2-7 present the final three sets of calibrated rock properties at zones with perched water, with base-case (mean), upper-bound, and lower-bound present-day infiltration scenarios, respectively. The modified "fracture" properties in the following three tables are close to those of the matrix, so that fractures in water perching layers are effectively removed.

Table 6.2-5. Calibrated Parameters of Perched-Water Conceptual Model for the Present-Day, Base-Case Infiltration Scenario

Model Layer	K_M (m ²)	α_M (1/Pa)	m_M (-)	K_F (m ²)	α_F (1/Pa)	m_F (-)	γ (-)
pcM38/ pcF38	3.00E-19	6.23E-6	0.286	3.00E-18	6.23E-6	0.286	0.00
pcM39/ pcF39	6.20E-18	4.61E-6	0.059	6.20E-17	4.61E-6	0.059	0.00
pcM1z/ pcF1z	9.30E-20	2.12E-7	0.349	9.30E-19	2.12E-7	0.349	0.00
pcM2z/ pcF2z	2.40E-18	2.25E-6	0.257	2.40E-17	2.25E-6	0.257	0.00
pcM5z/ pcF5z	2.40E-18	2.25E-6	0.257	2.40E-18	2.25E-6	0.257	0.00
pcM6z/ pcF6z	1.10E-19	1.56E-7	0.499	1.10E-19	1.56E-7	0.499	0.00
pcM4p/ pcF4p	7.70E-19	4.49E-7	0.474	7.70E-19	4.49E-7	0.474	0.00

Output DTN: LB03013DSSCP3I.001

Table 6.2-6. Calibrated Parameters of Perched-Water Conceptual Model for the Present-Day, Upper-Bound Infiltration Scenario

Model Layer	K_M (m ²)	α_M (1/Pa)	m_M (-)	K_F (m ²)	α_F (1/Pa)	m_F (-)	γ (-)
pcM38/ pcF38	3.00E-19	5.58E-6	0.286	3.00E-18	5.58E-6	0.286	0.00
pcM39/ pcF39	6.20E-18	4.61E-6	0.059	6.20E-17	4.61E-6	0.059	0.00
pcM1z/ pcF1z	9.30E-20	2.12E-7	0.349	9.30E-19	2.12E-7	0.349	0.00
pcM2z/ pcF2z	2.40E-18	2.25E-6	0.257	2.40E-17	2.25E-6	0.257	0.00
pcM5z/ pcF5z	2.40E-18	2.25E-6	0.257	2.40E-18	2.25E-6	0.257	0.00
pcM6z/ pcF6z	1.10E-19	1.56E-7	0.499	1.10E-19	1.56E-7	0.499	0.00
pcM4p/ pcF4p	7.70E-19	4.57E-7	0.474	7.70E-19	4.57E-7	0.474	0.00

Output DTN: LB03013DSSCP3I.001

Table 6.2-7. Calibrated Parameters of Perched-Water Conceptual Model for the Present-Day, Lower-Bound Infiltration Scenario

Model Layer	K_M (m ²)	α_M (1/Pa)	m_M (-)	K_F (m ²)	α_F (1/Pa)	m_F (-)	γ (-)
pcM38/ pcF38	3.00E-19	1.43E-6	0.286	3.00E-19	1.43E-6	0.286	0.00
pcM39/ pcF39	6.20E-18	4.61E-6	0.059	6.20E-18	4.61E-6	0.059	0.00
pcM1z/ pcF1z	9.30E-20	2.12E-7	0.349	9.30E-20	2.12E-7	0.349	0.00
pcM2z/ pcF2z	2.40E-18	2.25E-6	0.257	2.40E-18	2.25E-6	0.257	0.00
pcM5z/ pcF5z	2.40E-18	2.25E-6	0.257	2.40E-18	2.25E-6	0.257	0.00
pcM6z/ pcF6z	1.10E-19	1.56E-7	0.499	1.10E-19	1.56E-7	0.499	0.00
pcM4p/ pcF4p	7.70E-19	2.88E-7	0.474	7.70E-19	2.88E-7	0.474	0.00

Output DTN: LB03013DSSCP3I.001

The fourth and last parameter adjustment is the fracture permeability in the TSw unit under the present-day, mean infiltration scenario (see Section 6.4). The present-day, mean infiltration rate is used for gas flow calibration, because the pneumatic tests were conducted in a small time scale of days to years at present day conditions. This calibration of Section 6.4 was made from 3-D gas flow analysis with the calibrated fracture permeability results summarized in Table 6.2-8. In this table, the fracture permeabilities of several TSw units from the 1-D inversion are reduced by a factor of 15.

Table 6.2-8. Calibrated TSw Fracture Permeability for the Present-Day, Mean Infiltration Scenario

Model Layer	K_F (m ²)
tsw31	5.42E-12
tsw32	4.72E-12
tsw33	5.18E-12
tsw34	2.21E-12
tsw35	6.06E-12
tsw36	8.99E-12
tsw37	8.99E-12

Output DTN: LB03013DSSCP3I.001

The final results and calibrated parameter sets of the 3-D model studies are given in Tables I-1 to I-6 of Attachment I. Tables I-1, I-2, and I-3 are considered as base-case scenario parameter sets, and Tables I-4, I-5, and I-6 are regarded as alternative property sets for use in generating the 3-D flow fields and estimating tracer transport times.

6.2.4 Numerical Treatment and Solution Convergence

Numerical modeling of large-scale 3-D flow and transport in the UZ beneath Yucca Mountain is mathematically challenging. The principal difficulty stems from the highly nonlinear coupling of the flow system. First, the hydrogeological system is distinctly heterogeneous on all model scales, and there are orders-of-magnitude contrasts in permeabilities across geological layers or between fracture and matrix rock. Secondly, the two-phase flow functions of relative permeability and capillary pressure for Yucca Mountain tuffs are extremely nonlinear for both fractures and matrix systems. The mathematical difficulties become even more severe when using the dual-permeability modeling approach for handling fracture-matrix interaction. In this case, flows through fractures and matrix are on very different time scales, with fracture flow being orders of magnitude faster than matrix flow. Furthermore, fracture elements have a much smaller storage space than matrix elements. In general, it takes simulation times of thousands to millions of years for the system to equilibrate. Rapid flow through fractures, plus the slow response in the matrix, makes it very difficult to obtain steady-state solutions numerically (BSC 2001 [158726], p. 51).

For all flow simulations (this section and Section 6.7), the EOS9 module of TOUGH2 V1.4 (LBNL 2000 [146496]) was used to solve Richards' equation in the unsaturated flow calculations. In this method, air/gas flow dynamics are ignored by using a constant gas-phase pressure in an isothermal system. This simplified two-phase flow solution for the 3-D model calibrations and TSPA flow field simulations is the most computationally efficient approach,

while giving accurate results for isothermal two-phase flow. Two-phase flow problems are solved with one equation per gridblock instead of solving two or three equations, as required by the EOS3 module. Numerical tests allow one to conclude that for moisture flow and distributions at steady state, the EOS9 solutions are in general identical to EOS3, “true two-phase” flow solutions (BSC 2001 [158726], pp. 52–53).

Model calibrations and flow-field simulations are both based on steady-state solutions using the EOS9 module. In each simulation, fracture, fault, and zeolitic element volumes are increased by a factor of 10,000 in the grid to overcome convergence difficulties associated with these nodes, while keeping all other mesh geometric information unchanged. This approach does not affect the final solution as long as a “true” steady-state solution is obtained for a given run. The initial condition for a new scenario run is estimated using a default (uniform) initial condition or results of a previous run with a similar modeling condition. Each simulation is usually subdivided into stages. For the first-stage runs, a large convergence tolerance on the order of 10,000 or more is used to keep simulation progressing with a large time step. It has been found based on those studies that using large residual tolerance in the first stage has no effects on final, steady-state solutions as long as no oscillations or unphysical solutions occur. After running the solution to 10^9 years or more with a large tolerance, the convergence tolerance is reduced to $10^{-2} - 10^{-3}$, and the model is run until a steady-state solution is reached. The final steady-state solutions are confirmed using a global mass-balance check, as discussed in Sections 6.2.5 and 6.6.2.

6.2.5 Simulation Scenarios, Results, and Analyses

This section summarizes the 3-D flow model calibration scenarios performed for this Model Report, including simulation results and analyses. The model calibrations are performed using (1) the 3-D TSPA-LA grid (Figure 6.1-1) and nine net infiltration maps, as discussed in Section 6.1.4; (2) the three parameter sets (Table I-1, I-2 and I-3 in Attachment I of this Model Report); and (3) the UZ flow conceptual models of Section 6.2.2 above. Simulation results are called TSPA-LA flow simulations or base-case flow fields in this report. Simulation results with the alternative model will be discussed in Section 6.6.

Simulation Scenarios: Table 6.2-9 summarizes these nine simulation scenarios, associated parameter sets, and infiltration rates used.

Table 6.2-9. Nine UZ Flow Simulation Scenarios: Data Files, Parameter Sets, and Infiltration Maps for the UZ Model Calibrations

Designation/ Simulation	Parameter Set/ Calibration (Output-DTN: LB03013DSSCP3I.001)	Infiltration Map DTN: GS000308311221.005 [147613]
preq_IA	Parameter set from Table I-3, lower-bound infiltration	Present-day, lower-bound infiltration
preq_mA	Parameter set from Table I-1, present day/modern, mean infiltration	Present-day, mean infiltration
preq_uA	Parameter set from Table I-2, upper- bound infiltration	Present-day, upper-bound infiltration
monq_IA	Parameter set from Table I-3, lower-bound/present-day infiltration	Monsoon, lower- bound infiltration
monq_mA	Parameter set from Table I-1, present day/modern, mean infiltration	Monsoon, mean infiltration
monq_uA	Parameter set from Table I-2, upper-bound infiltration	Monsoon, upper-bound infiltration
glaq_IA	Parameter set from Table I-3, lower-bound/present-day infiltration	Glacial transition, lower-bound infiltration
glaq_mA	Parameter set from Table I-1, present day/modern, mean infiltration	Glacial transition, mean infiltration
glaq_uA	Parameter set from Table I-2, upper-bound infiltration	Glacial transition, upper-bound infiltration

Mass Balance and Solution Convergence: Table 6.2-10 shows the mass-balance results for the nine simulation scenarios. In Table 6.2-10, “inflow” is the total infiltration rate over the entire model top boundary, representing a net water recharge rate into the system for the infiltration scenario simulated. “Outflow” is the cumulative total-flow rate out of the model and into the lower boundary representing the water table. Global mass-balance errors between inflow and outflow from the system, as shown in Table 6.2-10, are all less than 0.06% for the nine simulations, leading to the conclusion that steady-state solutions are obtained for all the simulations.

Table 6.2-10. Mass-Balance Results for Nine Flow Simulations

Simulation Scenarios	Inflow from infiltration (kg/s)	Outflow to water table (kg/s)	Relative error (%)
preq_IA	1.5828143	1.5828216	0.0005
preq_mA	5.5922355	5.5908953	0.0240
preq_uA	13.564390	13.556891	0.0553
monq_IA	5.5922355	5.5922194	0.0003
monq_mA	14.939317	14.945912	0.0473
monq_uA	24.286298	24.286685	0.0016
glaq_IA	2.9648877	2.9648851	0.0001
glaq_mA	21.494950	21.495135	0.0009
glaq_uA	40.024949	40.024915	0.0001

Model Results - DTN: LB03023DSSCP9I.001

Model Calibrations and Results: As listed in Table 6.2-9, there are nine scenarios for model calibrations, sensitivity analyses as well as flow fields, covering nine infiltration rates for three climates. The nine simulations have been calibrated against the field-observed data of perched water. In addition, the observed matrix liquid saturations and water potentials (when available) are also used to examine these modeling results. A perched-water body is defined as fully liquid saturated gridblocks with zero capillary pressure for calibration. The data source used in the calibrations are listed in Section 4-1. Note that only *in situ* measurement water potentials among the water-potential data are used. In this section, the simulation results are presented and discussed in terms of (1) comparisons with matrix liquid saturation, water potential, and perched-water data, (2) examination of simulated perched-water bodies, and (3) examination of simulated percolation flux and fracture-matrix flow components.

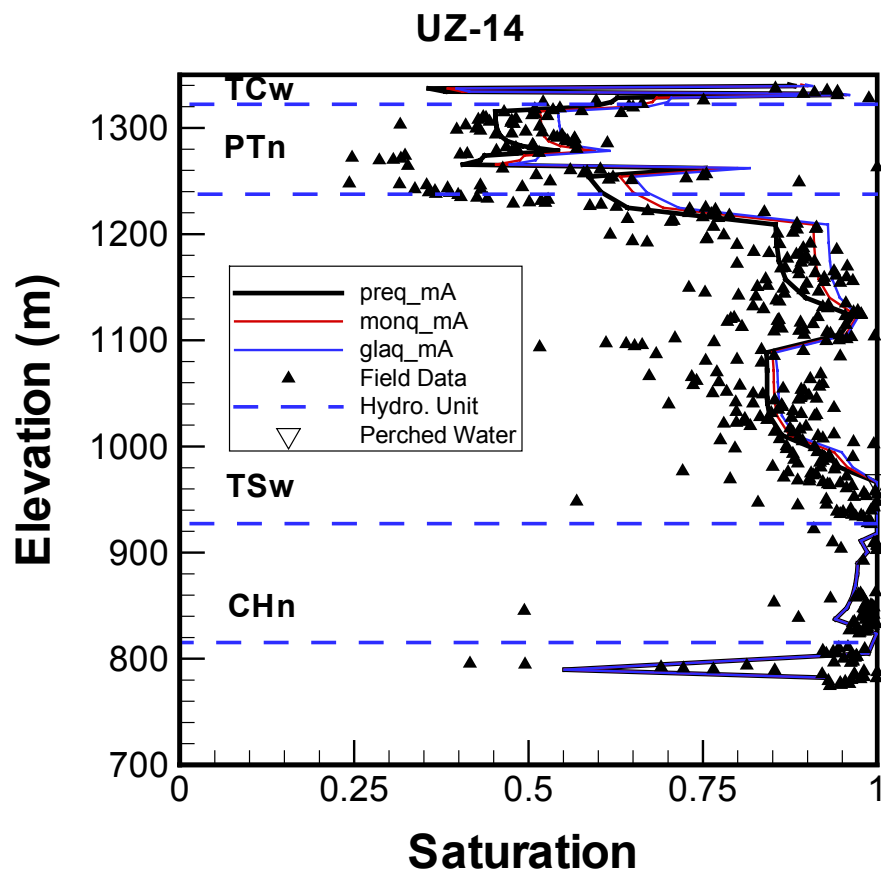
All nine simulations are checked against observed saturation, water potential, and perched-water data. (See Wang 2003 [162417], SN-LBNL-SCI-199-V1, pp. 131–157, 242–243, for detailed comparisons of the saturation and potential profiles of all boreholes evaluated by the model and for mass balance results of the simulations.) However, only a few of these comparisons are shown in the report, and boreholes UZ-14 and SD-12 are selected to show the match between observed and modeled vertical-saturation profiles and perched-water locations for six simulations with perched-water occurrence. Matches to other borehole data are similar. Note that most borehole observation data used in this section and the following sections are given relative to depth. In plots of this Model Report, we use elevations to show model results and comparisons. Attachment II lists the surface elevations and coordinates of selected boreholes for conversion from depth to elevation.

Here and in Section 6.6, higher future infiltration scenarios of monsoon and glacial transition, used in calibration and sensitivity analysis, are not intended to represent future climates. Instead, they are used to assess uncertainties with possible historical high infiltration and its impact on the current UZ condition. In addition, such simulation results quantify the range of variation in UZ conditions that spans the range of future climates, and are not expected to match measured data. In particular, the calibrated mean, lower and upper bound model properties have not been adjusted to match conditions generated by future climate infiltration rates.

Comparisons with Liquid Saturation, Water Potential and Perched-Water Data: Measured matrix liquid saturation, water-saturation data and perched-water elevations are compared against 3-D model results from the nine simulations. Matrix liquid saturation, water potential, and perched-water data used for comparisons are taken from nine boreholes (NRG-7a, SD-6, SD-7, SD-9, SD-12, UZ-14, UZ#16, WT-24 and G-2). The locations of these boreholes are shown in Figure 6.1-1.

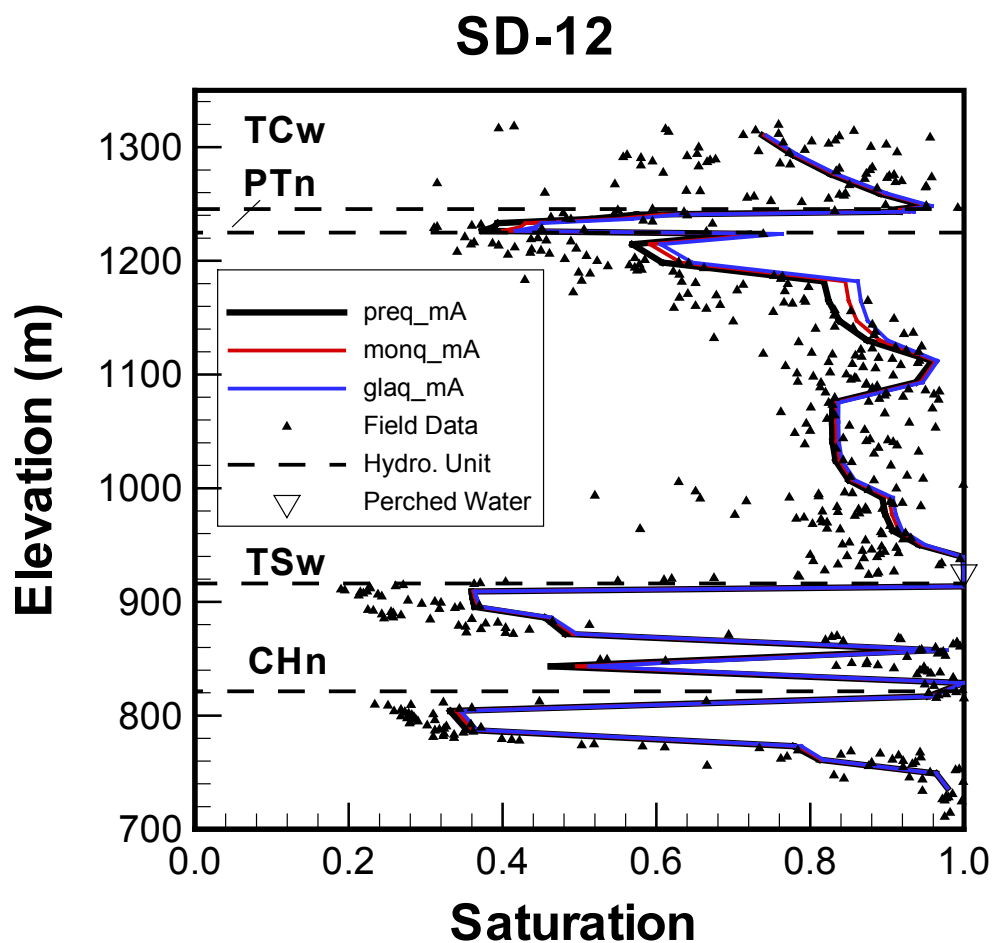
The comparisons of simulated and observed matrix liquid saturations along the vertical column representing boreholes UZ-14 and SD-12 are shown, as examples, in Figures 6.2-2 and 6.2-3 from the UZ flow models with nine infiltration scenarios. Figure 6.2-4 shows comparison with water potentials for SD-12. In general, the modeled results from the nine simulations with the UZ flow conceptual model are in reasonable agreement with the measured saturation and water-potential profiles, as shown in Figures 6.2-2, 6.2-3, and 6.2-4. It should be mentioned that the modeling results from the three lower infiltration scenarios show some differences from or compare more poorly than the rest of the model predictions. The differences between simulated

and observed saturation data, as shown in Figures 6.2-2 and 6.2-3, are primarily caused by heterogeneity and grid coarseness.



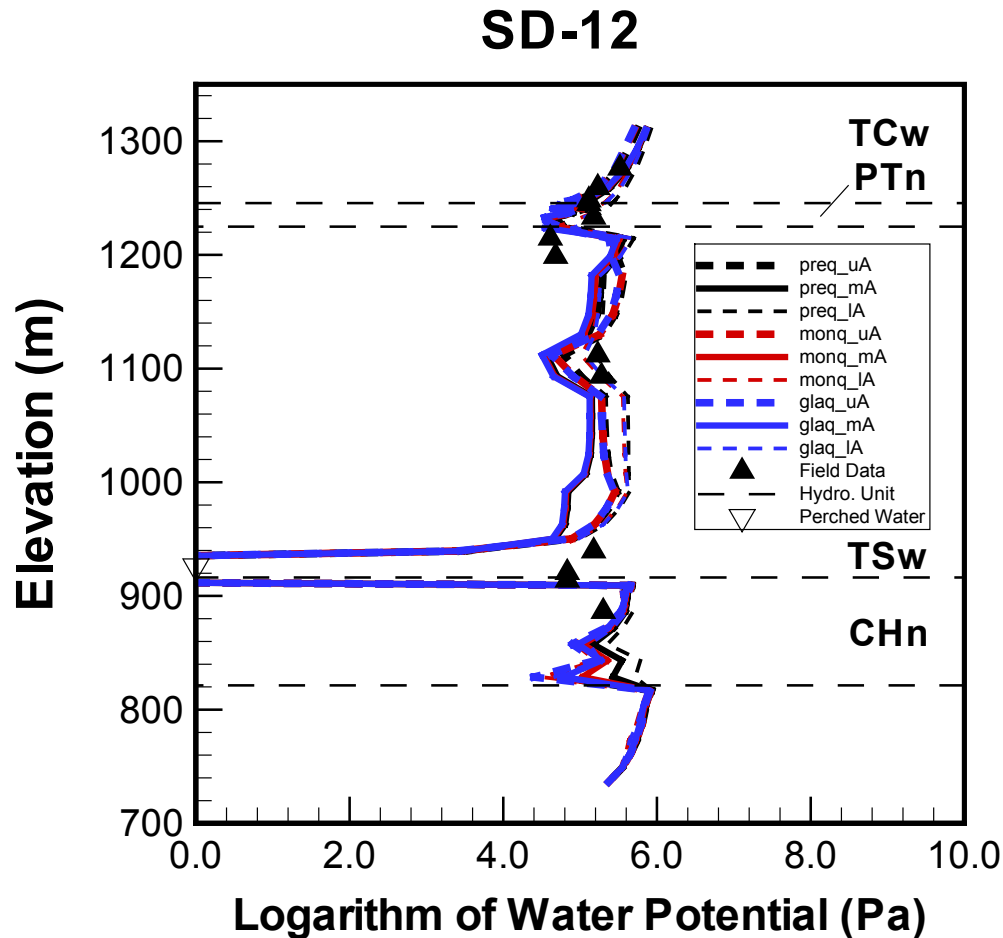
Data - DTN: GS960308312312.005 [107230]; MO0109HYMXPROP.001 [155989]; MO0004QGFMPICK.000 [152554];
Model Results - DTN: LB03023DSSCP9I.001

Figure 6.2-2. Comparison to the Simulated and Observed Matrix Liquid Saturations and Perched-Water Elevations for Borehole UZ-14, Using the Results of the Simulations with Three Mean Infiltration Rates



DTN: Rousseau et al. 1997 [100178]; MO0109HYMXPROP.001 [155989]; MO0004QGFMPICK.000 [152554];
 Model Results - DTN: LB03023DSSCP9I.001:

Figure 6.2-3. Comparison to the Simulated and Observed Matrix Liquid Saturations and Perched-Water Elevations for Borehole SD-12, Using the Results of the Simulations with Three Mean Infiltration Rates



DTN: MO0004QGFMPIK.000 [152554];
Model Results - DTN: LB03023DSSCP9I.001:

NOTE: Field data shown in figure are from DTN: LB991091233129.001 [125868], based on measured water potentials in DTNs: GS970808312232.005 [105978] and GS980408312232.001 [105982].

Figure 6.2-4. Comparison to the Simulated and Averaged Observed Water Potentials and Perched-Water Elevations for Borehole SD-12, Using the Results of the Simulations with Three Mean Infiltration Rates

Also shown in Figures 6.2-2, 6.2-3, and 6.2-4 are the perched-water elevations at the two boreholes, indicating a good agreement between observed and simulated data. In addition, each of the nine simulations has been compared to perched-water data as observed from the seven perched-water boreholes of Table 6.2-1 (See Wang 2003 [162417], SN-LBNL-SCI-199-V1, pp. 131–157, 242–243, for detailed comparisons). The results are as follows:

- Under the present-day, monsoon, or glacial transitional mean infiltration scenarios of the three climates (preq_mA, monq_mA, and glaq_mA, Table 6.2-9), the 3-D flow-simulation-results model generally matches water-perching conditions in the UZ Model domain.
- Under the present-day, monsoon, or glacial transitional upper-bound infiltration scenarios (preq_uA, monq_uA, and glaq_uA, Table 6.2-9), the 3-D flow-simulation-results model generally reproduces water-perching conditions in the UZ Model domain.

- Under the present-day, lower-bound infiltration scenarios (preq_1A, Table 6.2-9), the models in general do not match the perched-water data very well, except UZ-12, because of the low percolation fluxes at these borehole locations. While under the lower-bound monsoon or glacial transitional infiltration scenarios (monq_1A and glaq_1A, Table 6.2-9), the flow model results match well with observed perched-water data.

6.2.6 Features, Events, and Processes

The following table of features, events, and processes (FEPs) was taken from the LA FEP List (DTN: MO0301SEPFEPS1.000 [161496]). This table is somewhat different from the list of included FEPs assigned to this AMR in the *Technical Work Plan for: Performance Assessment Unsaturated Zone* (BSC 2002 [160819], Table 2-6). The changes include revision of the FEPs organization and description to address *The Enhanced Plan for Features Events and Processes (FEPs) at Yucca Mountain TDR-WIS-PA-000005* (BSC 2002 [158966], Section 3.2) and the *KTI Letter Report, Response to Additional Information Needs on TSPAI 2.05 and TSPAI 2.06 REG-WIS-PA-000003 REV 00 ICN 02* (Freeze 2003 [164178]).

The results of this model are part of the basis for the treatment of FEPs as discussed in the *Total System Performance Assessment-License Application Methods and Approach* (BSC 2002 [160146], Section 3.2.2). The cross-reference for each FEP to the relevant sections of this report is also given in Table 6.2-11.

The results of this and other model reports are used to fully document the technical basis for the include/exclude status of these FEPs for TSPA-LA. The UZ Department's documentation for the included FEPs listed in Table 6.2-11 is compiled from this and other model reports and can be found in the model abstraction reports as described in Sections 2.1.2 and 2.4 of the TWP (BSC 2002 [160819]) and the FEP report as described in Section 1.12.10 of the TWP (BSC 2002 [160819]). Excluded FEPs are to be documented in the FEP report as described in Section 1.12.10 of the TWP (BSC 2002 [160819]). Complete or partial treatment of FEPs is provided herein.

Table 6.2-11. FEPs Addressed in This Model Report

LA FEP Number	FEP Name	Section(s) Where FEP is Addressed	Summary Description	Treatment of FEP in This Model Report
1.2.02.01.0A	Fractures	6.1.5, 6.2.3, 6.2.5, 6.4, 6.6.3, 6.7.3, 6.8, 7.4	Groundwater flow in the Yucca Mountain region and transport of any released radionuclides may take place along fractures. The rate of flow and the extent of transport in fractures are influenced by characteristics such as orientation, aperture, asperity, fracture length, connectivity, and the nature of any linings or infills.	<p>Included.</p> <p>This FEP on "Fractures" is included in UZ process models, and for this model report, is relevant for mountain-scale unsaturated zone flow and transport. The UZ Flow Model is based on dual-permeability concept with the fractures represented by a continuum. The fracture continuum represents the spatially averaged flow through discrete fractures. The fracture continuum interacts with the matrix continuum which represents matrix blocks separated by fractures.</p> <p>Fracture continuum properties include permeability, porosity, interface area per unit volume, van Genuchten α and m parameters for the saturation-capillary pressure and relative permeability functions, and active fracture parameter. These parameters and associated range of values are presented in Section 4.1 of this report for each UZ Model layer (DTN LB0205REVUZPRP.001 [159525] listed in Table 4.1-1).</p> <p>Fracture permeability is based on field measurements, which integrate the discrete fracture characteristics such as orientation, aperture, asperity, fracture length, connectivity, and the nature of any linings or infills. Permeabilities and other properties are further calibrated as described in the Model Reports <i>Calibrated Properties Model</i> (BSC 2003 [160240]) and <i>Analysis of Hydrologic Properties Data</i> (BSC 2003 [161773]).</p> <p>The fracture continuum properties are used as inputs to the UZ Flow Model and their effects are incorporated into the output flow fields developed for use in TSPA (output flow fields are in DTN LB0305TSPA18FF.001).</p>
1.2.02.02.0A	Faults	6.1.5, 6.2.2, 6.2.5, 6.6.2, 6.6.3, 6.7.3	Numerous faults of various sizes have been noted in the Yucca Mountain Region and in the repository area specifically. Faults may represent (1) an alteration of the rock permeability and continuity of the rock mass, (2) alteration or short-circuiting of the flow paths and flow distributions close to the repository, and (3) represent unexpected pathways through the repository.	<p>Included.</p> <p>The faults are explicitly discretized in the mountain-scale flow and transport models described in this Model Report for the unsaturated zone. The major faults are represented in the UZ Model Grid as vertical or inclined discrete zones 30 meters wide. Specific hydrogeological properties are assigned to the fault zones.</p> <p>Fault properties (matrix and fracture parameters) are in DTN: LB02092DSSCFPR.002 [162128] as listed in Table 4.1-1 of this AMR. These properties have been calibrated as described in the Model Reports <i>Calibrated Properties Model</i> (BSC 2003 [160240]) and <i>Analysis of Hydrologic Properties Data</i> (BSC 2003 [161773]).</p> <p>The fault properties are used as inputs to the UZ Flow Model and their effects are incorporated into the output flow fields developed for use in TSPA (output flow fields are in DTN LB0305TSPA18FF.001).</p>

Table 6.2-11. FEPs Addressed in this Model Report (Continued)

LA FEP Number	FEP Name	Section Where FEP is Addressed	Summary Description	Treatment of FEP in this Model Report
1.3.01.00.0A	Climate change, global	6.1.4, 6.2.5, 6.5.1, 6.6, 6.7.2, 6.7.3	Climate change may affect the long-term performance of the repository. This includes the effects of long-term change in global climate (e.g., glacial/interglacial cycles) and shorter-term change in regional and local climate. Climate is typically characterized by temporal variations in precipitation and temperature.	<p>Included.</p> <p>Global climate change is addressed in TSPA using a climate model based on paleoclimate information in the Model Report <i>Future Climate Analysis</i> (USGS 2001 [158378]). That is, the record of climate changes in the past is used to predict the expected changes in climate for the future. Future climates are described in terms of discrete climate states that are used to approximate continuous variations in climate. The effects of seasonality are included in the climate model through the use of climate analogs with specific seasonal meteorological records. More specific information about the methods used to predict future climate change and the findings for the climate model are given in USGS (2001 [158378], Section 6). Climate modeling is incorporated into TSPA through the unsaturated zone flow fields that have different surface water infiltration as a result of different climates. A description of the modeling methods used for infiltration and how infiltration is affected by climate is given in USGS (2001 [160355], Section 6). The unsaturated zone flow model, which uses the infiltration results as upper boundary conditions for unsaturated zone flow calculations, is described in the UZ Flow Model of this AMR. The incorporation of unsaturated zone flow fields of this Model Report (DTN LB0305TSPA18FF.001) into the TSPA is done by FEHM software (BSC 2002 [160146], p.13).</p>
1.3.07.02.0B	Water table rise affects UZ	6.6.3	Climate change could produce increased infiltration, leading to a rise in the regional water table, possibly affecting the release and exposure from the potential repository by altering flow and transport pathways in the UZ. A regionally higher water table and change in UZ flow patterns might flood the potential repository.	<p>Included.</p> <p>The potential for water table rise due to climate change is included in TSPA calculations using a water table rise model (Forester et al. 1999 [109425], pp. 46, 56) based on paleoclimate data. The paleoclimate data indicates that the historical water table has never risen to the level of the potential repository (Forester et al. 1999 [109425], pp. 46, 56).</p> <p>Water table changes are implemented in the TSPA by allowing the water table to change elevation upon change in climate (implemented by the post-processor software WTRISE (LBNL 2003 [163453]) for radionuclide transport). WTRISE allows the user to specify a water table location and removes all the particles in the gridblocks below the specified water table instantaneously by setting full saturation to the submerged gridblocks. A part of the TSPA-LA model, the implementation of WTRISE is conditional on climate change, water table level is assumed.</p>

Table 6.2-11. FEPs Addressed in this Model Report (Continued)

LA FEP Number	FEP Name	Section Where FEP is Addressed	Summary Description	Treatment of FEP in this Model Report
1.4.01.01.0A	Climate modification increases recharge	6.1.4, 6.2.5, 6.6.2, 6.6.3, 6.7.2, 6.7.3	Climate modification (natural or artificial) causes an increase in recharge in the Yucca Mountain region. Increased recharge might lead to increased flux through the repository, perched water, or water table rise.	<p>Included.</p> <p>The effects of climate changes (BSC 2002 [160146], Section 4.1) on unsaturated zone flux through the potential repository are incorporated through the explicit simulations of UZ flow fields corresponding to the upper-bound, mean, and lower-bound infiltrations of three distinct different climates: present-day, monsoon, and glacial-transition. The 9 base-case flow fields and 9 alternative flow fields are presented in Section 6.6 of this Model Report. The output flow fields are in DTN: LB0305TSPA18FF.001, developed for use in Performance Assessment (BSC 2002 [160146]; BSC 2001 [158726], Section 6.6).</p> <p>Above the repository, no perched water bodies were observed in the fields and predicted by the UZ Flow Model. The potential effect of perched water above the repository is indirectly related to lateral diversion of percolation flux in the PTn above the repository. PTn effects on the flow field are discussed in Section 6.6 of this Model Report.</p> <p>The potential for water table rise due to climate change is included in TSPA calculations, using the water table rise model (implemented by software WTRISE (LBNL 2003 [163453], also see FEP 1.3.07.02.0B of this table) based on paleoclimate data (USGS 2001 [158378], Section 6.2).</p>
2.1.08.01.0A	Water influx at the repository	6.2.5, 6.6.3, 6.7.3	An increase in the unsaturated water flux at the repository affects thermal, hydrological, chemical, and mechanical behavior of the system. Increases in flux could result from climate change, but the cause of the increase is not an essential part of the FEP.	<p>Included.</p> <p>This FEP is considered to be included implicitly in the TSPA-LA. Changes in unsaturated zone flow in response to climate changes are incorporated in the output flow fields developed for use in the TSPA (output flow fields are in DTN LB0305TSPA18FF.001). Furthermore, the outputs from this model AMR are also used by other models and evaluations that are intermediate between this model and the TSPA-LA model.</p> <p>The thermal model output from this AMR is used for setting initial conditions for the downstream mountain-scale coupled process evaluation. The effects of changes in unsaturated zone flow due to climate change are also included in the calculations for the thermal-hydrological behavior of the potential repository system (BSC 2001 [158204], Section 6). The effects of transient flow driven by thermo-hydrological processes are also included in TSPA calculations for drift seepage in the Model Report <i>Abstraction of Drift Seepage</i>, MDL-NBS-HS-000019 (BSC 2003 [162268]). The effects of THC and THM on seepage are also addressed in the seepage abstraction report.</p> <p>Also, the fluxes from the output flow fields of this AMR serve as input to flow focusing estimation at drift scale as addressed in the Model Report <i>Abstraction of Drift Seepage</i>, MDL-NBS-HS-000019 (BSC 2003 [162268]) (Note: The flow focusing effects occurs at a scale less than the gridblock scale in the UZ Flow Model grid and are, therefore, not distinguishable in the results of this Model Report). In the seepage abstraction, a probabilistic approach is used to account for the spatial and temporal variability and inherent uncertainty of seepage-relevant properties and processes (BSC 2003 [162268], Section 6.5). In <i>Abstraction of Drift Seepage</i>, Section 6.5 provides the steps needed to relate site-scale percolation results (based on tuff layer representation in the UZ Flow Model) to drift-scale seepage calculations, with spatial heterogeneity explicitly taken into account) (also see FEP 2.2.07.04.0A of this table).</p>

Table 6.2-11. FEPs Addressed in this Model Report (Continued)

LA FEP Number	FEP Name	Section Where FEP is Addressed	Summary Description	Treatment of FEP in this Model Report
2.2.03.01.0A	Stratigraphy	6.1.1, 6.1.2	Stratigraphic information is necessary for the Performance Assessment. This information should include identification of the relevant rock units, soils and alluvium, and their thickness, lateral extent, and relationship to each other. Major discontinuities should be identified.	<p>Included.</p> <p>This FEP on "Stratigraphy" is included in the UZ Flow Model of this AMR by use of the grids developed with the information contained in the Geological Framework Model (GFM2000; MO0012MWDGFM02.002 [153777]). The stratigraphic unit and layers are developed into a model grid in the Model Report <i>Development of Numerical Grids for UZ Flow and Transport Modeling</i> (BSC 2003 [160109]).</p> <p>In as much as the assignment of hydrologic properties is associated with the grid used for the UZ flow model, the stratigraphy information is implicitly embedded in the TSPA through the output flow fields. Aspects that affect hydrogeologic properties for flow are further discussed in BSC (2003 [160109], Section 6 and BSC 2003 [160240], Section 6). See also the TSPA Disposition for FEP 2.2.03.02.0A in this table.</p>
2.2.03.02.0A	Rock properties of host rock and other units	6.1.5, 6.2.3, 6.4.2	Physical properties such as porosity and permeability of the relevant rock units, soils, and alluvium are necessary for the performance assessment. Possible heterogeneities in these properties should be considered. Questions concerning events and processes that may cause these physical properties to change over time are considered in other FEPs.	<p>Included.</p> <p>This FEP is similar to FEP 2.2.03.01.00 on stratigraphy. Rock properties are used to define for each of the stratigraphic units/layers classified in the Geological Framework Model (GFM2000; MO0012MWDGFM02.002 [153777]), which is further developed into model grid in the Model Report <i>Development of Numerical Grids for UZ Flow and Transport Modeling</i> (BSC 2003 [160109]).</p> <p>For the UZ Flow Model described in this AMR, heterogeneity is modeled in terms of the sequence of hydrogeologic units and discrete faults (BSC 2001 [158726], Section 6). Therefore, rock properties are implicitly embedded in the TSPA through the output flow fields, with site-scale layering and faults explicitly taken into account.</p> <p>On the drift scale, the effects of rock heterogeneity on seepage is discussed in the Model Report <i>Abstraction of Drift Seepage</i>, MDL-NBS-HS-000019 (BSC 2003 [162268]).</p>

Table 6.2-11. FEPs Addressed in this Model Report (Continued)

LA FEP Number	FEP Name	Section Where FEP is Addressed	Summary Description	Treatment of FEP in this Model Report
2.2.07.02.0A	Unsaturated ground-water flow in the geosphere	6.2, 6.6, 6.7	Groundwater flow occurs in unsaturated rocks in most locations above the water table at Yucca Mountain, including the location of the repository. See other FEPs for discussions of specific issues related to unsaturated flow. See related FEPs 2.2.07.03.0A (capillary rise), 2.2.07.04.0A (focusing of unsaturated flow), 2.2.07.05.0A (effects of episodic infiltration), 2.2.07.07.0A (perched water), 2.2.07.08.0A (fracture flow), 2.2.07.09.0A (matrix imbibition), 2.2.07.10.0A (condensation zone forms), 2.2.07.11.0A (resaturation of dryout zone), and 2.2.10.10.0A (two-phase flow/heat pipes).	Included. This FEP is included in the unsaturated zone process model for mountain-scale flow of this AMR and for drift seepage in the Model Report <i>Abstraction of Drift Seepage</i> , MDL-NBS-HS-000019 (BSC 2003 [162268]). The UZ Flow Model in this AMR is for three-dimensional, steady flow in a heterogeneous dual-permeability system including discrete fault zones. The flow fields (DTN LB0305TSPA18FF.001) generated by the UZ Flow Model of this AMR are used directly by the TSPA and are also implicitly included in the TSPA via the abstractions for drift seepage and radionuclide transport simulations. These models and abstractions use a quasi-steady flow-field approximation for climate change (BSC 2002 [160146]). The effects of soil depth on unsaturated zone flow at Yucca Mountain are included in the infiltration model (USGS 2001 [160355], Section 6).
2.2.07.03.0A	Capillary rise in the UZ	6.1.3	Capillary rise involves the drawing up of water, above the water table or above locally saturated zones, in continuous pores of the unsaturated zone, until the suction gradient is balanced by the gravitational pull downward. Capillary rise may provide a mechanism for radionuclides to reach the surface environment in locations where the water table is shallow.	Included. Capillary forces are included in the UZ Flow Model of this AMR. These forces affect the distribution of water in the unsaturated zone. Parameters used for capillarity modeling are incorporated within the matrix properties (DTN LB02091DSSCP3I.002 [161433]) and fracture properties (DTN LB0205REVUZPRP.001 [159525]) as described in Section 4.1 and Table 4.1-1 of this report. These parameters are used as direct input to the UZ Flow Model and are incorporated into the output flow fields used in the TSPA.

Table 6.2-11. FEPs Addressed in this Model Report (Continued)

LA FEP Number	FEP Name	Section Where FEP is Addressed	Summary Description	Treatment of FEP in this Model Report
2.2.07.04.0A	Focusing of unsaturated flow (fingers, weeps)	6.1.2, 6.2.5, 6.6.3, 6.7.3	Unsaturated flow can differentiate into zones of greater and lower saturation (fingers) that may persist as preferential flow paths. Heterogeneities in rock properties, including fractures and faults, may contribute to focusing. Focused flow may become locally saturated.	<p>Included.</p> <p>The UZ flow fields resulting from this Model Report represent the redistribution of infiltration through UZ layers, with faults explicitly taken into account. The flux redistribution based on tuff layer properties including fracture and matrix interaction as represented in the UZ Flow Model is discussed in detail in Section 6.6 of this Model Report. Faults are included in the UZ Flow Model in this AMR as discrete features; therefore, flow in faults is also included in the UZ Flow Model (this Model Report and CRWMS M&O 2000 [123913], Section 6).</p> <p>Also, the fluxes from the output flow fields of this AMR serve as input to flow focusing estimation at drift scale as addressed in the Model Report <i>Abstraction of Drift Seepage</i>, MDL-NBS-HS-000019 (BSC 2003 [162268]) (Note: The flow focusing effects occurs at a scale less than the gridblock scale in the UZ Flow Model grid and are, therefore, not distinguishable in the results of this Model Report). In the seepage abstraction, a probabilistic approach is used to account for the spatial and temporal variability and inherent uncertainty of seepage-relevant properties and processes (BSC 2003 [162268], Section 6.5). In <i>Abstraction of Drift Seepage</i>, Section 6.5 provides the steps needed to relate site-scale percolation results (based on tuff layer representation in the UZ Flow Model) to drift-scale seepage calculations, with spatial heterogeneity explicitly taken into account) (also see FEP 2.1.08.01.0A of this table).</p>
2.2.07.05.0A	Flow in the UZ from episodic infiltration	6.2.2	Episodic flow occurs in the UZ as a result of episodic infiltration. See also FEP 2.2.07.02.0A (unsaturated groundwater flow), 2.3.11.03.0A (infiltration), 2.2.07.04.0A (focusing of UZ flow), and 1.3.01.00.0A (climate change). Episodic flow may affect transport; for example, colloidal transport may be enhanced by episodic flow (FEP 2.2.08.10.0A).	<p>Screening Decision and Regulatory Basis: Excluded.</p> <p>Screening Argument: The process that drives infiltration in the unsaturated zone is precipitation, which is episodic in nature. Studies of episodic infiltration and percolation have found, however, that matrix-dominated flow in the PTn damps out the transient nature of the percolation such that unsaturated zone flow below the PTn is essentially steady (CRWMS M&O 1998 [100356], Section 2.4.2.8). Furthermore, the PTn is found over the entire repository block (in <i>Underground Layout Configuration</i> BSC 2003 [164325]). This damping of transient flow is due to capillary forces and high matrix permeability in the PTn that lead to matrix imbibition of water from fractures. Therefore, this FEP is excluded, because the unsaturated zone flow is steady at the repository and along radionuclide transport pathways.</p> <p>Very small amounts of fracture flow do appear to penetrate as transients through fault zones between the ground surface and the repository elevation, as evidenced by high ³⁶Cl concentrations in samples taken from the ESF (Fabryka-Martin et al. 1997 [100145]). Higher concentrations of this isotope found in the ESF can only be explained through surface deposition of ³⁶Cl from nuclear weapons testing and subsequent aqueous transport to certain ESF sampling locations over a period of approximately 50 years. However, the flow and transport models indicate that the quantity of water and dissolved constituents that do penetrate the PTn as flow transients is negligible with respect to repository performance (CRWMS M&O 1998 [100356], Section 2.4.2.8), generally less than 1% of the total infiltration (CRWMS M&O 1997 [124052], Section 6.12.4).</p>

Table 6.2-11. FEPs Addressed in this Model Report (Continued)

LA FEP Number	FEP Name	Section Where FEP is Addressed	Summary Description	Treatment of FEP in this Model Report
2.2.07.06.0A	Episodic / pulse release from repository		Episodic or pulse release of radionuclides from the repository and radionuclide transport in the UZ may occur, both because of episodic flow into the repository (see FEP 2.2.07.05.0A), and because of pulse releases from failed waste packages.	Included. The effects of intermittent waste package failure are included in the source term model for TSPA (BSC 2001 [155638], Section 6 and BSC 2002 [160146], Sec. 5.1, p. 69). This is done by modeling the environmental conditions of the waste packages in different parts of the repository and by modeling corrosion processes under the environmental conditions that lead to waste package failure (BSC 2002 [160146]). The effects of episodic flow at the mountain scale are excluded on the basis of low consequence, as discussed in FEP 2.2.07.05.0A of this Table.
2.2.07.07.0A	Perched water develops	6.2.2, 6.2.3, 6.2.5, 6.6.2, 6.6.3	Zones of perched water may develop above the water table. If these zones occur above the repository, they may affect UZ flow between the surface and the waste packages. If they develop below the repository, for example at the base of the Topopah Spring welded unit, they may affect flow pathways and radionuclide transport between the waste packages and the saturated zone.	Included. The seepage abstraction model contains a wide range of seepage possibilities, including flow focusing and variability (CRWMS M&O 2001 [154291], Section 6). Therefore, the potential for effects of perched water above the repository are indirectly captured in the seepage abstraction model through cases with high percolation flux (DTN LB0305TSPA18FF.001), as described in the Model Report <i>Abstraction of Drift Seepage</i> , MDL-NBS-HS-000019 (BSC 2003 [162268]). However, above the repository, no perched water bodies were observed in the fields predicted by the UZ Flow Model. The effects of existing perched water zones below the repository are also included, and potential changes in these perched-water zones due to climate changes are also included in the mountain-scale unsaturated zone flow model of this AMR (BSC 2001 [158726], Section 6). The potential for this effect is capture in the output flow fields developed for use in TSPA (output flow fields are in DTN LB0305TSPA18FF.001).
2.2.07.08.0A	Fracture flow in the UZ	6.2.5, 6.6.2, 6.6.3	Fractures or other analogous channels act as conduits for fluids to move into the subsurface to interact with the repository and as conduits for fluids to leave the vicinity of the repository and be conducted to the saturated zone. Water may flow through only a portion of the fracture network, including flow through a restricted portion of a given fracture plane.	Included. This FEP on "Fracture Flow" is included in UZ process models for mountain-scale unsaturated zone flow and transport. The UZ Flow Model is based on dual-permeability concept with the fractures represented by a continuum. The fracture continuum represents the spatially averaged flow through discrete fractures. The fracture continuum interacts with the matrix continuum which represents matrix blocks separated by fractures. Fracture continuum properties include permeability, porosity, interface area per unit volume, van Genuchten α and m parameters for the saturation-capillary pressure and relative permeability functions, and active fracture parameter are presented in Section 4.1 of this report for each UZ Model layer (DTN: LB0205REVUZPRP.001 [159525] listed in Table 4.1-1). Permeabilities and other properties are further calibrated as described in the Model Reports <i>Calibrated Properties Model</i> (BSC 2003 [160240]) and <i>Analysis of Hydrologic Properties Data</i> (BSC 2003 [161773]). The fracture continuum properties are used as inputs to the UZ Flow Model and their effects are incorporated into the output flow fields developed for use in TSPA (output flow fields are in DTN LB0305TSPA18FF.001). See also FEPs 1.2.02.01.0A and 2.2.07.02.0A of this table.

Table 6.2-11. FEPs Addressed in this Model Report (Continued)

LA FEP Number	FEP Name	Section Where FEP is Addressed	Summary Description	Treatment of FEP in this Model Report
2.2.07.09.0A	Matrix imbibition in the UZ	6.2.5, 6.6.2, 6.6.3, 7.6.3.2	Water flowing in fractures or other channels in the unsaturated zone is imbibed into the surrounding rock matrix. This may occur during steady flow, episodic flow, or into matrix pores that have been dried out during the thermal period.	Included. Matrix imbibition is included in the process model for unsaturated zone flow at the mountain scale (CRWMS M&O 2000 [141187], Section 6). Matrix imbibition refers to the movement of water into the matrix due to capillary forces. This process affects the distribution of flow between fractures and matrix in a dual-permeability flow model for fractured rock. The influence of matrix imbibition on episodic flow is discussed in Section 6.3.4 (FEP 2.2.07.05.0A of this table). Imbibition is captured in the UZ Flow Model through capillarity modeling, which again uses matrix and fracture properties as model input. Therefore, the effect of imbibition is implicitly incorporated in the output flow fields (DTN LB0305TSPA18FF.001) used in the TSPA.
2.2.07.19.0A	Lateral flow from Solitario Canyon fault enters drift	6.6.3	Water movement down Solitario Canyon Fault could enter waste emplacement drifts through lateral flow mechanisms in the Topopah Spring welded hydrogeologic unit. This percolation pathway is more likely to transmit episodic transient flow to waste emplacement locations due to the major fault pathway through the overlying units.	Included. The UZ Flow Model in this AMR contains potential hydrogeological connections between Solitario Canyon Fault and the waste emplacement horizon. The potential connection is captured using a property set of the PTn unit (Sections 6.2.2.1, 6.2.3 and 6.6 of this AMR) with calibrated fracture-matrix properties that favor later flow. Therefore, flow from this fault to waste emplacement locations is addressed. This water may seep into waste emplacement drifts if the flux is sufficient to overcome the capillary barrier represented in <i>the Seepage Calibration Model and Seepage Testing Data</i> (BSC 2003 [162267]). The lateral flow effect is implicitly incorporated in the output flow fields (DTN LB0305TSPA18FF.001) used in the TSPA.
2.2.08.05.0A	Diffusion in the UZ	6.5, 6.7.2, 6.7.3, 6.8.2, 7.5	Molecular diffusion processes may affect radionuclide transport in the UZ. This includes osmotic processes in response to chemical gradients. Discussion of diffusion in the drift shadow is addressed in FEP 2.2.07.21.0A.	Included. Diffusion of radionuclides between the fracture and matrix continua and partitioning through diffusion for radionuclides (released from drifts) between fractures and matrix are processes that are represented in the unsaturated zone radionuclide transport model (in process) and (BSC 2003 [163938], 6.4.1). The diffusion model used is based on a dual-porosity formulation in which the matrix water is stagnant. The abstraction for matrix diffusion includes the effects of partial saturation of the matrix, radionuclide sorption in the matrix, and finite spacing of fractures. Osmosis would tend to cause water from fractures to flow into the matrix, if the matrix presents a suitable barrier to the migration of dissolved salts. The UZ Flow Model in this AMR does not directly address the diffusion issue. However, the model flow fields and parameters (porosity) are used in the downstream transport Model Report for diffusion modeling (in process). Therefore, diffusion is indirectly and implicitly included in the flow fields (DTN LB0305TSPA18FF.001) used in the TSPA. More discussion on diffusion is referred to FEPs. Matrix Diffusion in the UZ (2.2.08.08.0B) and Diffusion in the UZ (2.2.08.05.0A).

Table 6.2-11. FEPs Addressed in this Model Report (Continued)

LA FEP Number	FEP Name	Section Where FEP is Addressed	Summary Description	Treatment of FEP in this Model Report
2.2.10.03.0B	Natural geothermal effects on flow in the UZ	6.3.4	The existing geothermal gradient, and spatial or temporal variability in that gradient, may affect groundwater flow in the UZ.	Included. Natural geothermal effects are included in the models of thermo-hydrological processes used to describe the effects of waste heat in the potential repository (BSC 2001 [158204], Sections 6.3.3, 6.4.3, 6.5.3) The thermal-hydrologic models contain the natural geothermal gradient in its initialization. This gradient is determined by the ground surface temperature, the water table temperature, and the thermal conductivity from layer to layer. The results of these models are used in the TSPA through abstraction of drift thermodynamic environment and percolation flux (CRWMS M&O 2001 [154594]). They are also used as boundary conditions for the mountain-scale coupled process Model Report (in process).
2.3.11.01.0A	Precipitation	6.5	Precipitation is an important control on the amount of recharge. It transports solutes with it as it flows downward through the subsurface or escapes as runoff. The amount of precipitation depends on climate.	Included. Precipitation affects the net infiltration, as discussed in <i>Simulation of Net Infiltration for Modern and Potential Future Climates</i> (USGS 2001 [160355]). The net infiltration map outputs (DTN: GS000308311221.005 [147613]) are used as a boundary condition for the UZ Flow Model of this AMR (Sections 6.1.3 and 6.1.4). Flow fields developed for use in TSPA (DTN LB0305TSPA18FF.001) using the UZ Flow Model therefore include the effects of precipitation and changes of precipitation under future climate conditions, including low, mean, and upper bounds of infiltrations in glacial, monsoon, and present (or modern) climatic scenarios.
2.3.11.03.0A	Infiltration and recharge	6.1.4, 6.5, 6.6.1, 6.7.2	Infiltration into the subsurface provides a boundary condition for groundwater flow. The amount and location of the infiltration influences the hydraulic gradient and the height of the water table. Different sources of recharge water could change the chemistry of groundwater passing through the repository. Mixing of these waters with other ground waters could result in precipitation, dissolution, and altered chemical gradients.	Included. The hydrological effects of infiltration and recharge are included in the infiltration model. This model includes the effects of seasonal and climate variations, climate change, surface-water runoff, and site topology such as hillslopes and washes (USGS 2001 [160355], Sections 6.4 and 6.5). This is incorporated into the TSPA through the unsaturated zone flow fields that use the infiltration model results (DTN GS000308311221.005 [147613]) as upper boundary conditions (BSC 2001 [158726], Section 6). (Flow fields of this AMR for TSPA-LA are in DTN LB0305TSPA18FF.001). The effects of chemistry of present-day water infiltrating from the ground surface are accounted for in the analysis of seepage water chemistry by using the measured pore-water chemistry in the unsaturated zone (BSC 2002 [158375], Section 6.1.2).

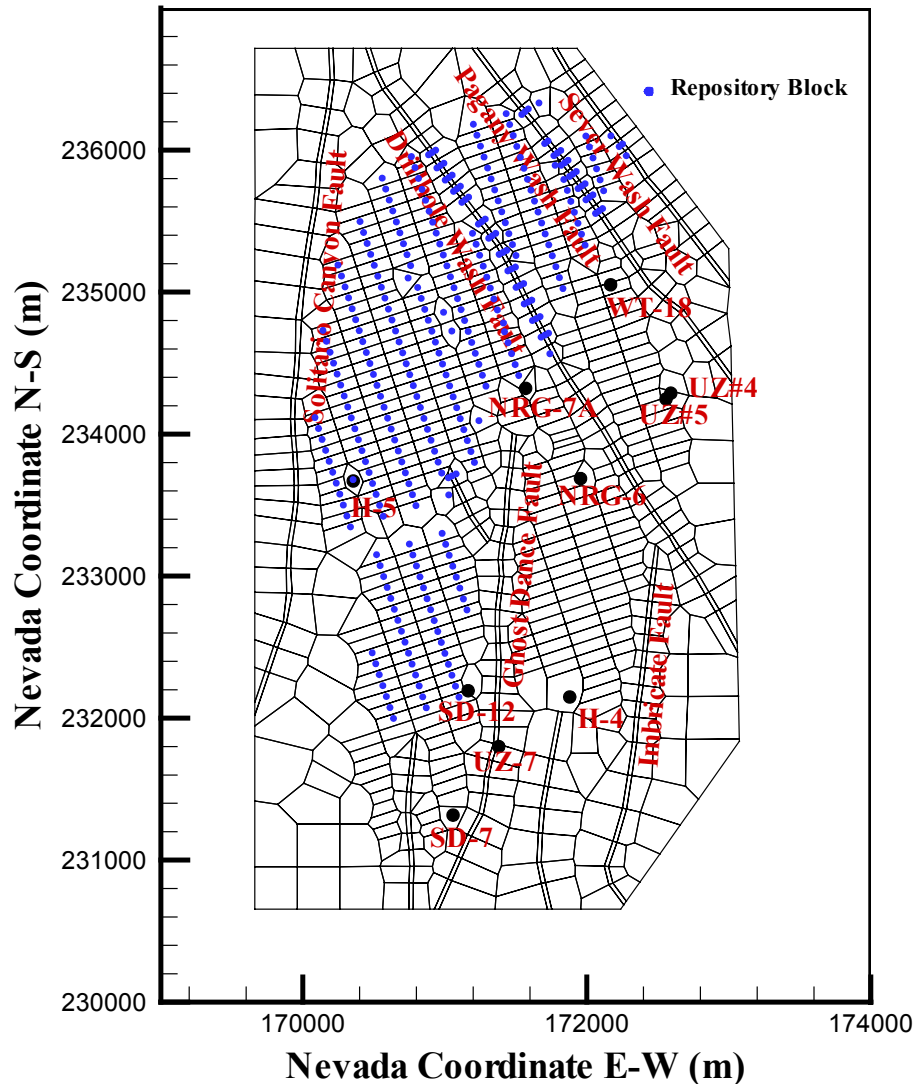
6.3 TEMPERATURE CALIBRATION

Prior to performing ambient, thermal-hydrological (TH) studies of the UZ system as well as repository performance studies under thermal-loading conditions, the ambient temperature, percolation and moisture distributions are first needed. The ambient geothermal and moisture conditions serve as the initial and boundary conditions of a thermal model. This section describes a 3-D ambient geothermal submodel of the UZ Model developed to evaluate steady-state, ambient thermal and moisture conditions of the UZ system for use in various scale TH modeling studies. Subsequent temperature calibration then provides an independent examination of percolation fluxes simulated by the UZ Flow Model. This is because the ambient temperature distribution within the UZ is related to percolation fluxes or infiltration rates (Bodvarsson et al. 2003 [162477]). By matching borehole temperature measurements, the TH model helps to constrain infiltration rate ranges as well as fracture-matrix parameter values.

6.3.1 3-D Thermal Model Grid

For thermal calibration as well as the gas flow calibration described in the next section, a new 3-D grid (Figure 6.3-1) smaller than the TSPA-LA grid (Figure 6.1-1) is developed. This grid is designed to relax intensive computational burdens needed in thermal modeling studies using a 3-D dual-permeability grid. The thermal model domain is selected to focus on geothermal conditions and thermal-loading effects at and near the repository area. The model domain is considered to provide sufficient accuracy for such studies because of the small thermal impact expected in the lateral directions.

This 3-D grid, featuring a smaller model domain than that of the UZ Flow Model (Figure 6.1-1), is referred to as the 3-D thermal model grid. As shown in the plan view of Figure 6.3-1, the thermal model grid domain covers approximately 20 km² of the area. Similar to the TSPA-LA grid of Figure 6.1-1, the thermal model grid (Figure 6.3-1) also uses a refined mesh in the vicinity of the repository and includes the locations of several boreholes used in temperature calibrations and analyses. In particular, the thermal grid explicitly incorporates every repository drift by taking into account orientations, lengths, elevations, and spacings of the drifts. A grid spacing of 81 m is used in the direction perpendicular to drifts, such that each individual drift segment can be inserted into the 3-D thermal grid for thermal-loading studies in a different report as documented in the TWP (BSC 2002 [160819], Section 1.12.7). In the model, faults are also represented in the model by vertical or inclined 30 m wide zones.



Output-DTN: LB0303THERMESH.001

Figure 6.3-1. Plan View of the 3-D Thermal Model Grid, Showing the Model Domain, Faults Incorporated, Several Borehole Locations, and TH Model Boundaries

The thermal model grid of Figure 6.3-1 consists of 980 mesh columns of both fracture and matrix continua, 86,440 gridblocks, and 343,520 connections in a dual-permeability grid. Vertically, the thermal grid has an average of 45 computational grid layers.

6.3.2 Top Boundary Temperature

To account for variations in atmospheric temperature with surface elevations in the mountain, measured mean surface temperatures and a linear equation that correlates surface temperature with elevation are used. The annual-average temperature was measured for near-surface sensors in boreholes NRG-6 and NRG-7a (DTN: GS960308312232.001 [105573], GS951108312232.008 [106756], and GS950208312232.003 [105572]), with several years of continuous temperature monitoring data. The surface temperatures T_s at any elevation Z are then

computed using the routine `toptemp_v0.f V1.0` (LBNL 2000 [147030]) and are treated as constants according to the following equation (Wu et al. 1999 [117161], Equation 4):

$$T_s = T_{\text{ref}} - \lambda[Z - Z_{\text{ref}}] \quad (\text{Eq. 6.3-1})$$

where T_{ref} is mean surface temperature at reference elevation Z_{ref} and λ is the dry adiabatic atmospheric lapse rate in $^{\circ}\text{C}/\text{m}$. This lapse is $0.01^{\circ}\text{C}/\text{m}$ (Driscoll 1986 [116801], p. 50). In this formulation, the surface reference temperature used is 18.23°C at an elevation of 1,231.0 m, averaged using measured data from borehole NRG-6. The averaged temperature measurement of NRG-7a at an elevation of 1,282.2 m is 17.78°C . The calculated mean lapse rate, based on these field measurements, is $0.009^{\circ}\text{C}/\text{m}$.

6.3.3 Bottom Boundary Temperature

The initial estimates of temperature distributions at the bottom boundary of the TH were taken from BSC (2001 [158726]). For that report, an effort was made to obtain accurate bottom-temperature boundary conditions for use in thermal-hydrological simulations. Following that work, the software routine of `get_temp_v0.f V1.0` (LBNL 2000 [147027]) was used to estimate temperatures at a flat surface of an elevation of 730 m. Because the water table is no longer flat with the current UZ and TH models, the actual estimates of the water table or bottom-model-boundary temperatures were interpolated between the values at 730 m elevation and the model surface boundary. Several non-Q measured temperature profiles (Sass et al. 1988 [100644]) were used as corroborative data (BSC 2001 [158726]) for an initial guess of the water-table-boundary temperature contours. In this Model Report, initially estimated water table temperatures are examined against the qualified temperature data in boreholes NRG-6, NRG-7a, SD-12 UZ#4, UZ#5 and UZ-7a (DTN: GS950208312232.003 [105572] and DTNs: GS970808312232.005 [105978], GS971108312232.007 [105980], GS960808312232.004 [105974], GS970108312232.002 [105975], GS980408312232.001 [105982]).

6.3.4 Calibration of Ambient Temperatures

The temperature profiles or geothermal gradients with the UZ system are controlled by several factors, such as formation thermal conductivity and net infiltration rates, in addition to the regional weather condition. Because of the small impact of uncertainties in measured thermal conductivities on simulated heat flow, the temperature calibration may be conducted using either ambient infiltration, or model boundary temperatures, or both. In this report, the ambient net infiltration rate is fixed as the present-day, mean infiltration rate with a value of 3.6 mm/yr within the grid domain (Figure 6.3-1). Temperatures are slightly adjusted from the estimated values along the top boundary only, and this results in a better match of observed borehole data. The reason behind the adjustment is, first, that insufficient temperature data was collected along these boundaries for accurate description of temperature distributions. Second, under steady-state moisture and heat flow conditions, both top and bottom boundary temperatures are spatially varying constants, which leaves room for adjusting to fit measured steady-state temperature profiles from boreholes.

The ambient temperature condition was calibrated using the 3-D thermal model grid of Figure 6.3-1 (Output-DTN: LB0303THERMESH.001), a dual-permeability mesh. The simulations were performed using TOUGH2 V1.4 (LBNL 2000 [146496]) with the EOS3 module. In

addition to the prescribed temperature conditions on top and bottom boundaries, the infiltration was described using the base-case, present-day, mean infiltration scenario. The model incorporated the parameter set of Table I-1 (Output-DTN: LB03013DSSCP3I.001), the thermal properties (DTN: LB0210THRMLPRP.001 [160799]), and the calibrated fault properties (DTN: LB02092DSSCFPR.002 [162128]). The simulations were all run to steady state for comparisons with measured borehole temperatures.

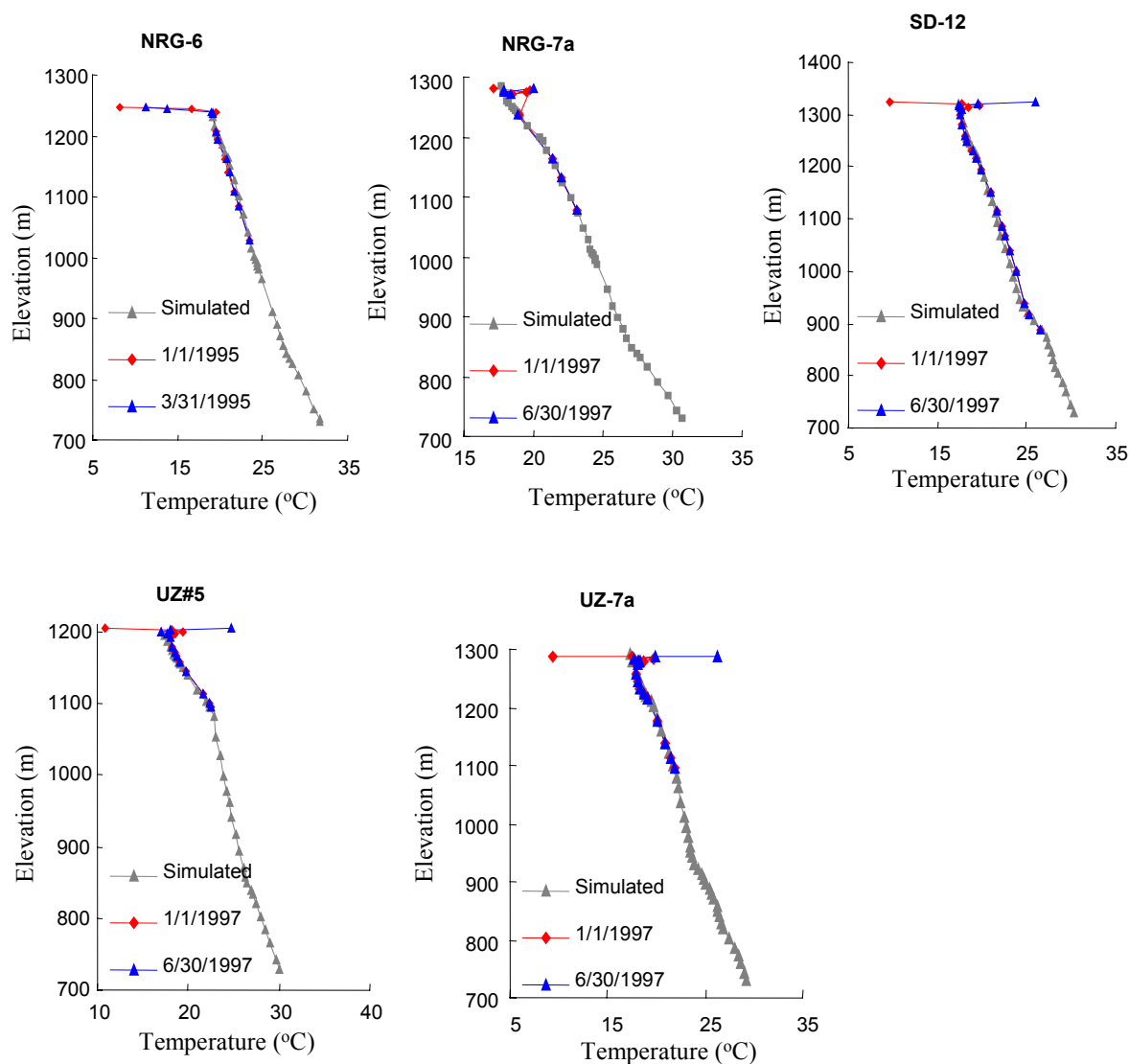
Table 6.3-1 lists the boreholes with qualified temperature measurements and the corresponding column element names used in the 3-D calibration of model ambient temperature. Note that in both the 3-D thermal model grid and the TSPA-LA grid, each element name is 8 characters long, consisting of numbers, alphabets, or symbols. The last three characters of 8-character names are assigned to stand for a vertical column, which are determined uniquely for each vertical grid column. As shown in Table 6.3-1, boreholes UZ#4 and UZ#5 are so close to each other that they fall into the same grid column. Therefore, we use only UZ#5 for calibrations (i.e., using temperature data from 5 of 6 boreholes). The comparison between UZ#4 and UZ#5 is documented in Wang (2003 [162417], SN-LBNL-SCI-199-VI, pp. 219, 223). During calibration, the corresponding simulated temperature profiles for the boreholes were extracted from the TOUGH2 output and then plotted against the measurements along each borehole.

Figure 6.3-2 shows the final model calibrated results and measured temperature profiles in the five temperature boreholes. The figure shows a good match between measured and simulated temperatures using the specified boundary conditions and the present-day, mean infiltration rate. Near the ground surface in five of the boreholes, observed temperatures show significant seasonal variations. However, these seasonal changes in surface temperature have little impact on steady-state heat flow or temperature profiles in the deeper (more than 20 m) UZ.

Table 6.3-1. Temperature Boreholes and Corresponding Element Columns of the Thermal Model Grid

Borehole	Element Column
NRG-6	h39
NRG-7A	h40
SD-12	h44
UZ#5	h45
UZ-7a	h74
UZ#4	h45

Output-DTN: LB0303THERMESH.001



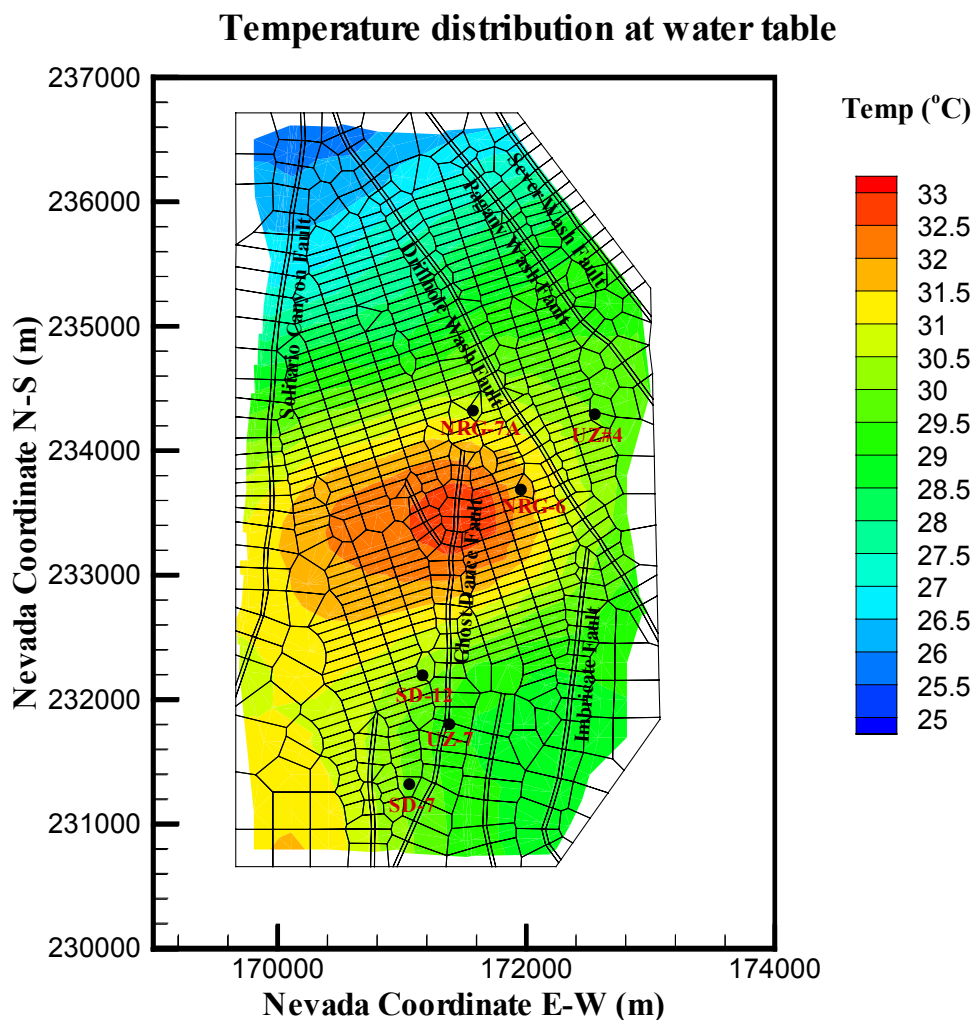
DTNs: GS970808312232.005 [105978]; GS971108312232.007 [105980]; GS960808312232.004 [105974];
 GS970108312232.002 [105975]; GS980408312232.001 [105982]
 Model Results DTN: LB0303THERMSIM.001

Figure 6.3-2. Comparisons between Measured and Modeled Ambient Temperature Profiles for the Five Boreholes under the Present-Day Mean Infiltration Rate

Figure 6.3-3 shows the contour plot of calibrated temperature distributions at the water table or the model bottom boundary. This temperature distribution is used for thermal simulations in which the model boundary temperature is fixed at the water table. Figure 6.3-3 indicates that the average temperature at the water table ranges from 27°C to 33°C, and lower temperatures are located in the north of the model domain where elevations and percolation fluxes are both higher. For the top model boundary, the estimated temperature distributions are shown in Figure 6.3-4. Based on calibration results, the ambient temperature distribution in the UZ TH model can be described to specify steady-state, mountain-scale temperature conditions.

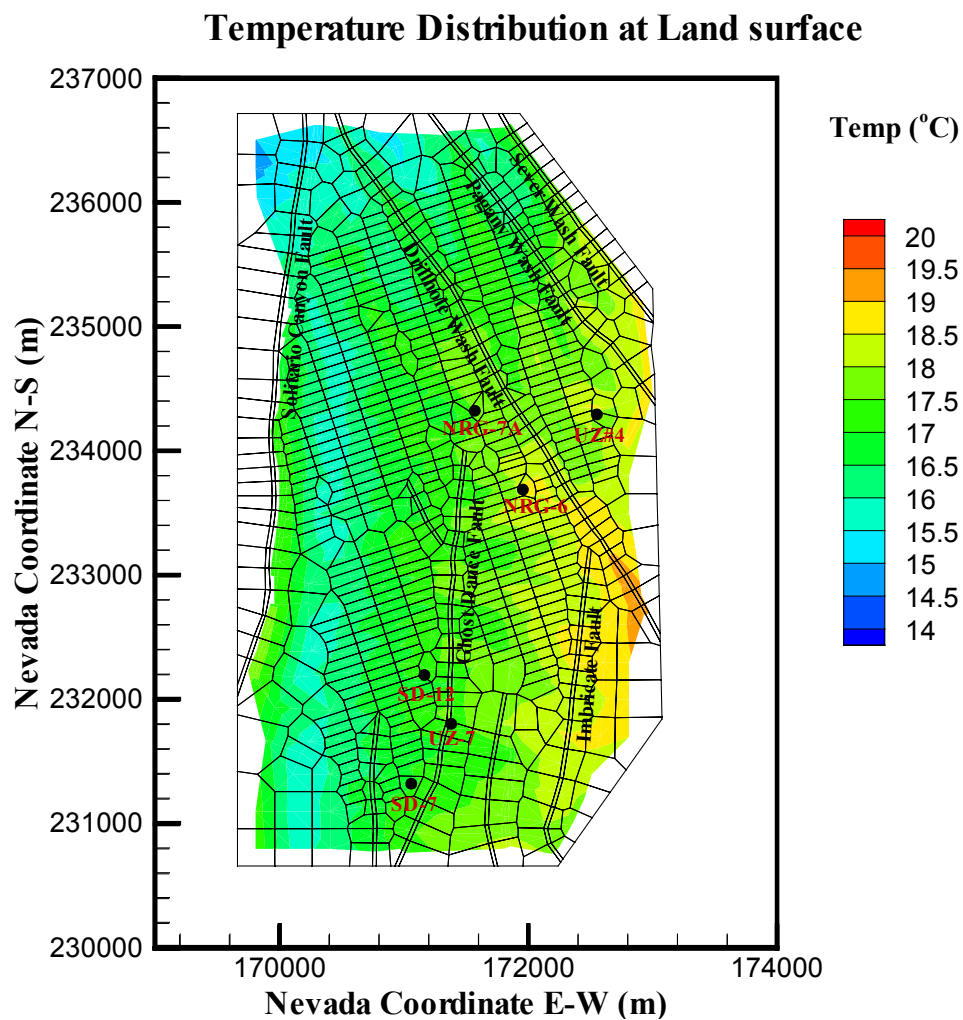
The UZ flow fields for ambient conditions are not sensitive to temperature distributions. For corroborative purpose and to build confidence in the flow field representations, the temperature contours in Figure 6.3-3 were developed over the years from all available data. Wu et al. (1999

[117161], Figure 12) identified that the data sources were from 25 boreholes documented mainly in Sass et al. (1988 [100644]) and observed that, in general, the measured data matched reasonably with early 3D model results (Bodvarsson et al. 1997 [100103]; Ahlers et al. 1995 [101180]). The majority of the early temperature data in Sass et al. (1988 [100644]) are currently not qualified. In this report, six qualified data sets of temperature distributions along boreholes are shown to be consistent with the water table distribution developed from the more extensive data set, demonstrating the consistency of water temperature distribution with unsaturated processes. The same extensive data set is also the basis for saturated zone interpretation of Fridrich et al. (1994 [100575], p. 133–168). Fridrich et al. (1994 [100575], p. 157) discussed the heat flow anomalies, upward and downward flows, and the uncertainty of ignoring unsaturated-zone processes. The consistency of different saturated zone and unsaturated zone interpretations can be further evaluated.



Model Results DTN: LB0303THERMSIM.001

Figure 6.3-3. Ambient Temperature Distributions at the Water Table for the Present-Day Mean Infiltration Scenario



Model Results DTN: LB0303THERMSIM.001

Figure 6.3-4. Temperature Distributions at the Mountain Surface, the Top Model Boundary, for the Present-Day Mean Infiltration Scenario

6.4 PNEUMATIC CALIBRATION

As part of the UZ model calibration effort, 3-D pneumatic simulations are conducted and summarized in this section. Calibration of the UZ model to pneumatic data will aid in estimates of large-scale fracture permeability for the UZ system. This is particularly useful for modeling studies of thermal loading, gas flow and transport of gaseous phase radionuclides for the site (Ahlers et al. 1999 [109715]). The results of these gas flow simulations are compared with field measured pneumatic data from several boreholes to re-estimate fracture permeability in several TSw layers. This section focuses on the model calibration and analysis using these pneumatic simulation results.

6.4.1 Model Parameters and Boundary Conditions

The 3-D mesh used in this gas flow simulation is the same 3-D thermal grid mesh (Figure 6.3-1), used for the thermal simulation. The mesh is described in Section 6.3. The grid domain covers approximately 20 km² of the area, which is smaller than the TSPA-LA grid (Figure 6.1-1). Similar to TSPA-LA grid, this grid also uses a finer mesh in the vicinity of the repository area.

The rock properties used for current 3-D pneumatic prediction are initially those developed using 1-D models for the present-day mean infiltration scenario (BSC 2003 [160240]; DTN: LB02091DSSCP3I.002 [161433]) and 2-D site-scale calibrated fault properties (DTN: LB02092DSSCFPR.002 [162128]). In addition, the model incorporated the parameter set of Table I-1 (Output-DTN: LB03013DSSCP3I.001), and also the thermal properties (DTN: LB0210THRMLPRP.001 [160799]).

The present-day, mean net infiltration rate (with a value of 3.6 mm/yr for the TH model grid) is used to describe the surface infiltration conditions. However, additional pneumatic boundary conditions needed on land surface are time-dependent and are specified using the routine TBgas3D V2.0 (LBNL 2002 [160107]), based on measured atmospheric barometric pressure data (DTN: LB0302AMRU0035.001 [162378]). The bottom water table boundary is treated as a Dirichlet-type boundary. The pressure conditions at the bottom boundary are based on measured surface pressures for boreholes USW SD-7 and SD-12 (DTN: LB991091233129.001 [125868]). First, the average surface pressure and the corresponding pressure at the horizon of 730 m are calculated for each borehole. Then, the average of the two subsurface pressures, 92 kPa, is used to determine the pressures at the water table boundary as a function of elevation change from 730 m. All lateral boundaries are treated as no-flow boundaries. The UZ system is set at an isothermal condition of 25°C, the average of the surface temperature and water table temperature. The steady state solution of flow simulation for the present-day mean infiltration scenario is taken as the initial moisture condition of the current model.

6.4.2 Modeling Approach and Calibration

The 3-D pneumatic simulation is run using EOS3 module of the TOUGH2 code V1.4 (LBNL 2000 [146496]) by neglecting the influence of liquid phase flow. The impact of liquid phase flow to the gas flow system is small for gas-flow simulation results. This was shown by examining the simulation results for the single-phase gas and two-phase water-gas flow, in which single-phase and two-phase flow simulations produce almost identical results in calculated gas pressures, as documented in the Scientific Notebook of Wang (2003 [162417], SN-LBNL-SCI-202-V1, pp.

84–85). The simulation of gas flow by itself is implemented by using the linear relative permeability function and choosing appropriate parameters to force the relative permeability of liquid phase to equal 0.

The pneumatic model was calibrated against the field-measured pneumatic data from two boreholes. The model calibration results indicated that some modification of rock properties in several TSw layers is necessary to match field observed gas pressures. In particular, it was found necessary to reduce the fracture permeability of TSw31-TSw37 subunits by a factor of 15. The lower fracture permeability for the 3-D model may be attributed to the original fracture permeability being estimated from inversion of 1-D models with 1-D vertical flow paths only. In a 3-D model, some high flux channels, such as faults, exist, and 3-D gas flow is able to find these high-permeability pathways with the least resistance for 3-D gas flow. As a result, the fracture permeability of a 3-D model may be lower than that estimated by 1-D models. The differences for the inversion of 1-D, 2-D, and 3-D pneumatic models for this site have been discussed by Ahlers et al. (1999 [109715]).

The two boreholes used for calibration are USW SD-7 and SD-12. Table 6.4-1 shows the sensor elevations, files for averaged observed data (DTN: LB991091233129.001 [125868], and LB02092DSSCFPR.001 [162422]) and observing-date ranges for comparison of these boreholes. The table also lists the corresponding mesh cells in the 3-D thermal model grid. For SD-12, data of the first 30 days are used for the calibration, and the second 30 days are compared to the prediction for validation, as discussed in Section 7.4.

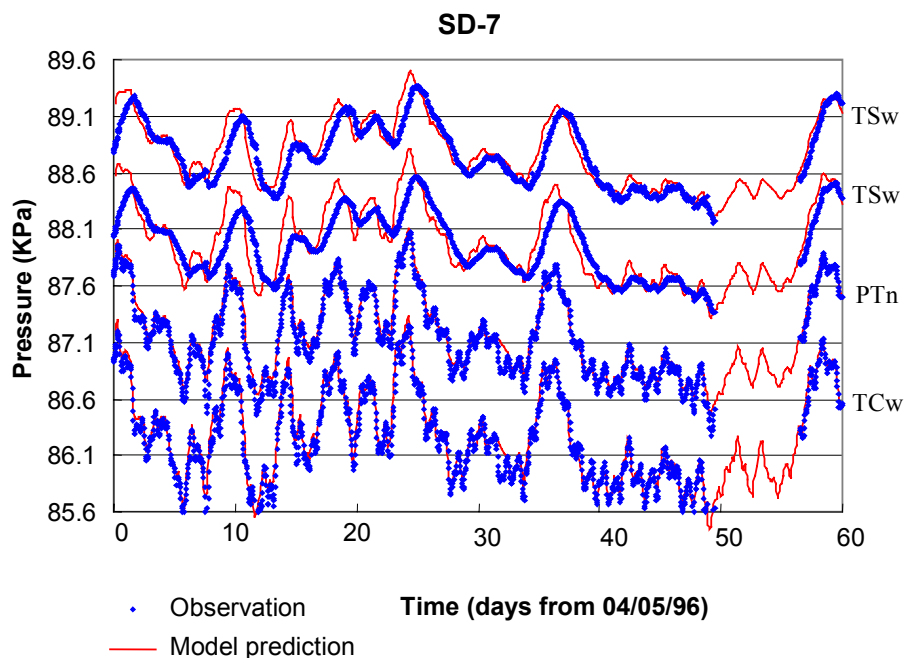
Table 6.4-1. Observation Data and Corresponding Grid Columns of Boreholes SD-7 and SD-12, Used in the Pneumatic Calibration

Sensor Elevation (m)	File for Observation Data	Date Range	Corresponding Observation Cells
Borehole USW SD-7 (LB991091233129.001 [125868])			
1271.6	Sd7_300_zone1.txt	4/5-6/4/96	F0003h42
1256.4	Sd7_350_zone2.txt	4/5-6/4/96	F0008h42
1241.4	Sd7_400_zone3.txt	4/5-6/4/96	F0010h42
1119.2	Sd7_800_zone11.txt	4/5-6/4/96	F013Ah42
Borehole USW SD-12 (LB991091233129.001 [125868])			
1258.5	Sd12_214_PT1679.txt	12/1/95-1/29/96	F002Bh44
1232.0	Sd12_301_PT1667.txt	12/1/95-1/29/96	F0009h44
1217.1	Sd12_350_PT1661.txt	12/1/95-1/29/96	F0011h44
1001.3	Sd12_1058_PT1619.txt	12/1/95-1/29/96	F014Bh44

6.4.3 Analysis of Results

Comparisons of the model simulation results and the field measurement data for boreholes SD-7 (60 days) and SD-12 (30 days) are shown in Figures 6.4-1 and 6.4-2, respectively. In general, the simulation results demonstrate a good match with measurement data for the two boreholes. Except in the TSw unit of SD-7, the 3-D simulation predicts a slightly smaller amplitude signal than the observation data. Many comparisons between model simulated pressures with and without fracture-permeability modifications against field measurements show that the calibrated 3-D model has improved consistently in matching observation data. Note that for borehole SD-7,

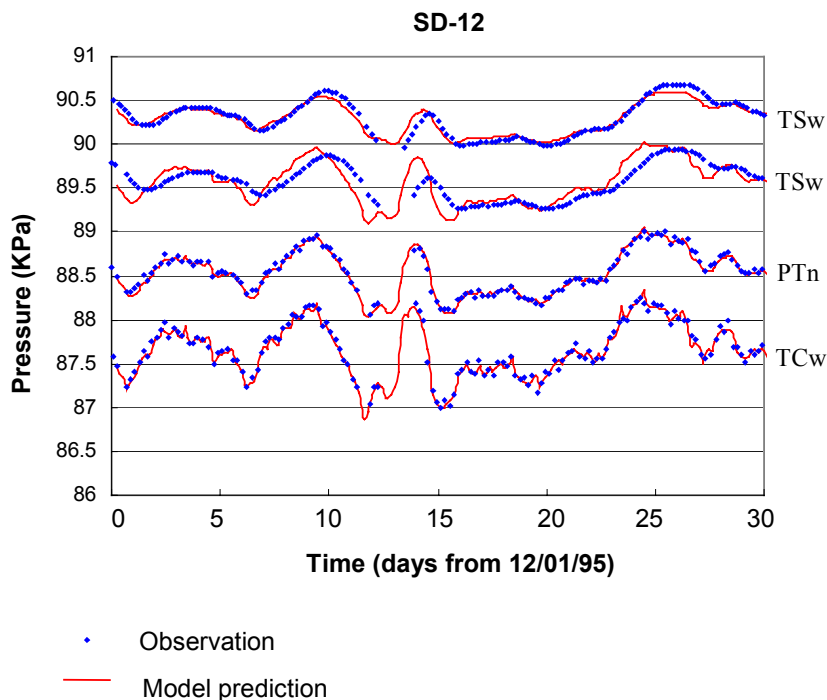
the calibrated-fracture-permeability values of the TSw unit may be even lower for a better match. This might be caused by the effect of the nearby fault on pneumatic signal propagation. In addition, slightly greater differences between simulated and observed gas pressures in the lower TSw unit may be caused by coarse-grid effects and the larger effect of heterogeneity with depth. Overall, a reduction by a factor of 15 (Table 6.2-9) for the TSw fracture permeability provides a better fit to observed pneumatic data for all locations and time periods.



Field Data: LB991091233129.001 [125868]
Model Results-DTN: LB0303GASFLW3D.001

NOTE: Field data from DTN: LB991091233129.001 [125868] are extracted from DTN: GS960908312261.004 [106784]. Both observations and simulations have been vertically offset for clearer display.

Figure 6.4-1. Comparison of Simulated and Observed Gas Pressure at Borehole SD-7 during a 60-Day Period



Field Data: LB991091233129.001 [125868]
Model Results—DTN: LB0303GASFLW3D.001

NOTE: Field data from DTN: LB991091233129.001 [125868] are extracted from DTN: GS960308312232.001 [105573]. Both observations and simulations have been vertically offset for clearer display.

Figure 6.4-2. Comparison of Simulated and Observed Gas Pressure at Borehole SD-12 during the First 30-Day Period

6.5 ANALYSIS AND MODELING OF PORE WATER CHEMICAL DATA

This study is part of the continuing effort to model and analyze geochemical data in the UZ at Yucca Mountain to support the conceptual model of UZ flow and build confidence in the predictive capacity of the model. It consists of using geochemical models to evaluate the hydrological systems, through assessing spatial distribution of surface net infiltration and the impact of variations in its magnitude.

The UZ system of Yucca Mountain has been the subject of intense geological, hydrological, and subsurface engineering study. One of the main issues is the percolation flux at the nuclear waste repository. Percolation flux strongly depends on infiltration rates and their spatial distribution. Much work has been done to estimate the infiltration flux based on various evaporation models (Hevesi et al. 1992 [116809]; Flint and Flint 1994 [103746]). The present-day mean infiltration rate across the study area ranges from one millimeter per year to several tens of millimeters per year (Table 6.1-2, DTN: GS000308311221.005 [147613]). The climate over the past 100,000 years has been used to estimate the possible range in infiltration rates over the next 10,000 years (Sonnenthal and Bodvarsson 1999 [117127]).

Geochemical data provide additional information to analyze the UZ system. Pore-water chemical concentration data are used in this section to calibrate the UZ model and to bound the infiltration flux, flow pathways, and transport time. The distribution of chemical constituents in both liquid

and solid phases of the UZ system depends on many factors, such as hydrological and geochemical processes of surface precipitation, evapotranspiration, and fracture-matrix interaction of flow and transport, large-scale mixing via lateral transport, and the history of climate changes and recharge.

The distribution of chloride in the UZ groundwater provides important information for UZ Model calibration and validation. In this study, pore-water chloride (Cl) concentration data are analyzed and modeled by 3-D chemical transport simulations using the dual-permeability modeling approach. In the UZ flow models on which this chloride transport modeling was based, the base-case flow models use the property set of the PTn (Section 6.2.3) that favor lateral diversion of flow in the PTn unit, as discussed in 6.6.3. Alternative flow models incorporate another property set of the PTn (Section 6.2.3) that is not likely to cause lateral flow.

6.5.1 Available Data

6.5.1.1 Pore-Water Chemical Concentration Data

Chloride transport processes were modeled in this model analysis. The chloride concentrations used in our modeling were measured from pore waters extracted from field samples. These samples were collected from a set of eleven surface-based boreholes, the ESF, and the ECRB. The boreholes are SD-6, SD-7, SD-9, SD-12, NRG-6, NGR-7a, UZ-14, UZ#16, UZ-7a, WT-24, and G-2. Data for each borehole are listed in Table 6.5-1.

Table 6.5-1. Chloride Data Sources*

Boreholes/Facilities	DTN *
SD-6	GS981008312272.004 [153677] A* LA0002JF12213U.001 [154760] B
SD-7	GS000608312271.001 [153407] C GS970908312271.003 [111467] D GS961108312271.002 [121708] F GS981008312272.004 [153677] A LA0002JF12213U.001 [154760] B LAJF831222AQ98.011 [145402] H
SD-9	GS970908312271.003 [111467] D GS961108312271.002 [121708] F LA0002JF12213U.001 [154760] B LAJF831222AQ98.011 [145402] H
SD-12	GS000608312271.001 [153407] C GS970908312271.003 [111467] D GS961108312271.002 [121708] F GS981008312272.004 [153677] A LA0002JF12213U.001 [154760] B
NRG-6	GS010708312272.002 [156375] I LA0002JF12213U.001 [154760] B LAJF831222AQ98.011 [145402] H
NRG-7a	GS961108312271.002 [121708] F GS981008312272.004 [153677] A GS010708312272.002 [156375] I LA0002JF12213U.001 [154760] B LAJF831222AQ98.011 [145402] H
UZ-14	GS010708312272.002 [156375] I GS961108312271.002 [121708] F GS990208312272.001 [146134] J LA0002JF12213U.001 [154760] B LAJF831222AQ98.011 [145402] H
UZ#16	GS010708312272.002 [156375] I GS990208312272.001 [146134] J LA0002JF12213U.001 [154760] B LAJF831222AQ98.011 [145402] H

Table 6.5-1 Chloride Data Sources* (Continued)

Boreholes/Facilities	DTN *
UZ-7a	LA0002JF12213U.001 [154760] B GS981008312272.004 [153677] A
WT-24	GS981008312272.004 [153677] A LA0002JF12213U.001 [154760] B LAJF831222AQ98.011 [145402] H
G-2	LAJF831222AQ98.011 [145402] H
ECRB	LA9909JF831222.004 [145598] K LA0002JF12213U.002 [156281] L
ESF	GS961108312261.006 [107293] M LA0002JF12213U.002 [156281] L LA9909JF831222.010 [122733] N

NOTE: * The letters following the DIRS number is not a part of the DTN number. Each letter corresponds to the identification of the same DTN in the column.

6.5.1.2 Chloride Flux

The sources contributing to the chloride in recharge waters are precipitation, runoff, and runoff. The portion of these waters that forms net infiltration is small. The modern mean infiltration is approximately 5 mm/yr, and the glacial maximum infiltration rate at 28,000 years ago was about 28 mm/yr (Sonnenthal and Bodvarsson 1999 [117127], p. 148, Figure 23; Flint et al. 1996 [100147]). As an approximation, a glacial infiltration scenario in this section was obtained by multiplying the present-day mean infiltration rate by a factor of 5 with the same distribution pattern.

Four case studies corresponding to four climate scenarios were chosen. They represent modern (or present) mean, modern low and modern upper bounds, and glacial mean. Their mean fluxes are listed in Table 6.5-2, calculated from four infiltration maps (DTN: GS000308311221.005 [147613]). Also listed in the table are the notations for these infiltration scenarios. The upper-case “A” represents the corresponding 3-D flow model having a property set for the PTn that would allow lateral diversion. The upper-case “B” is an alternative model that does not account for lateral flow at the PTn (Section 6.2.3). The lower case u, m, and l in the notations stand for flow models of upper, mean, and lower infiltration, on which the chloride models were built. These notations are consistent with the ones used in flow models (Section 6.2). The chloride transport model uses the same flow model as the notation indicates. Chloride recharge fluxes to these transport models are calculated accordingly for these climate scenarios.

The sources of chloride recharge into the UZ includes dissolved material in rain, particulate in snow, and a contribution from windblown dusts (Tyler et al. 1996 [108774]). Precipitation on the land surfaces would experience physical processes such as evaporation, which leaves behind Cl^- in the remaining water. The chloride mass flux to the chloride transport model depends on the amount of water flux and its chloride concentration. In our modeling, we consider the fluxes as precipitation, runoff, and runoff. Thus, the water fluxes contributing to chloride recharge can be calculated using the following equation:

$$F = F_{prec} + F_{runon} - F_{runoff} \quad (\text{Eq. 6.5-1})$$

where F is net flux contributing to chloride in the recharging water (defined as net recharge in Table 6.5-2, independent of net infiltration of Table 6.1-2), F_{prec} is precipitation flux, F_{runon} is runon, and F_{runoff} is runoff flux. These water flux terms are eventually converted to have units of $\text{kg}/(\text{m}^2 \cdot \text{sec})$ as input. The calculation of each term in F is performed using the routine infil2grid V1.7 (LBNL 2002 [154793] and DTN: GS000308311221.005 [147613]).

Table 6.5-2. Present-Day and Glacial Infiltration Fluxes at Different Scenarios (Averaged over Model Domain, mm/year)

Scenario Notations †	Scenarios	Precipitation	Runon	Runoff	‡ Net Recharge Used in Calculation of Chloride Flux
preq_uA preq_uB	Modern upper	267.1	171.9	9.1	429.9
preq_mA preq_mB	Modern mean	189.5	41.1	3.5	227.1
preq_IA preq_IB	Modern low	185.9	13.6	1.0	198.5
glac_mA*	Glacial mean	316.9	292.0	14.4	594.5

Source: Fluxes calculated as described in Attachment III, Section III.1.1, data from DTN: GS000308311221.005 [147613]

NOTE: † The upper-case letter A in the notation denotes the base-case model property set used by the corresponding flow model that would favor lateral flow diversion, and upper-case B denotes the alternative model, in which the property set of the PTn would not likely cause flow diversion (Section 6.2.3).

‡ Net water flux contributing to the chloride recharge is calculated by Equation 6.5-1.

* In our modeling of the glacial scenario, a special case of the model was run for simulating 100,000 years to steady state with glacial chloride flux and then switched to present-day mean chloride recharge for 11,000 years. The simulation is given the notation glac_pmA.

Surface chloride concentrations are discussed by Sonnenthal and Bodvarsson (1999 [117127], pp. 113-114). The range of 0.55–0.73 mg/L was considered to bound the average value. Similar value was obtained by combining a mean annual precipitation of about 170 mm/year with a present-day chloride surface flux of 106 $\text{mg}/(\text{m}^2\text{-year})$, yielding a mean chloride concentration of about 0.62 mg/L (Fabryka-Martin et al. 1997 [100145]). A value of 0.55 mg/L (Sonnenthal and Bodvarsson 1999 [117127]; Triay et al. 1996 [101014]) is used in the present simulations, applied to all infiltrating water in the forms of precipitation, runon, and runoff (Sonnenthal and Bodvarsson 1999 [117127], p. 148). Then, the chloride flux is calculated using the following formula:

$$F_{Cl} = C_{Cl,p} \times 10^{-6} (F_{prec} + F_{runon} - F_{runoff}) \quad (\text{Eq. 6.5-2})$$

where F_{Cl} is chloride flux (kg/sec), F_{prec} is precipitation flux ($\text{kg water}/\text{sec}$), F_{runon} is runon ($\text{kg water}/\text{sec}$), and F_{runoff} is runoff flux ($\text{kg water}/\text{sec}$). $C_{Cl,p}$ is chloride concentration in

precipitation (mg/kg water). Actual calculations and procedures using this equation in preparing input files for chloride simulations are summarized in Attachment III, Section III.1.

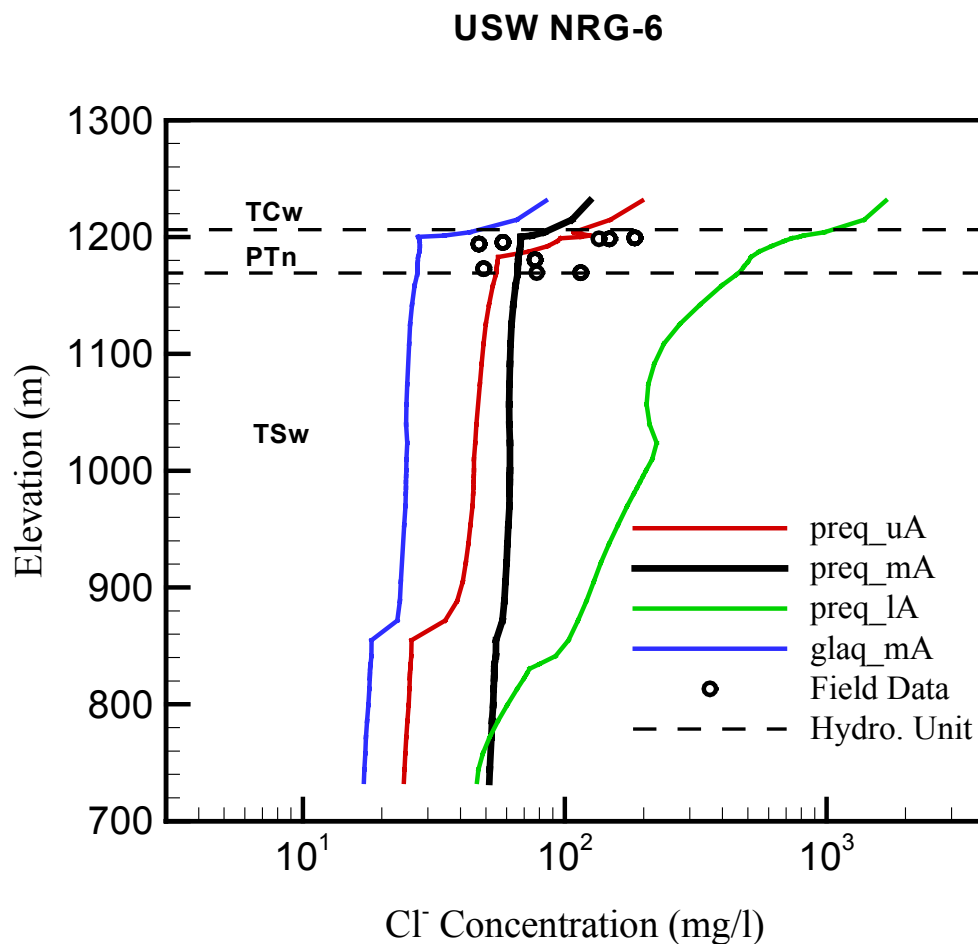
6.5.2 Three-Dimensional Simulations

Chloride transport for the UZ hydrological system was simulated under two-phase isothermal flow conditions of water and air. A three-dimensional dual-permeability model and the T2R3D V1.4 (LBNL 1999 [146654]) of the TOUGH2 code were employed for the simulations. The steady-state liquid-flow fields were obtained using the EOS9 module of T2R3D (LBNL 1999 [146654]). Chemical distributions were then computed from transport equations using the decoupled T2R3D module (LBNL 1999 [146654]). Flow boundary conditions, simulation grids, and the basic hydrological properties of the rock matrix and fractures are the same as those used in the 3-D UZ flow simulation of nonperched-water model. Boundary conditions for chemical components were treated similarly to those for flow simulations, with mass flux described at the top boundary and no-flow and water table conditions at the lateral and bottom boundaries, respectively. The dispersivities for both fracture and matrix continua in the simulation were assumed to be zero (Sonnenthal and Bodvarsson 1999 [117127], Section 5.3, p. 129). The same diffusion coefficient used for Cl^- , $2.032\text{E-}9 \text{ m}^2/\text{s}$, is used for chemical ions at 25°C , which is the average of the surface temperature and water table temperature, and dilution in water (Lide 2002 [160832], p. 5-96). The tortuosity was set to 0.7 for fracture and 0.2 for matrix, respectively (BSC 2001 [158726]; Grathwohl 2000 [141512]).

6.5.2.1 Modeling Results

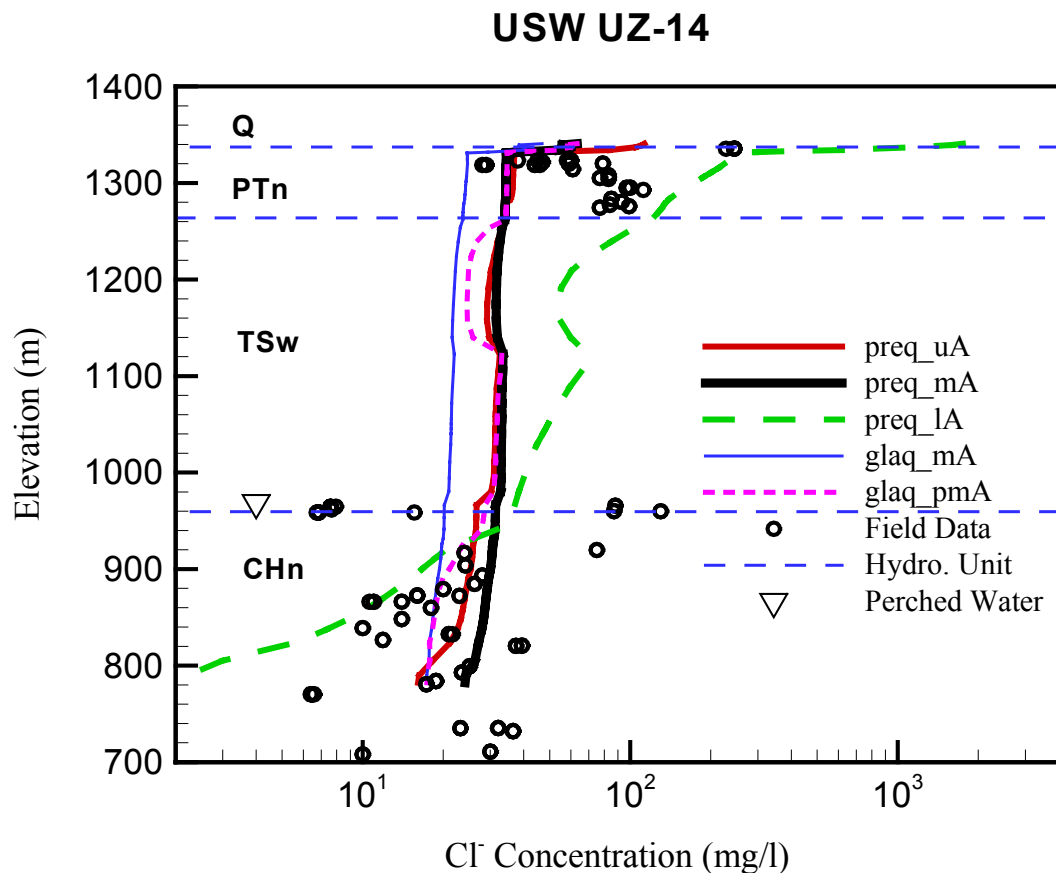
The modeling results are represented in Figures 6.5-1 and 6.5-2 for boreholes NRG-6 and UZ-14. These figures plot the chloride profiles of present infiltration rates of mean infiltration with lower and upper bounds. The results demonstrate that the mean infiltration case has the closest match between the calculated concentrations and the field-measured chloride data. The upper-bound case shows a moderate match; the lower-bound case shows the poorest match.

The glacial scenario yields generally lower chloride concentration than the present case, upper bound (Figures 6.5-1 and 6.5-2). A special scenario run (glaq_pmA) with the glacial case was conducted (Figure 6.5-2, purple line). The model was run for 100,000 years to steady state with glacial recharge, and then was switched to present-day recharge for 11,600 years. The model yields a closer match than the glacial recharge case.



Field Data: GS010708312272.002 [156375]; LA0002JF12213U.001 [154760]; LAJF831222AQ98.011 [145402].
 Model Results—DTN LB0303CLINFL3D.001

Figure 6.5-1. Chloride Concentration (mg/L) Profiles at Borehole USW NRG-6 for Present Recharge with Mean, Upper, and Lower Bounds and Glacial Recharge



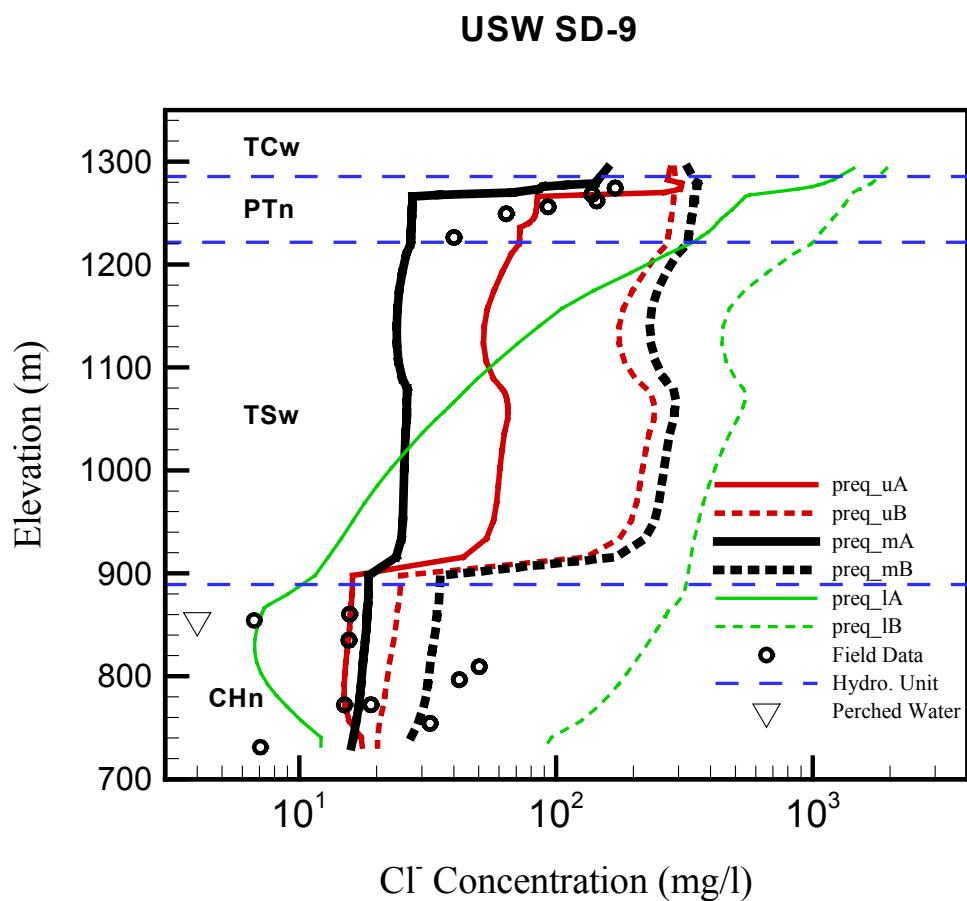
Field Data: GS010708312272.002 [156375]; GS961108312271.002 [121708]; GS990208312272.001 [146134];
 LA0002JF12213U.001 [154760]; LAJF831222AQ98.011 [145402].
 Model Results—DTN LB0303CLINFL3D.001

Figure 6.5-2. Chloride Concentration (mg/L) Profiles at Borehole USW UZ-14 for Present Recharge with Mean, Upper, and Lower Bounds and Glacial Recharges

6.5.2.2 Alternative Model

In the above base case (A), the property set for the PTn would favor lateral diversion of flow. The alternative model (B) uses a different property set for the PTn, one that does not favor large-scale lateral diversion (Table 6.5-2). A comparison between the base-case model and the alternative model results are presented for borehole USW SD-9 and the ECRB in Figures 6.5-3 and 6.5-4).

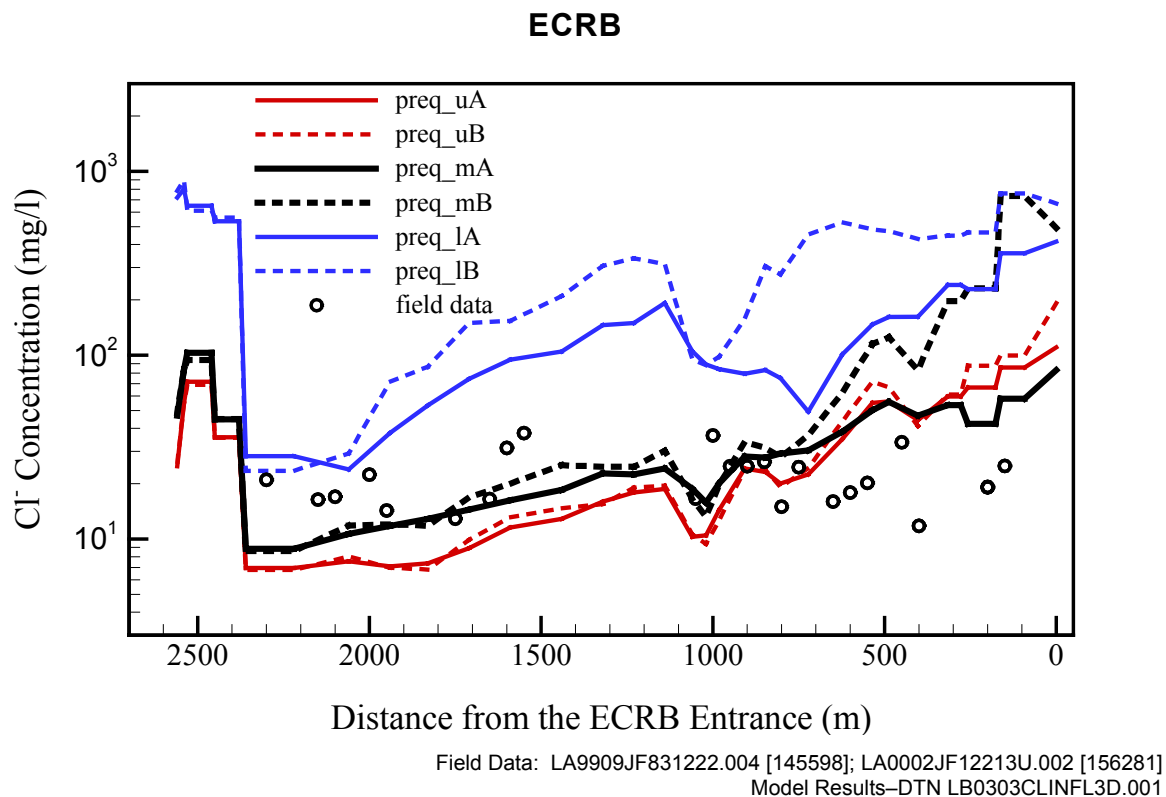
Comparative studies of chloride distributions within the UZ, simulated using the base-case and alternative flow fields, indicate consistently that the base-case flow field simulation results provide an overall better match with the observed chloride. As discussed in Sections 6.2.5 and 6.6.3, the main difference between the base-case and alternative flow fields is whether there is large- or small-scale lateral flow within the PTn unit, with the base-case flow fields predicting relatively large lateral diversion in general. The model calibration results with chloride data of this section further reveal that large lateral diversion may exist in the PTn Unit. Therefore, pore water chloride may provide key evidence for understanding flow through the PTn, which has a direct impact on chloride transport and distributions.



Field Data: GS970908312271.003 [111467]; GS961108312271.002 [121708];
 LA0002JF12213U.001 [154760]; LAJF831222AQ98.011 [145402].
 Model Results—DTN LB0303CLINFL3D.001

NOTE: The upper-case letter A denotes the base-case model property set. The uppercase letter B denotes the alternative model.

Figure 6.5-3. Chloride Concentration (mg/L) Profiles at Borehole USW SD-9 for Present Recharge with Mean, Upper, and Lower Bounds and Glacial Recharge



NOTE: The upper-case letter A denotes base-case model property set. The upper-case letter B denotes the alternative model.

Figure 6.5-4. Chloride Concentration (mg/L) Profiles at the ECRB for Present Recharge with Mean, Upper, and Lower Bounds

6.6 FLOW PATTERN ANALYSIS OF TSPA-LA 3-D FLOW FIELDS

This section analyzes and summarizes the 18 flow simulation scenarios. Nine of the flow fields are the base-case flow fields of Section 6.2, as summarized in Table 6.2-9, and have been submitted to TSPA-LA for performance analyses. The remaining nine flow fields are considered as alternatives. The 18 model simulations are performed using the TSPA-LA grid (Figure 6.1-1) and nine infiltration maps, as discussed in Section 6.1, and the six calibrated parameter sets in Attachment I of this Model Report, and the UZ Flow Model of Section 6.2.2.

6.6.1 Simulation Scenarios

Table 6.6-1 summarizes the nine alternative simulation scenarios, associated with parameter sets (Tables I-4, I-5, and I-6), respectively, for the nine infiltration maps. The alternative property set "B" uses different rock parameters for the PTn unit such that less lateral diversion in the PTn is expected.

Table 6.6-1. Nine Simulation Scenarios of Alternative UZ Flow: Data Files, Parameter Sets, and Infiltration Maps for the UZ Flow Fields

Designation/ Simulation	Parameter Set/ Calibration (Output-DTN: LB03013DSSCP3I.001)	Infiltration Map (DTN: GS000308311221.005 [147613])
preq_IB	Parameter set from Table I-6, lower-bound infiltration	Present-day, lower-bound infiltration
preq_mB	Parameter set from Table I-4, present day/modern, mean infiltration	Present-day, mean infiltration
preq_uB	Parameter set from Table I-5, upper-bound infiltration	Present-day, upper-bound infiltration
monq_IB	Parameter set from Table I-6, lower-bound infiltration	Monsoon, lower-bound infiltration
monq_mB	Parameter set from Table I-4, present day/modern, mean infiltration	Monsoon, mean infiltration
monq_uB	Parameter set from Table I-5, upper-bound infiltration	Monsoon, upper-bound infiltration
glaq_IB	Parameter set from Table I-6, lower-bound infiltration	Glacial transition, lower-bound infiltration
glaq_mB	Parameter set from Table I-4, present day/modern, mean infiltration	Glacial transition, mean infiltration
glaq_uB	Parameter set from Table I-5, upper-bound infiltration	Glacial transition, upper-bound infiltration

As shown in Table 6.6-1, simulations with the alternative model are also carried out for the same three climatic scenarios (i.e., present-day, monsoon, and glacial transition), and mean, lower-bound, and upper-bound infiltration rates as for the base-case simulations.

6.6.2 UZ Alternative Flow Model Results

Similar to the calibration simulations of the base-case flow fields, the mass-balance check has been conducted for the nine alternative model simulations. Table 6.6-2 lists the global mass-balance results for the nine alternative model simulations. Global mass-balance errors between inflow and outflow of the system for the nine flow fields, as shown in Table 6.6-2, are all smaller than 0.06%, indicating that solutions approximate steady state for these cases.

Table 6.6-2. Mass-Balance Results for Nine Simulations of Alternative Flow Model

Simulation Scenarios	Inflow from Infiltration (kg/s)	Outflow to Water Table (kg/s)	Relative Error (%)
preq_IB	1.5828143	1.5828178	0.0002
preq_mB	5.5922355	5.5951199	0.0516
preq_uB	13.564390	13.568112	0.0274
monq_IB	5.5922355	5.5920365	0.0036
monq_mB	14.939317	14.936880	0.0163
monq_uB	24.286298	24.277515	0.0362
glacq_IB	2.9648877	2.9648838	0.0001
glacq_mB	21.494950	21.495094	0.0007
glacq_uB	40.024949	40.024939	0.0000

Model Results—DTNs: LB03033DSSFF9I.001.

Alternative Model Result Examination: In addition to the nine base-case flow fields of Section 6.2.5, the nine alternative 3-D flow fields have also been compared against the field-observed data of matrix liquid saturation, as well as available water-potential and perched-water data. The available data used in the model checking are listed in Table 6.2-1. Overall, examination results are as follows (see Wang 2003 [162417], SN-LBNL-SCI-199-V1, pp. 158–186, 243, for detailed comparisons):

- The simulation results with the nine alternative flow fields are also able to fit the available matrix liquid saturation and water potential data from the nine boreholes (Table 6.2-1) well, similarly to the base-case flow fields of Section 6.2.5, including PTn units.
- For calibrations with perched-water data, except for water-potential results for lower-bound infiltration (in SD-7 and SD-9), the six simulations with mean, lower-bound, and upper-bound present-day infiltration rates, in general, match perched-water data.

6.6.3 Flow Fields and Analyses

Percolation flux through the UZ is one important natural-barrier factor affecting overall repository performance in TSPA calculations. The quantity as well as the spatial and temporal variations in percolation flux will directly affect: (1) the amount of water flowing into waste emplacement drifts; (2) moisture conditions and the corrosion environment of waste packages within the drifts; (3) radionuclide release from the repository; and (4) radionuclide migration from the UZ to the saturated zone. Percolation fluxes through unsaturated fractured tuffs cannot be readily measured in the field, and thus indirect data and model results have to be used to estimate these fluxes.

Model studies (Wu et al. 1999 [117161] and 2002 [160195]) indicate that the accuracy of model predictions for percolation fluxes in the UZ at Yucca Mountain depend on many factors including (1) net infiltration rates over the surface boundary (Wu et al. 1999 [117161], pp. 208–210 and Figure 13; 2002 [160195], p. 227, Figure 6); (2) geological and conceptual models; (3) distribution of rock-property values for fractures and matrix; and (4) treatment of fracture-matrix flow and interaction. In this section, percolation fluxes at the repository horizon are analyzed using the 18 simulation results (Tables 6.2-9 and 6.6-1) of the UZ flow models for TSPA-LA. In the analysis, the percolation flux is defined as total vertical liquid mass flux through both fractures and matrix, and is converted to millimeter per year (mm/yr) per unit area using a constant water density.

Figures 6.6-1 to 6.6-3 show examples of percolation fluxes along the repository layer for the three mean infiltration scenarios of the three climates, respectively, with the base-case flow fields. (Note: see Attachment IV for relevant data compilation for the PTn/TSw interface flux.) Comparisons of the calculated repository percolation fluxes of Figures 6.6-1, 6.6-2, and 6.6-3 with those of the surface infiltration maps (Figures 6.1-2, 6.1-3 and 6.1-4, respectively), indicate that percolation fluxes at the repository are very different from surface infiltration patterns. Note that surface infiltration rates and distributions are independent of faults. The major differences in percolation flux at the repository level (Figures 6.6-1–6.6-3) are (1) flow mainly through faults in the very northern part of the model domain (with the north coordinate > 237,000 m); (2) flow diverted into or near faults located in the model domain; and (3) about a 500 m lateral flow of the high infiltration zones from south to north along the crest located to the east. This large-scale lateral flow from west to east (in general) is illustrated by “Lateral Flow Scale” on Figures 6.6-1, 6.6-2, and 6.6-3, respectively, for the three mean infiltration scenarios. Lateral flow may also occur from the Solitario Canyon fault to the east, reaching the repository blocks, since the fault is very close to the repository (Figure 6.1-1), included in the 18 flow fields. Note that flow redistribution in the very northern part of the model domain (far beyond the repository block) results from the repository gridlayer horizon laterally intersecting the CHn zeolitic and perched-water zones, with major flow paths being faults. Overall, percolation results as shown in Figures 6.6-1, 6.6-2, and 6.6-3 display very different patterns from the surface infiltrations, because of the substantial amount of large-scale lateral flow within the PTn unit. This indicates that within the PTn unit, lateral flow has a significant impact on percolation flux distribution in the repository layer.

Simulated percolation fluxes in the repository layer, in addition to those shown in Figures 6.6-1, 6.6-2, and 6.6-3 (for three mean infiltration rates), include three lower bounds and three upper bounds of infiltration rates for the nine base-case flow fields, as well as the nine infiltration rates

of the three climates with the alternative flow fields. Further examination of all nine base-case simulation results against their corresponding surface infiltration maps indicates that more significant lateral flow occurs in the PTn for lower-bound and mean infiltration scenarios than for the upper bound infiltration. A further examination of all flow fields indicates that the lower the infiltration rates, the larger the lateral flow scales. (For examples, see Wang (2003 [162417], SN-LBNL-SCI-199-V1, pp. 125, 128–130; SN-LBNL-SCI-199-V2, pp. 17, 24, 25).) This is because the lower infiltration results in drier condition with stronger capillarity (Wu et al. 2002 [161058]). On the other hand, the simulation results with the nine alternative flow fields show small lateral flow occurrence in the PTn in the area above the repository. These results show that the flow patterns through PTn have a large impact on percolation flux distribution in the repository horizon.

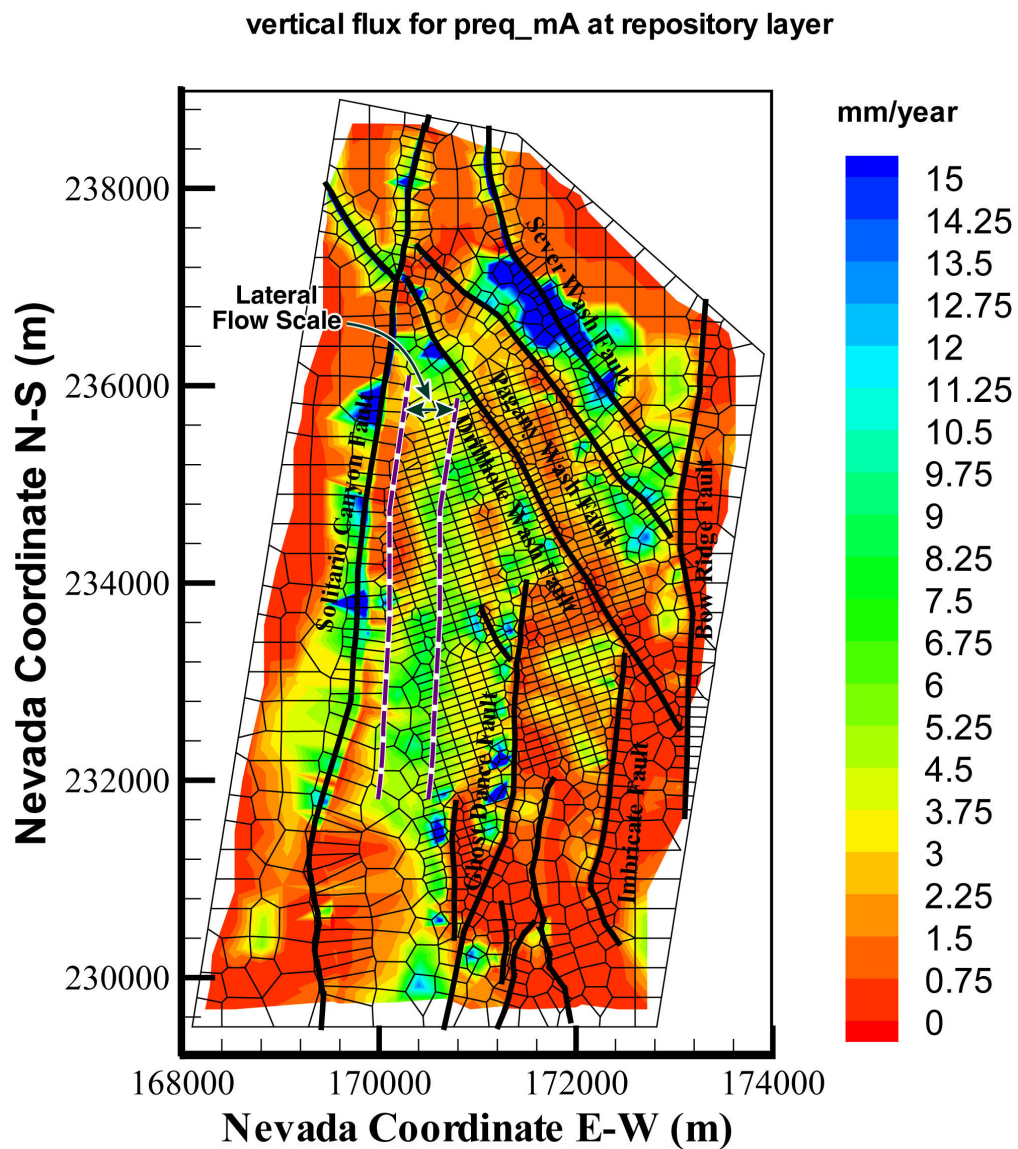
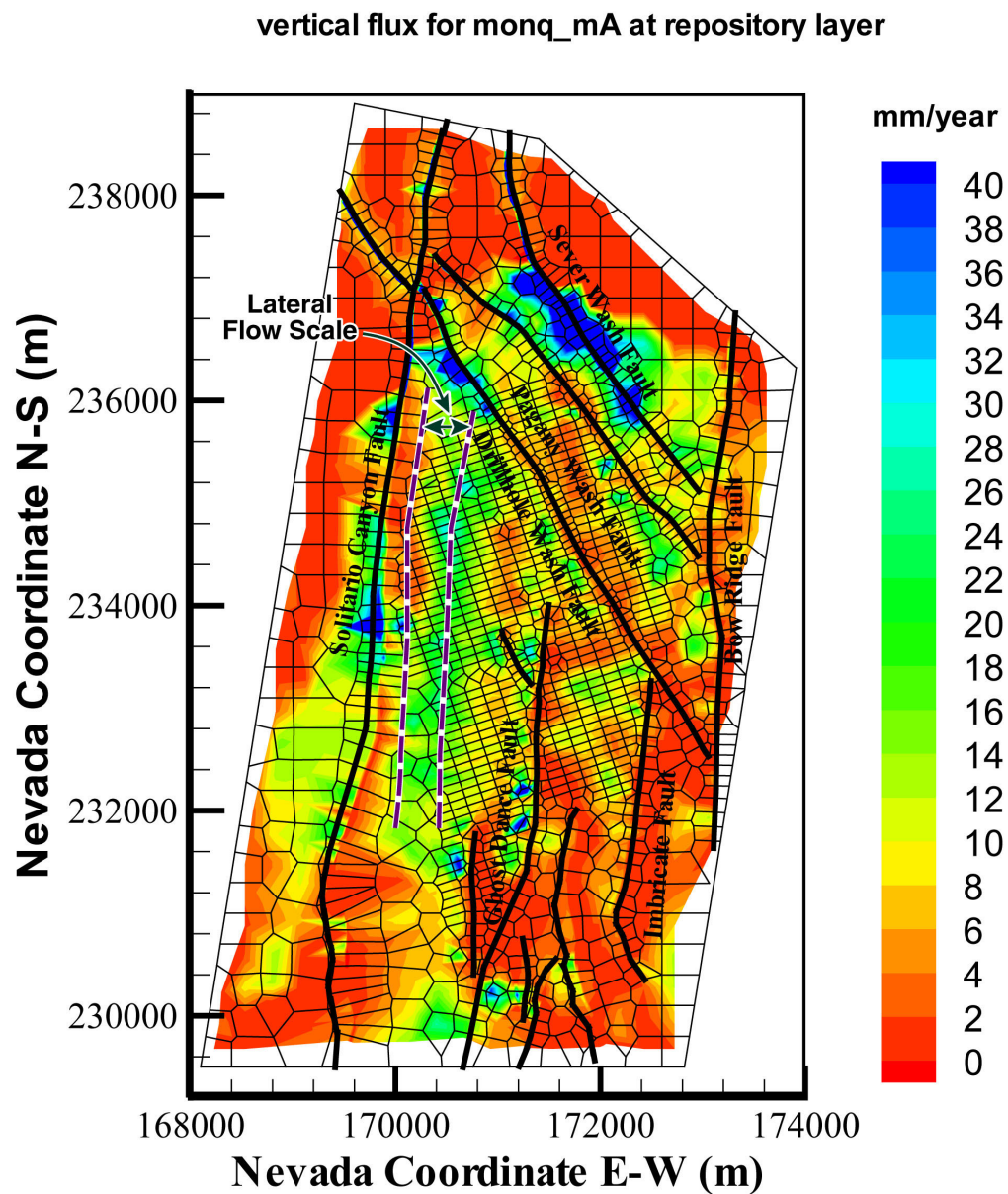
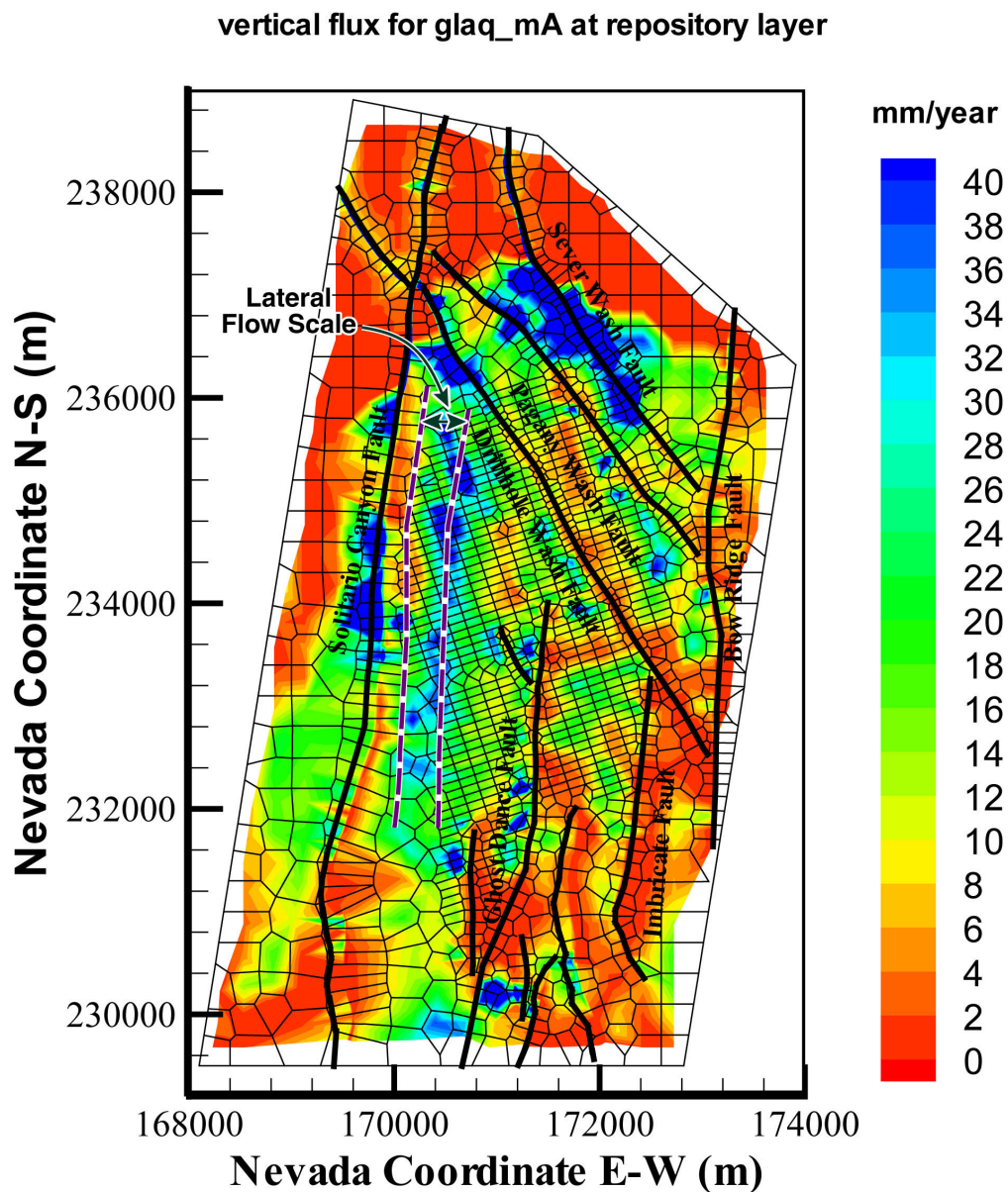


Figure 6.6-1. Simulated Percolation Fluxes at the Repository Horizon under the Present-Day, Mean Infiltration Scenario Using the Results of Simulation preq_mA



Model Results-DTN: LB03023DSSCP9I.001.

Figure 6.6-2. Simulated Percolation Fluxes at the Repository Horizon under the Monsoon, Mean Infiltration Scenario Using the Results of Simulation monq_mA



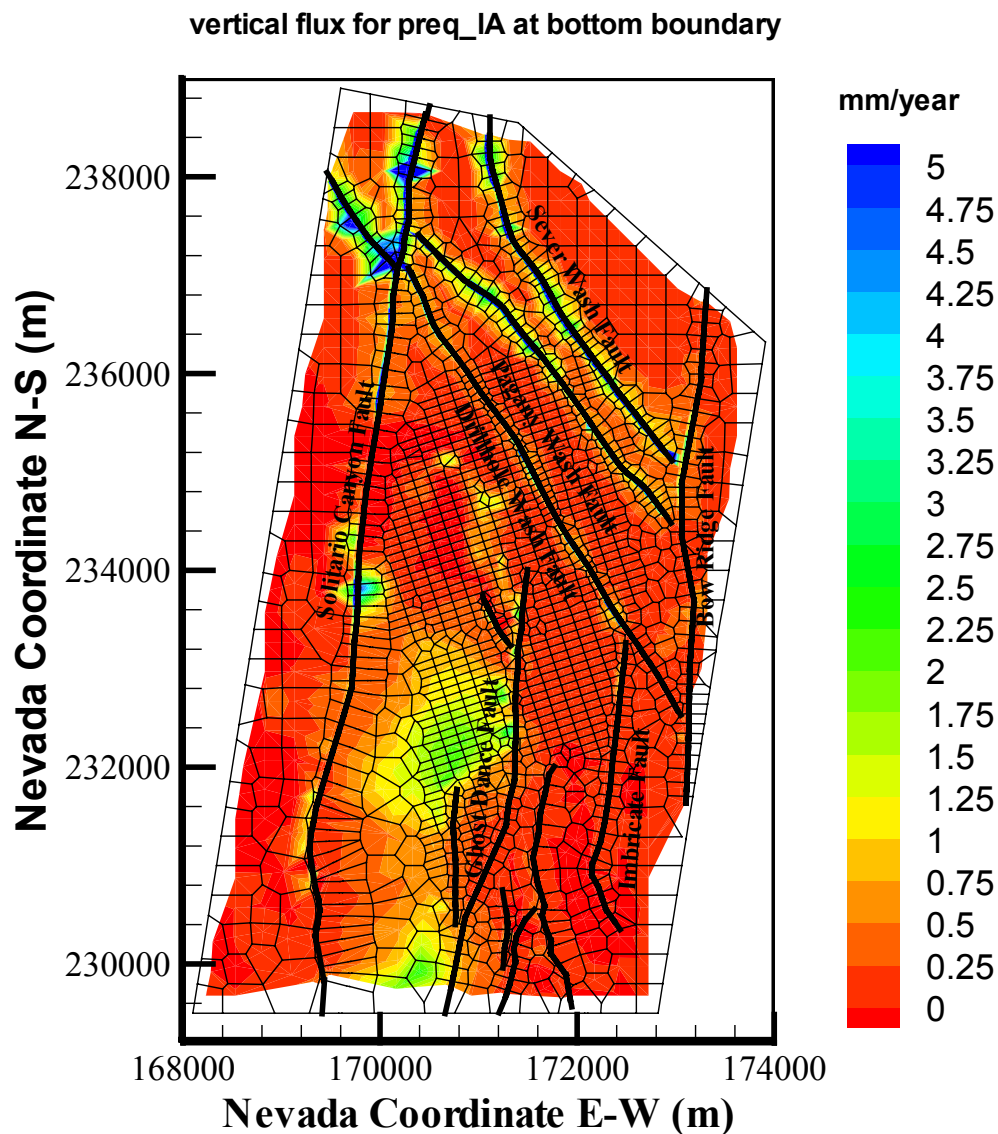
Model Results—DTN: LB03023DS SCP9I.001.

Figure 6.6-3. Simulated Percolation Fluxes at the Repository Horizon under the Glacial Transition Mean Infiltration Scenario Using the Results of Simulation glaq_mA

Figures 6.6-4 through 6.6-21 show the simulated percolation fluxes at the water table using the nine base-case and nine alternative flow simulations with nine infiltration scenarios of the three climates. When comparing the percolation fluxes at the repository (e.g., Figures 6.6-1-, 6.6-2, and 6.6-3), as well as with themselves from the two models (e.g., Figure 6.6-4 versus Figure 6.6-5), we find the following:

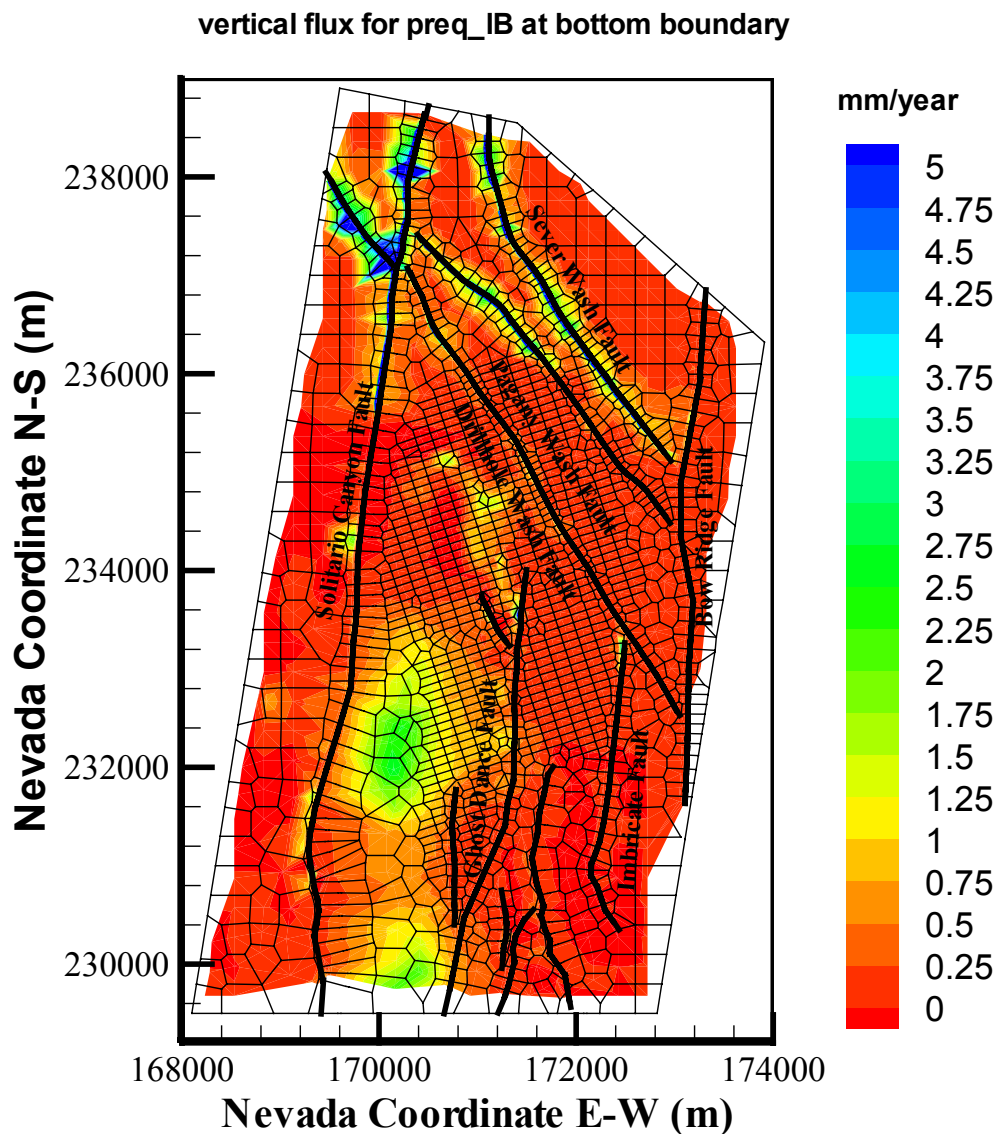
- There are fewer differences in the calculated percolation fluxes for the two models at the water table than those at the repository level for the same infiltration scenarios.
- In the northern half of the domain, the base-case flow fields are very similar to the alternative ones. Because of the impact of perched water and zeolitic units, flow is mainly focused into major faults.
- In the central and southern portions of the model domain, the base-case flow fields at the water table show lateral flow of several hundreds of meters to the east in the area directly below the southern repository. This is the area where vitric zones are located within the CHn unit.

Note that all 18 flow fields are calculated using a fixed water table. These flow fields can also be used for a rising-water-table case in the future. This is because the water table is handled as a sink term in the model, and the flow at or above the water table is determined by the upstream or upper-layer conditions. Therefore, a water-rise situation can be handled by simply transecting the flow fields vertically at a new water table elevation. The software WTRISE V2.0 (LBNL 2003 [163453]) is available to obtain those results; however, it has not been used in this report.



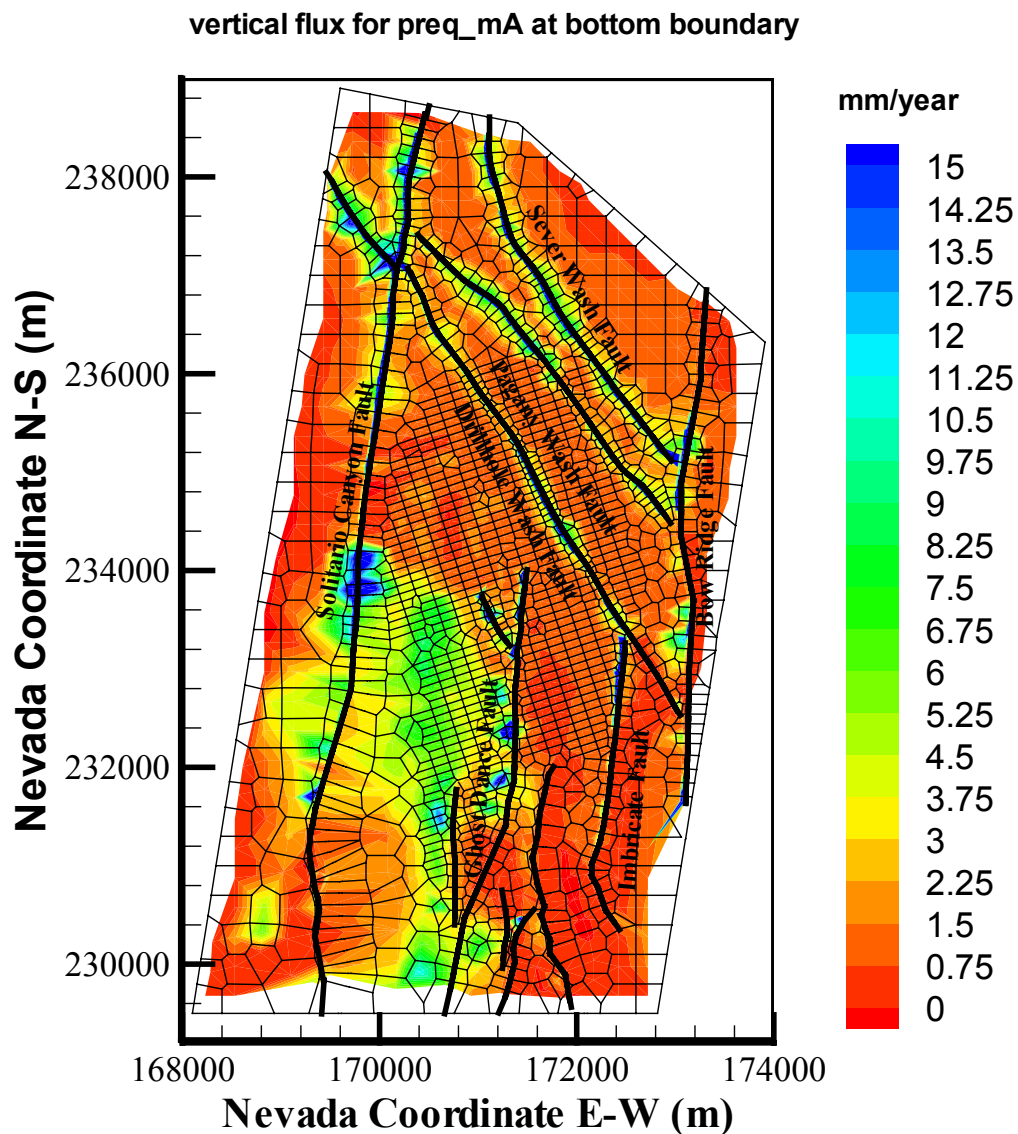
Model Results-DTN: LB03023DSSCP9I.001.

Figure 6.6-4. Simulated Percolation Fluxes at the Water Table under the Present-Day, Lower-Bound Infiltration Scenario Using the Results of Simulating the Base-Case Model: preq_IA



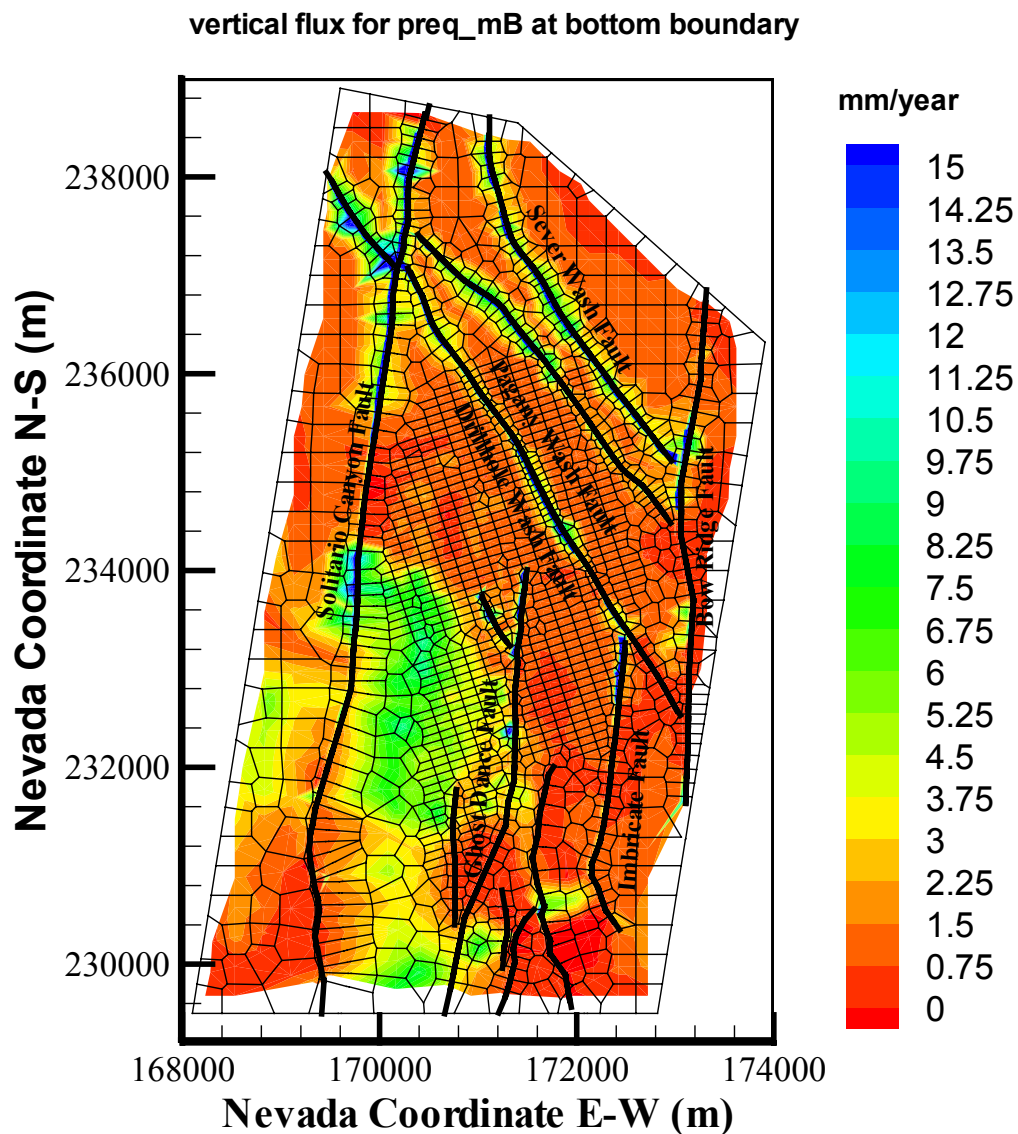
Model Results—DTN: LB03033DSSFF9I.001.

Figure 6.6-5. Simulated Percolation Fluxes at the Water Table under the Present-Day, Lower-Bound Infiltration Scenario Using the Results of Simulating the Alternative Model: preq_IB



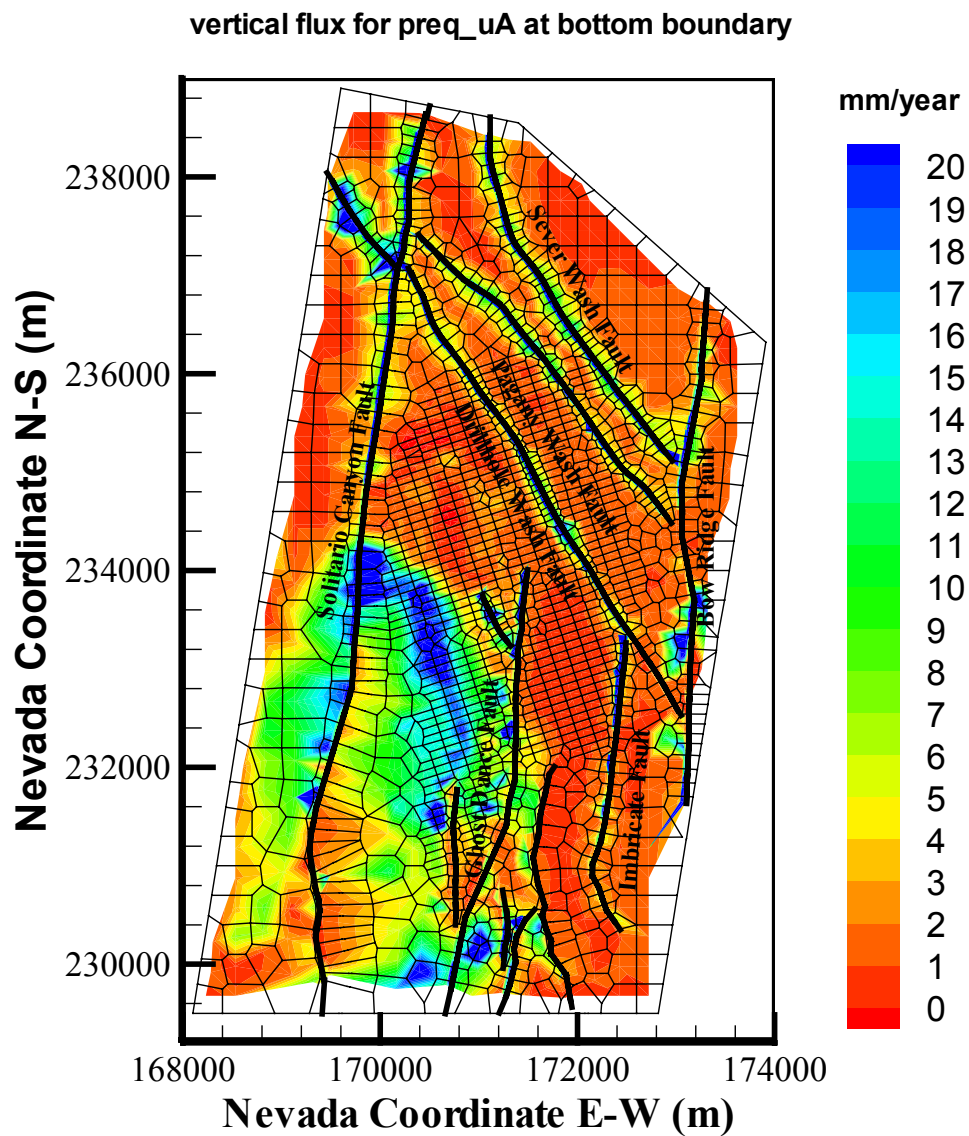
Model Results—DTN: LB03023DSSCP9I.001.

Figure 6.6-6. Simulated Percolation Fluxes at the Water Table under the Present-Day, Mean Infiltration Scenario Using the Results of Simulating the Base-Case Model: preq_mA



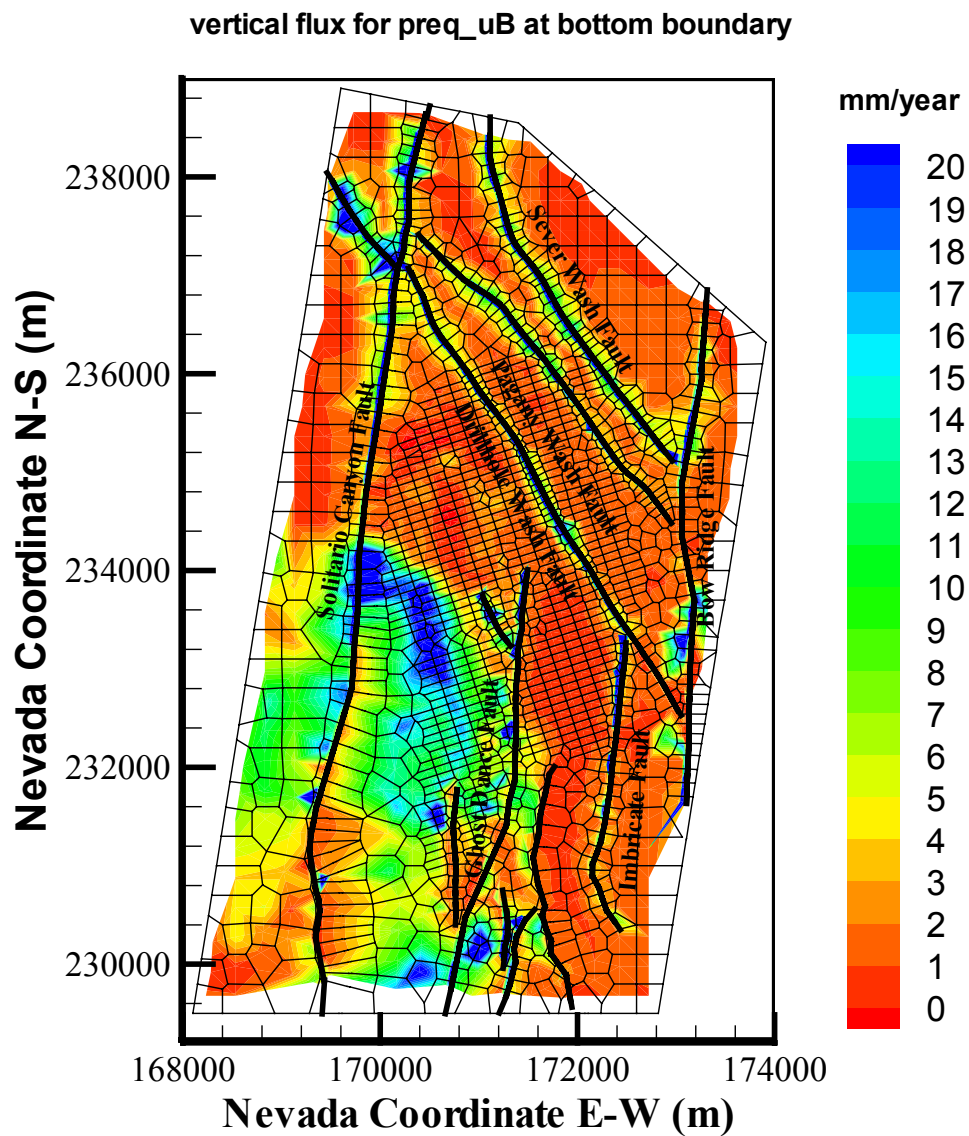
Model Results—DTN: LB03033DSSFF9I.001.

Figure 6.6-7. Simulated Percolation Fluxes at the Water Table under the Present-Day, Mean Infiltration Scenario Using the Results of Simulating the Alternative Model: preq_mB



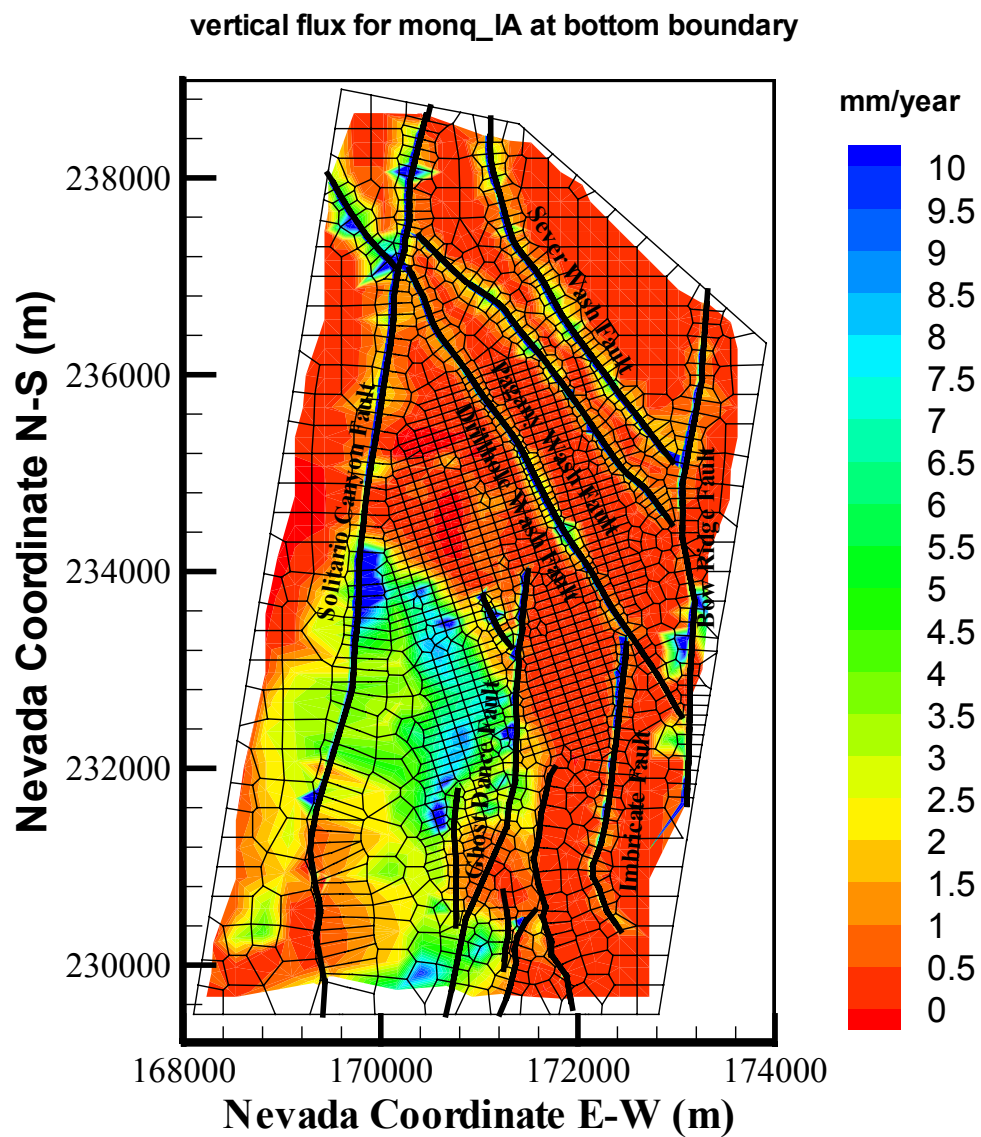
Model Results-DTN: LB03023DSSCP9I.001.

Figure 6.6-8. Simulated Percolation Fluxes at the Water Table under the Present-Day, Upper-Bound Infiltration Scenario Using the Results of Simulating the Base-Case Model: preq_uA



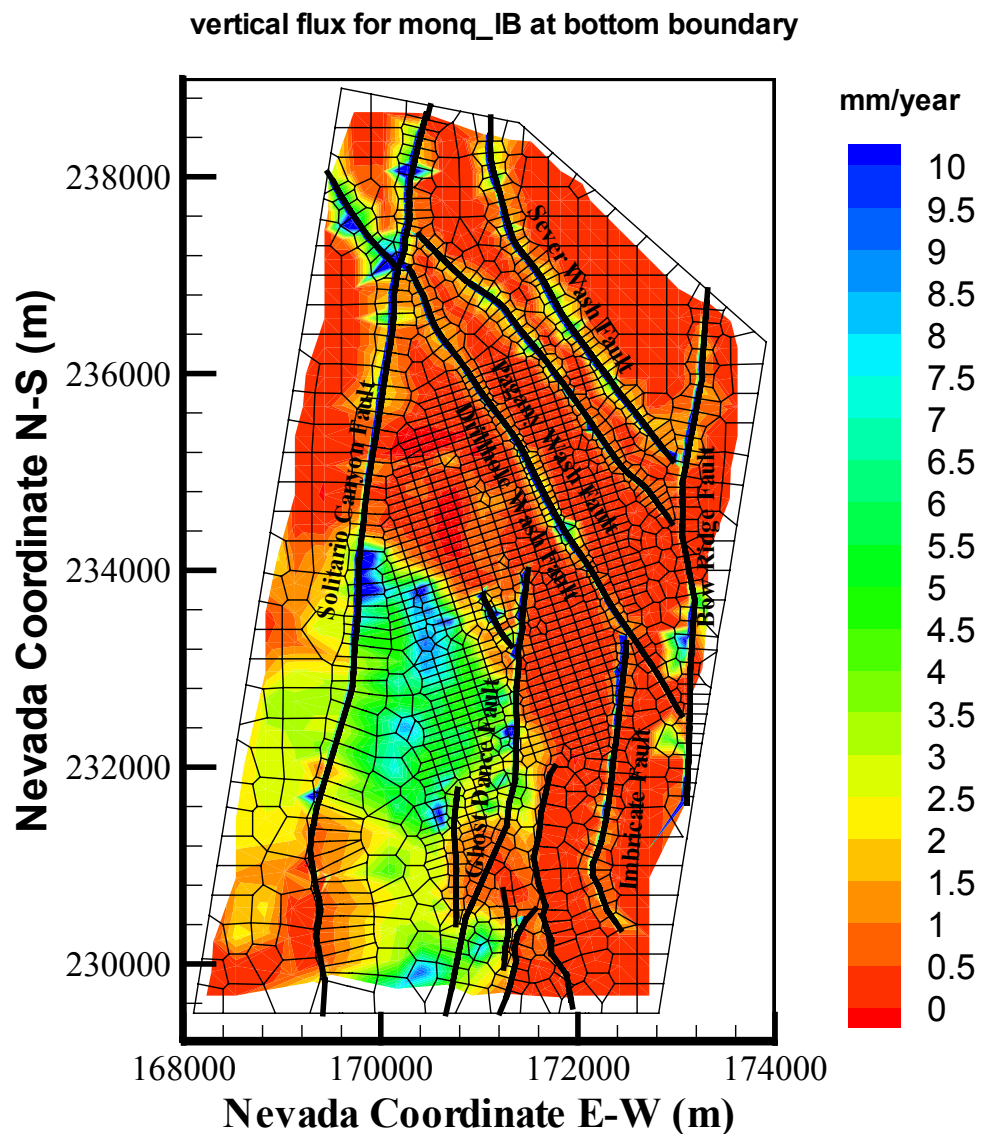
Model Results-DTN: LB03033DSSFF9I.001.

Figure 6.6-9. Simulated Percolation Fluxes at the Water Table under the Present-Day, Upper-Bound Infiltration Scenario Using the Results of Simulating the Alternative Model: preq_uB



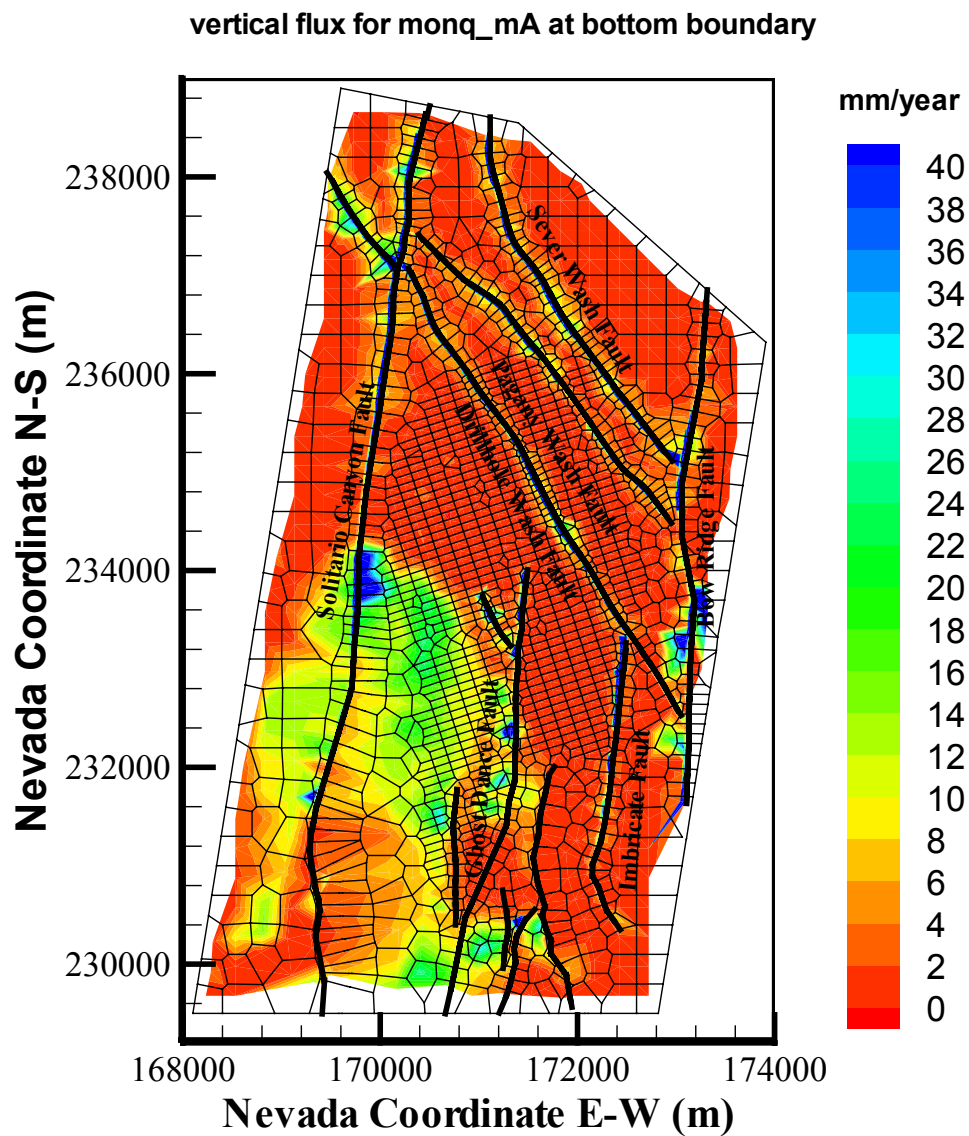
Model Results-DTN: LB03023DSSCP9I.001.

Figure 6.6-10. Simulated Percolation Fluxes at the Water Table under the Monsoon, Lower-Bound Infiltration Scenario Using the Results of Simulating the Base-Case Model: monq_IA



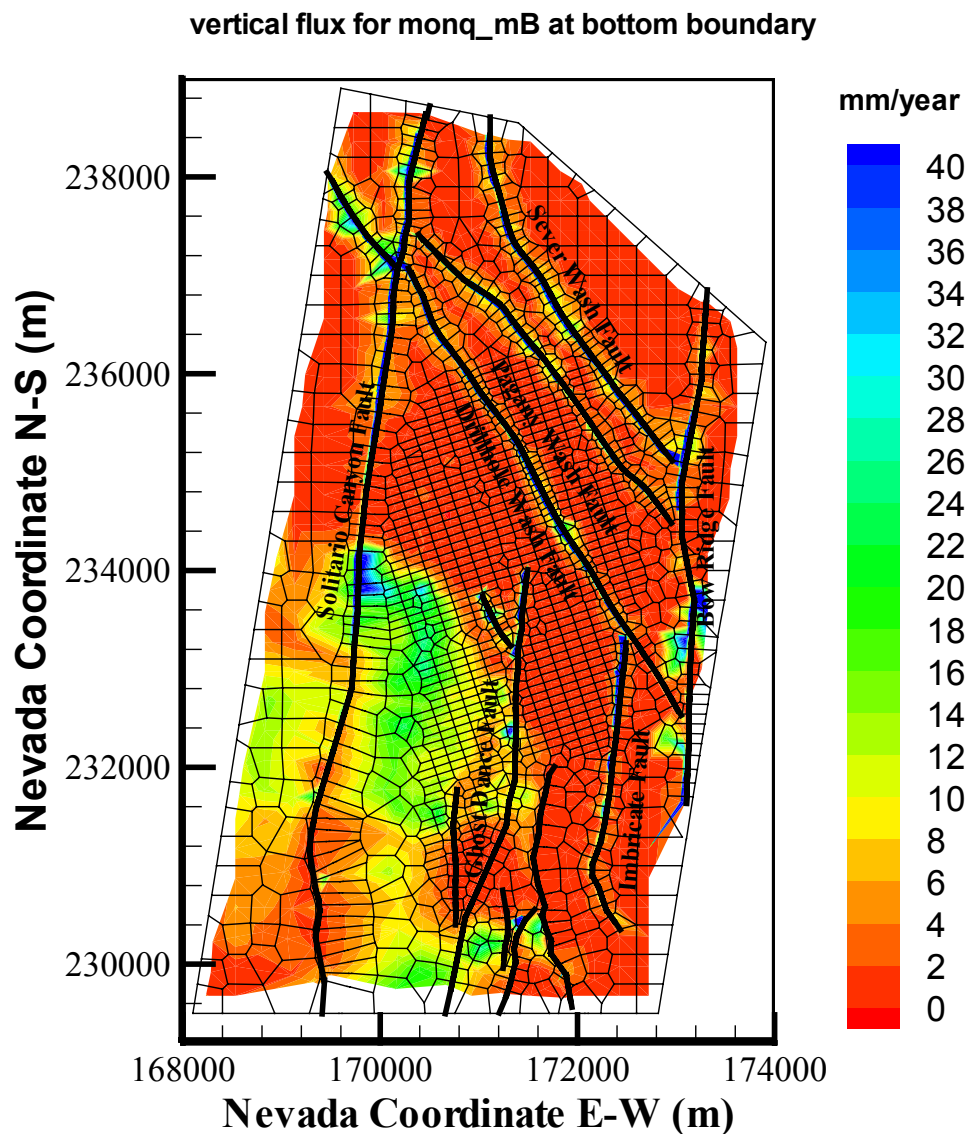
Model Results—DTN: LB03033DSSFF9I.001.

Figure 6.6-11. Simulated Percolation Fluxes at the Water Table under the Monsoon, Lower-Bound Infiltration Scenario Using the Results of Simulating the Alternative Model: monq_IB



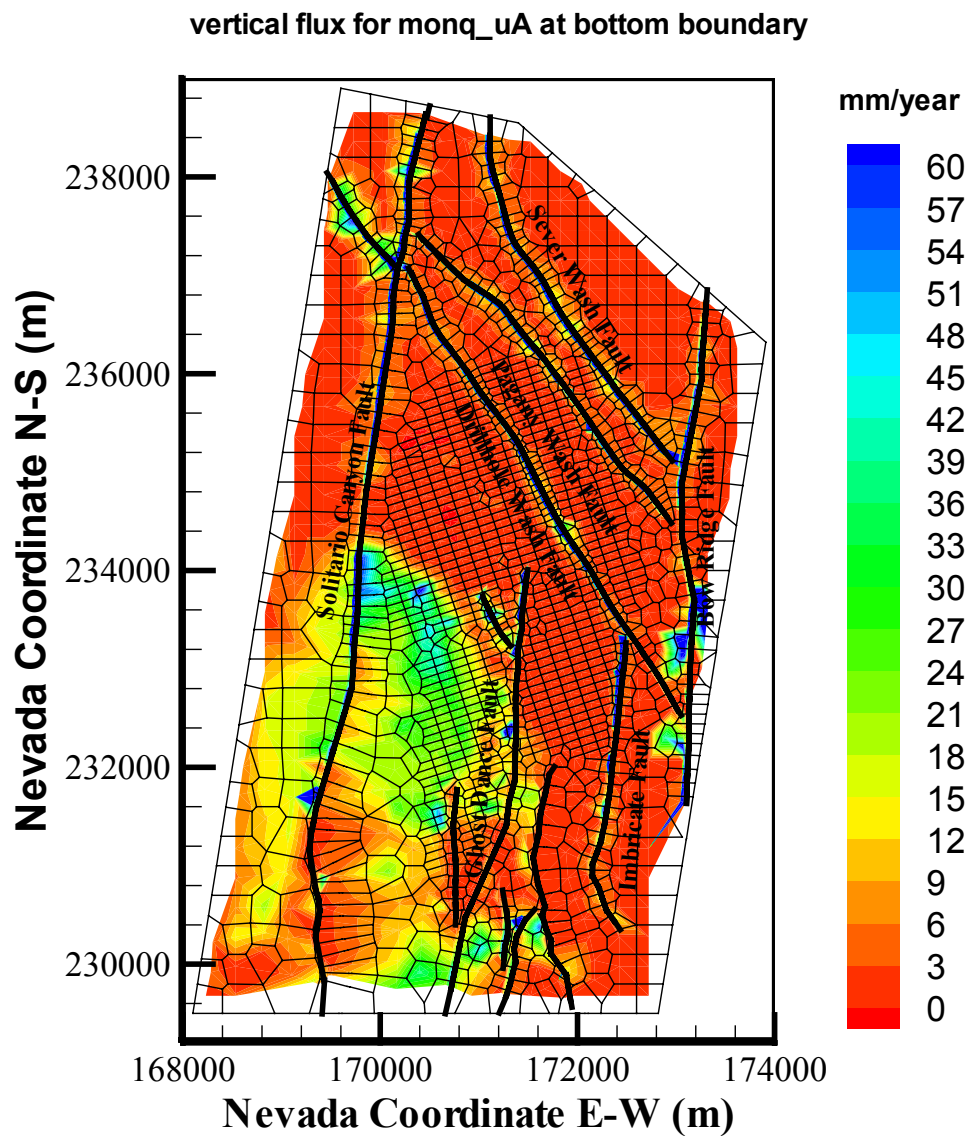
Model Results—DTN: LB03023DSSCP9I.001.

Figure 6.6-12. Simulated Percolation Fluxes at the Water Table under the Monsoon, Mean Infiltration Scenario Using the Results of Simulating the Base-Case Model: monq_mA



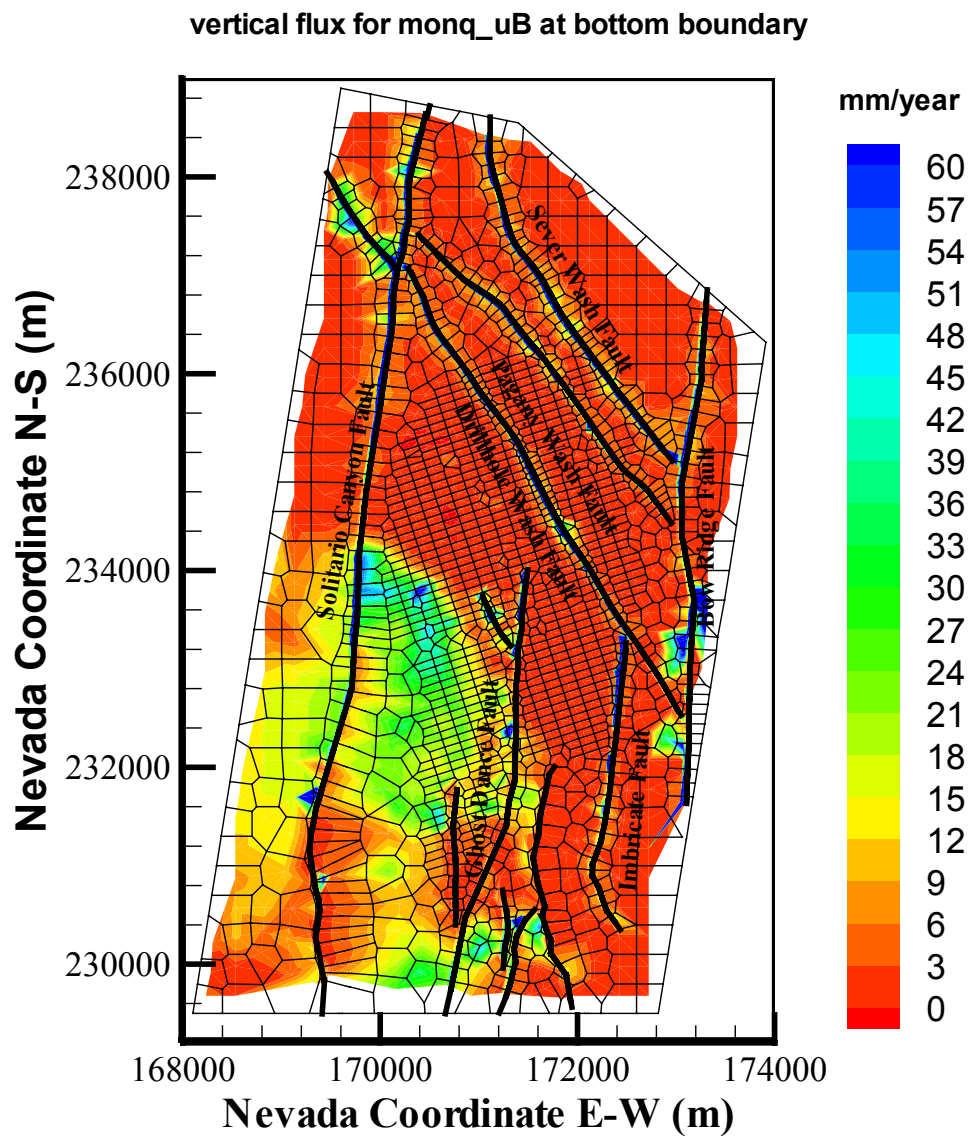
Model Results—DTN: LB03033DSSFF9I.001.

Figure 6.6-13. Simulated Percolation Fluxes at the Water Table under the Monsoon, Mean Infiltration Scenario Using the Results of Simulating the Alternative Model: monq_mB



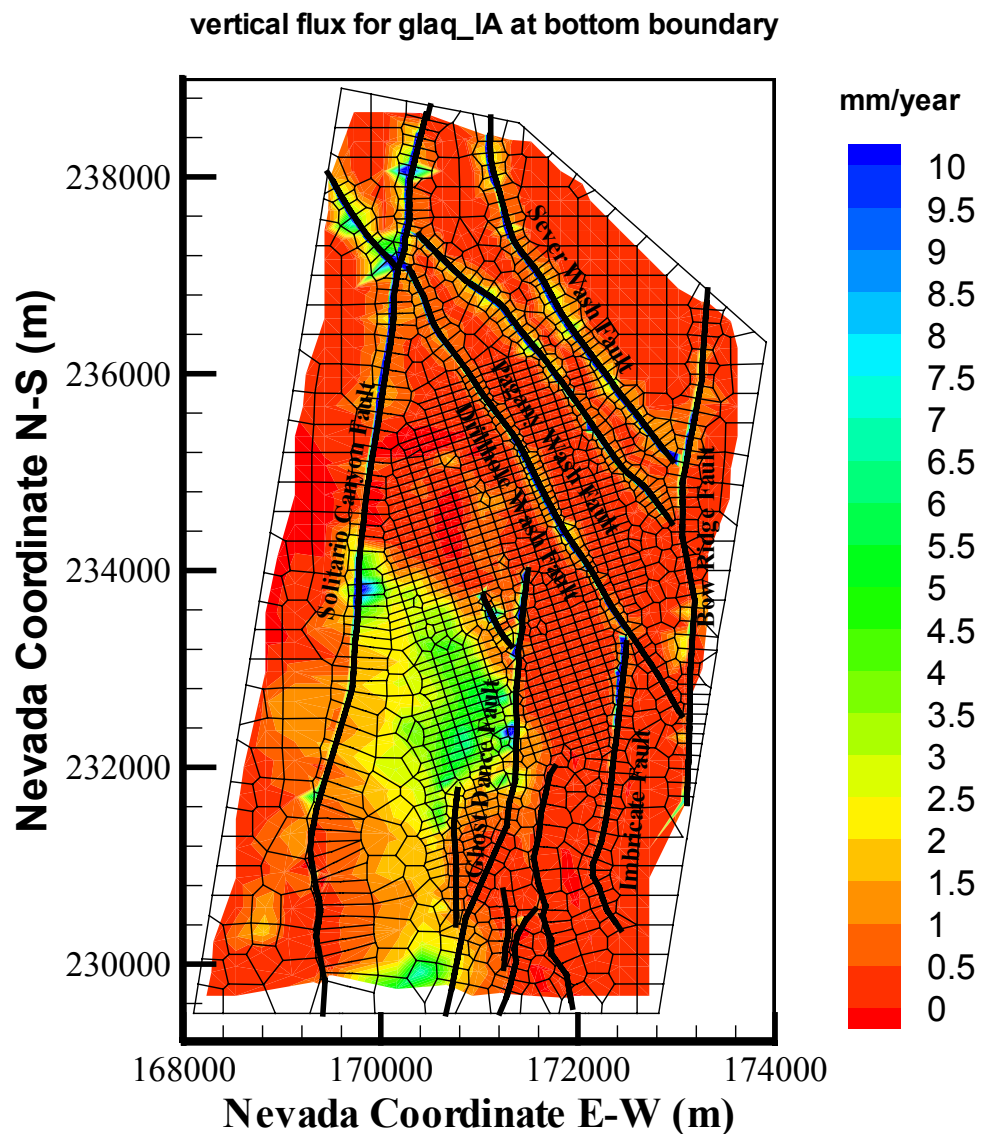
Model Results—DTN: LB03023DSSCP9I.001.

Figure 6.6-14. Simulated Percolation Fluxes at the Water Table under the Monsoon, Upper-Bound Infiltration Scenario Using the Results of Simulating the Base-Case Model: monq_uA



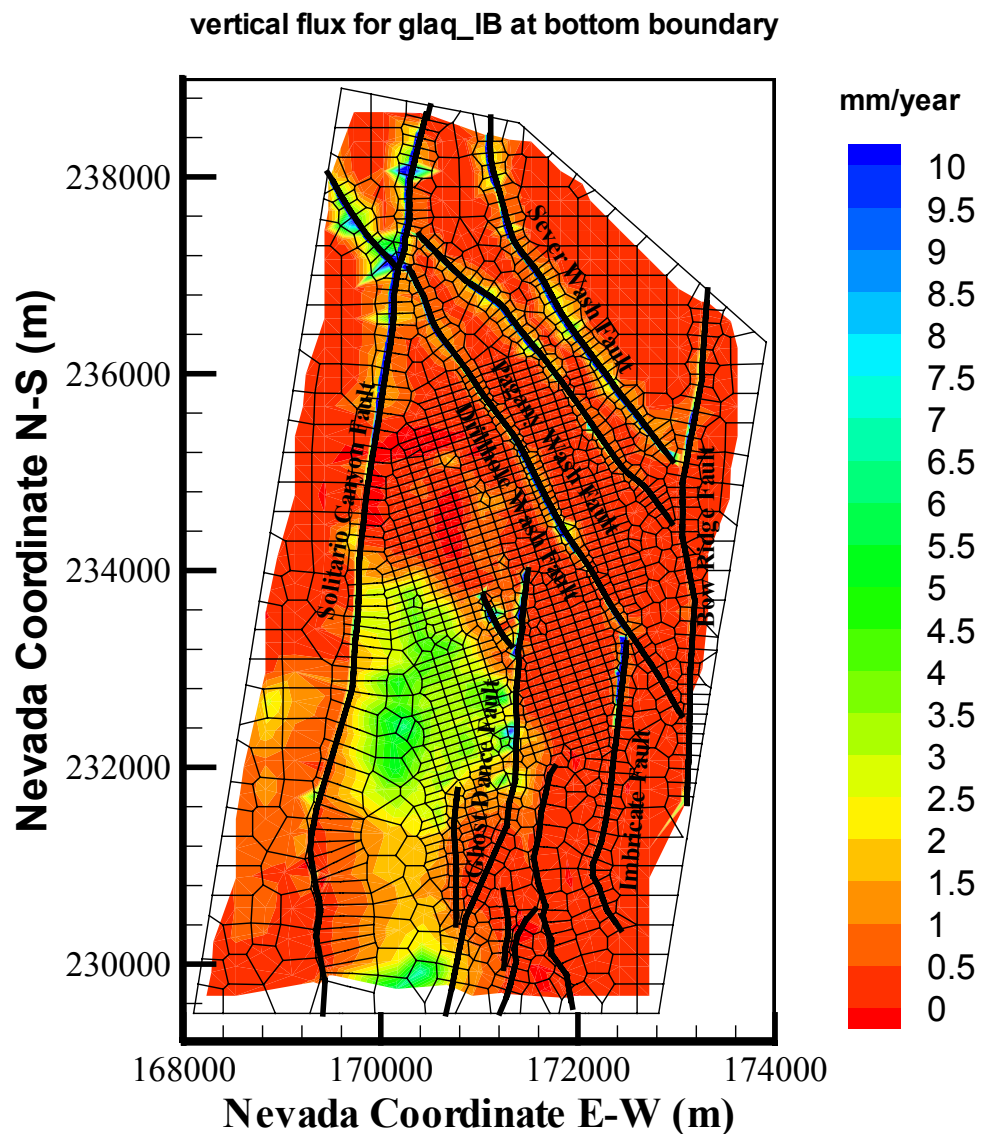
Model Results—DTN: LB03033DSSFF9I.001.

Figure 6.6-15. Simulated Percolation Fluxes at the Water Table under the Monsoon, Upper-Bound Infiltration Scenario Using the Results of Simulating the Alternative Model: monq_uB



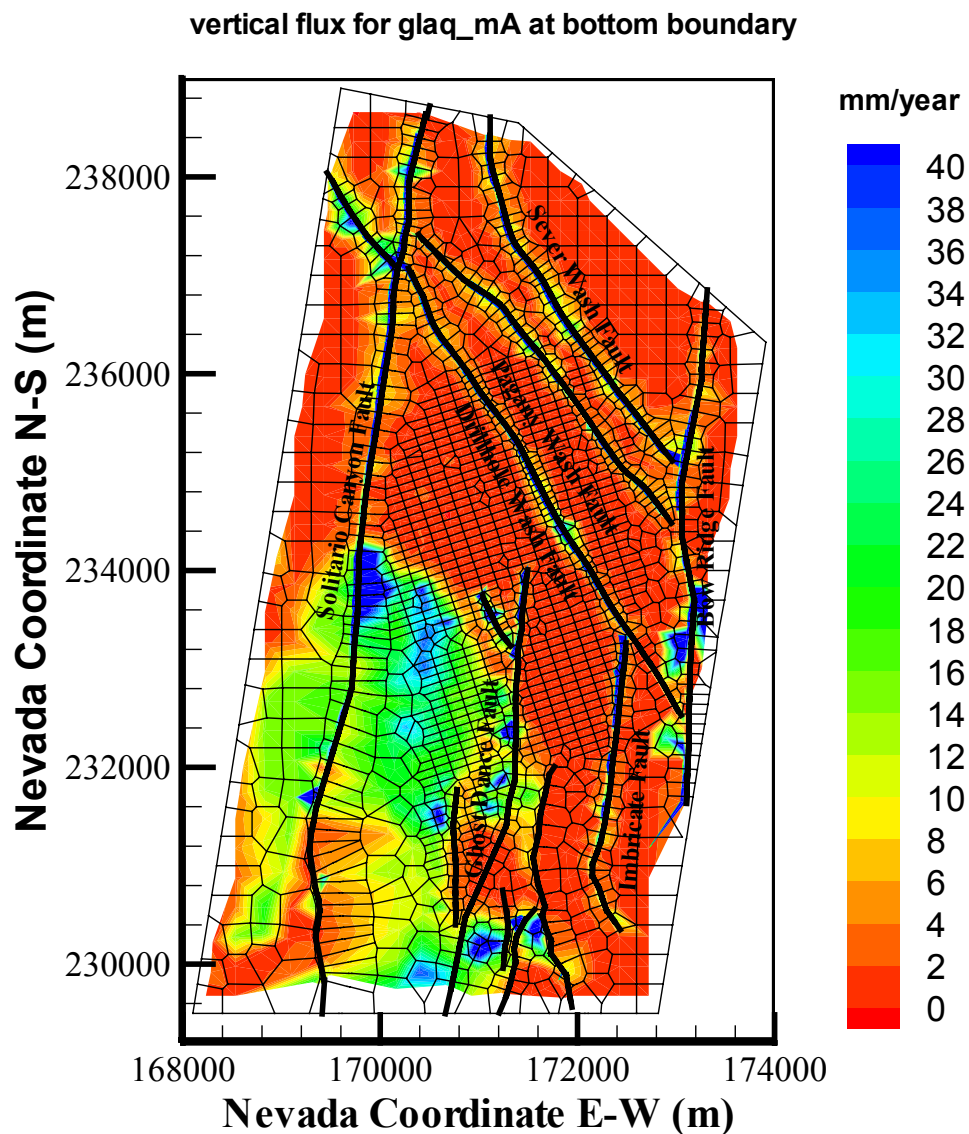
Model Results—DTN: LB03023DSSCP9I.001.

Figure 6.6-16. Simulated Percolation Fluxes at the Water Table under the Glacial Transition, Lower-Bound Infiltration Scenario Using the Results of Simulating the Base-Case Model: glaq_IA



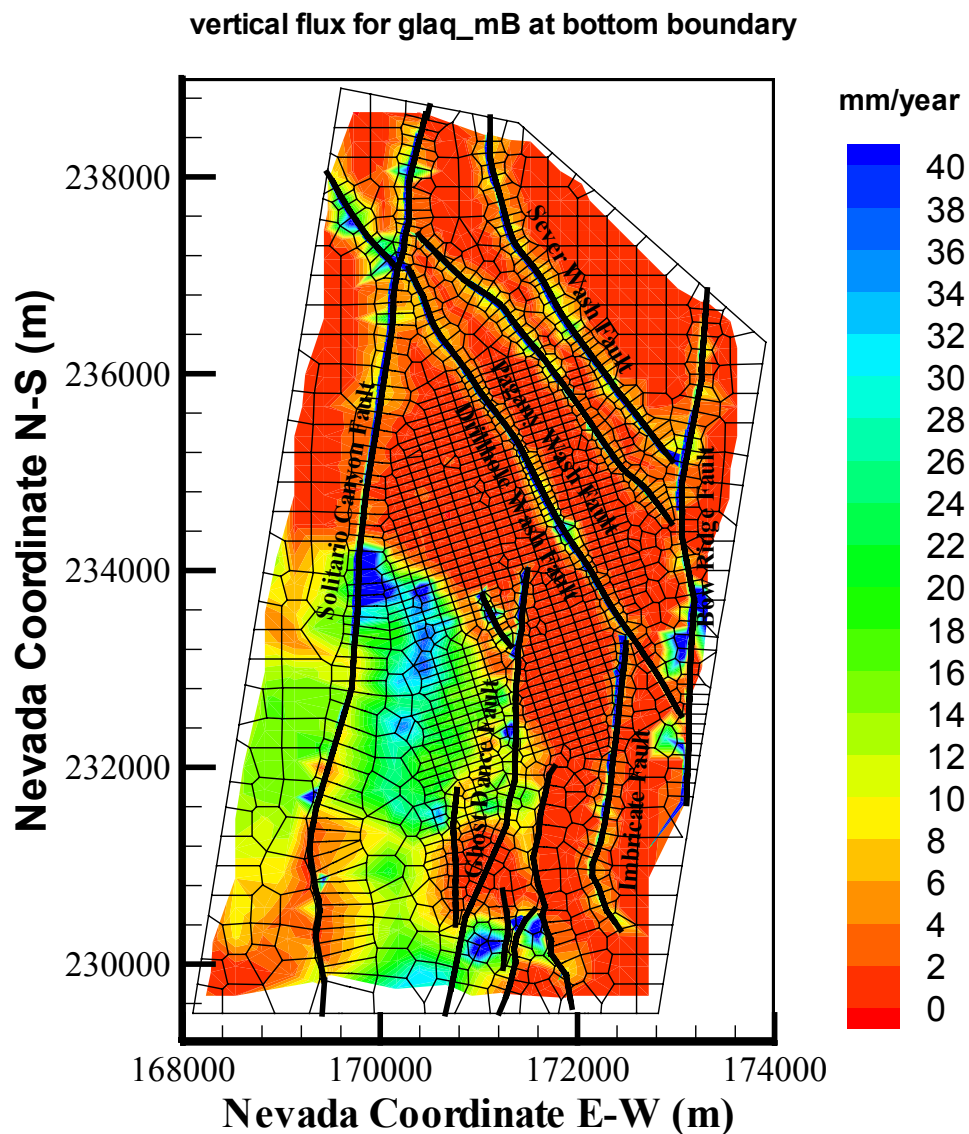
Model Results—DTN: LB03033DSSFF9I.001.

Figure 6.6-17. Simulated Percolation Fluxes at the Water Table under the Glacial Transition, Lower-Bound Infiltration Scenario Using the Results of Simulating the Alternative Model: glaq_IB



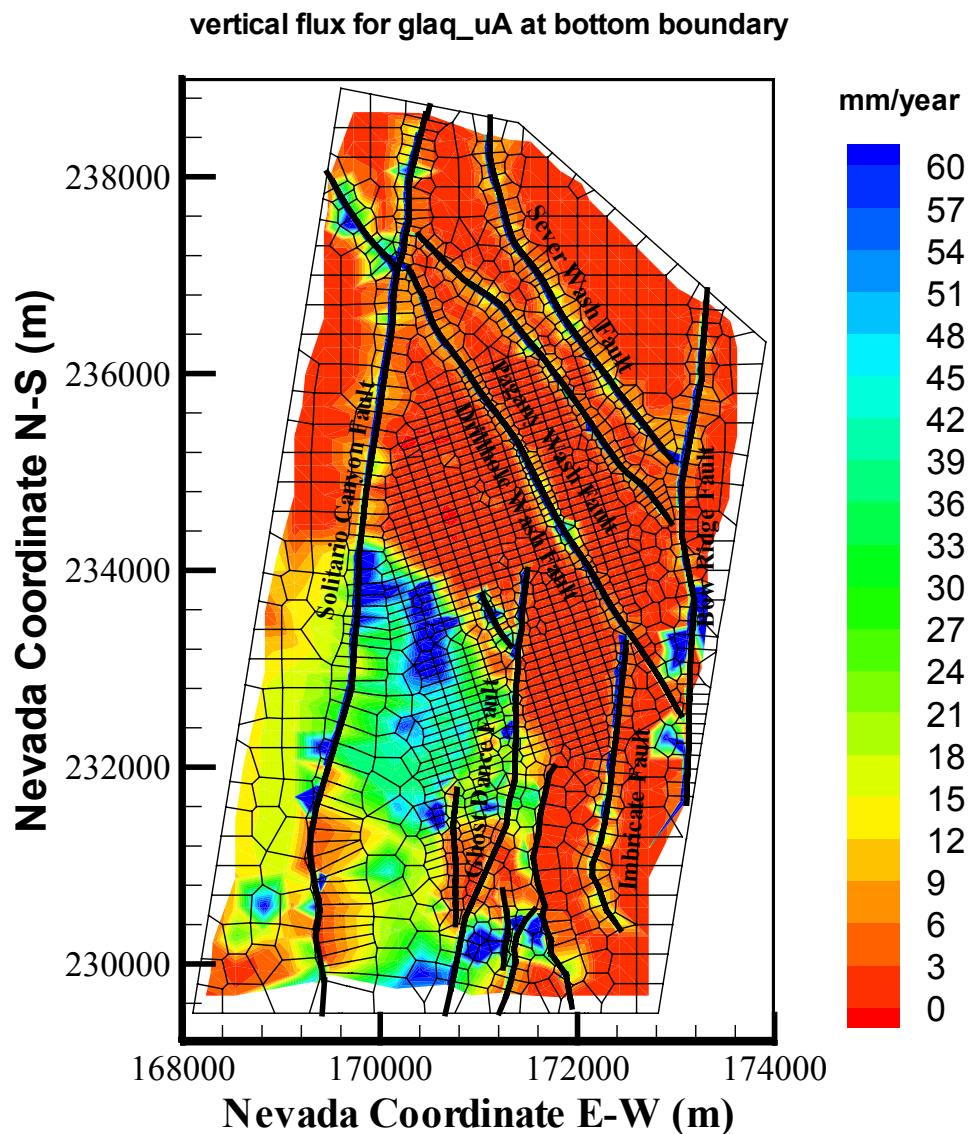
Model Results—DTN: LB03023DSSCP9I.001.

Figure 6.6-18. Simulated Percolation Fluxes at the Water Table under the Glacial Transition, Mean Infiltration Scenario Using the Results of Simulating the Base-Case Model: glaq_mA



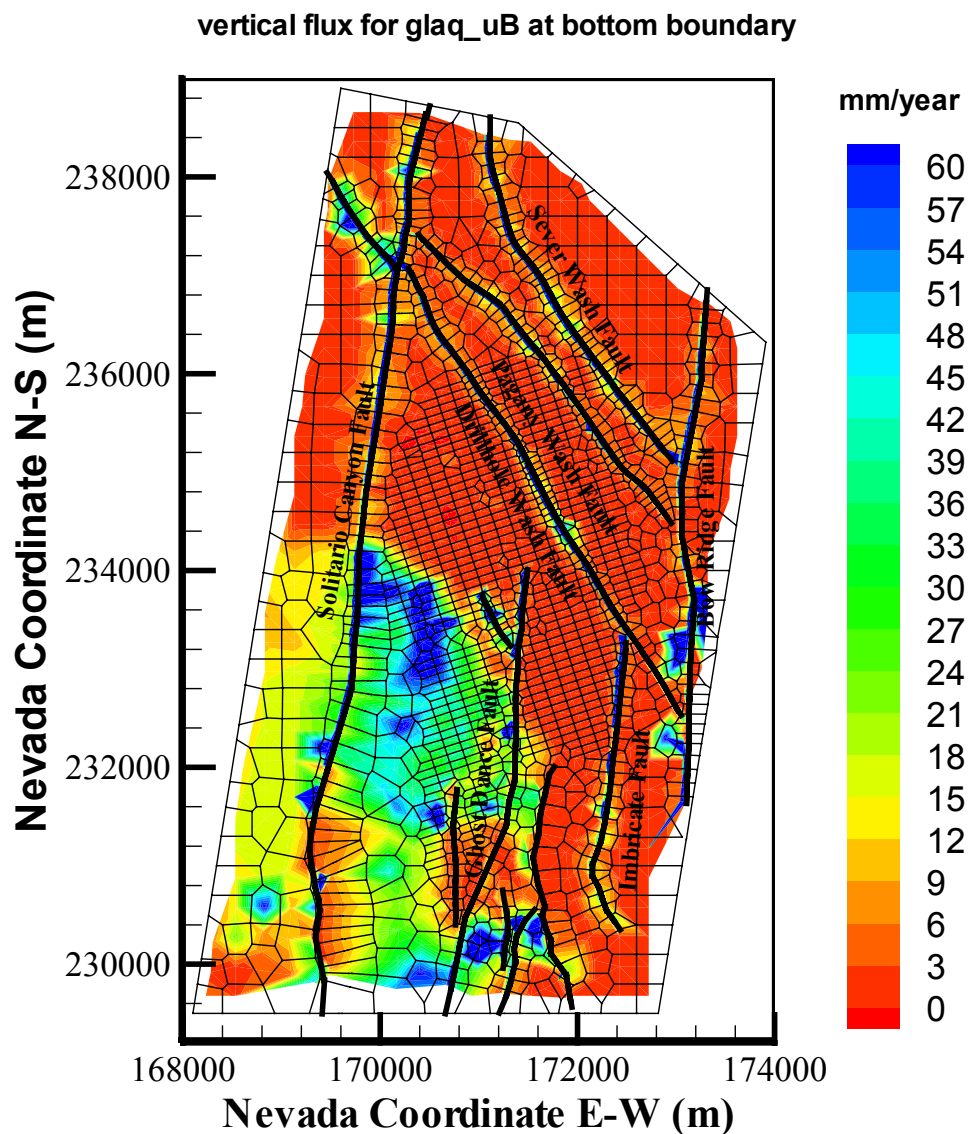
Model Results—DTN: LB03033DSSFF9I.001.

Figure 6.6-19. Simulated Percolation Fluxes at the Water Table under the Glacial Transition, Mean Infiltration Scenario Using the Results of Simulating the Alternative Model: glaq_mB



Model Results—DTN: LB03023DSSCP9I.001.

Figure 6.6-20. Simulated Percolation Fluxes at the Water Table under the Glacial Transition, Upper-Bound Infiltration Scenario Using the Results of Simulating the Base-Case Model: glaq_uA



Model Results—DTN: LB03033DSSFF9I.001.

Figure 6.6-21. Simulated Percolation Fluxes at the Water Table under the Glacial Transition, Upper-Bound Infiltration Scenario Using the Results of Simulating the Alternative Model: glaq_uB

Tables 6.6-3 and 6.6-4 list percentages of fracture-matrix flow components and fault flow at the repository horizon and the water table within the model domain. Fracture and matrix percentages sum to 100%, while fault flow percentages represent total vertical flux through fault blocks (procedures for calculating the percentages are explained in Attachment III, Section III.2). These statistics are calculated from vertical flow along each grid column, using the nine base-case and nine alternative flow fields. A comparison between the statistical data of the two tables indicates that the two models generate similar results in terms of fracture-matrix flow components and fault flow percentage at the repository layer. This is because the two models differ only in the PTn properties (a unit above) and also because the statistics are taken from averaging an entire layer without considering spatial distributions of flow percentage. These statistics indicate that fracture flow is dominant both at the repository horizon and at the water table. At the repository level, fracture flow consists of more than 90–95% of the total percolation fluxes. Fracture flow at the water table takes 70–80% of the total flow. On the other hand, fault flow percentage increases from about 30–40% at the repository to about 60% at the water table, except for the case of the present-day, lower-bound infiltration. Note that according to the active fracture concept (Liu et al., 1998 [105729]), not all fractures are transmitting percolation fluxes. Actual active fracture spacings (i.e., fracture flow intervals) in the flow fields are much larger than measured fracture spacings in different units.

Table 6.6-3. Comparison of the Water Flux through Matrix, Fractures, and Faults as a Percentage of the Total Flux at Two Different Horizons (1) at the Repository and (2) at the Water Table for the Nine Base-Case Flow Fields

Simulation Designation	Flux at Proposed Repository Horizon (%)			Flux at Water Table (%)		
	Fracture	Matrix	Fault	Fracture	Matrix	Fault
preq_1A	91.35	8.65	58.78	78.05	21.95	71.78
preq_mA	94.29	5.71	28.62	70.29	29.71	53.73
preq_uA	94.02	5.98	27.41	77.72	22.28	60.68
monq_1A	93.46	6.54	31.89	71.37	28.63	66.54
monq_mA	94.57	5.43	26.83	72.33	27.67	61.06
monq_uA	94.34	5.66	26.04	78.86	21.14	64.25
glaq_1A	92.11	7.89	36.71	70.37	29.63	65.40
glaq_mA	94.58	5.42	24.27	70.34	29.66	61.57
glaq_uA	94.53	5.47	23.81	76.44	23.56	65.37

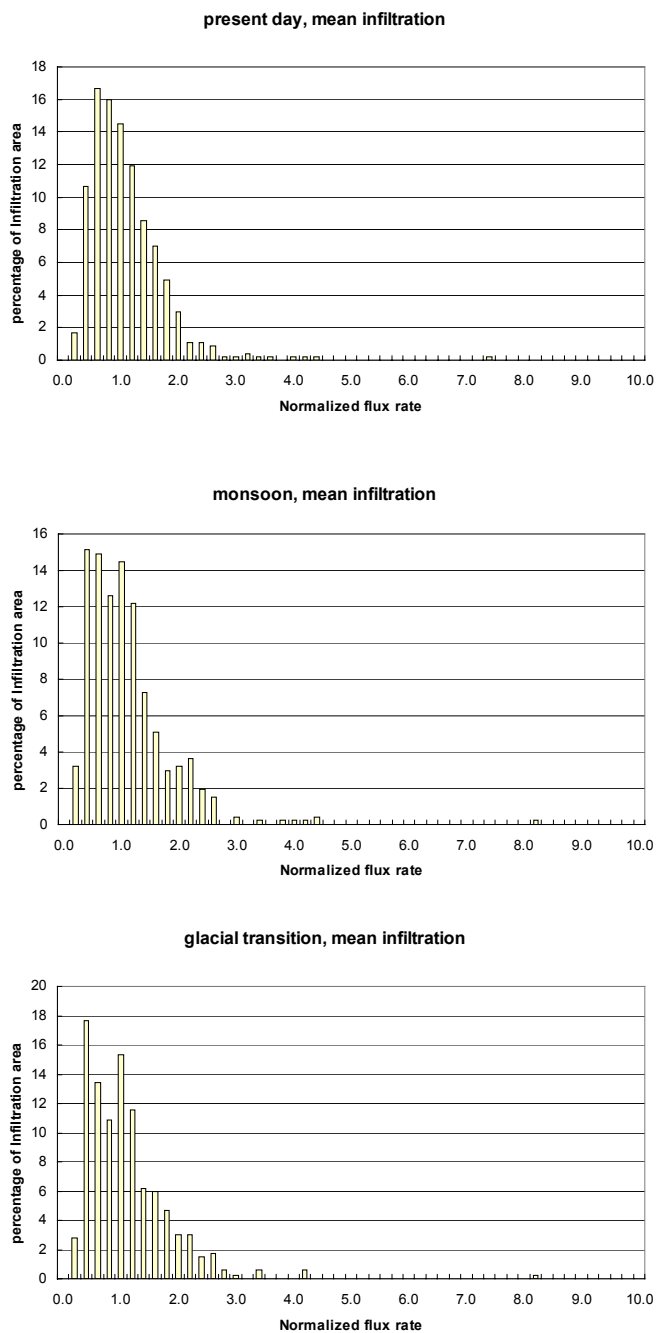
Model Results – Output DTNs: LB03023DSSCP9I.001.

Table 6.6-4. Comparison of the Water Flux through Matrix, Fractures, and Faults as a Percentage of the Total Flux at Two Different Horizons, at the Repository and at the Water Table, for the Nine Alternative Flow Fields

Simulation Designation	Flux at Proposed Repository Horizon (%)			Flux at Water Table (%)		
	Fracture	Matrix	Fault	Fracture	Matrix	Fault
Preq_IB	90.78	9.21	65.66	79.70	20.30	73.39
Preq_mB	93.92	6.08	32.86	70.58	29.42	53.79
Preq_uB	93.79	6.21	30.49	78.32	21.68	60.84
Monq_IB	93.34	6.66	37.55	70.03	29.97	66.66
Monq_mB	93.97	6.03	28.80	72.81	27.19	61.13
Monq_uB	94.25	5.75	28.39	79.37	20.63	64.25
Glaq_IB	91.60	8.40	43.69	71.64	28.36	66.36
Glaq_mB	94.07	5.93	26.97	70.72	29.28	61.55
Glaq_uB	94.44	5.56	25.74	76.60	23.40	65.36

Model Results – Output DTNs: LB03033DSSFF9I.001.

Distributions of Percolation Fluxes within the Repository: Percolation fluxes within the repository footprint can be further analyzed using a frequency distribution plot. This plot displays the average percentage of the repository area subject to a particular percolation rate. Note that the normalized flux rates are determined by normalizing an infiltration value with respect to the averaged infiltration rate for the scenario. For example, 1 for the normalized flux rate corresponds to 4.43, 11.83, and 17.02 mm/yr (Table 6.1-2), respectively, for the three mean infiltration scenarios. The information, as shown in Figure 6.6-22 (See Attachment III.2.5 for details of the calculation), is important to drift-scale modeling studies of flow and transport at drifts and flow-redistributing phenomena through the TSw. Figure 6.6-22 shows the frequency distribution of normalized percolation flux within the repository horizon for the three mean infiltration rates of the three climates.

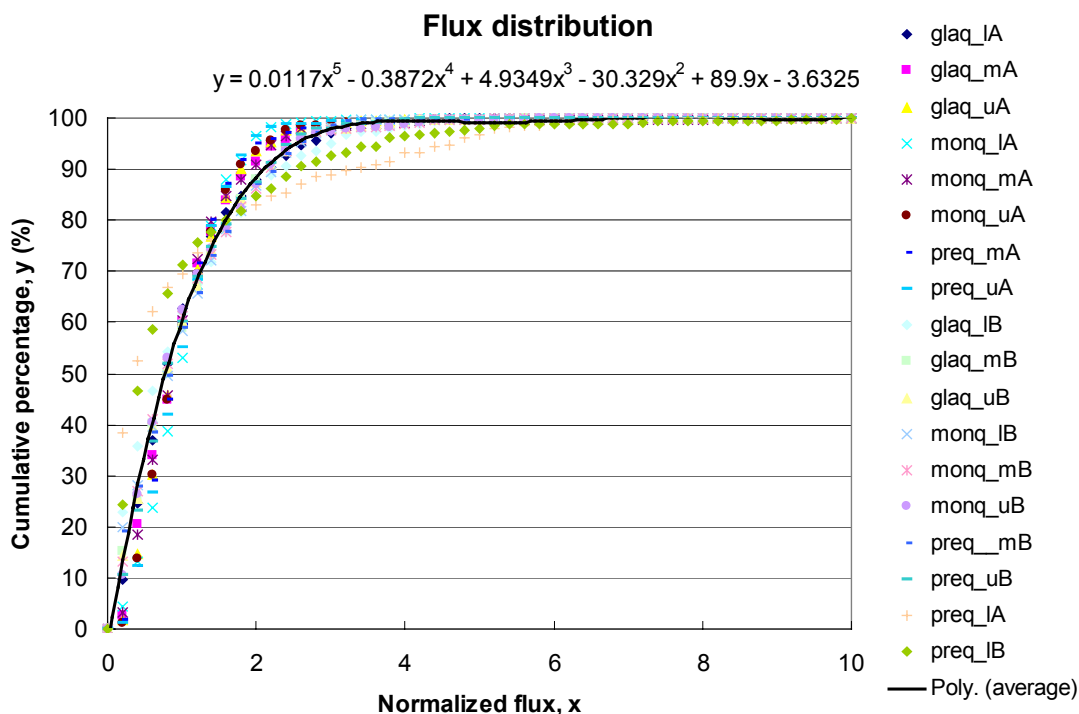


Model Results – DTN: LB03023DSSCP9I.001

Figure 6.6-22. Areal Frequency and Distribution of Simulated Percolation Fluxes within the Repository Domain Normalized to the Three Mean Infiltration Rates: (a) Present Day, (b) Monsoon, and (c) Glacial Transition

Figure 6.6-22 indicates that the highest flux frequencies have a normalized flux of about 0.5 or less and occur over about 50% of the repository area. The area with normalized percolation fluxes greater than 5 comprises less than 1% of the total repository area. In general, the modeling results for all of the 18 flow fields show that the percolation flux value with highest areal frequencies is always lower than the average values of the corresponding infiltration rates.

The results of the 18 flow fields analyses, as shown in Figure 6.6-22, can be used to define a cumulative flux-frequency distribution, as shown in Figure 6.6-23 (See Attachment III.2.6 for details of the calculation). Figure 6.6-23 also presents a regression curve that incorporates the 18 flow fields. The cumulative frequency of Figure 6.6-23 can be used, for example, in selecting ambient flow boundary conditions for drift-scale modeling. The similarity in flux distribution patterns for the 18 flow fields helps to define a flux-distribution factor for seepage estimation in the TSPA calculations on the scale of the site-scale UZ Model, but is not recommended for use in small-scale models, such as the drift-scale seepage models. The regression curve, with the equation given on the figure, may be used to correlate cumulative flux frequency within the repository with net infiltration rates for any future climatic scenarios. For example, use of the equation with $x = 1, 2,$ and 5 gives results of 60%, 88%, and 99%. This indicates that 60%, 88%, and 99% repository blocks are subject to less than normalized fluxes of 1, 2 and 5, respectively. This provides data for PA calculations.



Model Results – DTNs: LB03023DSSCP9I.001; LB03033DSSFF9I.001

NOTE: Equation is valid for $0.05 < x < 10$.

Figure 6.6-23. Cumulative Flux Distribution and Range as Functions of Normalized Percolation Flux within the Repository from the 18 Flow Fields

6.7 TRACER TRANSPORT TIMES

This section summarizes simulated tracer transport using the nine base-case flow fields and the nine alternative flow fields. The results present an evaluation of tracer transport processes from the repository to the water table (saturated zone) and within the mountain, including the effects of different infiltration scenarios and adsorption. Studies described in this section provide insight into UZ flow patterns and transport processes.

6.7.1 Methodology and Transport Parameters

Simulation results and analyses of this section are based on transport studies of conservative and reactive tracers using the T2R3D V1.4 code (LBNL 1999 [146654]). The dual-permeability modeling approach with the 3-D TSPA-LA grid (Figure 6.1-1), as discussed in Section 6.1.1, is used in the transport simulations. The 18 steady-state, 3-D flow fields of Section 6.6 are directly input to the T2R3D code for modeling transport from the repository to the water table.

To assess tracer transport times from the repository to the water table, tracers are treated as conservative (nonadsorbing) and reactive (adsorbing) components transported through the UZ. In both cases, hydrodynamic/mechanical dispersion through the fracture-matrix system is ignored, because sensitivity studies indicated that mechanical dispersion has an insignificant effect on the cumulative breakthrough curves of tracers at the water table (BSC 2001 [158726]). A constant molecular diffusion coefficient of $3.2 \times 10^{-11} \text{ m}^2/\text{s}$ is used for matrix diffusion of the conservative component and $1.6 \times 10^{-10} \text{ m}^2/\text{s}$ is used for the reactive component (DTN: LA0003JC831362.001 [149557]). The two diffusion coefficients are multiplied by porosity and tortuosity in the simulation to account for various units. In the case of a reactive or adsorbing tracer, several K_d values are used, as given in Table 6.7-1, for different units. These values were selected to approximate those for neptunium (^{237}Np) transport (DTNs: LA0010JC831341.001 [162476]; LA0010JC831341.002 [153321]; LA0010JC831341.003 [153322]; LA0010JC831341.004 [153323]; LA0010JC831341.005 [153320]; LA0010JC831341.006 [153318]; LA0010JC831341.007 [153319]). For a conservative tracer, K_d is set to zero. These molecular diffusion coefficients and K_d values are selected to represent technetium and neptunium, respectively. Model parameters such as porosity and rock grain density were taken from the thermal properties (DTN: LB0210THRMLPRP.001 [160799]).

Transport simulations were conducted for 1,000,000 years using nine constant infiltration rates of three climates. An initial, constant-source concentration was specified for the fracture continuum gridblocks representing the repository, released at the starting time of simulation. In addition, tracer transport was also investigated with tracers initially released from the matrix continuum of the repository block under the present-day mean infiltration scenario.

Table 6.7-1. K_d Values Used for Reactive Tracer Transport in Different Hydrogeologic Units

Hydrogeologic Unit	K_d (cc/g)
Zeolitic matrix in CHn	4.0
Vitric matrix in CHn	1.0
Matrix in TSw	1.0
Fault matrix in CHn	1.0
Fractures and the matrix in the rest of units	0.0

NOTE: K_d values selected from ranges in the following DTNs:

LA0010JC831341.001 [162476], LA0010JC831341.002 [153321],
 LA0010JC831341.003 [153322], LA0010JC831341.004 [153323],
 LA0010JC831341.005 [153320], LA0010JC831341.006 [153318],
 and LA0010JC831341.007 [153319]

6.7.2 Simulation Scenarios

For each TSPA-LA flow simulation, as listed in Tables 6.2-9 and 6.6-1, there are two transport runs, one for conservative (*_tc) and one for reactive (*_np) tracer transport. For most cases, tracer first releases from fracture gridblocks within the repository. Tables 6.7-2 and 6.7-3 summarize a total of 18×2 tracer-fracture-release simulation scenarios, corresponding to the 18 TSPA-LA flow fields for the nine infiltration maps of three climates, respectively. There are only four tracer-matrix-release simulations, two each for the base-case and alternative flow fields (*tcM and *npM for Tc and Np, respectively).

Table 6.7-2. Transport Simulation Scenarios: Data Files and Corresponding Nine Base-Case Flow Fields with Nine Infiltration Rates

Designation/ Transport Simulation	Designation/ Flow Simulation (Output-DTN: LB03023DSSCP9I.001)	Infiltration Map (DTN: GS000308311221.005 [147613])
preqlA_tc preqlA_np	preq_IA	Present-day, lower-bound infiltration
preqmA_tc preqmA_tcM* preqmA_np preqmA_npM*	preq_mA	Present-day, mean infiltration
prequA_tc prequA_np	preq_uA	Present-day, upper-bound infiltration
monqlA_tc monqlA_np	monq_IA	Monsoon, lower-bound infiltration
monqmA_tc monqmA_np	monq_mA	Monsoon, mean infiltration
monquA_tc monquA_np	monq_uA	Monsoon, upper-bound infiltration
glaqlA_tc glaqlA_np	glaq_IA	Glacial transition, lower-bound infiltration
glaqmA_tc glaqmA_np	glaq_mA	Glacial transition, mean infiltration
glaquA_tc glaquA_np	glaq_uA	Glacial transition, upper-bound infiltration

Output-DTN: LB03033DUZTRAN.001

NOTE: * Tracer release from repository matrix blocks

Table 6.7-3. Transport Simulation Scenarios: Data Files and Corresponding Nine Alternative Fields with Nine Infiltration Rates

Designation/ Transport Simulation	Designation/ Flow Simulation Output-DTN: LB03033DSSFF9I.001	Infiltration Map DTN: GS000308311221.005 [147613]
preqlB_tc preqlB_np	preq_IB	Present-day, lower-bound infiltration
preqmB_tc preqmB_tcM* preqmB_np preqmB_npM*	preq_mB	Present-day, mean infiltration
prequB_tc prequB_np	preq_uB	Present-day, upper-bound infiltration
monqlB_tc monqlB_np	monq_IB	Monsoon, lower-bound infiltration
monqmB_tc monqmB_np	monq_mB	Monsoon, mean infiltration
monquB_tc monquB_np	monq_uB	Monsoon, upper-bound infiltration
glaqlB_tc glaqlB_np	glaq_IB	Glacial transition, lower-bound infiltration
glaqmB_tc glaqmB_np	glaq_mB	Glacial transition, mean infiltration
glaquB_tc glaquB_np	glaq_uB	Glacial transition, upper-bound infiltration

Output-DTN: LB03033DUZTRAN.001

NOTE: * Tracer release from repository matrix blocks

6.7.3 Simulation Results and Analyses

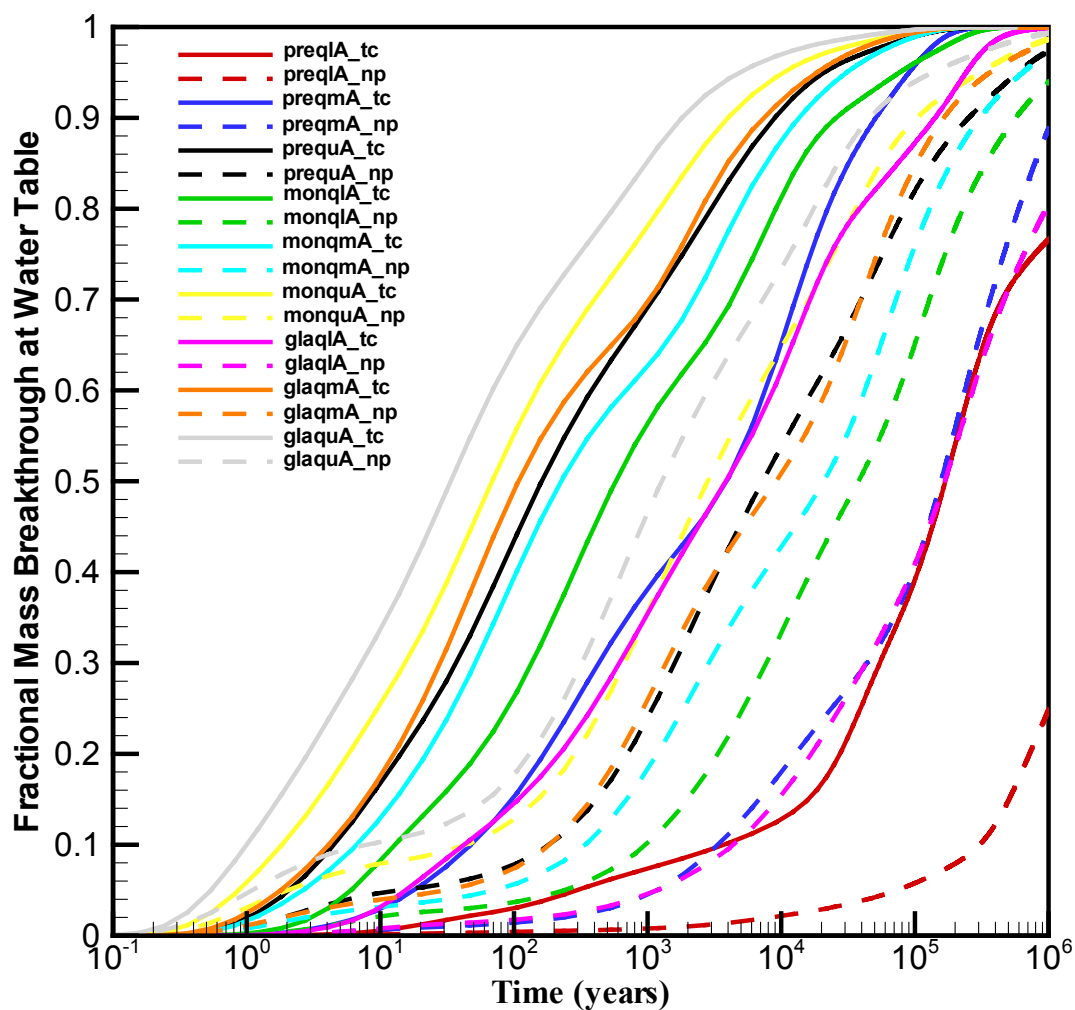
Tracer transport times (since release from the repository to the water table) may be analyzed using a cumulative fractional breakthrough curve, as shown in Figures 6.7-1, 6.7-2, and 6.7-3 for 1 million years. The fractional mass breakthrough in these figures is defined as the cumulative mass of a tracer arriving at the water table over the entire bottom model boundary over time, normalized by the total mass of the component initially introduced at the repository. In the figures, solid-line and dotted-line curves of the same color represent simulation results of conservative/nonadsorbing tracer transport and adsorbing tracer transport respectively. The three figures show a wide range of tracer transport times with different infiltration rates and types of tracers considered in the 40 simulations, listed in Tables 6.7-2 and 6.7-3.

As indicated by Figures 6.7-1 and 6.7-2, the predominant factors in controlling tracer transport are (1) surface-infiltration rates or net water recharge, (2) adsorption effects, i.e., whether the tracer is conservative or reactive, and (3) whether it is initially released from fracture or matrix

blocks in the repository. The figures also show that the base-case flow fields (Figure 6.7-1) and the alternative flow fields (Figure 6.7-2) result in very similar tracer transport times. However, the base-case flow scenarios generate slightly shorter travel times or more conservative results in general.

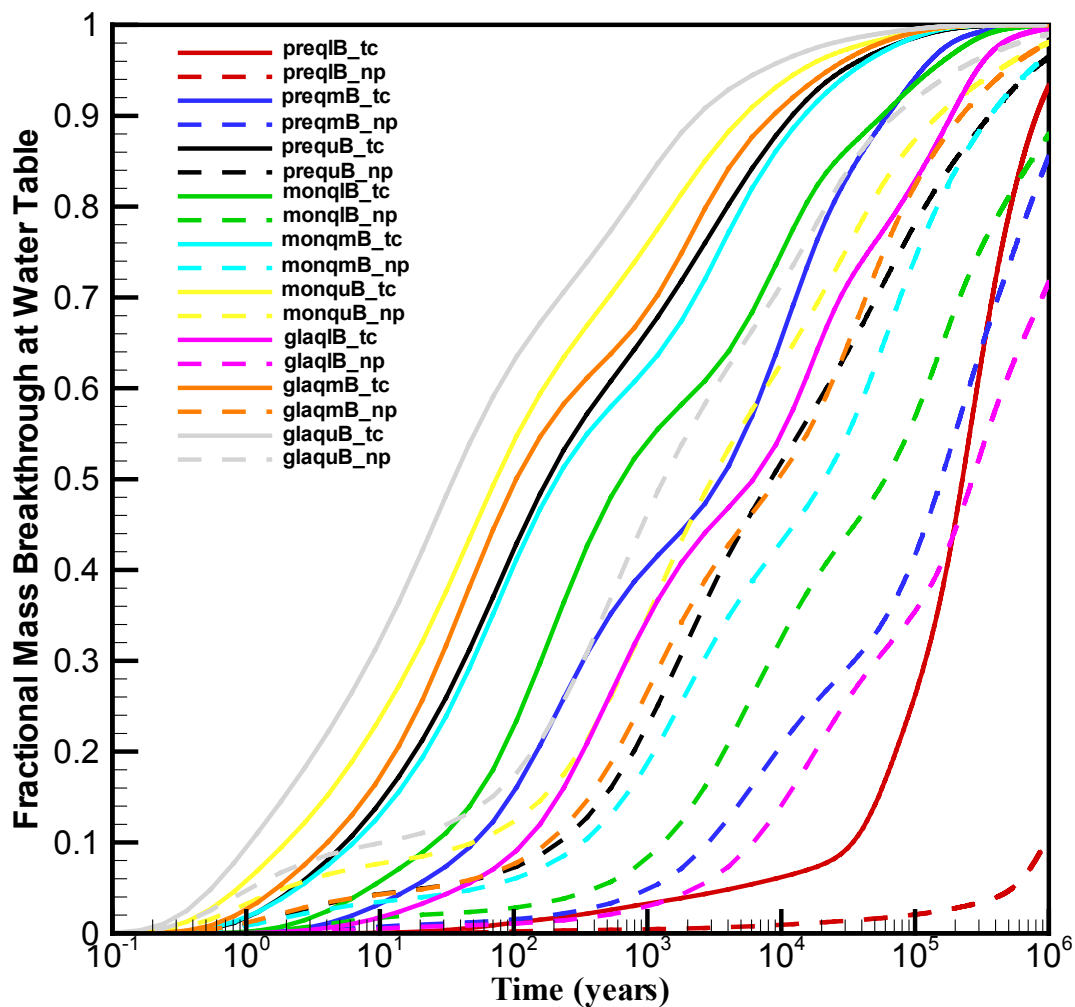
Statistics of tracer transport times of 10% and 50% mass breakthrough at the water table for the 36 simulation scenarios of tracer-fracture release plus four tracer-matrix-release scenarios, are given in Tables 6.7-4 and 6.7-5, respectively. Figure 6.7-4 correlates average infiltration rates and tracer transport times at 50% mass breakthrough for the 36 simulation scenarios of tracer-fracture release. Figures 6.7-1, 6.7-2, 6.7-3 and 6.7-4, and the statistical data of Tables 6.7-4 and 6.7-5, show the following:

- Tracer transport times vary inversely to the average surface infiltration (net water recharge) rate over the model domain (Figure 6.7-4). When the average infiltration rate increases from 5 to 35 (mm/yr), average tracer transport (50% breakthrough) times decrease by more than one order of magnitude for both adsorbing and nonadsorbing species.
- Nonadsorbing tracers migrate (from the repository to the water table) one to two orders of magnitude faster than an adsorbing tracer under the same infiltration condition (Figure 6.7-4).
- Tracer transport times are significantly longer when tracers are initially released from repository matrix blocks instead of fractures. For conservative (i.e., nonadsorbing) transport, travel times are increased by one to two orders of magnitude (Figure 6.7-3, Tables 6.7-4 and 6.7-5). For reactive (i.e., adsorbing) tracers, the travel times are increased by more than one order of magnitude at 10% mass breakthrough and by approximately two times at 50% breakthrough.
- A comparison of travel/transport times obtained from the nine base-case flow fields with those from the nine alternative flow fields indicates that the base-case flow fields show slightly shorter travel times (or slightly more conservative results in general) under the same infiltration scenarios.



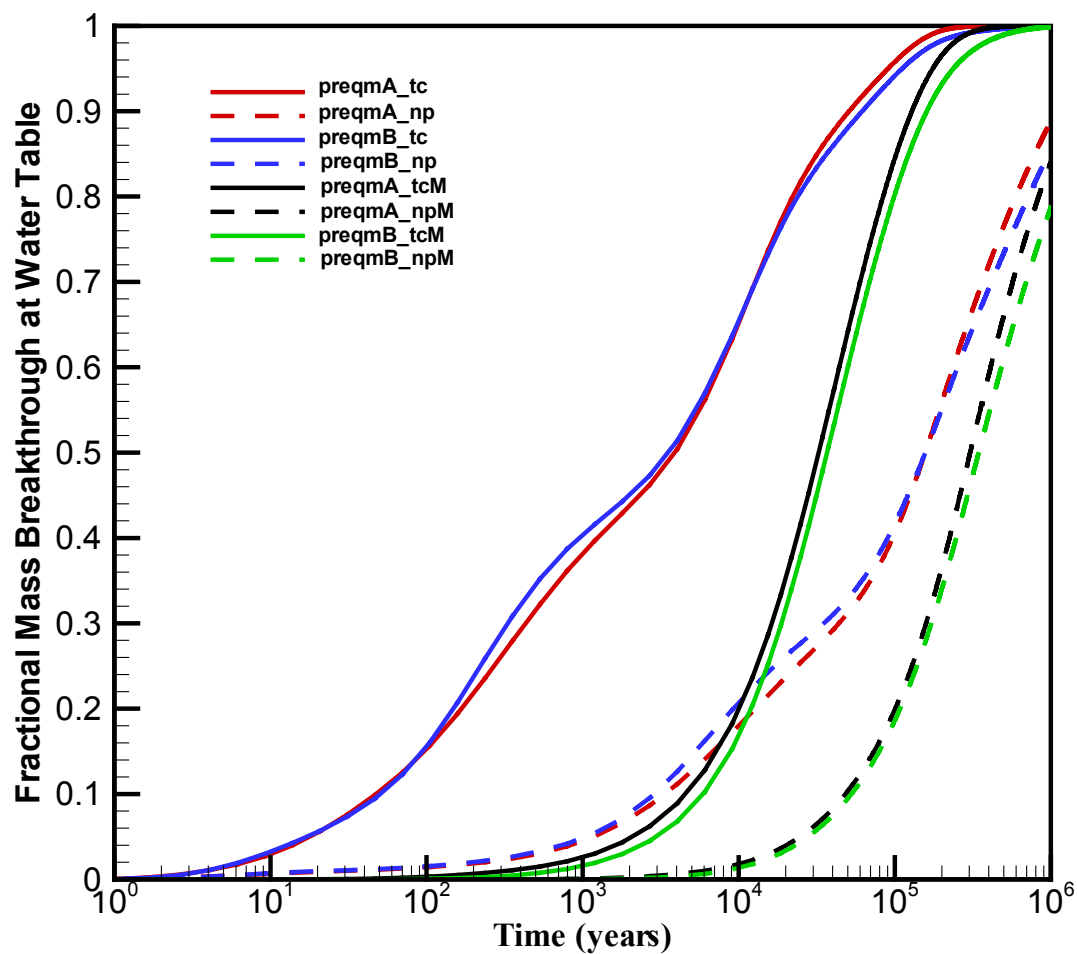
Model Results - DTN: LB03033DUZTRAN.001.

Figure 6.7-1. Simulated Breakthrough Curves of Cumulative Tracer Mass Arriving at the Water Table, after Release from Fractures in the Repository, Using the Base-Case Flow Fields with the Nine Infiltration Scenarios for Nonadsorbing and Adsorbing Tracers



Model Results - DTN: LB03033DUZTRAN.001.

Figure 6.7-2. Simulated Breakthrough Curves of Cumulative Tracer Mass Arriving at the Water Table, after Release from Fractures in the Repository, Using the Alternative Flow Fields with the Nine Infiltration Scenarios for Nonadsorbing and Adsorbing Tracers



Model Results - DTN: LB03033DUZTRAN.001.

Figure 6.7-3. Comparison of Simulated Breakthrough Curves of Cumulative Tracer Mass Arriving at the Water Table, after Release from Fractures and Matrix Blocks in the Repository, Using the Base-Case and Alternative Flow Fields under the Present-Day Mean Infiltration Flow Fields with the Nine Infiltration Scenarios for Nonadsorbing and Adsorbing Tracers

Table 6.7-4. Tracer Transport Times at 10% and 50% Mass Breakthrough Times for 18 Transport Simulation Scenarios, Corresponding to the Nine Base-Case Flow Fields with Nine Infiltration Rates

Designation/ Transport Simulation	Types of Tracer	10% Breakthrough Times (years)	50% Breakthrough Times (years)
preqlA_tc	Nonadsorbing	3,800	169,000
preqlA_np	Adsorbing	305,000	> 1,000,000
preqmA_tc	Nonadsorbing	50	3,900
preqmA_tcM*	Nonadsorbing	4,600	33,000
preqmA_np	Adsorbing	3,400	157,000
preqmA_npM*	Adsorbing	48,000	300,000
prequA_tc	Nonadsorbing	5	160
prequA_np	Adsorbing	190	7,400
monqlA_tc	Nonadsorbing	13	590
monqlA_np	Adsorbing	980	38,000
monqmA_tc	Nonadsorbing	7	230
monqmA_np	Adsorbing	340	21,000
monquA_tc	Nonadsorbing	2	69
monquA_np	Adsorbing	44	2,800
glaqlA_tc	Nonadsorbing	43	3,900
glaqlA_np	Adsorbing	4,400	167,000
glaqmA_tc	Nonadsorbing	4	110
glaqmA_np	Adsorbing	187	9,200
glaquA_tc	Nonadsorbing	1	34
glaquA_np	Adsorbing	8	1,300

Model Results - DTN: LB03033DUZTRAN.001

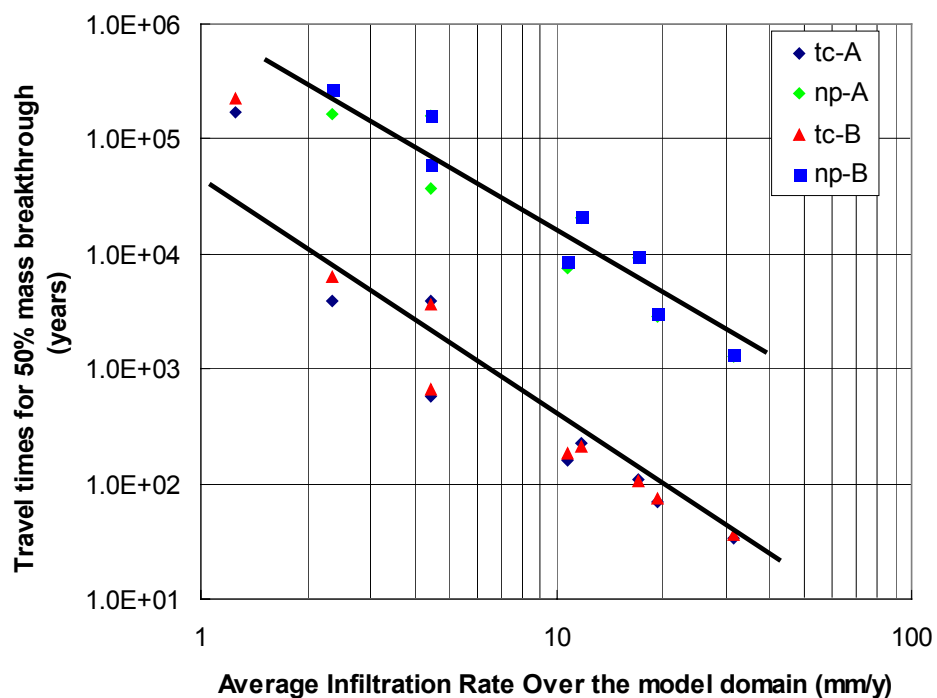
NOTE: * Tracer release from repository matrix blocks

Table 6.7-5. Tracer Transport Times at 10% and 50% Mass Breakthrough Times for 14 Transport Simulation Scenarios, Corresponding to the Nine Alternative Flow Fields with Nine Infiltration Rates

Designation/ Transport Simulation	Types of Tracer	10% Breakthrough Times (years)	50% Breakthrough Times (years)
preqlB_tc	Nonadsorbing	34,000	226,000
preqlB_np	Adsorbing	940,000	> 1,000,000
preqmB_tc	Nonadsorbing	51	3,600
preqmB_tcM*	Nonadsorbing	5,900	37,000
preqmB_np	Adsorbing	2,900	157,000
preqmB_npM*	Adsorbing	53,000	345,000
prequB_tc	Nonadsorbing	6	180
prequB_np	Adsorbing	220	8,500
monqlB_tc	Nonadsorbing	26	660
monqlB_np	Adsorbing	1,300	60,000
monqmB_tc	Nonadsorbing	6	210
monqmB_np	Adsorbing	330	21,000
monquB_tc	Nonadsorbing	2	74
monuB_np	Adsorbing	50	3,100
glaqlB_tc	Nonadsorbing	120	6,200
glaqlB_np	Adsorbing	6,200	268,000
glaqmB_tc	Nonadsorbing	4	105
glaqmB_np	Adsorbing	180	9,500
glaquB_tc	Nonadsorbing	1	36
glaquB_np	Adsorbing	10	1,350

Model Results - DTN: LB03033DUZTRAN.001

NOTE: * Tracer release from repository matrix blocks



Model Results - DTN: LB03033DUZTRAN.001.

NOTE: Some pairs of points for "A" and "B" simulations are superposed. See Tables 6.7-4 and 6.7-5.

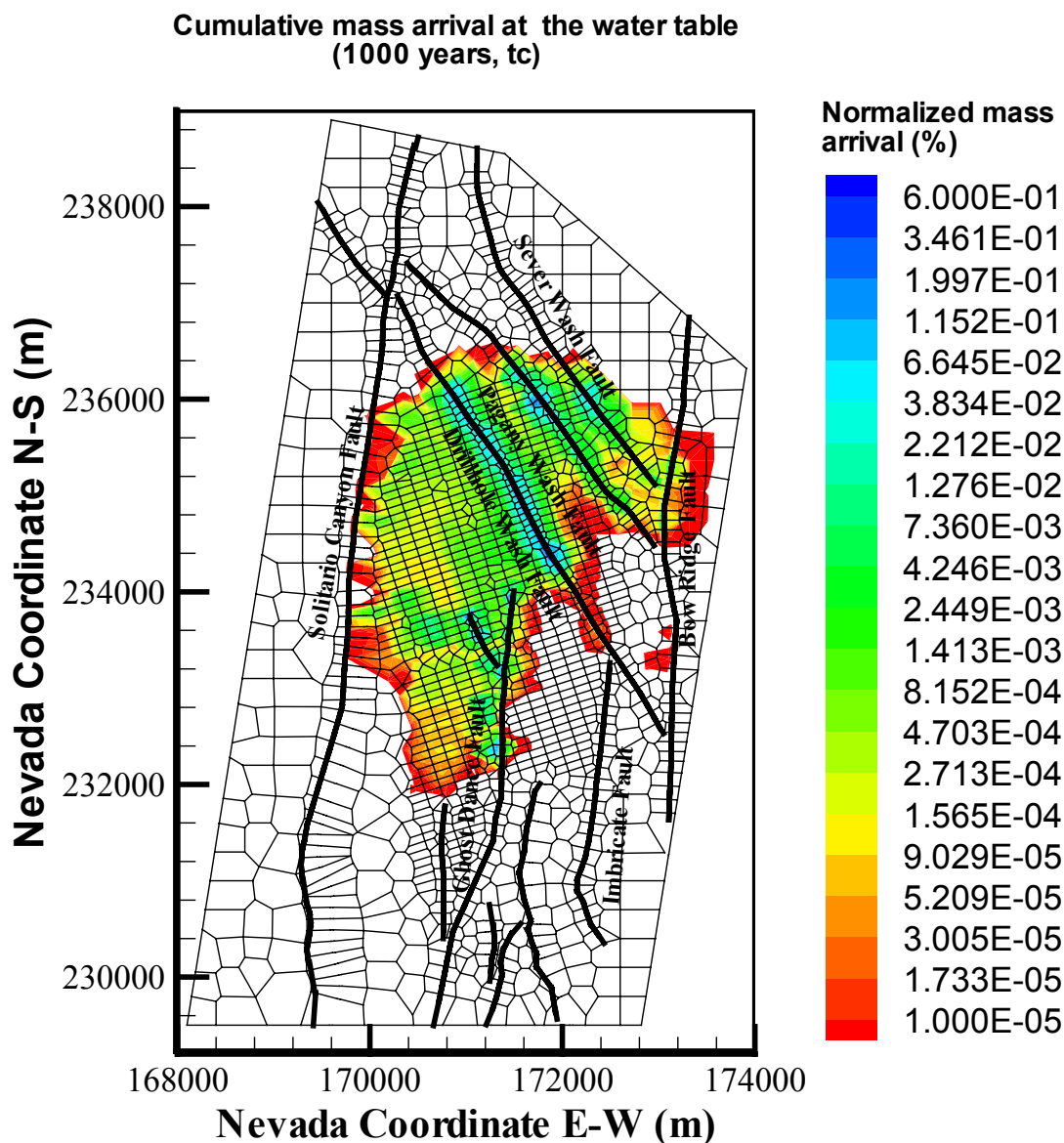
Figure 6.7-4. Correlation of Average Infiltration Rates and Tracer Transport Times at 50% Mass Breakthrough for the 36 Tracer-Fracture-Release Simulation Scenarios

The tracer transport times, as shown in Figures 6.7-1, 6.7-2, and 6.7-3 and Tables 6.7-4 and 6.7-5, are relatively shorter than those estimated using the UZ flow and transport model for TSPA-SR (BSC 2001 [158726]) for the same infiltration rates. This is primarily because the LA repository design is close to or at several faults, such as the Drill Hole Wash fault (Figure 6.1-1), which provide fast flow pathways for tracer transport. Moreover, the current LA UZ model predicts higher fracture flow components at the repository level, e.g., fracture flow percentage is 94% for the case of *preq_mA* (Table 6.6-3), compared with 84% of the previous SR case of *pa_pchm1* (BSC (2001 [158726], Table 6-22) for the same infiltration scenario.

The tracer-transport-simulation results can also be used to estimate potential locations or areas where radionuclides are most likely to break through along high-flux flow paths at the water table. Figures 6.7-5, 6.7-6, 6.7-7, and 6.7-8 show cumulative and normalized mass arrival contours at the water table at 1,000 and 1,000,000 years. The cumulative mass arrival is defined as cumulative mass arrived at each grid column of the water table over time, normalized by the total initial mass released at the repository. These figures present examples of breakthrough at the water table for conservative and reactive tracer transport with the present-day, mean infiltration rate.

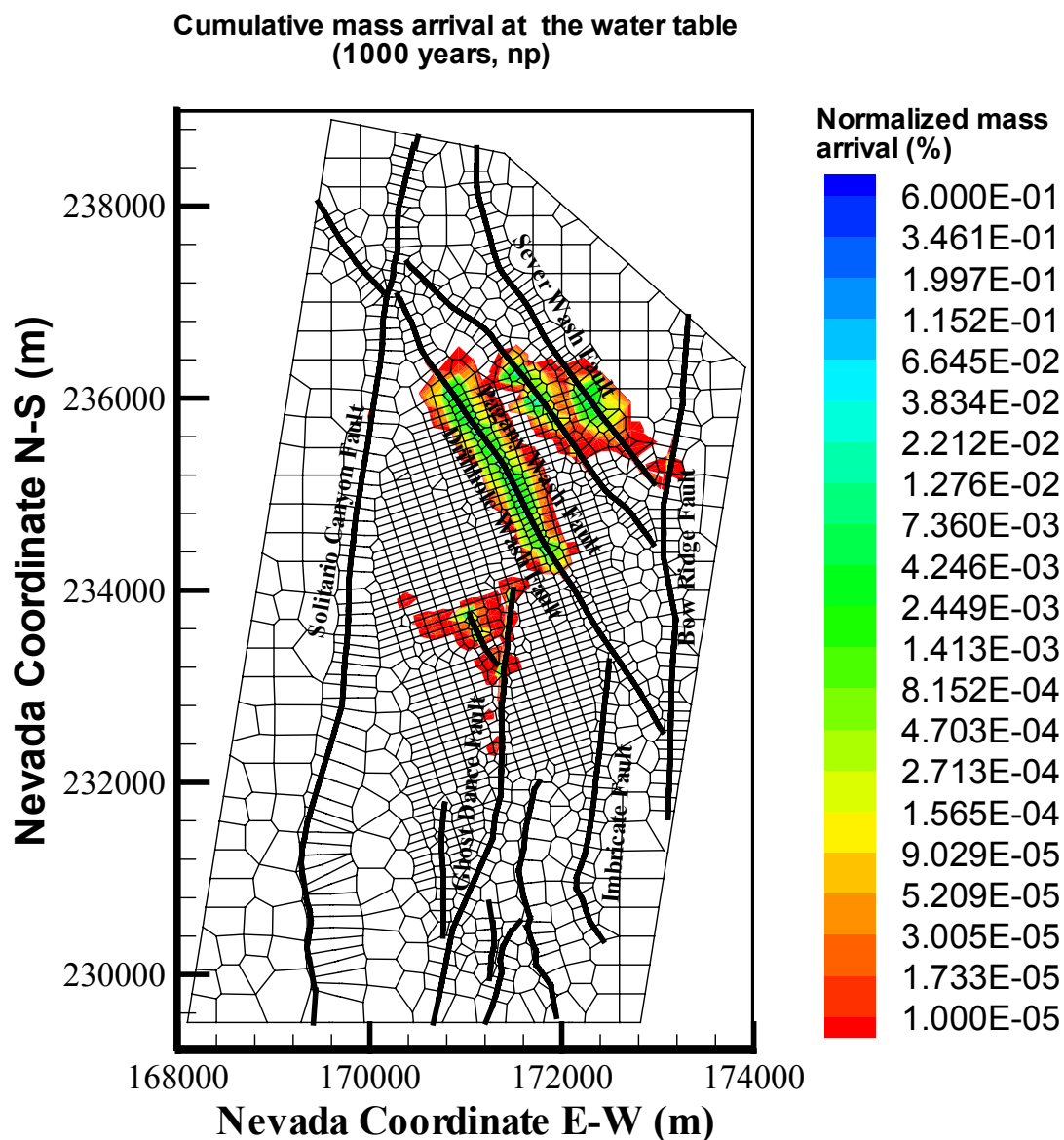
Figures 6.7-5 and 6.7-6 compare percentage mass arrival contours of a conservative and reactive tracer, respectively, at the water table after 1,000 years, simulated using the present-day, mean infiltration of the base-case flow field (*preq_mA*). The two figures clearly indicate a significant difference from the two tracer modeling results in distributions of tracer mass arrivals along the water table. Without adsorption, in 1,000 years the conservative tracer (*Tc*) has a much larger area of breakthrough, covering the entire area directly below the repository footprint, spreading to the east in the north. At this time, about 40% of the total initial mass of conservative tracers has arrived at the water table (see Figure 6.7-3), whereas only about 2% of the reactive tracer (*Np*) breaks through, and only along and near the major faults, owing to adsorption effects in the rock matrix.

At a later time of 1,000,000 years, Figures 6.7-7 and 6.7-8 show nearly identical mass arrival contours for the two tracers below the repository footprint. This is because 90–100% of both tracers have arrived at the water table at this time, which are transported under the same flow field. The 1,000- and 1,000,000-year contours are used to illustrate the predominantly downward percolation flow patterns, early influence of faults (especially the in-block faults), and small long-term effects of slow diffusion. The flow patterns are for hypothetical nonsorbing and sorbing tracers without taking into consideration the radioactive decay which reduce the concentrations. The 1,000- and 1,000,000-year flow pattern results can be further verified by comparing results at intermediate times between 1,000- and 1,000,000-years from radionuclide transport models using the unsaturated zone flow fields (transport models described in BSC 2002 [160819], Section 1.11). The information depicted in Figures 6.7-7 and 6.7-8 does not provide direct feeds to TSPA-LA; radionuclide transport is studied in detail in the downstream transport models.



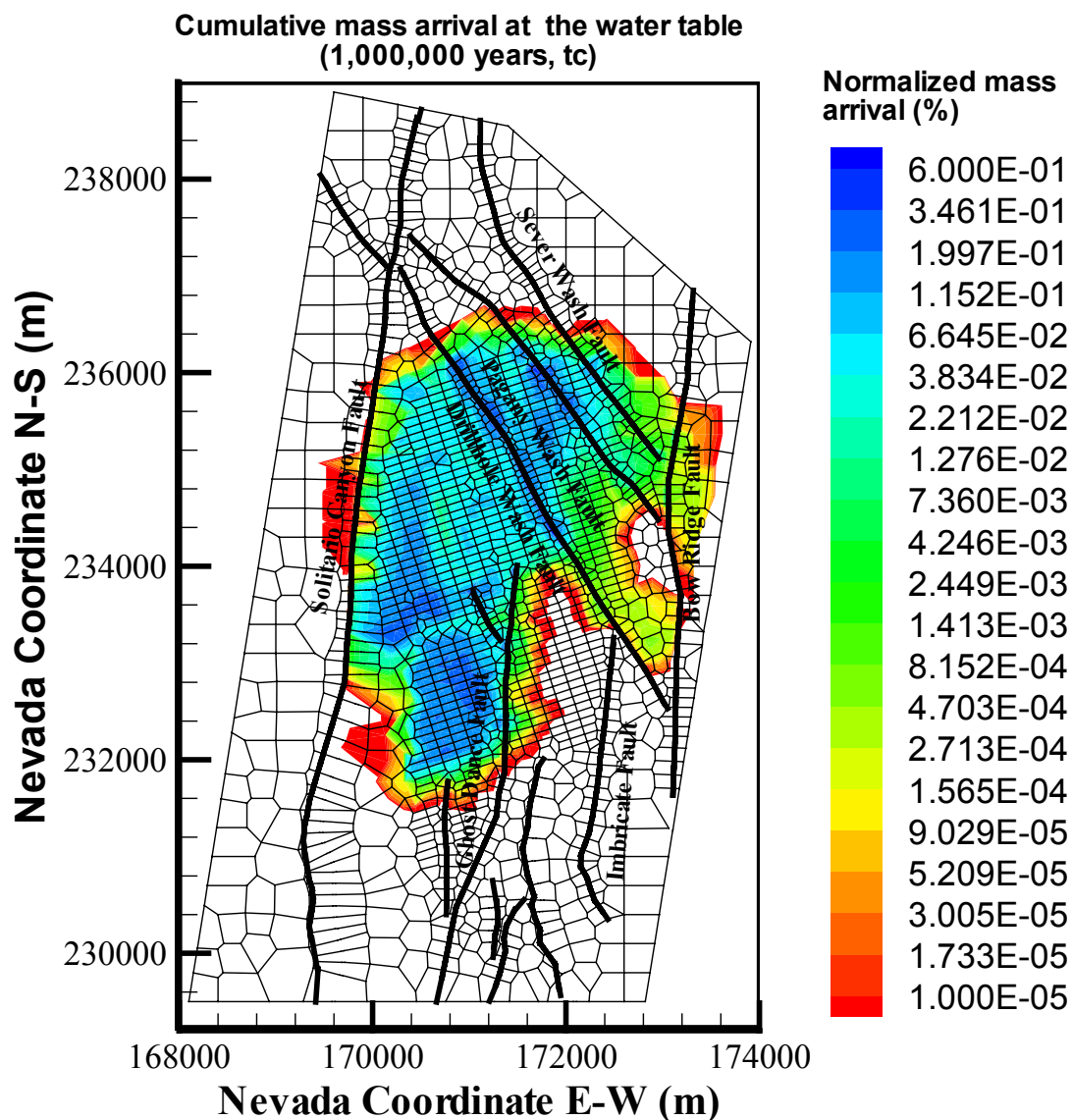
Model Results - DTN: LB03033DUZTRAN.001.

Figure 6.7-5. Simulated Cumulative, Normalized Mass Arrival Contours of a Conservative Tracer at the Water Table after 1,000 Years, Indicating Potential Breakthrough Locations at the Time, Using the Present- Day, Mean Infiltration Scenario



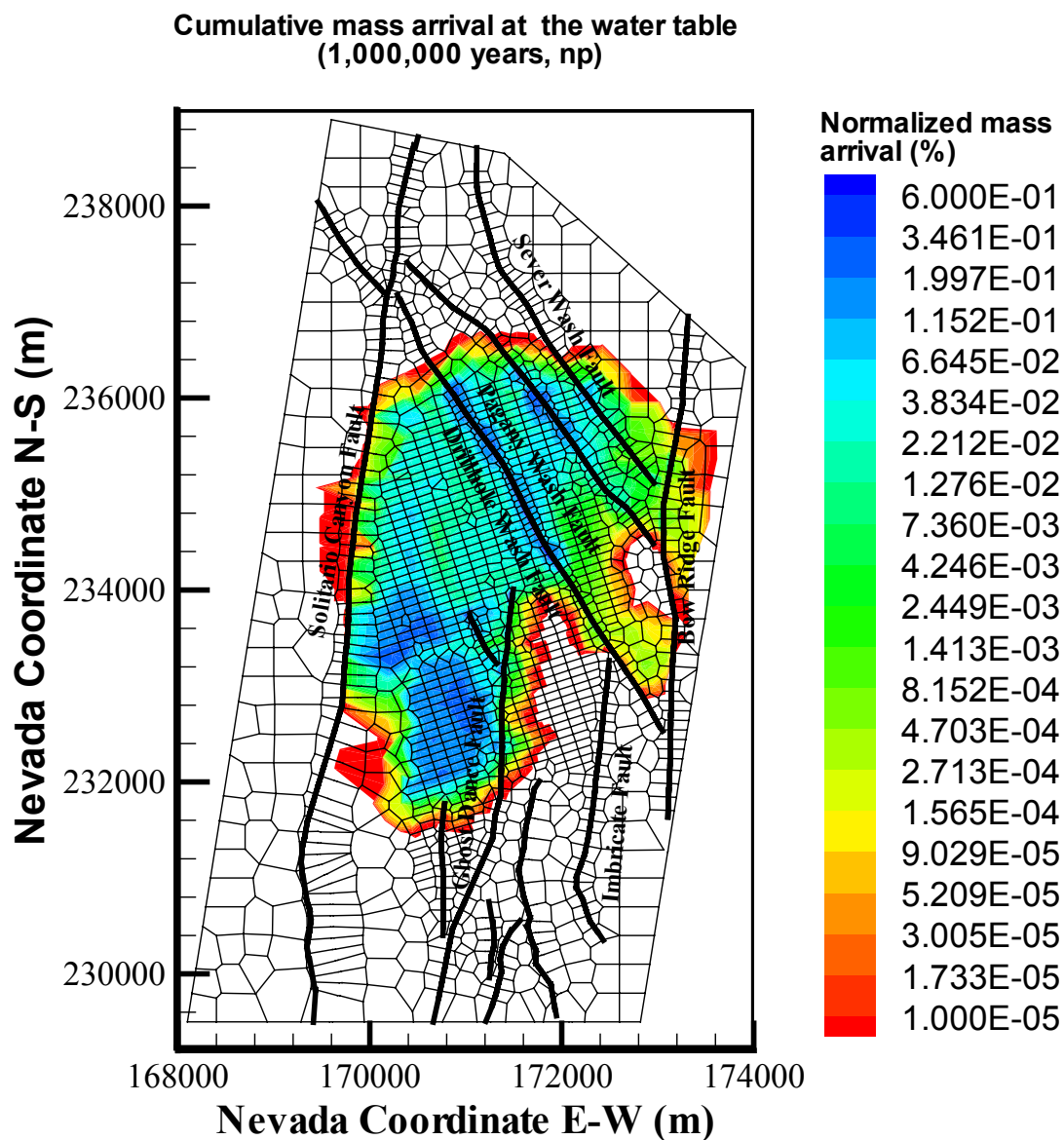
Model Results - DTN: LB03033DUZTRAN.001.

Figure 6.7-6. Simulated Cumulative, Normalized Mass Arrival Contours of a Reactive Tracer at the Water Table after 1,000 Years, Indicating Potential Breakthrough Locations at the Time, Using the Present-Day, Mean Infiltration Scenario



Model Results - DTN: LB03033DUZTRAN.001.

Figure 6.7-7. Simulated Cumulative, Normalized Mass Arrival Contours of a Conservative Tracer at the Water Table after 1,000,000 Years, Indicating Potential Breakthrough Locations at the Time, Using the Present-Day, Mean Infiltration Scenario



Model Results - DTN: LB03033DUZTRAN.001.

Figure 6.7-8. Simulated Cumulative, Normalized Mass Arrival Contours of a Reactive Tracer at the Water Table after 1,000,000 Years, Indicating Potential Breakthrough Locations at the Time, Using the Present-Day, Mean Infiltration Scenario

6.8 SENSITIVITY ANALYSES OF ACTIVE FRACTURE PARAMETER AND FRACTURE POROSITY

In the Active Fracture Model conceptualization (AFM, Liu et al. 1998 [105729], pp. 2638–2641) only a portion of fracture networks are active (hydraulically conductive) under unsaturated conditions. Numerically, this active portion is defined as a function of water saturation S and the active fracture parameter γ (Liu et al. 1998 [105729], pp. 2638–2641). By definition, γ ranges between 0 and 1, with $\gamma=0$ or $S=1$ (corresponding to a saturated condition) signifying that all fractures are active, and $\gamma=1$ signifying the smallest active fracture portion for a given saturation.

Water flux in TSw layers of Yucca Mountain tuff is mainly dominated by fracture flow. Uncertainties in γ impact the partition of water content and water flux between matrix and fractures of model gridblocks and, in turn, affect (possibly insignificantly) the entire flow field by determining the effective fracture permeability and the effective interface area between fracture and matrix (Liu et al. 1998 [105729], pp. 2638–2641). For transport, in addition to the effects of changing the flow field, the determination of effective fracture–matrix interface area by γ will significantly impact the diffusive solute flux between fractures and matrix, and all transport behavior is sensitive to γ .

As planned in BSC (2002 [160819], Section 1.10.4), the active fracture parameter, γ , was evaluated in BSC (2003 [161773]), using carbon-14 data. In Section 6.8.1 of the present Model Report, additional sensitivity studies are reported to analyze the sensitivities of simulated water saturation, water potential, and percolation flux with respect to γ .

In addition, the sensitivity of tracer transport with respect to γ and fracture porosity are discussed in Section 6.8.2.1 and Section 6.8.2.2, respectively.

6.8.1 Sensitivity Analyses of Flow Field with Respect to the Active Fracture Parameter (γ)

In these analyses, we consider the γ of TSw units, except for TSw31, as a sensitivity analysis case and the units below the repository horizon (including the units at where the repository is located) as another sensitivity analysis case (Table 6.8-1). According to the evaluation of γ using carbon-14 data, conducted in BSC (2003 [161773], pp. 78–82), the proper γ value of TSw32–TSw38 ranges between 0.2–0.4. However, the calibrated values in DTN: LB0208UZDSCPMI.002 [161243] for these units are 0.6 (TSw32–TSw33) and 0.569 (TSw34–TSw38), which are out of the proper range suggested in BSC (2003 [161773], pp. 78–82). To test the impact of γ uncertainties on flow field, we set up two 3-D flow simulations using γ values different from the calibrated values (Table 6.8-1). The γ values used in the sensitivity analyses simulations are half of the calibrated values of the respective units. For TSw32–TSw38, these values are within the suggested range. One simulation was performed using reduced γ values of TSw32–TSw39 (Table 6.8-1, simulation ID: TSw). The simulation is focused on evaluating the impact of uncertainties in TSw units. Another simulation used the reduced γ values of all units below the repository (Table 6.8-1, simulation ID: UnderRepo). The simulations take the input to the base case flow field simulation (Output-DTN: LB03023DSSCP9I.001, present-day mean infiltration, DTN: GS000308311221.005 [147613]) and change the γ values of the corresponding units (Table 6.8-1).

Table 6.8-1. The γ Values Used in Flow Simulations for Sensitivity Analyses

Rock units	γ Values		
	Base Case	TSw	UnderRepo
TSw31	0.129	0.129	0.129
TSw32, TSw33	0.600	0.300	0.600
TSw34–TSw38	0.569	0.284	0.284
TSw39z	0.370	0.185	0.185
TSw39v	0.250	0.125	0.125
CH1z–CH6z, PP4z, PP1z, BF2z and TR2z	0.370	0.370	0.185
CH1v–CH6v	0.250	0.250	0.125
PP3d, PP2d, BF3d and TR3d	0.199	0.199	0.100

Output-DTN: LB0303RDTRNSNS.001

NOTE: Base-case values are from DTN: LB0208UZDSCPMI.002 [161243] and the same with those used in the flow field simulations.

The results of these sensitivity analyses (Figure 6.8-1 and Figure 6.8-2) show that changing γ results in only small changes in matrix liquid saturations and water potentials. The details are discussed below.

6.8.1.1 Liquid Saturation and Potential

Figure 6.8-1 shows that implementing a γ of one half the calibrated value (used for base case present-day, mean infiltration flow field simulation, Table 6.8-1) in TSw layers leads to some small changes in the simulated matrix water saturation and water potential. The matrix liquid saturation and water potential changes in response to the changes of γ in all units below the repository are also small (Figure 6.8-2). Thus, the saturation and water potential are not sensitive to the uncertainties in γ . In addition, the sensitivity analysis results also indicate that the change of γ values has an insignificant effect on fracture liquid saturation and water potential. In fact, a comparison at SD-6 using the two γ values indicates that average absolute changes in fracture saturation and capillarity pressure are only 0.004 and 230 Pa, respectively.

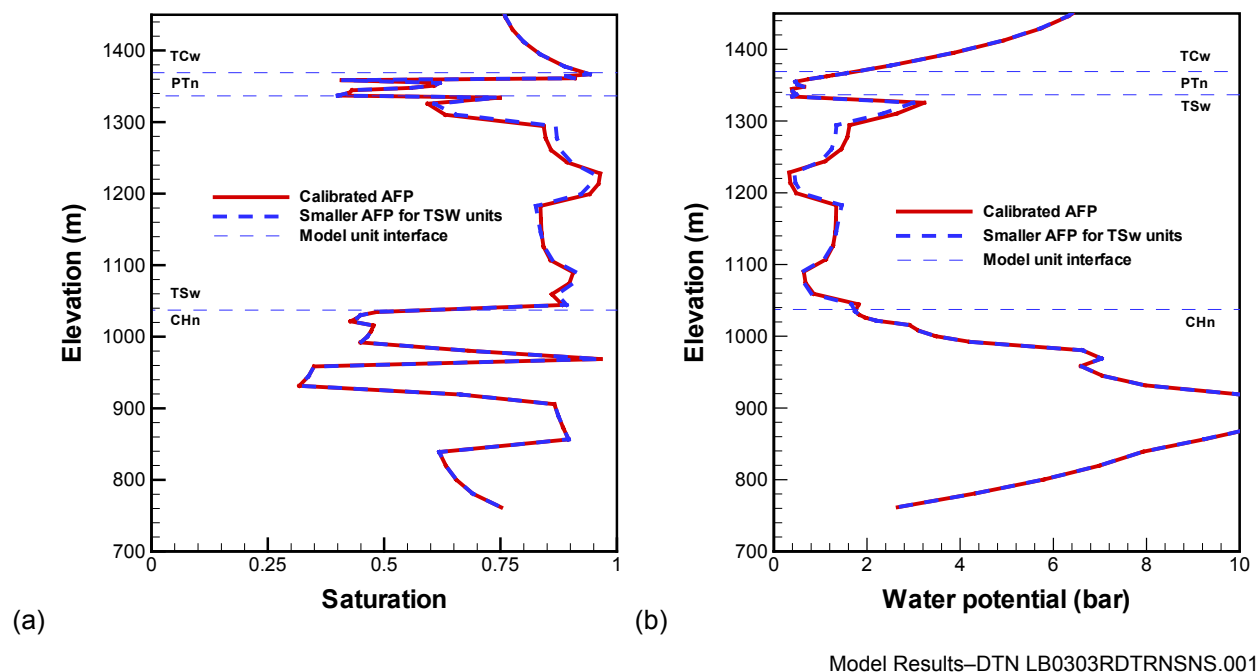


Figure 6.8-1. Comparison of (a) Simulated Matrix Liquid Saturation and (b) Water Potential Using Calibrated Hydraulic Properties (Solid Line) with That Obtained Using Smaller (Half) γ of TSw Units (Dashed Line) for Borehole USW SD-6

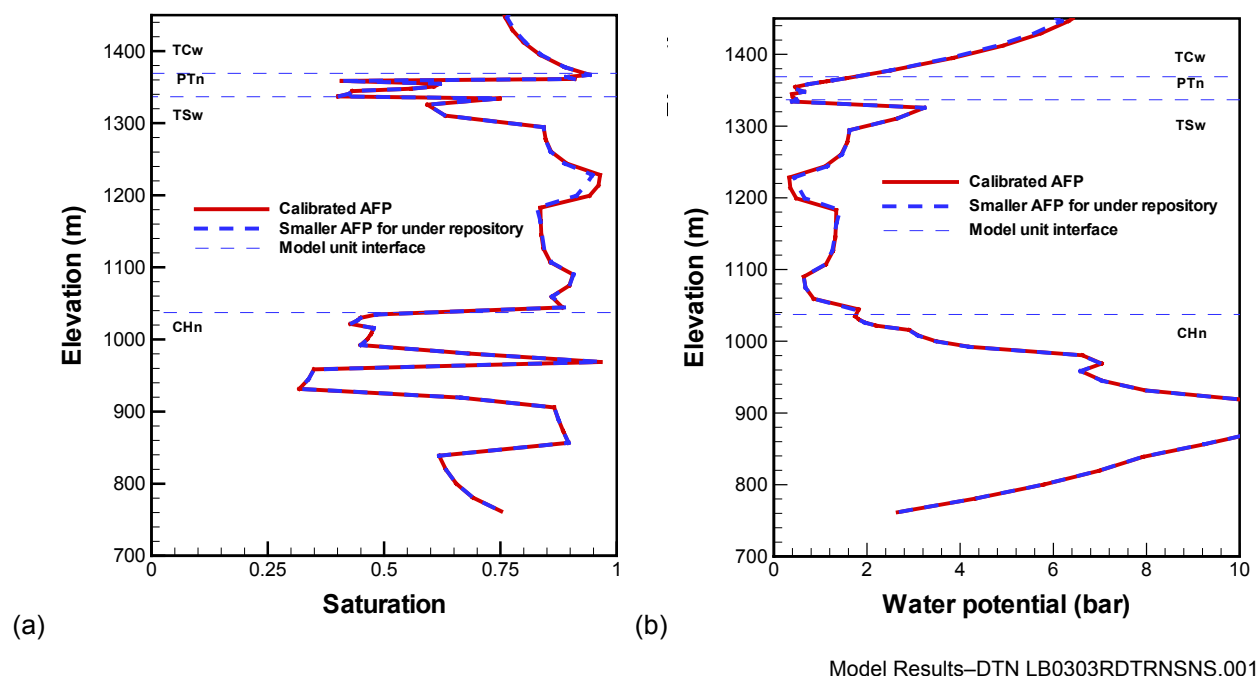


Figure 6.8-2. Comparison of (a) Simulated Matrix Liquid Saturation and (b) Water Potentials Using Calibrated Hydraulic Properties (Solid Line) with That Obtained Using Smaller (Half) γ of Under Repository Units (Dashed Line) for Borehole USW SD-6

6.8.1.2 Percolation Flux through Repository Layers

As listed in Table 6.8-2, the average fracture flux change within the repository area, caused by the γ changes in TSw layers, is -0.285% . The fracture fluxes, within the repository area, change -0.497% , on average, in response to the γ changes in units below the repository. Average values for the entire repository layer and the water table are also listed in Table 6.8-2 (for calculation details, see Attachment III, Section III.3).

Table 6.8-2. Relative Changes of Fracture Flux in Response to the Changes in γ

Simulation ID	Within the Repository Area	Entire Repository Layer	Water Table
TSw	-2.85E-3	1.51E-2	2.48E-2
UnderRepo	-4.97E-3	-2.32E-2	-2.32E-2

Output-DTN: LB0303RDTRNSNS.001

NOTE: Calculation is shown in Attachment III, Section III.3.

Therefore, considering the rather small changes in modeled saturation, water potential, and the very small change in percolation flux (on average), one can conclude that the water flow field is not significantly sensitive to γ .

6.8.2 Sensitivity Analyses of Transport

6.8.2.1 Transport Sensitivity to γ

Solute transport through tuff is mainly carried out by advection and diffusion. Because of the small flux rate, hydraulic dispersion plays a very minor role and therefore is generally ignored in simulations. Advection is determined by water flux and thus not sensitive to γ . However, because the fracture Darcy velocity is two to three orders of magnitude larger than matrix Darcy velocity, the advective solute flux in fractures is much faster than in the matrix. This leads to a short-term concentration difference between fractures and matrix, causing significant diffusion between them. At steady state, when the concentrations in fractures and matrix must reach equilibrium, the diffusion between fractures and the matrix will vanish. Therefore, the steady-state concentration is insensitive to γ . The short-term transport behavior may be sensitive to the changes in γ , but the long-term transport behavior will be relatively insensitive to the changes of this parameter.

Diffusion is driven by the concentration gradient and the effective diffusion coefficient of rocks. Numerically, the diffusion between fractures and matrix is calculated upon the concentration differences between matrix and fractures, the active (effective) interface area between fractures and matrix, and the fracture spacing. The active interface area between matrix and fractures is related to γ . A larger γ defines a smaller effective interface area. Therefore, the diffusion between the matrix and fractures must be sensitive to this parameter, and the entire transport rate is affected.

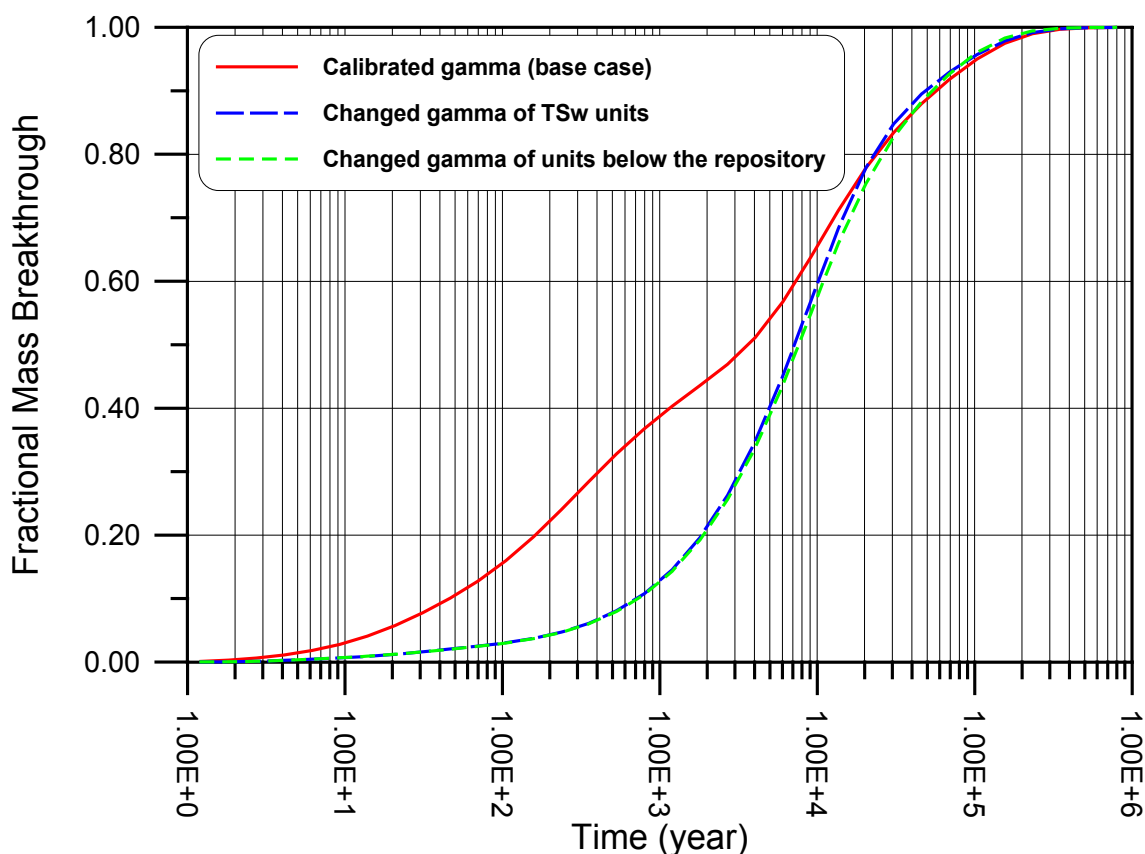
In the Yucca Mountain UZ, transport is dominated by the fracture advective flux (BSC 2001 [161340], pp. 35–36). The diffusion from fractures into matrix functions as a buffer for the

advection through fractures, similar to kinetic sorption, which impedes the transport through fractures (BSC 2001 [161340], p. 38).

To test the sensitivity of tracer transport to the active fracture parameter, γ , three conservative-tracer transport simulations were performed. One simulation is the base case (or reference case), using the calibrated γ and the base-case flow field; and the other two are for sensitivity analysis. Of these other two, one has a smaller γ (1/2 of the calibrated value) for TSw units except for TSw1, the same as the first flow-sensitivity-analysis simulation in Section 6.8.1 (simulation ID: TSw in Table 6.8-1). The other has a smaller γ (1/2 of the calibrated value) for repository units and all units below the repository, similar to the second flow-sensitivity-analysis simulation (Simulation ID: UnderRepo in Table 6.8-1, see Section 6.8.1). All simulations were performed using T2R3D V1.4 (LBNL 1999 [146654]). The base-case flow field (using calibrated rock properties) comes from flow simulation (Output-DTN: LB03023DSSCP9I.001, see Section 6.2.5). The flow fields for two reference simulations were taken from flow sensitivity analyses (Section 6.8.1).

The transport models simulate the tracer transport processes from the repository to the groundwater table. The tracer is represented by technetium, with diffusion coefficients of $3.20 \times 10^{-11} \text{ m}^2/\text{s}$ (DTN: LA0003JC831362.001 [149557]). The cumulative relative mass of the tracer arriving at the groundwater table (breakthrough curves), obtained from simulations using different γ values, are presented in Figure 6.8-3. The figure shows that tracer transport is relatively sensitive to γ . The base case is conservative, the differences among the cases are small after 7,000 years and become negligible after 20,000 years. With the base-case parameter, the tracer arrives at the water table faster than the two reference cases. In the base case, 20% of the total input mass arrives at the water table at (approximately) 150 years (Figure 6.8-3), and 50% of the total mass arrives at the water table at (approximately) 3,400 years (Figure 6.8-3). The two sensitivity analyses cases give similar results: 20% mass arrival at 1,900 years and 50% at (approximately) 7,100 years, (Figure 6.8-3). However, the times for 100% mass arrival at the groundwater table in all three cases are similar. This indicates that long-term transport behavior is not very sensitive to the change in γ .

The base-case with the larger γ values defines a smaller active interface area between fracture and matrix. Consequently, the buffer effect of matrix diffusion is smaller. This causes faster breakthrough of the tracer. In the two sensitivity cases, a smaller γ defines a larger active interface area and hence larger buffer effects from matrix diffusion. Therefore, the overall transport is slower. In summary, this study indicates that larger γ values give more conservative or faster tracer transport times from the repository to the water table.



Model Results-DTN: LB0303RDTRNSNS.001

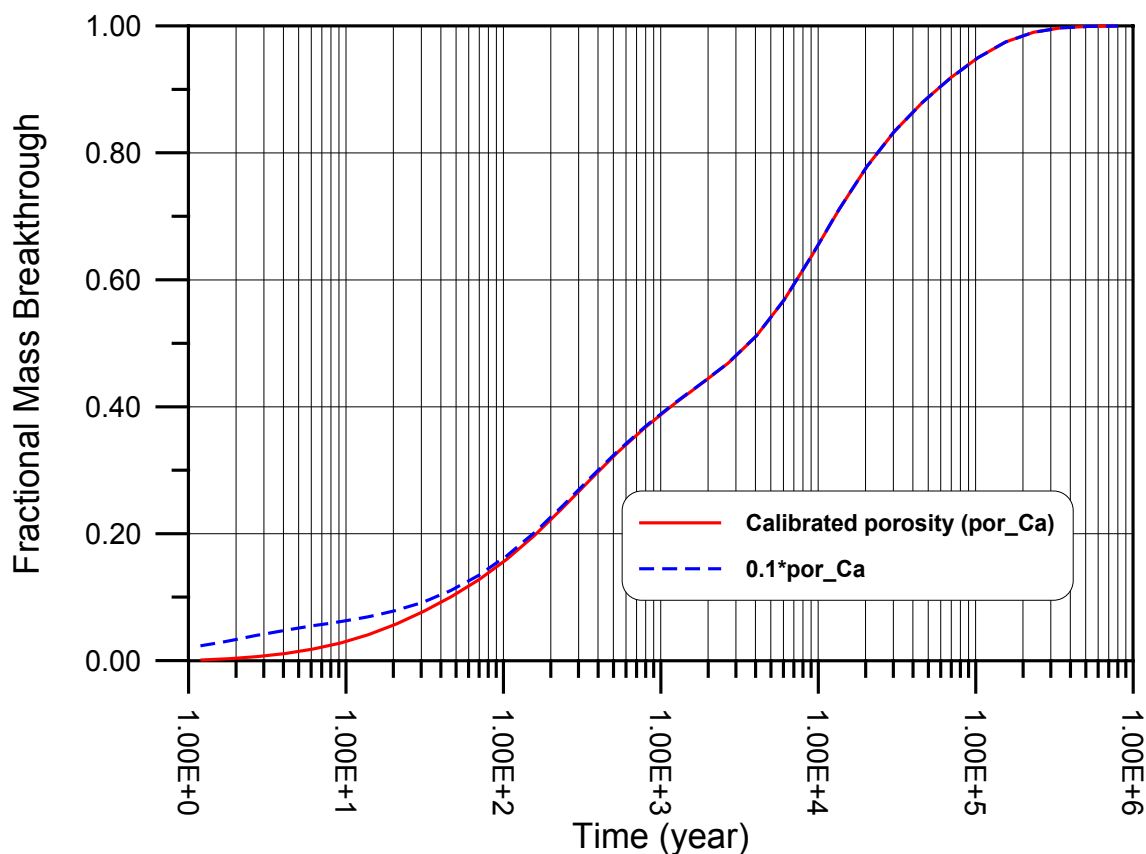
Figure 6.8-3. Comparison of a Simulated Breakthrough Curve of Relative Tracer Mass at the Groundwater Table Obtained for the Base Case (Using Calibrated Rock Hydraulic Properties, Red Solid Line), a Case Using the Smaller γ of TSw Units (Blue Dash Line), and Another Case Using the Smaller γ of All Units below the Repository (Green Dash Line)

6.8.2.2 Transport Sensitivity to Fracture Porosity

To test the sensitivity of tracer transport with respect to the uncertainties in fracture porosity, a transport simulation, using the same input data as the base-case simulation in Section 6.8.2.1 (except for fracture porosity), was performed. This simulation uses smaller fracture porosity (1/10 of the calibrated values) for all units. However, the steady-state flow field is independent of fracture porosity, and only the changes in repository units and units below the repository may impact the early travel time of the tracer arriving at the groundwater table. Simulation results are plotted in Figure 6.8-4 and compared to the base-case results in the figure. The figure shows that the fractional mass breakthrough of the tracer arrived at the water table is larger only during the first 50 years if the fracture porosity is one order of magnitude smaller than the calibrated value. However, the accumulated breakthrough mass arrival is quite small during this period in both cases (less than 15% of the released mass). After 100 years, both simulation cases give similar results: almost 50% of the tracer mass arrives at the groundwater bottom at 3,400 years, and the two breakthrough curves are not differentiable (Figure 6.8-4).

This result indicates that radionuclide transport is sensitive to fracture porosity only at the early times (less than 50 years), and in long-term evolution, transport behavior is not sensitive to this

parameter. Overall, this sensitivity analysis shows that fracture porosity has an insignificant effect on tracer transport.



Model Results—DTN: LB0303RDTRNSNS.001

Figure 6.8-4. Comparison of Simulated Breakthrough Curve of Relative Tracer Mass at the Groundwater Table Obtained for the Base Case (Using Calibrated Rock Hydraulic Properties, Red Solid Line), and a Case Using a Smaller (1/10) Fracture Porosity (Blue Dash Line)

6.9 UNCERTAINTIES AND ALTERNATIVE MODELS

The calibrated model parameters of Section 6.2, as well as the 18 3-D flow fields of Section 6.6, are currently the best estimates with the UZ Flow Model. The validation efforts of Section 7 will further show the validity of the model in describing the UZ hydrological, geochemical, and geothermal conditions. It should be recognized, however, that some uncertainties are associated with these model parameters and output results, although they are based on qualified field-observation data, hydrogeological conceptual understanding, and integrated modeling studies. Uncertainties arise from (1) uncertainty in observed parameters and field data; (2) uncertainty in estimated present-day and future climates; (3) approximations used in hydrogeological conceptual models, such as steady-state flow conditions; (4) scale-dependent heterogeneity and model input parameters in the UZ fracture-matrix system; (5) the complexity of different UZ coupled processes; and (6) the limitations of current modeling and large volume-average approaches.

Numerical representation of a real-world hydrogeologic system involves discretization of a model volume into a large number of elements, with each element assigned the necessary attributes or properties. For the model used, the necessary properties are known at only a relatively few locations within the model domain. Limitations of the software used to develop the UZ models at Yucca Mountain may also create a potential source of uncertainty, which is addressed in the Software Qualification per AP-SI.1Q, *Software Management*.

Efforts have been made to quantify and reduce uncertainties associated with model parameters and output results in this Model Report. A total of six sets of model input parameters are developed, with three base cases and three alternatives, which cover the effect of uncertainties in lower, mean, and upper bound infiltration rates. Uncertainties with present-day and future climates are investigated using three scenarios—present day, monsoon and glacial transition climates—which combine for nine different net infiltration scenarios. In addition, sensitivity and uncertainty with the active fracture model parameter, γ , is evaluated for its impact on flow and transport modeling results. The sensitivity analysis shows that γ has little effect on simulated percolation fluxes, but a large impact on tracer transport. The γ value used in the UZ Model produces more conservative transport results.

Uncertainties with UZ conceptual flow models are studied using two conceptual models of the PTn unit, i.e., base-case and alternative models, and using a permeability-barrier perched water model. The base-case PTn model is selected for its better predictions of chloride data as well as moisture data. Each of the conceptual models uses three different parameter sets for lower, mean, and upper bound infiltration rates to cover the uncertainties and possible ranges with model parameters and infiltration rates. This results in nine base-case and nine alternative 3-D UZ flow fields. In general, the nine base-case flow fields show more lateral flow occurring within the PTn than those predicted by the alternative model. Furthermore, analyses have been done for the impact of behavior on tracer or radionuclide transport for the nine base-case and nine alternative flow fields. The results of 40 3-D tracer-transport simulations show a wide range of tracer transport times from the repository to the water table, and the base-case model gives slightly more conservative estimates in general.

Uncertainty may exist in the analysis of lateral flow in the PTn unit because of the choice of approach. Different approaches may yield different conclusions. Flint et al. (2003 [163967]) concluded that lateral flow may occur in the PTn on a smaller scale than indicated in Figures 6.6-1 to 6.6-3. However, their conclusion is based on a different approach from the one used in this Model Report. First, Flint et al. (2003 [163967]) use an analytical solution which is only applicable to single-porosity porous-medium flow with two semi-infinite layers, and may not be suitable for the multi-layered fracture-matrix system, to estimate lateral flow. Second, the analytical solution uses a Gardner's equation for relative permeability, which is different from what is used in this Model Report. Third, Flint et al. (2003 [163967]) present a 2-D modeling study without including 3-D effects, and also acknowledge that no one approach, analysis, or data set provides can establish whether large-scale lateral flow occurs above the repository.

In addition to different flow fields, the timing for changes of climate states is uncertain. Two recent studies estimate the future climate states at Yucca Mountain based on past climate records, with USGS (2001 [158378]) focusing on the period from present to 10,000 years and Sharpe (2003 [161591]) focusing on the period from 10,000 to 1,000,000 years. The TSPA-LA presently plans to use essentially the results of USGS (2001 [158378]) to define the future

climate changes over the next 20,000 years. The following evaluation supports the TSPA base timing sequence with present climate from 0 to 600 years, monsoon climate from 600 to 2,000 years, and glacial transition climate from 2,000 years to 20,000 years. Sharpe (2003 [161591]) is used to evaluate the timing uncertainty.

Both USGS (2001 [158378], p. 26) and Sharpe (2003 [161591], Table 6-5) confirm the existence of a long-duration modern (interglacial) climate state for at least the last 9,000 years (–9,000 years). USGS (2001 [158378], p. 26) estimates that the modern climate regime started between –10,000 and –9,000 years. Sharpe (2003 [161591], Table 6-5) calculates that the interglacial climate lasted from –12,000 years to –1,000 years, and the present climate is a monsoon climate.

Table 6.9-1 compares the estimated timing for the future climate between the two analyses. There are three timing differences between the two future estimates during the next ~20,000 years before glacial climate. These are:

1. Transition from modern to monsoon, difference is 1,600 years (between 600 and –1,000 years).
2. Transition from monsoon to intermediate, difference is 1,500 years (between 2,000 and 500 years).
3. Presence of a second 1,500-year monsoon state occurring between 18,500 and 20,000 in Sharpe (2003 [161591], Table 6-5).

Table 6.9-1. Comparison between the Two Timing Estimates of Future Climate States for the Next ~50,000 Years

USGS Analysis ¹		DRI Analysis (Sharpe 2003 [161591])	
Modern	0 to 600 yr. A.P. [600]	Interglacial	N/A
Monsoon	600 to 2,000 yr. A.P. [1,400]	Monsoon	–1,000 yr. B.P. to 500 yr. A.P. [1,500]
Glacial-Transition	2,000 to 30,000 [28,000]	Intermediate	500 to 18,500 yr. A.P. [18,000]
		Monsoon	18,500 to 20,000 yr. A.P. [1,500]
		Intermediate	20,000 to 38,000 yr. A.P. [18,000]
Glacial	30,000 ending before 50,000 yr. A.P. [<20,000]	Glacial	38,000 to 49,000 yr. A.P. [11,000]

Source: Source: Sharpe 2003 [161591], Table 6-6

NOTE: yr. A.P. = years after present; B.P. = years before present; brackets denote duration in years

¹ USGS (2001 [158378], Table 2, p. 67) reported durations of modern climate for 400–600 years, and monsoon climate for 900–1,400 years. USGS (2001 [160355], p. 57) selected 600 years and 1,400 years as the duration for these changes in climate states.

The differences in timing are considered to be insignificant for two reasons. First, both estimates are based on the Devils Hole record chronology. Each Devils Hole sample integrates an average time interval representing about 1,800 years (Winograd et al. 1992 [100094], p. 255). Therefore, the differences of 1,600 years and 1,500 years for the first two timing differences are less than the Devils Hole sample resolution of 1,800 years. The duration of the 1,500-year monsoon interval is also less than the Devils Hole sampling resolution. Since the monsoon is between two intermediate states of long duration (18,500 years), the uncertainties of timing for both the beginning and the end of the monsoon climate are dominated by the uncertainties of the

intermediate states. Second, the DRI analysis reports the timing of climate states (Sharpe 2003 [161591], Table 6-5) to the nearest 500 years. Consequently, the timing of future climate estimated in this report confirms the future climates timing suggested in USGS (2001 [158378], p. 76).

INTENTIONALLY LEFT BLANK

7. VALIDATION

The validation activities for the UZ Flow Model include *corroboration with experimental data* and *modeling studies* using the following: (1) Enhanced Characterization of Repository Block (ECRB) observation data within the Exploratory Studies Facility (ESF); (2) WT-24 perched-water data; (3) gas-flow data from boreholes SD-12 and UZ-7a; (4) measured C-14 borehole data; and Alcove 8/Niche 3 flow and seepage test results. In addition, validation efforts are also performed for the ambient thermal model, chloride model, calcite model, and strontium model.

In all these cases, simulation results of the UZ Model and submodels are able to match different types of available observation data, such as water potentials, perched-water locations, temperatures, tracer concentrations, and pneumatic pressures. These efforts have provided validation of the UZ Model and its submodels for their accuracy and reliability in describing hydrogeological, thermal, and chemical conditions and predicting flow and transport processes in the Yucca Mountain UZ.

In addition, the key flow and transport processes pertaining to the UZ at Yucca Mountain have been investigated through natural analogues (CRWMS M&O 2000 [141407]). These analogue studies contained both literature studies and analyses. One of the important case studies was the flow experiment and tracer infiltration test in fractured media at the Box Canyon (CRWMS M&O 2000 [141407], Section 6.5.1.1). The field tests at the site provided calibrations of numerical models using extensive *in situ* measured data. A consistent set of parameters was obtained from calibrating the site-wide model using the dual-permeability approach to both pneumatic and infiltration tests. The studies demonstrated that conceptual models and large-scale, volume-averaged numerical modeling approaches use for the UZ Flow and Transport model at Yucca Mountain can be applied with confidence (CRWMS M&O 2000 [141407], Section 7). The model validation effort of this section is intended to further build confidence in the UZ Flow Model and submodels with regard to their ability to predict flow and transport processes in the Yucca Mountain UZ system.

7.1 THE VALIDATION CRITERIA

Validation activities for the UZ Flow Model and submodels are carried out based on the *Technical Work Plan for: Performance Assessment Unsaturated Zone* (BSC 2002 [160819], Attachment I-1-2). The models will be accepted as valid for their purposes through validation efforts of *corroboration with experimental data* in this section, if all the following criteria are met:

- The water-potential data measured from ECRB are used for validation by comparing with simulation results of the UZ Model. The criterion for the validation is that simulated water-potential values are within the range of measurements along the ECRB tunnel (BSC 2002 [160819], Attachment I-1-2-1). Demonstration that this criterion was met is shown in Section 7.2.
- WT-24 perched-water elevation data is used to validate the UZ Model. The criterion for the validation is that simulated perched elevation matches the observed value within 10

m (BSC 2002 [160819], Attachment I-1-2-1). Demonstration that this criterion was met is shown in Section 7.3.

- For pneumatic data measured in SD-12 (for the second 30 days) and UZ-7a (60 days) are used for validation. The criterion for the validation is that simulated gas pressures and their patterns of variations consistently compare closely with the observed values. That is, the simulations will consistently reproduce increases and decreases resulting from changes in barometric pressure at the ground surface (BSC 2002 [160819], Attachment I-1-2-1). Demonstration that this criterion was met is shown in Section 7.3.
- Carbon-14 data from gas samples provide approximate C-14 residence times for pore water. The residence times can be interpreted as tracer travel time from the ground surface to where the gas samples were collected, based on the current conceptual model for UZ flow and transport. These data are used to validate the UZ Model. The criterion for the validation is that simulated tracer travel times (i.e., peak of the breakthrough curve at the sample-collection locations for a pulse input at the ground surface or the time for first moment of concentration) are within the range of times estimated from data in the TSw unit (BSC 2002 [160819], Attachment I-1-2-1). Demonstration that this criterion was met is shown in Section 7.5.
- Data from Alcove 8/Niche 3 flow and seepage test results are used to validate the UZ Flow Model. The tests involve a fault test and a large-infiltration-plot test. The fault test includes water infiltration and liquid tracer experiments. Test data from the latter test are not available in time for this report and therefore are not used here for model validation. Flow and seepage test results are used for model validation. The criterion for validation is that the predicted results for the time to reach a given concentration of a conservative tracer are within a factor of 5 of the observed times, or that explanations can be found for why the observed and simulated results deviate significantly (BSC 2002 [160819], Attachment I-1-2-1). Demonstration that this criterion was met is shown in Section 7.6.
- Boreholes H-5, H-4, and WT-18 observed temperature data are used to validate the ambient thermal model, since no temperature measurements of ECRB specified in the TWP are available in the TDMS. The validation criterion is the same as that in TWP, i.e., to match the observed values with less than 3°C difference (BSC 2002 [160819], Attachment I-1-2-2). Demonstration that this criterion was met is shown in Section 7.7.
- For the chloride model, simulated pore-water chloride concentrations in the ESF are compared with analysis of samples. The criterion for validation is that the range of the simulated chloride concentration falls within the range of measured concentrations (BSC 2002 [160819], Attachment I-1-2-3). Demonstration that this criterion was met is shown in Section 7.8.
- The calcite model is used to validate the UZ Flow Model with the abundance data of calcite mineral. The calcite model is validated by comparing 1-D simulation results with measurements. The criterion is that the simulated volume fraction of calcite coating for each UZ model layer falls within the range of measurements for that layer (BSC 2002 [160819], Attachment I-1-2-4). Demonstration that this criterion was met is shown in Section 7.9.

- Borehole and ECRB strontium (Sr) concentrations are used to check the UZ Model results using the Sr modeling analysis. The criterion for validation is qualitative agreement between the simulated strontium concentrations and the average of the observations at the same elevation, and agreement with the vertical trends (BSC 2002 [160819], Attachment I-1-2-5). Demonstration that this criterion was met is shown in Section 7.10.

In addition, journal publications are used to provide corroboration for our model validation. A three-dimensional UZ numerical model was developed to simulate flow and distribution of moisture, gas, and heat at Yucca Mountain (Wu et al. 1999 [117161]). Flow and transport processes within the UZ were characterized under current and future climates (Wu et al. 2002 [160195]). Studies of capillary barriers in the unsaturated rock of Yucca Mountain have also been published (Wu et al. 2002 [161058]). The perched-water phenomena in the UZ at Yucca Mountain have been investigated (Wu et al. 1999 [117167]). Subsurface pressure variations have been used to determine the pneumatic diffusivity of important geological features (Ahlers et al. [109715]). Subsurface borehole temperature data were used to estimate percolation flux (Bodvarsson et al. 2003 [162477]). Chloride measurements were used to calculate infiltration rates along the ESF (Fabryka-Martin et al. 1998 [146355]). Chloride data, in conjunction with hydrostructural and hydrogeological features, were also used to constrain infiltration rates (Liu et al. 2003 [162478]). In addition, chloride and strontium geochemistry was investigated using 3-D modeling for insights into the hydrology of the UZ (Sonnenthal and Bodvarsson 1999 [117127]).

7.2 VALIDATION USING ECRB WATER-POTENTIAL MEASUREMENTS

The 3-D UZ numerical model at Yucca Mountain has been the subject of several journal articles. In one of them, flow in the UZ was simulated in conjunction with distribution of moisture, gas, and heat (Wu et al. 1999 [117161]). In another study, flow and transport processes within the UZ under current and future climates were investigated using a three-dimensional numerical model, which incorporates a wide variety of field data in the highly heterogeneous, unsaturated fractured porous rock (Wu et al. 2002 [160195]). The capillary barriers in the unsaturated rock of Yucca Mountain were also studied (Wu et al. 2002 [161058]).

An east-west cross drift was constructed in 1997 as part of the ECRB program (see Figure 6.1-1 for the location of the ECRB tunnel). Water-potential data (DTN: GS980908312242.036 [119820]) were collected from heat-dissipation probes installed in the tunnel wall (at a depth of 2 m) along the ECRB tunnel inside the ESF. Water-potential data were collected from heat dissipation sensors that have been calibrated for matrix potential. Though the boreholes were dry drilled, the sensors were installed with wet cement. Thus, the sensors were fully saturated and surrounded with contact media to ensure good contact with rock, and equilibrated with the matrix potential of the rock. Following the equilibration, the probe would gradually dry out from ventilation effects. Since this was the first group of probes installed in the tunnel wall, no steps were taken to reduce the effects of ventilation drying in the tunnel. Extra steps, such as installing multiple doors, were taken during subsequent installation and monitoring of probes in the ECRB tunnel.

As part of the 3-D flow and transport modeling validation process, modeled results of water potentials were compared to field-observation data collected from the wall of the tunnel to check the accuracy of the modeling predictions. The three base-cases (preq_uA, preq_mA and preq_lA

with Output-DTN: LB03023DSSCP9I.001) were selected for validation of the UZ Model, as discussed in Section 6.2.5. Here the ‘l’ stands for low bounds of infiltration, ‘m’ mean infiltration, ‘u’ upper bounds, and “A” the base-case flow field with the infiltration rate. A complete list of modeling scenarios is in Table 6.7-1. The infiltration boundary conditions are the three present-day infiltration rates (DTN: GS000308311221.005 [147613]). The calibrated properties used for the 3-D prediction are those developed and listed in Tables I-1, I-2 and I-3 (Output-DTN: LB03013DSSCP3I.001) and the calibrated fault properties (DTN: LB02092DSSCFPR.002 [162128]).

Figure 7.2-1 shows a comparison of simulated and measured matrix water potentials along the wall of the ECRB drift (note that water potential is defined as the absolute value of capillary pressure in this report). As shown in the figure, observation data are available only along part of the tunnel. Most of the observed water-potential data are distributed between 0.1 (10^4 Pa) and 1 (10^5 Pa) bars, with a maximum of 3.4 bar. The model predicted approximately 1 bar for the same section of tunnel, which is higher than most of the observed data. The predicted water potentials along the ECRB from the UZ Model ranged between 0.30 and 1.92 bars (Figure 7.2-1) for the present-day, mean infiltration scenario (preq_mA).

The available data for field measured matrix water potentials at the ECRB were distributed in a range between 0.1 (10^4 Pa) and 1 (10^5 Pa) bar. Their comparison with simulation results may have been affected by scale. This is because the model has a gridblock at the ECRB of about $100 \times 100 \times 10$ m in x, y, and z directions, respectively. Thus, simulated water potentials are the results of large-scale average of tuff matrix, which is intercepted by many fractures. On the other hand, measurements were made on a much smaller, local scale on the order of a meter, thus controlled by local heterogeneity.

Even though the data available for comparison at the ECRB drift are limited, results indicated that the UZ Model generally predicted the range of the water-potential data from *in situ* measurements. Therefore, the criterion of validation is satisfied.

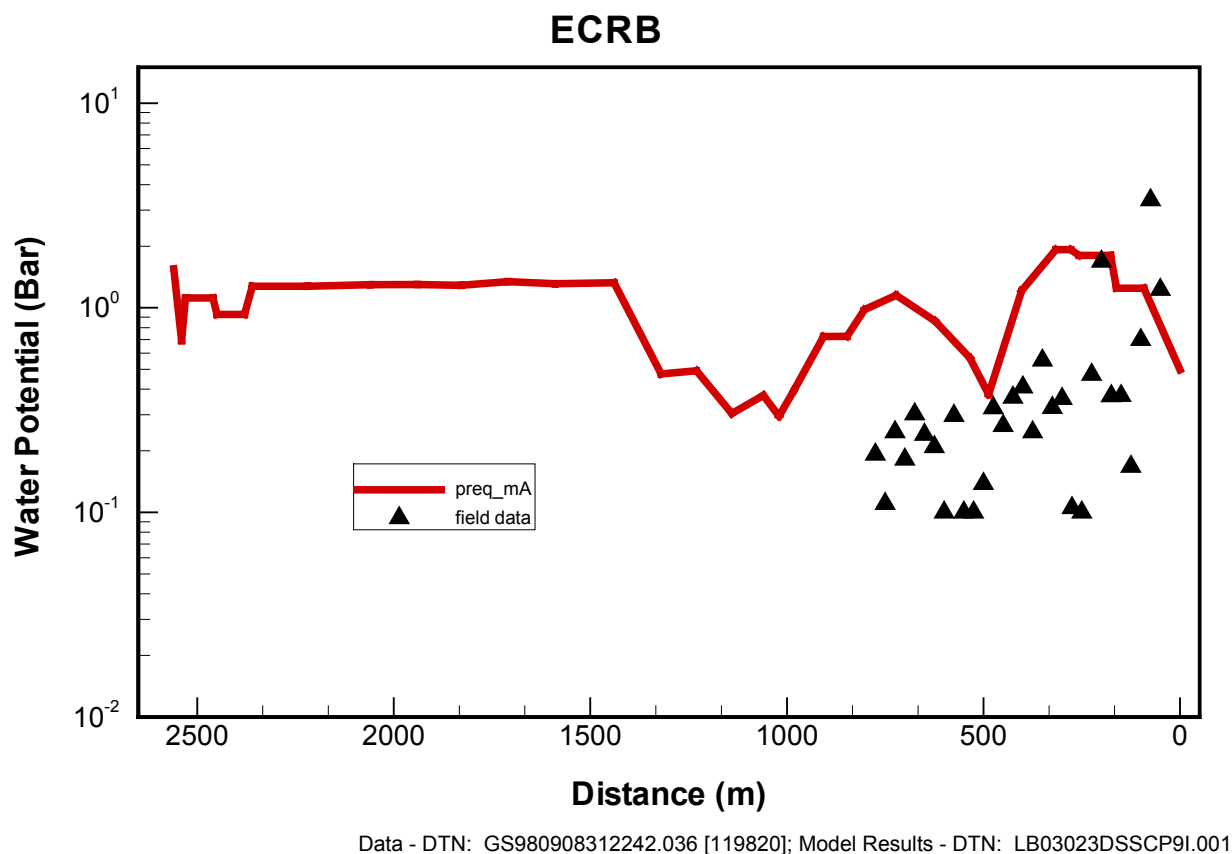


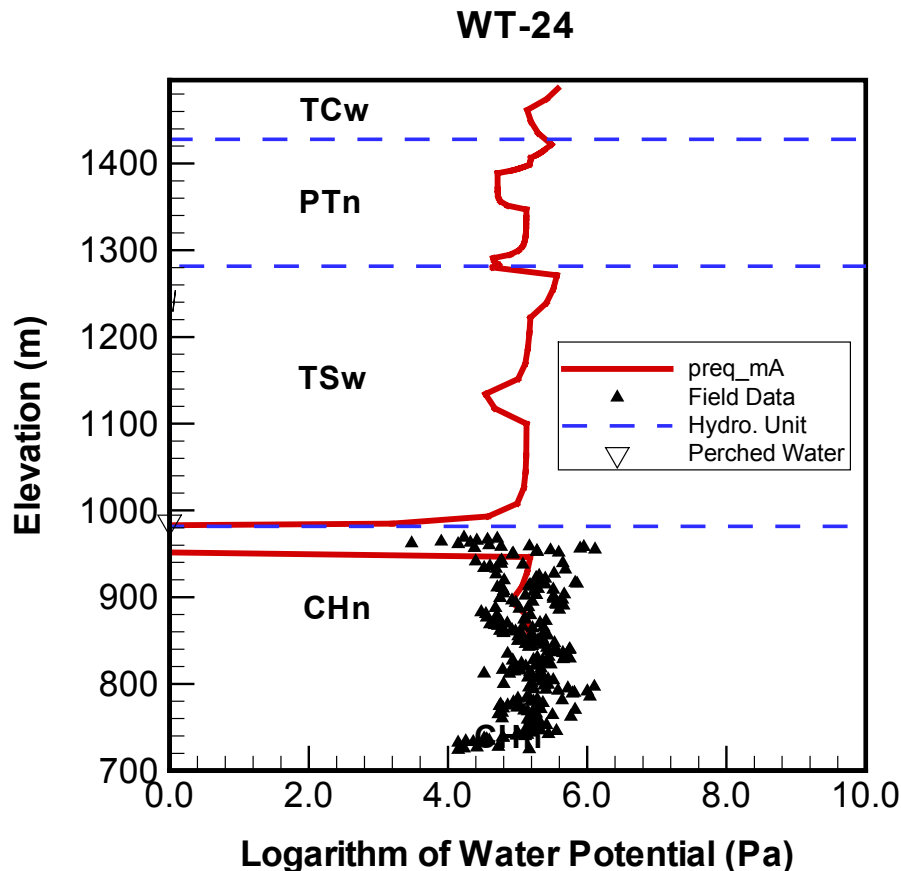
Figure 7.2-1. Comparison of Predicted and Measured Water Potential along ECRB Using the Present-Day, Mean Infiltration Rates (preq_mA)

7.3 VALIDATION USING PERCHED-WATER DATA AT WT-24

The perched-water phenomena in the UZ at Yucca Mountain were investigated in a multiphase subsurface flow model (Wu et al. 1999 [117167]). In that paper, the simulation results were shown to agree with the observed perched water data, including water saturation, potential profile, and perched-water elevation. In this validation, we use the field-measured perched-water data at borehole WT-24. Borehole WT-24 was drilled in 1997 as part of the ECRB program (see Figure 6.1-1 for borehole locations). Observed saturation data were collected from the borehole (see Section 4-1 for DTNs), and perched water was detected within the basal vitrophyre of the TSw at an elevation of approximately 986.69 m (DTN: GS980508312313.001 [109746]). As part of the model validation process, modeled results were compared to the field-observation perched-water elevation to check the accuracy of the modeled predictions.

The model scenario (preq_mA, with Output-DTN: LB03023DSSCP9I.001) of the present-day, mean infiltration rate is used for the comparison. Figure 7.3-1 shows a comparison of simulated matrix water-potential results with field measurement data at borehole WT-24. The observed elevation of perched water is also shown in the figure. As indicated there, the field-measured data for potentials are limited to the deeper section of the borehole (mostly in the CHn unit). The UZ Model prediction closely matches the field measurements of both water potentials and perched water elevations. Note that a simulated perched water zone is indicated by zero water potential. It should be mentioned that the field-measured perched-water elevation is only

measured at one point, at the onset of a pumping test (DTN: GS980508312313.001 [109746]). During pumping, the perched-water table was lowered by 20.66 m (DTN: GS980508312313.001 [109746]). The actual perched-water zone thickness may be larger than this fluctuation of water levels. The value of 20.66 m is very close to the simulated perched water thickness of about 30 m, as shown in Figure 7.3-1. Examination of simulated and observed perched water elevations show a difference of 6.55 m. This satisfies the validation criterion of 10 m.



Field Water Potential Data - DTN: GS980708312242.010 [106752];
 Perched Water - DTN: GS980508312313.001 [109746];
 Model Results - DTN: LB03023DSSCP9I.001

Figure 7.3-1. Comparison of Predicted and Measured Matrix Water Potentials and Perched-Water Elevations at Borehole WT-24 Using the Present-Day Mean Infiltration Rate (peq_mA)

7.4 3-D PNEUMATIC MODEL PREDICTION

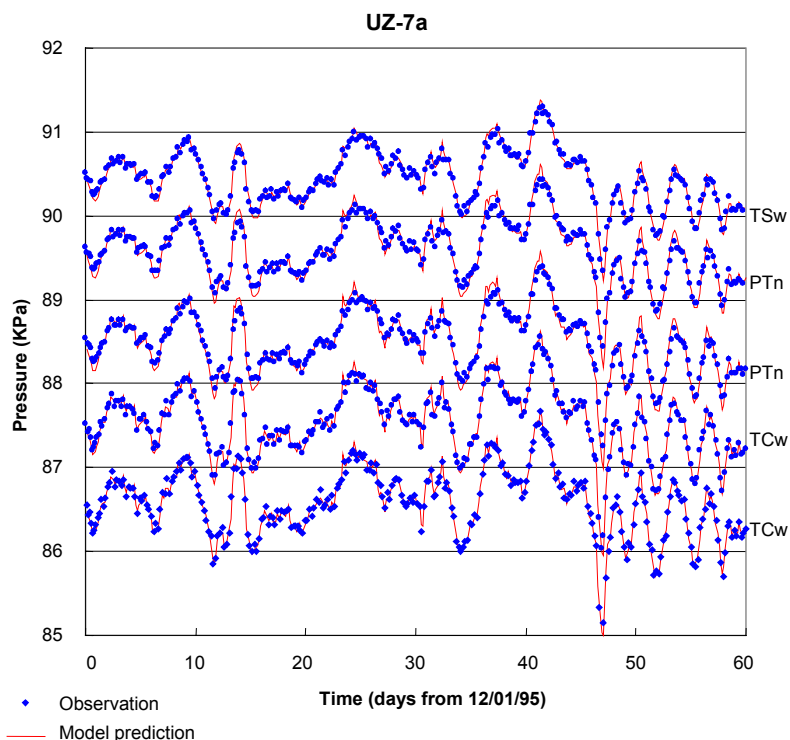
Subsurface gas-pressure variations have been used to determine the pneumatic diffusivity of important geological features. One-, two-, and three-dimensional numerical models have been used to simulate the observed subsurface pressure variations (Ahlers et al. 1999 [109715]). For this model validation, the same 3-D gas flow model is used as discussed in Section 6.4. Pneumatic data measured in SD-12 and UZ-7a boreholes are used for the model validation. The 60-day period of observation data from UZ-7a and the second 30-day period (immediately following the first 30 days of data used for calibration) from SD-12 are compared to the simulation predictions from the 3-D gas flow simulation results. The criterion for the validation is that simulated gas pressures and their pattern variations are consistent with the observed values. That is, the simulations will consistently reproduce increases and decreases resulting from changes in barometric pressure at the ground surface.

Table 7.4-1 lists the sensor locations, files for observation data, observation period, and corresponding model mesh cells for borehole UZ-7a (the information for borehole SD-12 is given in Table 6.4-1). Figures 7.4-1 and 7.4-2 show the comparisons of simulation results and field-measured values at these observation locations of the validation periods. UZ-7a is close to a fault; therefore it “sees” the surface signal quickly and with little attenuation (Figure 7.4-1). The signal to SD-12 at the TSw may be affected by attenuation through the PTn. Overall, both figures show good agreement between the predicted gas pressures and observed data. The good match in Figures 7.4-1 and 7.4-2 builds confidence that the base-case infiltration-scenario calibrated properties are appropriate for gas flow simulations. The comparisons between simulated and observed gas pressures at different locations of the two boreholes, shown in the two figures, prove that simulated gas pressures and their patterns of variations are consistent with observed values. In particular, the simulations consistently reproduce increases and decreases resulting from changes in barometric pressure at the ground surface. This satisfies the validation criterion for this case.

Table 7.4-1 Observation Sensors in Borehole USW UZ-7a

Sensor elevation (m)	File for observation data	Date range	Corresponding observation cells
1243.0	uz7a1343.prn	12/1/95-1/29/96	F002Bh74
1232.3	uz7a1337.prn	12/1/95-1/29/96	F0003h74
1221.6	uz7a1331.prn	12/1/95-1/29/96	F0007h74
1213.4	uz7a1325.prn	12/1/95-1/29/96	F0009h74
1177.8	uz7a1319.prn	12/1/95-1/29/96	F011Ah74

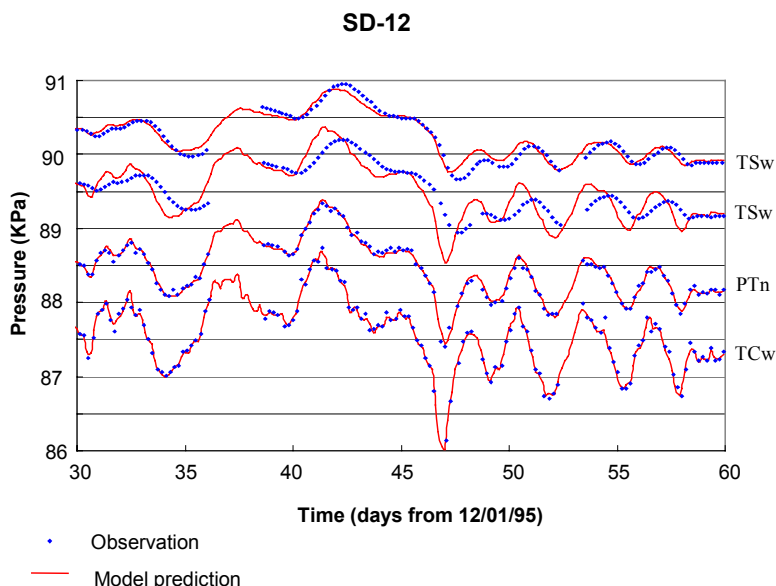
DTN: LB02092DSSCFPR.001 [162422]



Field Data—DTN: LB02092DSSCFPR.001 [162422]; Model Results—DTN: LB0303GASFLW3D.001

NOTE: Field data from DTN: LB02092DSSCFPR.001 [162422] are extracted from DTN: GS960308312232.001 [105573]. Both observations and simulations have been vertically offset for clearer display.

Figure 7.4-1. Comparison of 3-D Pneumatic Prediction to Observation Data from Borehole UZ-7a



Field Data—DTN: LB991091233129.001 [125868]; Model Results—DTN: LB0303GASFLW3D.001

NOTE: Field data from DTN: LB991091233129.001 [125868] are extracted from DTN: GS960308312232.001 [105573]. Both observations and simulations have been vertically offset for clearer display.

Figure 7.4-2. Comparison of 3-D Pneumatic Prediction to Observation Data from Borehole SD-12

7.5 MODEL VALIDATION WITH CARBON-14 DATA

The UZ of Yucca Mountain is a quasi-steady-state flow system, with very small infiltration and percolation rates. The matrix pore-water age corresponds to the mean time required for the groundwater to travel from the ground surface to where it is sampled in the system. The age can be considered constant at each location in this quasi-steady-state flow system, but spatially variable. The migration of water molecules is governed by advection and diffusion, similar to solute transport (Goode 1996 [162573]). Thus, tracer transport times (ages) can be simulated using a conservative transport model. The tracer travel time within the matrix (or matrix pore-water age) was defined as the time corresponding to a tracer concentration peak from an initial tracer pulse applied on the ground surface. If the simulated age well matches the available measured data (age), the transport model is validated.

In this validation effort, we estimate the groundwater age in the UZ, using a tracer transport model based on the calibrated groundwater flow field (Output-DTN: LB03023DSSCP9I.001). The simulated groundwater age is compared to available field-measured water age data (carbon-14).

Carbon-14 data were collected from perched water, pore water, and gas samples from the Yucca Mountain UZ (BSC 2002 [160247], Section 6.6.4). Pore-water carbon-14 data from various boreholes at Yucca Mountain were not representative of the pore-water residence time, because of the contamination by atmospheric $^{14}\text{CO}_2$ during drilling, which may result in apparently younger residence times (Yang 2002 [160839], Section 4.1.2; BSC 2002 [160247], Section 6.6.4.2). Carbon-14 data from gas samples are considered to be most representative of *in situ* conditions (Yang 2002 [160839], Section 4.1.2), because exchange of ^{14}C with the atmosphere was prevented since the borehole was closed. Carbon-14 is also considered as the most sensitive isotope measuring the groundwater age at the Yucca Mountain UZ, due to its half-life duration, which is in the same order of magnitude as the groundwater age in the UZ, and its detectable abundance. Gas samples were collected from different kinds of boreholes including open and instrumented surface-based boreholes. The data from the latter boreholes (USW SD-12 and USW UZ-1) are more reliable indicators of *in situ* matrix pore-water ages (BSC 2002 [160247], Section 6.6.4.3). Carbon-14 ages (BSC 2002 [160247], Table 20) calculated using the data from these two boreholes, are used for validating the UZ Model.

Gas-phase ^{14}C ages (DTN: GS961108312271.002 [121708] for borehole USW SD-12 and MO0012CARB1314.000 [153398] for borehole USW UZ-1) are interpreted to be representative of ages of the *in situ* pore water. The rationale for this interpretation is provided by Yang (2002 [160839], Section 4.1.2). This interpretation is based on the rapid exchange of gas-phase CO_2 (reaching equilibrium in hours to days) with dissolved CO_2 and HCO_3^- in pore water. Furthermore, the amount of carbon in an aqueous-phase reservoir is greater by orders of magnitude than carbon in the CO_2 gas-phase reservoir. Consequently, the aqueous phase will dominate the gaseous phase when exchange occurs, indicating the reasonableness of the interpretation (Yang 2002 [160839], Section 4.1.2). The continuous calcite precipitation in the unsaturated zone removes carbon from groundwater. Although ^{14}C behaves a little differently from total carbon, the effect on the carbon isotopic fraction is minor, and the calcite precipitation is considered to have an insignificant impact on the ^{14}C activity in the groundwater and gas (Codell and Murphy 1992 [100719]). Therefore, we chose the measured gas phase ^{14}C age to be

the representative age data for the matrix pore-water age of the Yucca Mountain UZ in the following model validation effort.

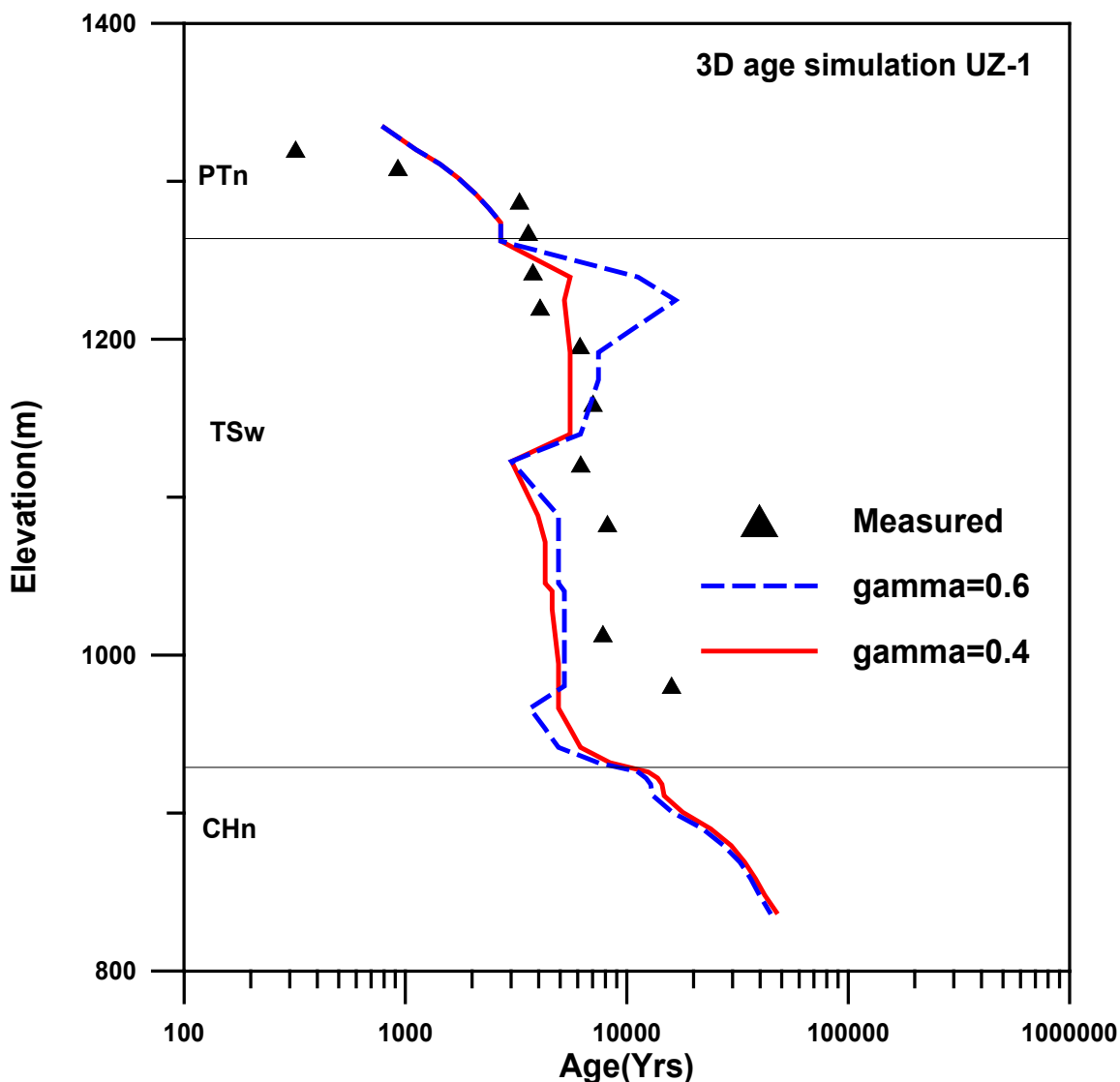
A 3-D transport model simulation was performed using T2R3D V1.4 (LBNL 1999 [146654]) decoupled version. The 3-D flow field obtained with the base-case water-flow simulation (present day mean infiltration, Output-DTN: LB03023DSSCP9I.001) is incorporated to simulate the matrix pore-water age in the entire model domain. The numerical grid used in this transport simulation is the same as that used in the base-case flow simulation (Figure 6.1-1). As discussed in Section 6.8, hydrodynamic dispersion was ignored because of low water percolation fluxes. Thus, the transport processes were being carried out by advective and diffusive solute fluxes. An effective-diffusion-coefficient value of $1.97 \times 10^{-10} \text{ m}^2/\text{s}$ was adopted, equal to the average value of measured coefficients for tritiated water through Yucca Mountain tuffs (DTN: LA000000000034.002 [148603]; BSC 2001 [160828], Table 16). We introduce a tracer source, as a pulse, on the ground surface through fractures and observe the tracer concentration in rock matrix in the entire domain. The simulated matrix pore-water age, at a specific location, is then identified as the time required for the tracer pulse (appeared as concentration peaks in the UZ) to travel to that location, and is determined from the concentration breakthrough. Then, we compare the simulated ages to the measured matrix pore water carbon-14 age. The simulated matrix pore-water age for boreholes UZ-1 and SD-12 were plotted and compared to available measured age data (^{14}C) (Figure 7.5-1 [UZ-1] and 7.5-2 [SD-12]).

Figure 7.5-1 (UZ-1) and Figure 7.5-2 (SD-12) show that the simulated matrix pore-water ages (curves identified by ' $\gamma = 0.6$ ' on the figures, with γ being the active-fracture-model parameter) in the upper portion of the TSw unit are larger than the measured ^{14}C ages. This is caused mainly by the underestimated advective and diffusive solute flux between fractures and matrix along these subunits. The smaller the flux or the slower the diffusion from fractures to matrix, the older the ages for matrix pore water. As analyzed in Section 6.8, advective and diffusive fluxes are both proportional to the effective interface area between fractures and matrix and, in turn, related to the larger γ values. The calibrated γ values, 0.6 for TSw32 and TSw33, 0.569 for TSw34–TSw38, were determined from inverse models of flow processes (DTN: LB0208UZDSCPMI.002 [161243]). When compared to transport analyses, sensitivity studies (BSC 2003 [161773], pp. 78–82) indicate that a more appropriate range of γ value for TSw32–TSw38 is between 0.2 and 0.4. A smaller γ corresponds to a larger effective fracture–matrix interface area, leading to larger advective or diffusive flux. Therefore, another simulation was performed using γ equal to 0.4 for TSw2 through TSw8. The simulated ages are also plotted in the same figures.

Figure 7.5-1 (UZ-1) shows that the simulated matrix pore-water ages for the upper TSw units with $\gamma = 0.4$ match the measured ^{14}C ages well. Simulated ages for lower TSw units are a little bit younger than the measurements, but still meet the criterion (the simulated ages for TSw unit are also within the range of measured ^{14}C age of TSw units, Section 7.1). Figure 7.5-2 (SD-12) shows that the match between the simulated groundwater ages using $\gamma = 0.4$ and the measurements is reasonably close, and the deviations meet the criterion (the simulated ages for TSw unit are within the range of the measured ^{14}C age of TSw units, Section 7.1).

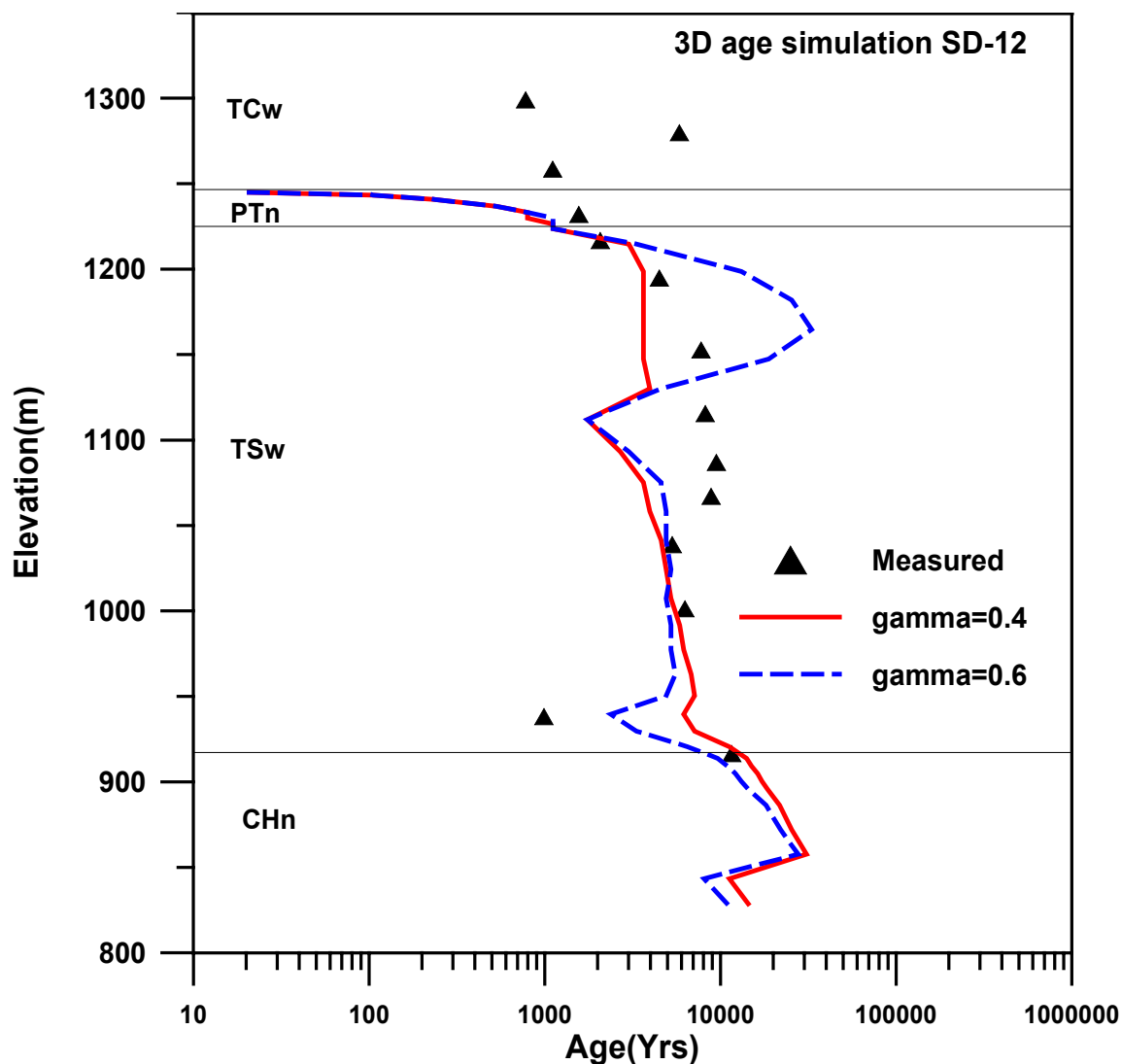
A larger gamma (0.6 for the TSw units) was used in the base-case UZ flow model. As demonstrated in Section 6.8 (which describes the sensitivity of UZ flow and transport processes

to the gamma factor), the larger gamma gives slightly earlier breakthrough times for solute transport from the repository to the water table, and therefore provides more conservative results. This is because a larger gamma factor corresponds to a larger fracture pore velocity and a smaller effective fracture-matrix interface area (or a smaller degree of fracture-matrix interaction).



Field Data—DTN: MO0012CARB1314.000 [153398] and converted to ages (Wang 2003 [162417], SN-LBNL-SCI-227-V1, p. 87);
Model Results—DTN: LB0303C14INF3D.001.

Figure 7.5-1. Simulated Groundwater Age for UZ-1 Borehole Compared to the Measured ^{14}C Age



Field Data—DTN: GS961108312271.002 [121708] and converted to ages (Wang 2003 [162417], SN-LBNL-SCI-227-V1, p. 87);
 Model Results—DTN: LB0303C14INF3D.001.

NOTE: Only one sample is plotted for each depth.

Figure 7.5-2. Simulated Groundwater Age for SD-12 Borehole Compared to the Measured ^{14}C Age

In summary, the comparison between simulated matrix pore-water age and observed ^{14}C ages indicates that with $\gamma = 0.4$ (for UZ Model layers tsw32–tsw38), the simulated tracer transport time can reasonably represent the measured ^{14}C ages of boreholes UZ-1 and SD-12. In addition, the simulated matrix pore-water age is sensitive to the active fracture parameter, γ .

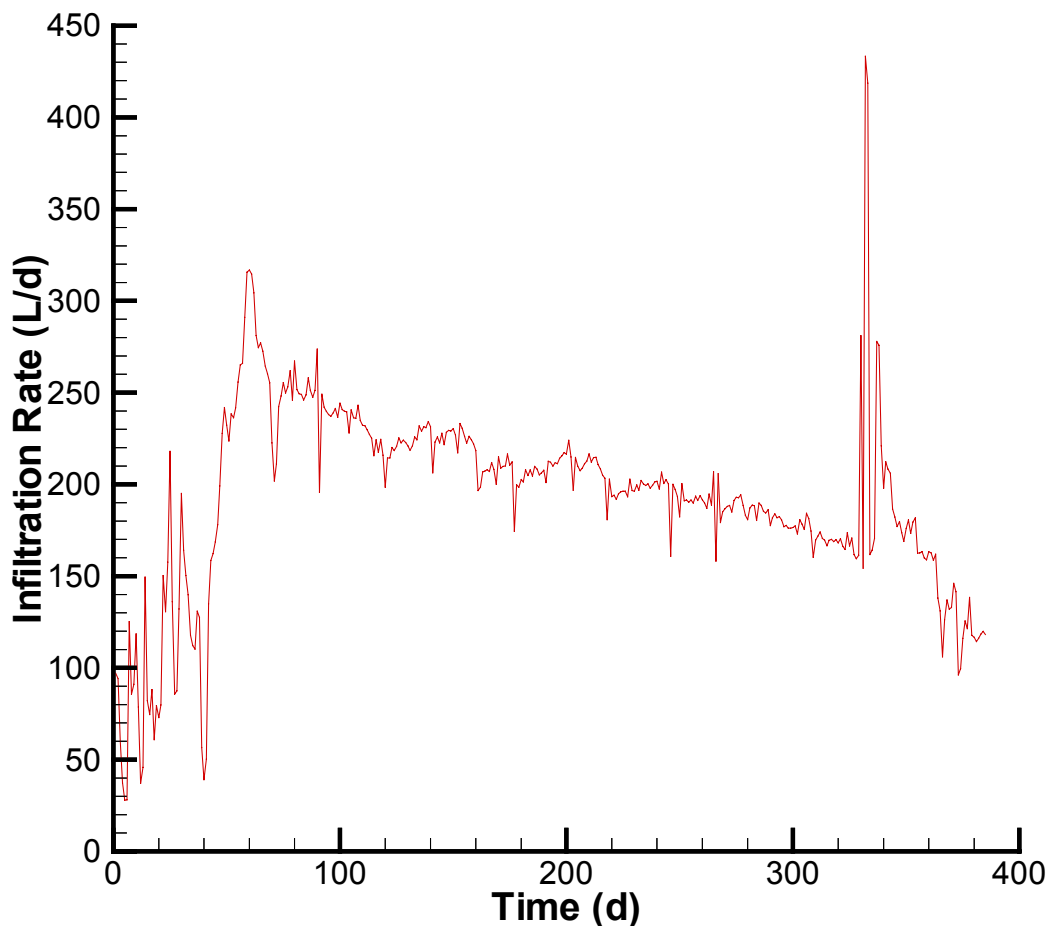
7.6 MODELING ANALYSIS OF ALCOVE 8/NICHE 3 FAULT TESTS

This section simulates *in situ* field tests of artificial infiltration along a fault at Alcove 8/Niche 3. The fault tests caused localized saturated conditions below the test spot, in an otherwise unsaturated zone. Under this field condition, test data are compared to results of simulations using the same conceptual model, methodology, and modeling approach as those used in the UZ Model. This modeling activity presents a different case of validation for the UZ Model. The results will build confidence in the UZ Model from a different perspective (in terms of different-scale model results and field conditions).

This modeling analysis uses both model calibration and prediction. Comparisons between simulated and observed data are useful for evaluating the validity of the methodology used in the UZ Flow Model for capturing UZ flow and transport processes. The criterion for validation is that the predicted results for the time required for a conservative tracer to reach a given concentration (e.g., peak concentration) are within a factor of five of the observed time. (BSC 2002 [160819], Section I-1-2-1). As demonstrated in Section 7.6.3.2 below (the discussion of modeling results), the criterion is met. This modeling activity is also documented in a Scientific Notebook by Wang (2003 [162417], SN-LBNL-SCI-215-V1, pp. 107–119). Note that the modeling analysis of Alcove 8/Niche 3 fault tests has been used to validate both UZ flow and UZ transport models (BSC 2002 [160819], Sections I-1-2-1 and I-2-1-2).

7.6.1 Field Observations

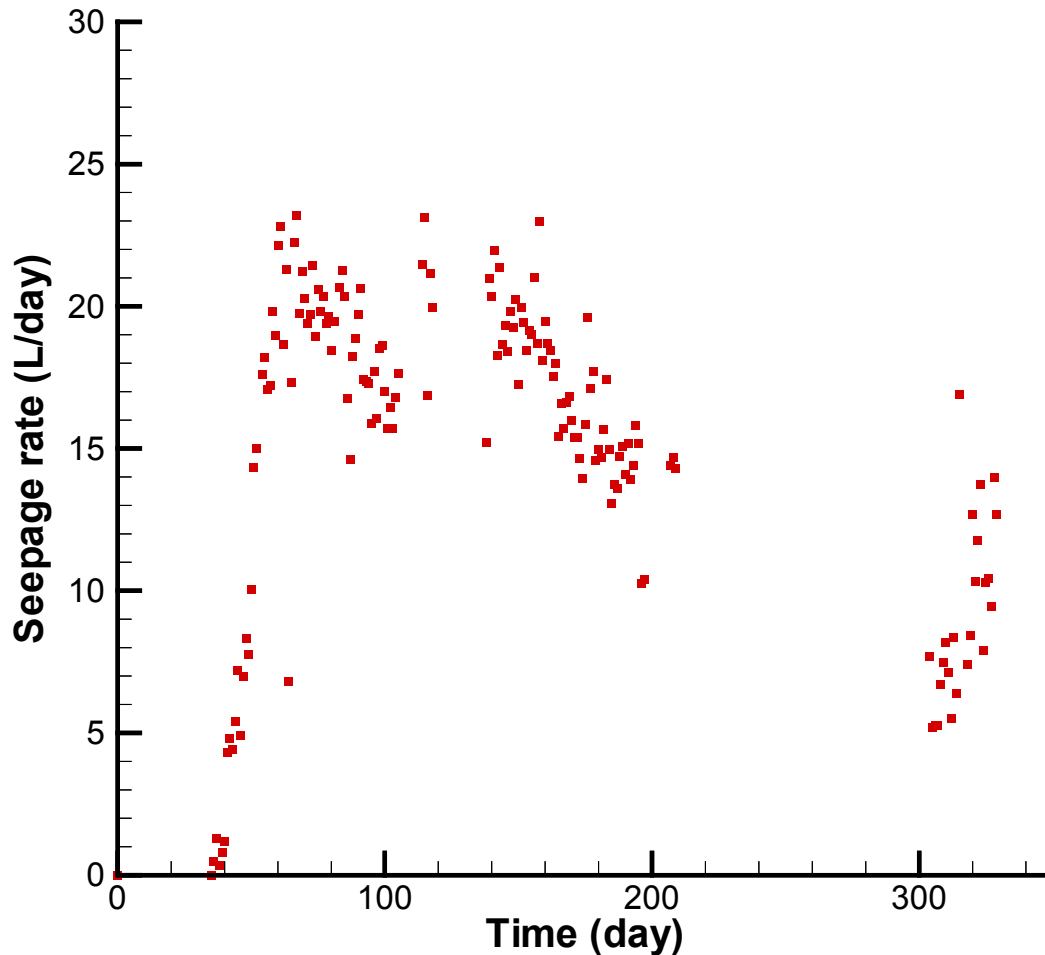
Infiltration rate, seepage rate, and tracer concentration data from the fault test are used to corroborate model simulations. The fault test used water and two liquid tracers. The test was carried out in the upper lithophysal and middle nonlithophysal subunits in the Yucca Mountain UZ. These geological subunits correspond to model layers tsw33 and tsw34, respectively, in the UZ Model. The tsw33 has some lithophysal cavities that may intersect fractures. Liquid water, first without and then with tracers, was released at the floor of an alcove along the fault (about 5 m long (DTN: GS020508312242.001 [162129])) within tsw33. Seepage from the fault into a niche and tracer concentrations of seeping liquid were monitored as functions of time. The niche is located within tsw34, about 20 m below the floor of the alcove; the interface between tsw33 and tsw34 is about 15 m below the floor of the alcove (DTN: LB0301N3SURDAT.001 [162130]).



Output DTN: LB0303A8N3MDLG.001 (File: inf_sum.dat)
Based on DTNS: GS020508312242.001 [162129] and GS020908312242.002 [162141].

Figure 7.6-1. Infiltration Rate as a Function of Time

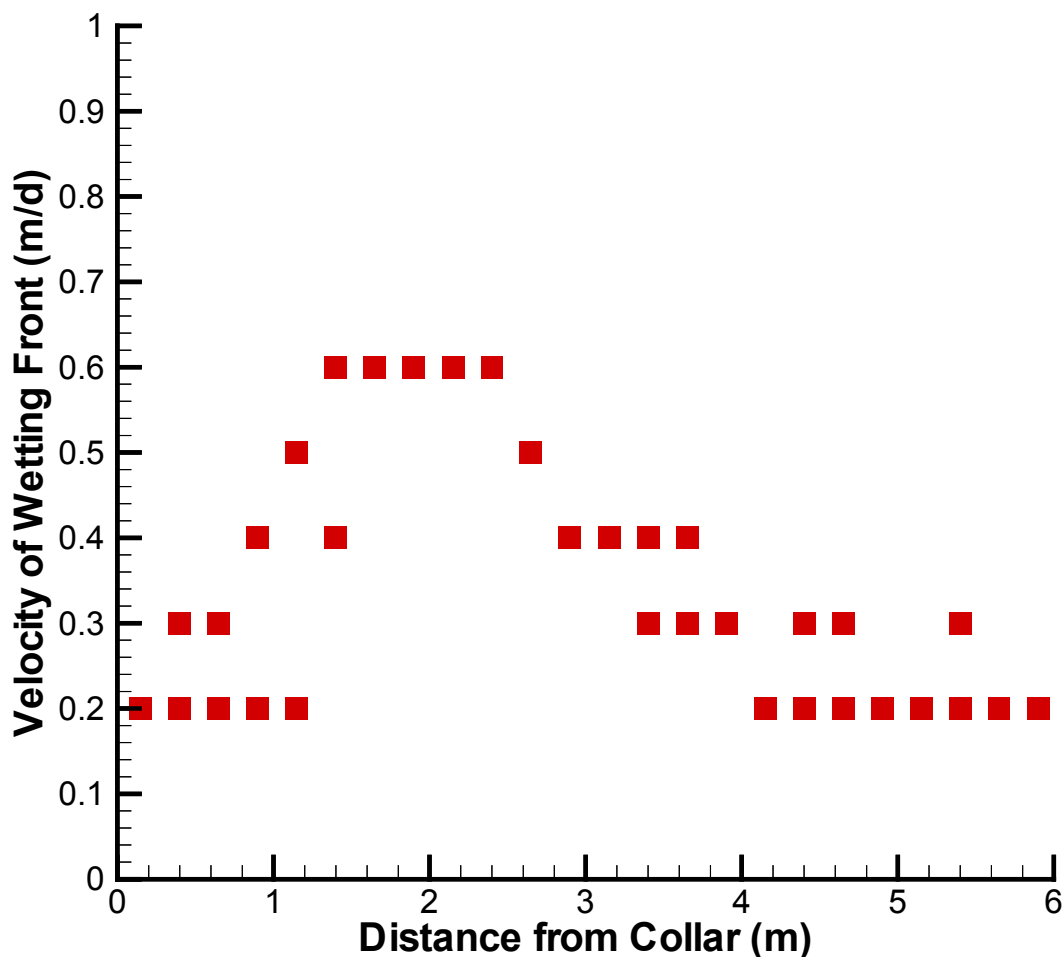
A pressure head of 2 cm was maintained at the infiltration plot along the fault at the alcove. The plot consists of four trenches that have different infiltration rates as a result of subsurface heterogeneity along the fault. Figure 7.6-1 shows the total infiltration rate as a function of time (DTNs: GS020508312242.001 [162129] and GS020908312242.002 [162141]; Wang 2003 [162417], SN-LBNL-SCI-215-V1, p. 107). For simplicity, our model considers the uniformly distributed infiltration rate along the infiltration plot to be consistent with the uniform property distribution in the UZ Model. One consideration in our modeling study is to evaluate approaches used in the site-scale model. Considerable temporal variability in the infiltration rate occurred during the test, as a result of infilled materials within the fault just below the infiltration plot (Figure 7.6-1). In other words, the effective permeability of the fault just below the plot changed with time. It is also expected that most portions of the fault and the surrounding fractures away from the plot would still be unsaturated, although pressure head at the plot was positive during the test. Based on these observations, total infiltration rate (instead of a pressure head of 2 cm) was used as the boundary condition in our model.



DTN: LB0303A8N3LIQR.001 [162570] (file: All_seepage.xls)

Figure 7.6-2. Total Seepage Rate as a Function of Time

Seepage from the fault into the niche was measured during the test, with a number of trays used to cover the areas where seepage might occur. Seepage was found to be highly spatially variable. The total seepage rate as a function of time is given in Figure 7.6-2 (DTN: LB0303A8N3LIQR.001 [162570]). Several boreholes were installed around the niche. Water arrival times at these boreholes were monitored by electrical resistivity (ER) probes. Figure 7.6-3 shows average water travel velocities determined from the arrival times from two boreholes just above the ceiling of the niche (DTN: LB0303A8N3LIQR.001 [162570]). The fault is about 2 m from the borehole collars in Figure 7.6-3 (DTN: LB0303A8N3LIQR.001 [162570]). Note that relatively uniform water-travel-velocity distribution within and near the fault was observed from these two boreholes.

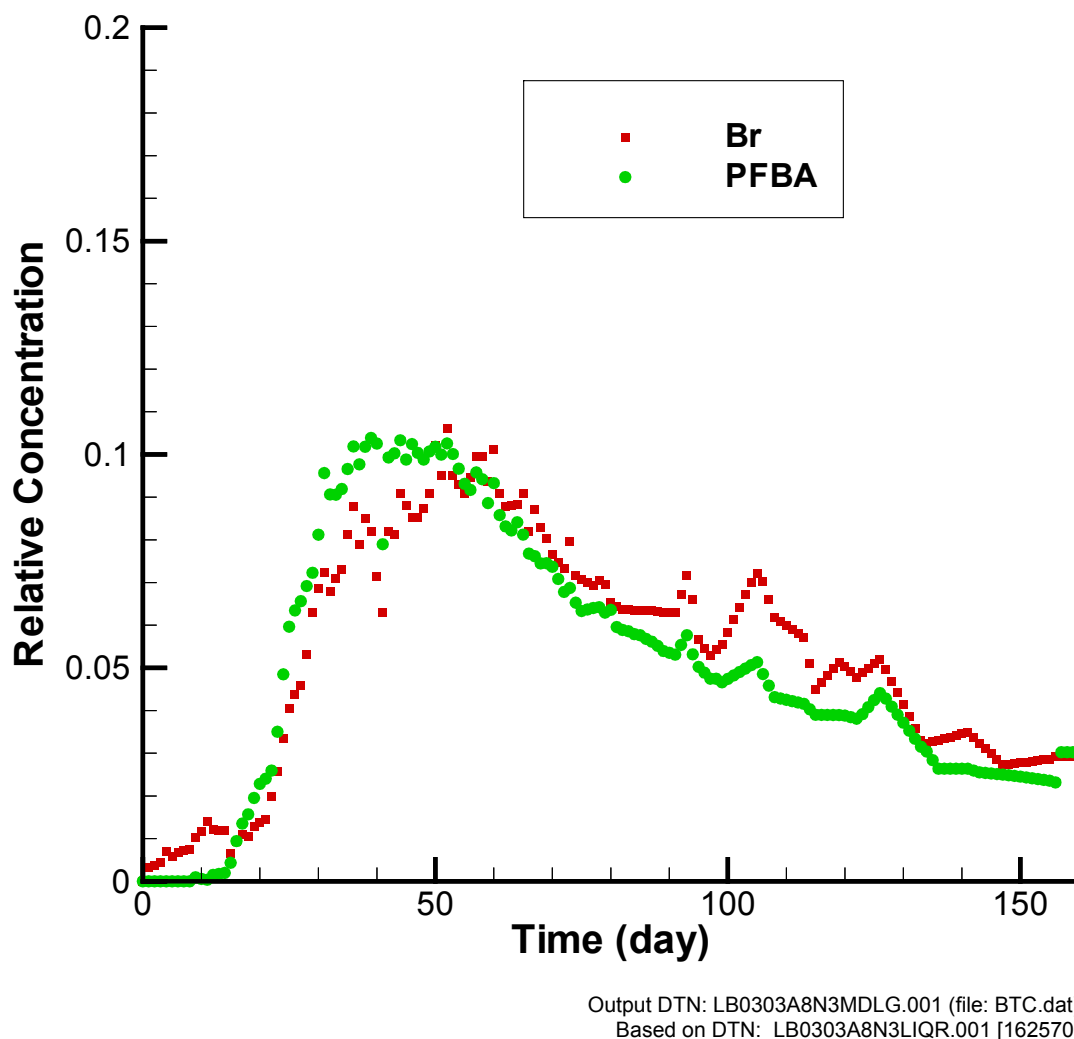


DTN: LB0303A8N3LIQR.001 [162570]

NOTE: Observation boreholes are approximately perpendicular to the fault. The distance from a borehole collar (called distance from collar) to the fault is about 2 m

Figure 7.6-3. Water Travel Velocity Data for Boreholes 9 and 10

After 209 days, two tracers with different molecular diffusion coefficients, Br and pentafluorobenzoic acid (PFBA) were introduced into infiltrating water at the infiltration plot. Tracer concentrations in three of the trays (at the niche) capturing seeping water from the fault were measured (DTN: LB0303A8N3LIQR.001 [162570]). Seepage rates corresponding to these three trays were not measured during the period of tracer concentration measurement. In this study, a flux-averaged breakthrough curve (concentration as a function of time) from these trays was used to represent the average breakthrough curve for all trays at the niche where seepage was captured (Wang 2003 [162417], SN-LBNL-SCI-215-V1, pp. 108–109). A constant flux value for each of the three trays was used for calculating the flux-averaged breakthrough curve shown in Figure 7.6-4. The constant flux values for the three trays were determined as the averaged value over 56 days before tracers were introduced. This flux-averaged breakthrough curve was compared with simulation results.



Source: Wang 2003 [162417], SN-LBNL-SCI-215-V1, pp. 108-109

Figure 7.6-4. Observed Flux-Average Breakthrough Curve

7.6.2 Numerical Model

A numerical model was developed for the fault test site to compare the simulation results with the relevant field observations. (The grid was generated with a software routine Smesh.f V1.0. (LBNL 2002 [162142]).) While comparison results will be presented below in Section 7.6.4, in this section, the focus is on schemes used for developing the numerical model.

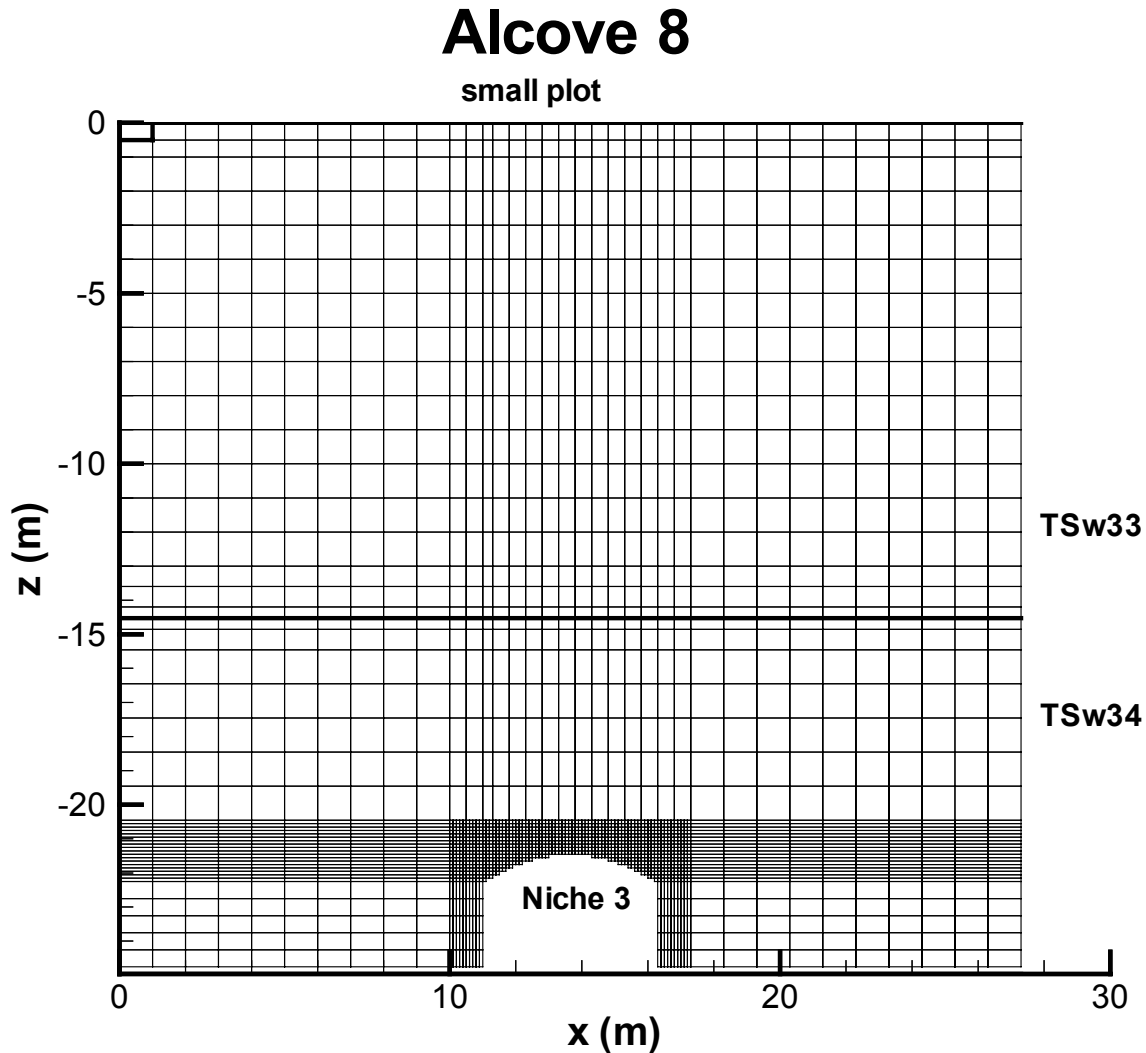


Figure 7.6-5. Cross Sectional Schematic of the 3-D Numerical Grid Used for Modeling Studies of Alcove 8/Niche 3

A three-dimensional numerical grid is constructed for simulating the fault test (Figure 7.6-5). The fault is represented as a vertical fracture, and surrounding fractured rock is approximated as a dual-continuum system (consisting of overlapped, interacting fracture and matrix continua). Global water flow and solute transport are allowed to occur in both continua. Figure 7.6-5 shows a cross section of the grid within the fault. The thickness of the grid in the direction perpendicular to fault walls is 3 m along each side of the fault. The fracture frequency used for generating the dual-continuum grid is 1.03 for tsw33 (determined from the fracture map at the alcove floor) and 1.72 for tsw34 (determined from the fracture map at the ceiling of the niche) (DTN: GS030108314224.001 [162131]; Wang 2003 [162417], SN-LBNL-SCI-215-V1, pp. 111–112). As shown in Figure 7.6-5, within a cross section of the grid along the fault, the grid spacing is 10 cm just above the ceiling of the niche, enabling the seepage process to be accurately simulated. The grid spacings in the direction perpendicular to the fault are 0.024 m, 0.168 m, 0.456 m, 0.756 m, and 1.44 m, respectively. The smallest spacing is adjacent to the fault, so that water imbibition and tracer diffusion into the fractured rock from the fault can be accurately captured. Cross sections in parallel to the fault walls have identical grid meshes

(Figure 7.6-5) for different distances from the fault. The niche is represented by an opening at the bottom of the grid (Figure 7.6-5), with the geometry of the opening determined from the survey data of the niche near the fault. Note that this is only an approximation of the geometry of the test site; a three-dimensional geometry of the niche with an underground tunnel connected to the niche are difficult to incorporate into the model. However, since our main concern is flow and transport processes within the fault, this geometric representation is adequate.

Temporally variable inflow rates are imposed on the top boundary, corresponding to the infiltration plot at the alcove floor (Figure 7.6-1). The side boundary corresponds to zero-flow conditions (in the direction perpendicular to the simulation domain). The niche wall boundary is modeled by a zero capillary-pressure condition, representing capillary barrier effects (Birkholzer et al. 1999 [105170]). The bottom boundary was assigned a constant matrix saturation of 0.85, which is consistent with field observations under ambient conditions (Flint 1998 [100033], p. 44, Table 7). Also based on field observations of Flint (1998 [100033], p. 44), matrix saturations are initially assigned to be 0.72 for tsw33 and 0.85 for tsw34. Other initial conditions for the rock mass within the model domain are that it is solute-free and has little water saturation ($1.05\text{E-}2$) in both the fractures and the fault. Rock properties used in model simulations are presented in Section 7.6.3.1.

Model calibration is performed using an inverse modeling code iTOUGH2 V4.0 (LBNL 1999 [139918]). The model calibration is defined herein as the adjustment of rock hydraulic parameters to make simulation results match the corresponding data. The goodness of match is measured using the standard least squares approach, which minimizes the sum of the squared residuals weighted by the inverse of variance of the data. T2R3D V1.4 (LBNL 1999 [146654]) is used for modeling tracer transport.

7.6.3 Model Simulations and Discussions

The numerical model was first calibrated against only the seepage and water-travel-velocity data to obtain the calibrated rock properties and the corresponding water flow field using iTOUGH2. Then, forward tracer transport simulations with different chemical transport parameters were carried out using T2R3D to evaluate the effects of matrix diffusion and other related processes on solute transport in the fault.

7.6.3.1 Calibration of Seepage-Rate Data and the Average Water-Travel-Velocity Data

Both fracture and matrix properties were assumed to be homogeneous within each geological subunit (tsw33 and tsw34). Fault properties were assumed to be the same for both units. This is based mainly on the following three considerations:

- (1) Consideration of the heterogeneity within each subunit would introduce a large number of rock properties that need to be determined by more data than was available from the test site.
- (2) These treatments have been used by the site-scale model of the Yucca Mountain UZ. It is of interest to examine how well this simple representation of subsurface heterogeneity can be used to model the fault test.

- (3) A study by Zhou et al. (2003 [162133]) implies that flow and transport in the Yucca Mountain UZ are mainly determined by large-scale heterogeneity, characterized by property differences between different geological units rather than by property variability within a geological unit.

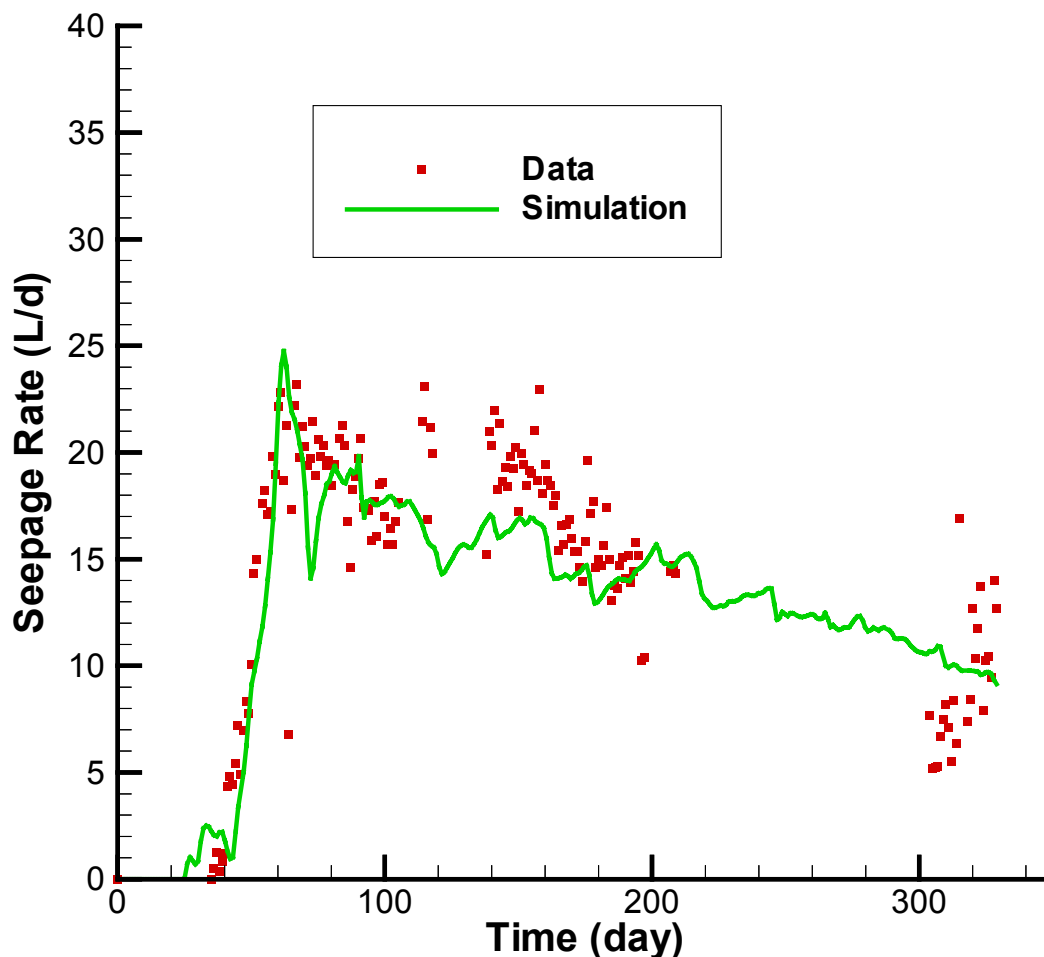
Rock hydraulic properties needed as inputs into the model include fracture and matrix permeabilities, fracture and matrix porosities, fault aperture and permeabilities, van Genuchten (1980 [100610]) parameters (for matrix, fractures, and the fault), and the parameter of the active fracture model, γ , for fractures (DTNs: LB997141233129.001 [104055]; LB980901233124.101 [136593]; LB990861233129.001 [110226]; and LB990501233129.001 [106787]; Wang 2003 [162417], SN-LBNL-SCI-215-V1, pp. 114–115). Because fracture van Genuchten parameters for tsw33 and tsw34 are similar (Table 7.6.1), a simple average of these parameters was used as the corresponding parameters for the fault (Wang 2003 [162417], SN-LBNL-SCI-215-V1, pp. 114–115). The averaged k/ϕ (where k is fracture permeability and ϕ is the corresponding fracture porosity) was calculated as fault permeability. Note that because there is no matrix in the fault in our model (or $\phi = 1$), the weighted k/ϕ (rather than weighted k) is employed for estimating fault permeability. The aperture of the fault was estimated as the average of fracture apertures of the two subunits. Note that the active fracture model was developed for fracture networks rather than for a single fracture. Consequently, the active fracture model does not apply to the fault here. In fact, most of the parameter values mentioned above and given in Table 7.6-1 are not site specific for the fault test site. These values were used as initial guesses for model calibration against the seepage rate and water-travel-velocity data observed from the fault test. To reduce the number of variables in model calibration (or inverse modeling), parameters expected to significantly affect simulated tracer travel time and seepage rate were varied in the calibration, while other parameters were kept unchanged. The varied parameters were fracture and fault permeabilities, fracture porosity, fault aperture, and fracture and fault van Genuchten α values.

Table 7.6-1. Uncalibrated Rock Properties

Rock property	Fault ^e	tsw33		tsw34	
		Fracture	Matrix	Fracture	Matrix
Permeability (m ²)	4.34E-11	5.5E-13 ^c	3.08E-17 ^a	0.35E-13 ^e	4.07E-18 ^a
Porosity	1.00	6.6E-3 ^d	0.154 ^a	1.E-2 ^d	0.11 ^a
Fracture frequency (m ⁻¹)		1.03 ^e		1.5 ^e	
Fracture aperture (m)	1.12E-3	1.49E-3 ^e		1.14E-3 ^e	
Active fracture model parameter γ	0.0	0.41 ^a		0.41 ^a	
van Genuchten α (Pa ⁻¹)	1.0E-3	1.46E-3 ^a	2.13E-5 ^a	5.16E-4 ^a	3.86E-6 ^a
van Genuchten m	0.608	0.608 ^a	0.298 ^a	0.608 ^a	0.291 ^a

^a DTN:LB997141233129.001 [104055],^b DTN: LB980901233124.101 [136593],^c DTN: LB990861233129.001 [110226]^d DTN: LB990501233129.001 [106787]^eWang (2003 [162417], SN-LBNL-SCI-215-V1, pp. 114-115)

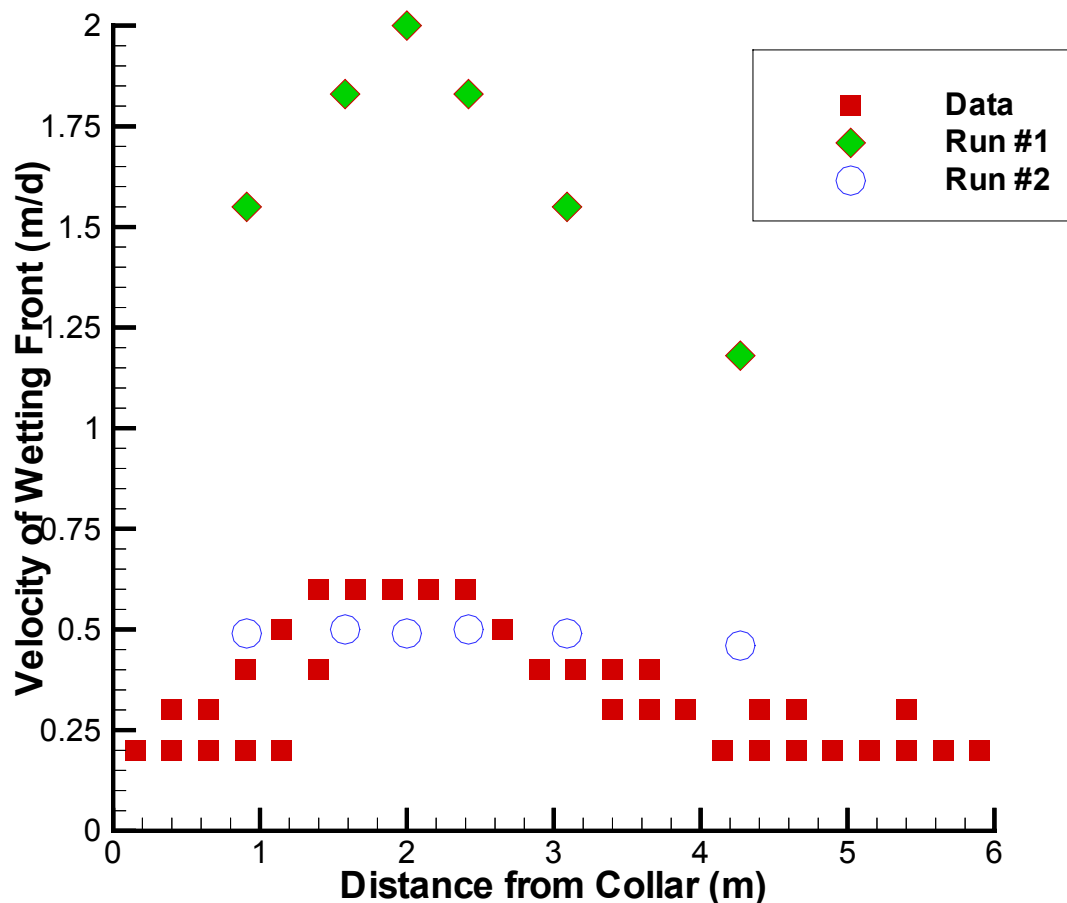
Infiltration-seepage processes in the fault and the surrounding fractured rock were determined by several mechanisms. Liquid water applied at the alcove floor (Figure 7.6-5) flowed first into the fault and then into fractured networks connected to the fault. Matrix imbibition occurred at interfaces between fractures and the matrix and between the fault and the matrix. When water arrived at the intersection between the fault and the niche, it might not immediately seep into the niche until the capillary pressure became zero because of capillary barrier effects (Philip et al. 1989 [105743]; Birkholzer et al. 1999 [105170]). Such effects can divert flow away from the opening, resulting in only a portion of the water arriving at the niche ceiling actually seeping into the niche. Tracer travel time was determined by fracture porosity, fault aperture, and the matrix imbibition process.



Field Data—DTN: LB0303A8N3LIQR.001 [162570] (file: All_seepage.dat);
 Model Results—DTN: LB0303A8N3MDLG.001 (file: lrun1i.tec)

Figure 7.6-6. A Comparison between Simulated Seepage Rates as a Function of Time (Run #1) and Field Observations

Figure 7.6-6 shows a comparison between seepage-rate data and the simulation result from a model calibration (Run #1) without considering the water-travel-velocity data. In this calibration run, fracture porosity and fault aperture were not varied. A fairly good match to the observed seepage data was obtained (Figure 7.6-6); however, water travel velocity is significantly overestimated (Figure 7.6-7). Water travel velocities were calculated from water arrival times at locations about 1 m above the middle of the opening in Figure 7.6-5 (Wang 2003 [162417], SN-LBNL-SCI-215-V1, pp. 116–119). The travel time was defined as the time when fault or fracture saturation was increased from the initial value of $1.05\text{E-}2$ to $1.06\text{E-}2$. This comparison implies that seepage rate as a function of time may be mainly controlled by rock properties near seepage locations (influence zone of capillary barrier, Liu et al. 2002 [160230], Section 3.3). On the other hand, water travel velocities are determined by rock properties from the infiltration plot to the locations where water travel velocities are monitored. Table 7.6-2 gives the calibrated properties obtained from Run #1.



Field Data—DTN: LB0303A8N3LIQR.001 [162570];
 Model Results—DTN: LB0303A8N3MDLG.001 (files: WV_Irun1Ni.tec; WV_Irun4Ni.tec)

Figure 7.6-7. A Comparison among Calculated Water Travel Velocities from Two Calibration Runs and the Velocity Data Observed from the Fault Test

Table 7.6.2. Rock Properties Calibrated from Seepage Rate Data (Run #1)

Rock property	Fault	tsw33	tsw34
Fracture Permeability (m^2)	6.67E-11	8.93E-13	3.16E-14
Fracture van Genuchten α (Pa^{-1})	1.15E-3	1.67E-3	4.59E-4

Source: Output-DTN: LB0303A8N3MDLG.001 (file: lrun1i.par)

NOTE: All other rock properties are the same as those in Table 7.6.1. Rock names "tswF3", "NetF3" and "NetF4" in file lrun1i.par correspond to "Fault", "tsw33" and "tsw34", respectively, in this table.

The overestimation of the water travel velocities may result from the following: (1) some cavities in tsw33 are connected to fractures and might contribute to increasing the storage in the fracture continuum; (2) in reality, the fault is a zone rather than a single fracture. The effective

aperture from this zone may be much larger than the assumed aperture value for the fault (Table 7.6-1). Neither of these factors was considered in Run #1 (first calibration). Taking these factors into consideration, the new calibration (Run #2) allowed both fault aperture and fracture porosity in tsw33 to be varied. The resultant values are 3 cm for fault aperture and 0.066 for fracture porosity of tsw33 (Table 7.6-3). While the actual width of the fault zone is unknown, the estimated equivalent fault aperture (3 cm) is considered to be acceptable. The estimated fracture porosity is consistent with those estimated from water release tests performed in the same geological unit (BSC 2001 [158463], Section 6.11.3.2).

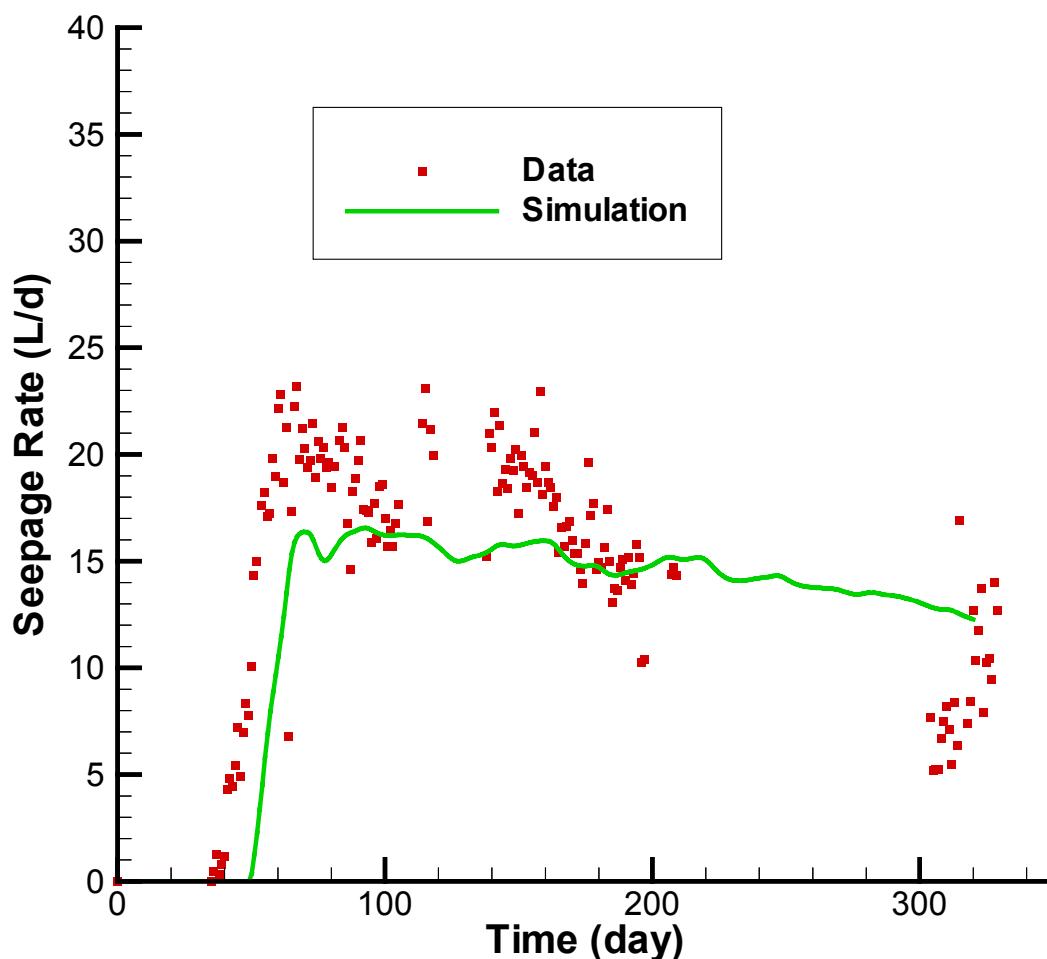
Table 7.6.3. Rock Properties Calibrated from Both Seepage Rate and Water Travel Velocity Data (Run #2)

Rock property	Fault	tsw33	tsw34
Fracture Permeability (m ²)	1.12E-10	1.23E-12	5.01E-13
Fracture Porosity		0.066	
Fracture aperture (m)	0.03		
Fracture van Genuchten α (Pa ⁻¹)	1.24E-3	2.19E-3	1.09E-3

Source: Output-DTN: LB0303A8N3MDLG.001 (file lrun4Ni.par)

NOTE: All other rock properties are the same as those in Table 7.6.1. . Rock names "tswF3", "NetF3" and "NetF4" in file lrun1i.par correspond to "Fault", "tsw33" and "tsw34", respectively, in this table.

Figure 7.6-7 shows a comparison among calculated water travel velocities from two calibration runs and the velocity data observed from the fault test. The simulated water travel velocities from Run #2 are much closer to the observed data than those from Run #1 (especially near the fault). However, the water travel velocities away from the fault are still overestimated. One possible explanation is that matrix imbibition from fractures above the niche were underestimated because the dual-continuum approach considerably underestimates the pressure gradient near a fracture matrix interface during transient flow conditions (Pruess and Narasimhan 1985 [101707]). While this problem can be resolved with the multiple interacting continua model of Pruess and Narasimhan (1985 [101707]), the computational intensity of the inverse model problem under consideration would be significantly increased. Note that a model calibration involves a great number of forward simulation runs. Considering that (1) the transient flow effects would be considerably reduced later in the test and that (2) our focus here is on flow and transport within and near faults, simulated flow field and calibrated rock properties from Run #2 were used for simulating tracer transport at the test site. Figure 7.6-8 also shows a comparison between simulated seepage rates as a function of time (Run #2) and field observations. The match is reasonable. Figure 7.6-8 matches both wetting-front velocity and seepage-rate, and it is therefore, considered a better calibration than Figure 7.6-6, which only matches the seepage rate data. Note that to give a reasonable prediction of solute transport, the water flow must be correctly modeled.



Field Data-DTN: LB0303A8N3LIQR.001 [162570] (file: All_seepage.dat);
 Model Results -DTN: LB0303A8N3MDLG.001 (file: lrun4Ni.tec)

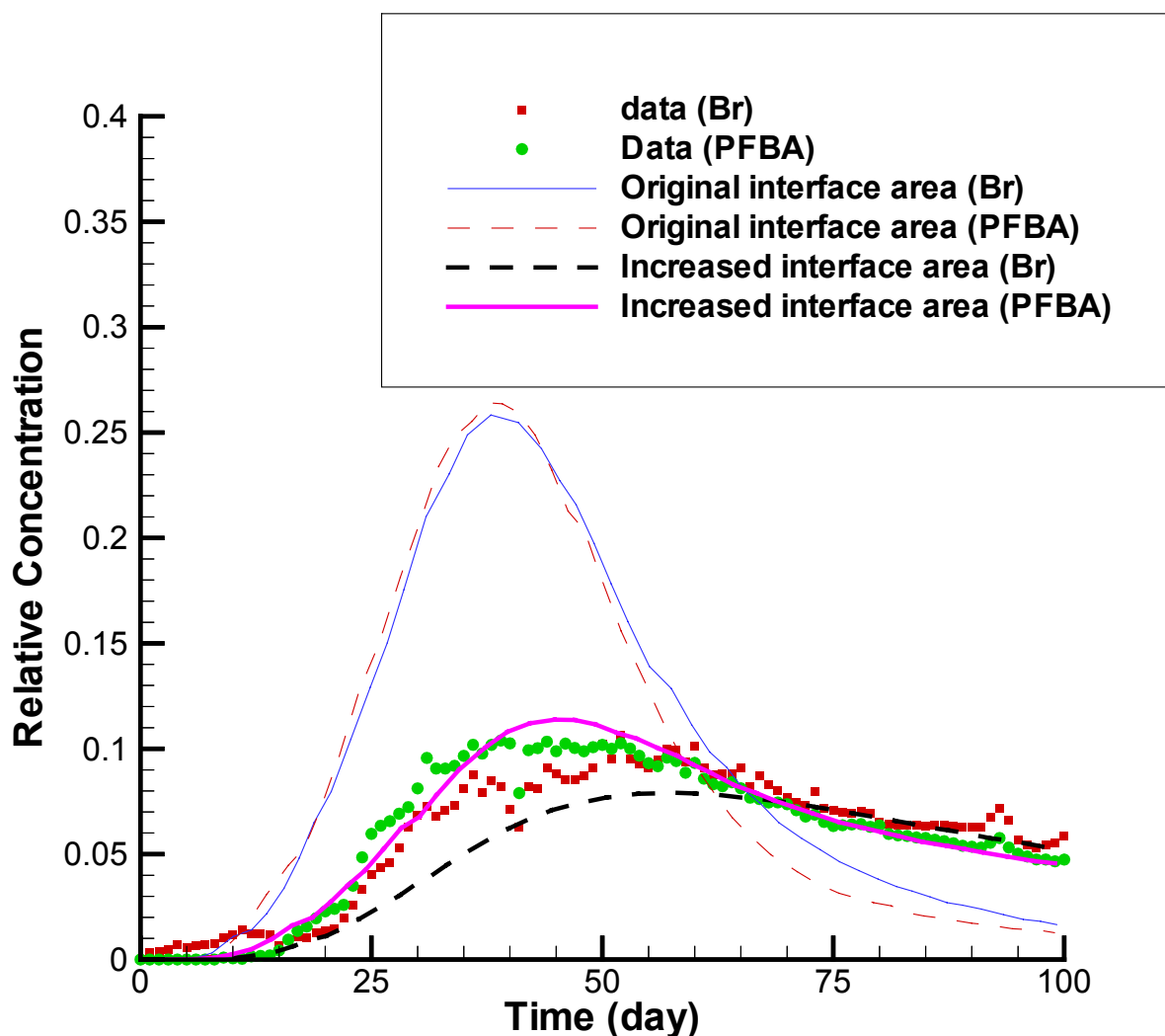
Figure 7.6-8. A Comparison between Simulated Seepage Rates as a Function of Time (Run #2) and Field Observations

7.6.3.2 Effects of Matrix Diffusion

Tracer transport within the fault is controlled by several processes, including advection, diffusion into the matrix blocks (matrix diffusion), mass exchange between the fault and the surrounding fracture networks, and dispersion. Our special attention in this study is given to evaluating the relative importance of matrix diffusion. To do so, we used the flow field obtained from calibration Run #2 to simulate tracer transport processes and compare simulation results with field observations (Figure 7.6-4). The breakthrough curve is obtained from the output of T2R3D V1.4 (LBNL 1999 [146654]) using a software routine Bkread.f V1.0 (LBNL 2002 [162143]).

Two conservative tracers with different molecular diffusion coefficients ($2.08 \text{ E-}9 \text{ m}^2/\text{s}$ for Br (Lide 2002 [160832]) and $7.60\text{E-}10 \text{ m}^2/\text{s}$ for PFBA (Benson and Bowman 1996 [153427])) were used in the fault test. Based on analyses of the relevant diffusion experiment results, Moridis et al. (2003 [161902], Table 1) reported that the tortuosity factor for the tuff matrix can be approximated by the corresponding matrix porosity. Therefore, the average matrix porosity for tsw33 and tsw34 (0.13) was used as the tortuosity factor. The effective diffusion coefficient for

the matrix diffusion process is the product of the molecular diffusion coefficient and tortuosity factor.



Model Results-DTN: LB0303A8N3MDLG.001 (files: BTC.dat; BTC_odis.dat)

Figure 7.6-9. Comparisons between Simulated Breakthrough Curves at the Niche for Two Different Fault-Matrix Interface Areas and the Observed Data

Figure 7.6-9 shows comparisons between simulated breakthrough curves at the niche for two different fault-matrix interface areas and the observed data. One simulation corresponds to an interface area defined in the original numerical grid, which considers the fault as a fracture with two vertical walls. The criterion for validation is that the predicted results for the time required for a conservative tracer to reach a given concentration (e.g., peak concentration) are within a factor of five of the observed time (BSC 2002 [160819], Section I-1-2-1). Note that this criterion is met (Figure 7.6-9). The other simulation corresponds to an interface area increased by 45 times over that in the first simulation. In these two simulations, the dispersivity is assumed to be zero. (The relative importance of the dispersion will be discussed later.) Since the diffusive flux from the fault to the matrix is proportional to the product of the tortuosity factor and the fault-

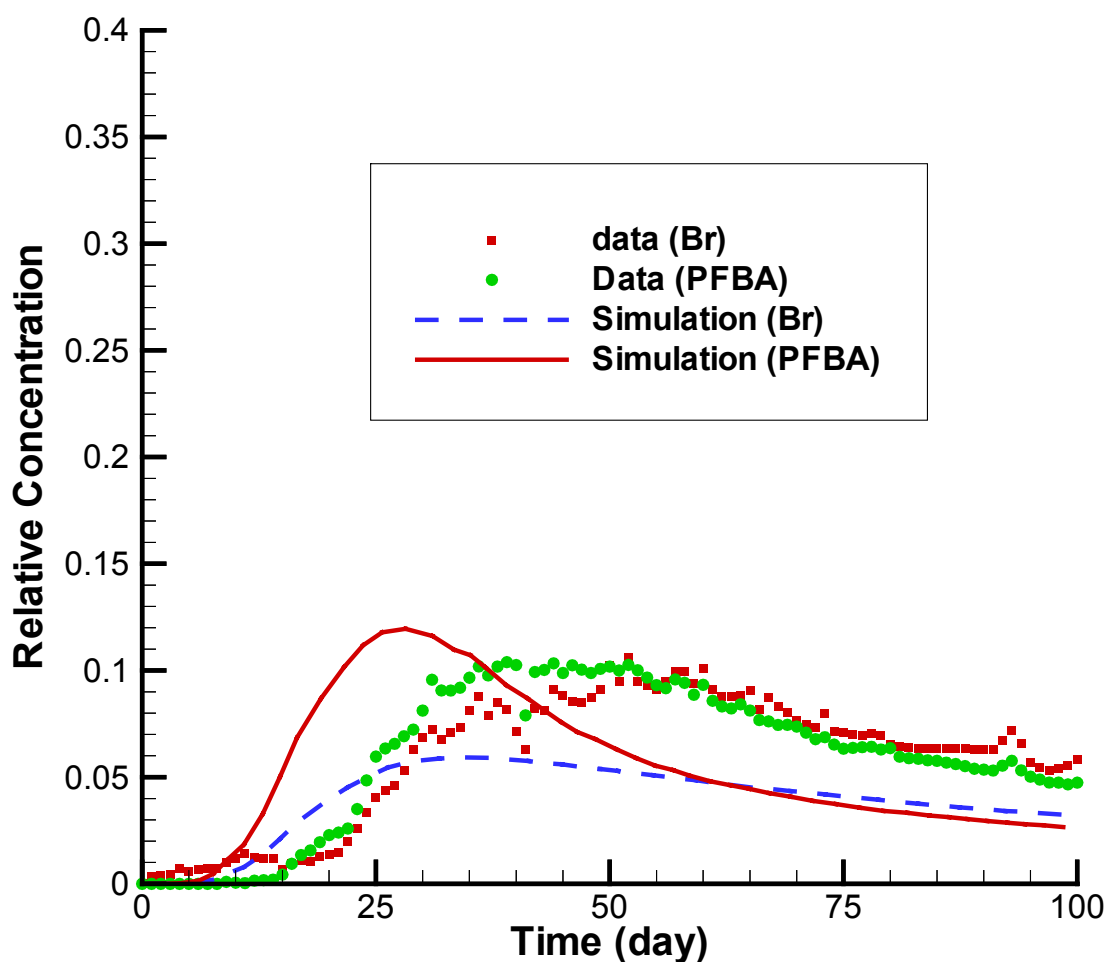
matrix interface area, changes in the interface area for a given tortuosity factor are equivalent to changes in tortuosity factor for a given interface area. For simplicity, the tortuosity factor value was changed in actual simulations, but the numerical grid (defining the interface area) was kept unchanged. Note that changes in the interface area do not significantly alter the flow field during the period of the tracer test. Tracers were introduced into infiltrating water at about 200 days after infiltration started, resulting in the matrix near the fault being almost saturated during the tracer test and the matrix imbibition being insignificant. As shown in Figure 7.6-9, the simulated breakthrough curve with the original interface area is very different from the observed data. It exhibits much larger concentration peak values and much earlier arrival times for these peaks. The observed data are favorably matched by the simulated result with increased interface area, indicating that matrix diffusion significantly affects the overall solute transport behavior and is underestimated by the simulation using the original interface area.

The need to increase interface areas between fractures (or faults) and the matrix in matching the field observations of tracer transport in fractured rock has been recently reported by several researchers. Shapiro (2001 [162132]) interpreted concentration measurements for tritium and dichlorodifluoromethane collected from a glacial drift and fractured crystalline rock over 4 km² in central New Hampshire. He found that the effective diffusion coefficient at the kilometer scale is at least three orders of magnitude greater than laboratory estimates of diffusion in crystalline rock. Neretnieks (2002 [162140]) presented comparisons between several analytical solutions and tracer test results at the Äspö site and reported a need for a factor 30–50 times larger for the fracture-matrix interface area than expected. He also indicated that nine other research groups reached a similar conclusion in their interpretation of the same test data set. Our results in this study are consistent with these previous findings.

Several mechanisms regarding the increase in the interface area have been reported in the literature. They include (1) advective mass exchanges from high-permeability fractures to low-permeability fractures (Shapiro 2001 [162132], Section 7), (2) diffusion into stagnant water zones (Neretnieks 2002 [162140]), and (3) enhanced fracture-matrix interface areas for fractures with small-trace lengths that do not contribute to global flow and are not considered in the survey data (and therefore not included in the numerical grid). In addition to these potential mechanisms, two other factors also contribute to the increase in the interface area. First, in the relevant analytical and numerical solutions to tracer transport, fracture walls are generally assumed to be flat. However, it is now well known that fracture walls are rough and characterized by fractal geometry (National Research Council 1996 [139151], pp. 105–111). Consequently, the actual interface areas between fractures (and faults) and the matrix are larger than what are calculated using flat fracture walls. Second, a fault zone may include a great number of crushed matrix blocks that have smaller sizes than the fracture spacing in a nonfault zone. These crushed matrix blocks can make a significant contribution to the matrix diffusion within the fault, but are not considered in our numerical grid, where the fault is simply treated as a vertical fracture. To compensate for the effects of these mechanisms mentioned above, an increase in fault-matrix interface areas is obviously needed.

Although simulation results with the increased interface area reasonably match the observed data (Figure 7.6-9), the concentration difference at a given time for the two tracers is generally overestimated by the model. One plausible explanation is that the crushed matrix blocks within the fault zone have much smaller sizes than the fracture spacing. This, however, is not considered in our model, in which the matrix block size is characterized by fracture spacing. The

smaller sizes correspond to the shorter times needed by the equilibrating tracer concentration at the center and outer surface of a matrix block, reducing the difference between the effects of matrix diffusion on overall solute transport behavior for different molecular-diffusion coefficients. This can be further illustrated by an extreme case: an infinitely small block size within the fault and without mass exchange between the fault and nonfault fractured rock. In this case, the concentrations of the matrix block within the fault can be equilibrated simultaneously with those at the outer surface of the block for two tracers with different molecular diffusion coefficients. Consequently, although the existence of this kind of matrix block can still significantly retard tracer transport within the fault, identical breakthrough curves may be observed at Niche 3 for the two tracers. This issue was not further explored in the current modeling study because the matrix block size distribution within the fault cannot be independently estimated or observed.



Model Results—DTN: LB0303A8N3MDLG.001 (files: BTC.dat; BTC_dis.dat)

Figure 7.6-10. Comparisons between Simulated Breakthrough Curves (Considering Dispersion) at the Niche for the Increased Fault-Matrix Interface Areas and the Observed Data

Compared with matrix diffusion, the macrodispersion process is not considered to be significant within the fault for this particular test. Field measurements indicate that water travel-velocity distribution is quite uniform within and near the fault (Figure 7.6-3), whereas macrodispersion results from variability in water velocity. These experimental observations are consistent with

the findings from our model analyses: the observed data were very difficult to match when a considerable degree of dispersion was included in the model. For example, Figure 7.6-10 shows simulated breakthrough curves with a longitudinal dispersivity value of 1 m and a transverse dispersivity value of 0.1 m (and with the increased fault-matrix interface area), compared to results in Figure 7.6-9 (without considering dispersion). Larger dispersivity values generally correspond to earlier arrival times of peak concentrations and to a larger difference between these peak concentrations for the two different tracers.

7.6.3.3 Implication for Radionuclide Transport in the Yucca Mountain UZ

Matrix diffusion has been identified as a key mechanism for retarding radionuclide transport in both unsaturated and saturated fractured rock (e.g., Bodvarsson et al. 2001 [160133]; Neretnieks 2002 [162140]). The enhancement of the fracture (fault)–matrix interface area (or effective matrix diffusion coefficient) seems to be common for matching field-scale solute transport observations, as suggested by this study and previous studies (Shapiro 2001 [162132]; Neretnieks 2002 [162140]). The current site-scale model for the Yucca Mountain UZ does not include the effects of this enhancement. Consequently, the estimated performance of the repository, estimated based on the site-scale model, may be conservative.

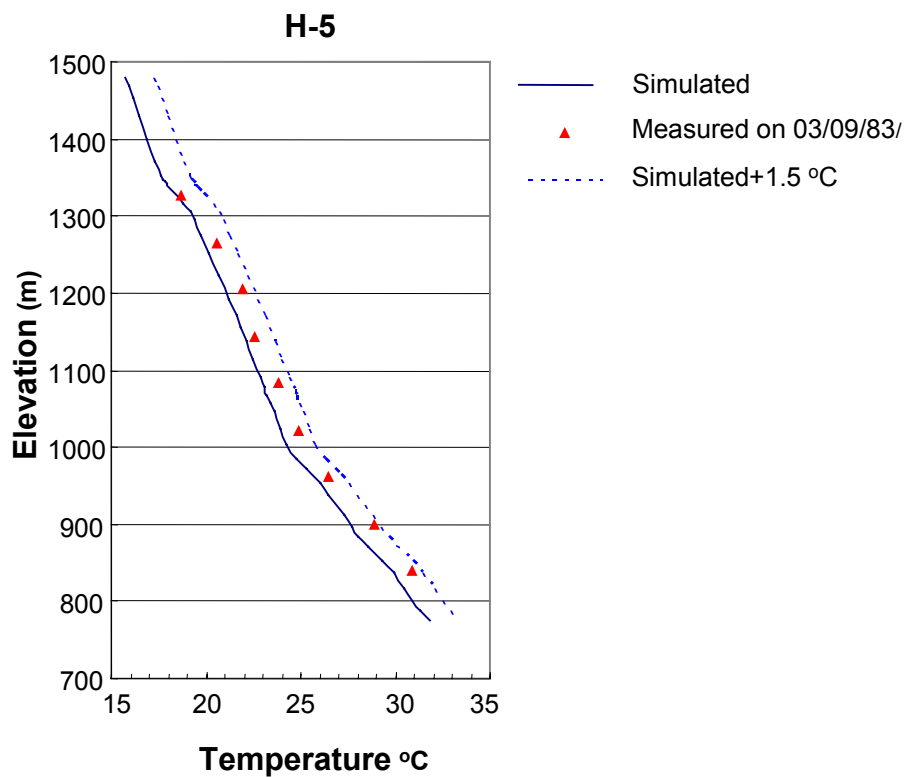
The other related issue is the effects of cavities (existing in several geological layers at the Yucca Mountain site) on water flow and radionuclide transport processes. One may intuitively expect the cavities connected to fractures to act as capillary barriers under unsaturated conditions, because the cavity openings are much larger than fracture apertures. However, both this study and analyses of water-release tests performed in the related geological units at the Yucca Mountain site suggest that cavities are accessible by water within fracture networks, and therefore are retarding the downward water flow and radionuclide transport processes. This is also supported by field observation that mineral coatings exist in many cavities (BSC 2002 [160247], Section 6.9). The coating is a signature for liquid-water flow paths. Although the cavity openings are larger than fracture apertures, the roughness of cavity walls may result in film flow (along cavity walls) from fractures to the cavities (Tokunaga and Wan 1997 [139195]). The effects of cavities are also not considered in the site-scale model for the Yucca Mountain UZ. This omission would result in further underestimating the performance of the repository.

7.7 AMBIENT THERMAL MODEL

A site-scale model of heat flow and geothermal conditions in the Yucca Mountain UZ was developed in Wu et al. (1999 [117161]). Percolation flux was estimated from temperature data (Bodvarsson et al. 2003 [162477]). This ambient thermal model simulates large-scale UZ geothermal and heat flow conditions. In addition, the thermal model provides thermal, gas, and moisture boundaries, and initial conditions for the mountain-scale and drift-scale thermal-hydrological (TH), thermal-hydrological-chemical (THC), and thermal-hydrological-mechanical (THM) coupled process models. The 3-D ambient thermal model, as discussed in Section 6.3, has been calibrated against qualified temperature data measured from five boreholes. The model uses the 3-D UZ Model and the base-case, mean infiltration property set as input parameters and simulates advective and conductive heat transfer processes within the UZ at ambient, steady-state conditions.

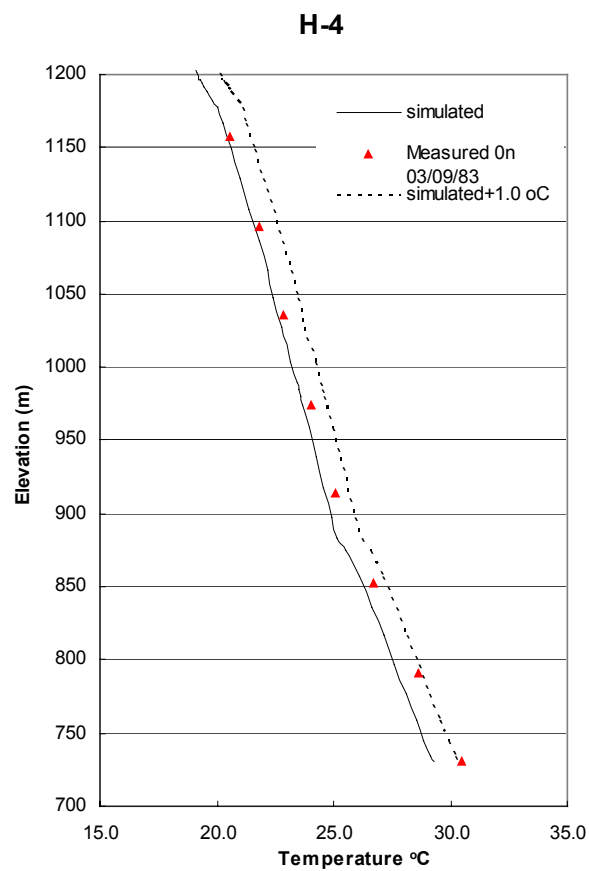
To validate the thermal model, modelers use borehole-measured temperature as corroborative evidence in this section. Based on the validation plan (BSC 2002 [160819], Attachment I-1-2-2), ECRB temperature data, if available in the Technical Data Management System (TDMS), would be used for the validation. Since no ECRB temperature measurements are currently available from the TDMS, the temperature data measured from boreholes H-5, H-4 and WT-18 (Sass et al. 1988 [100644]; with DTN: GS950408318523.001 [107244]) are used instead in the following validation. The criterion is the same as planned for ECRB data: agreement within ± 3 °C. These boreholes were not used for calibration in Section 6.3.

The locations of boreholes H-5, H-4, and WT-18 are plotted Figure 6.3-1. All these boreholes penetrate the repository block and the entire UZ. The comparisons of simulated and observed temperature profiles along this borehole are shown in Figures 7.7-1, 7.7-2, and 7.7-3, indicating a good match between the 3-D model prediction and observed data. Borehole H-5 is close by the ECRB, and Figures 7.7-1 and 7.7-2 show that the simulated temperatures differ from observed values by less than 1.5°C in all elevations. In borehole WT-18, the simulated results again prove to be a reasonable match with field-measured data. All these simulation results are within 2°C of the measured temperature, which is smaller than the criterion of validation of 3°C in the Technical Work Plan. Therefore, the validation criterion is satisfied.



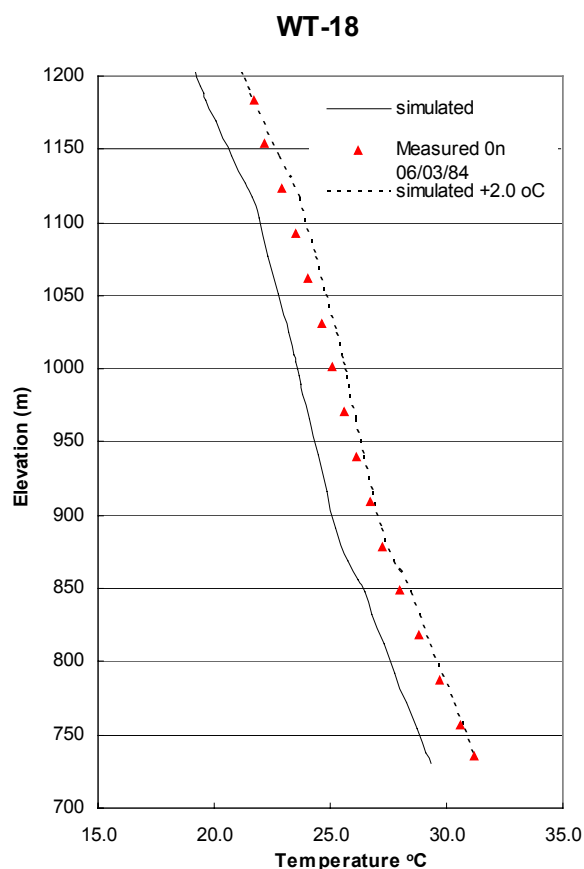
Field Data—DTN: GS950408318523.001 [107244];
Model Results—DTN: LB0303THERMSIM.001

Figure 7.7-1. Comparison of Simulated and Observed Temperature Profiles for Borehole H-5



Field Data—DTN: GS950408318523.001 [107244];
Model Results—DTN: LB0303THERMSIM.001

Figure 7.7-2. Comparison of Simulated and Observed Temperature Profiles for Borehole H-4



Field Data-DTN: GS950408318523.001 [107244];
Model Results-DTN: LB0303THERMSIM.001

Figure 7.7-3. Comparison of Simulated and Observed Temperature Profiles for Borehole WT-18

7.8 VALIDATION USING CHLORIDE MEASUREMENTS ALONG ESF

Natural chemical tracers in subsurface systems can be useful tools in examining water flow and solute transport and their history. Chloride is hydrologically very mobile and chemically inert, and a nearly ideal natural tracer for the study of water movement in the liquid phase. Chloride has been used already in some relevant applications to flow and transport modeling of Yucca Mountain UZ. It has been used to calculate infiltration rates along the ESF (Fabryka-Martin et al. 1998 [146355]). Liu et al. (2003 [162478]) calibrated infiltration rates using chloride data, in conjunction with hydrostructural and hydrogeological features, and demonstrated that the impact of infiltration alteration on percolation fluxes is less than that on chloride concentration. Chloride has been used in this Model Report to calibrate UZ Flow Model predictions of percolation fluxes and moisture distributions within the UZ system, as discussed in Section 6.5.

The chloride model simulates large-scale UZ chloride transport processes. It uses the 3-D flow fields calculated by the UZ Model and incorporates chloride-in-precipitation data to model advective and diffusive chloride transport in the UZ. Its purpose is to validate the UZ Model by testing it with data not used in the development or calibration of the UZ Model. The simulated pore-water chloride concentration is compared with analysis of samples collected along the ESF.

Chloride concentrations of the ESF at different infiltration scenarios are plotted in Figure 7.8-1. The range of the simulated chloride concentration of the base case flow field (preq_mA) in the ESF fall in general within the range for measured concentrations, which satisfies the validation criterion. The figure also indicates that the trend of chloride concentrations in samples is preserved in the calculated chloride concentrations. Note that measured chloride data are clustered around three areas with distances of about 1,000, 3,600, and > 6,800 m. For the first two locations, at 1,000 and 3,600 m, the simulated (preq_mA) results are either within or at the range of measurements. For the last portion, however, the simulations are well within the range of measurement for > 7,000 m and are close to (but a little higher than) the measurement.

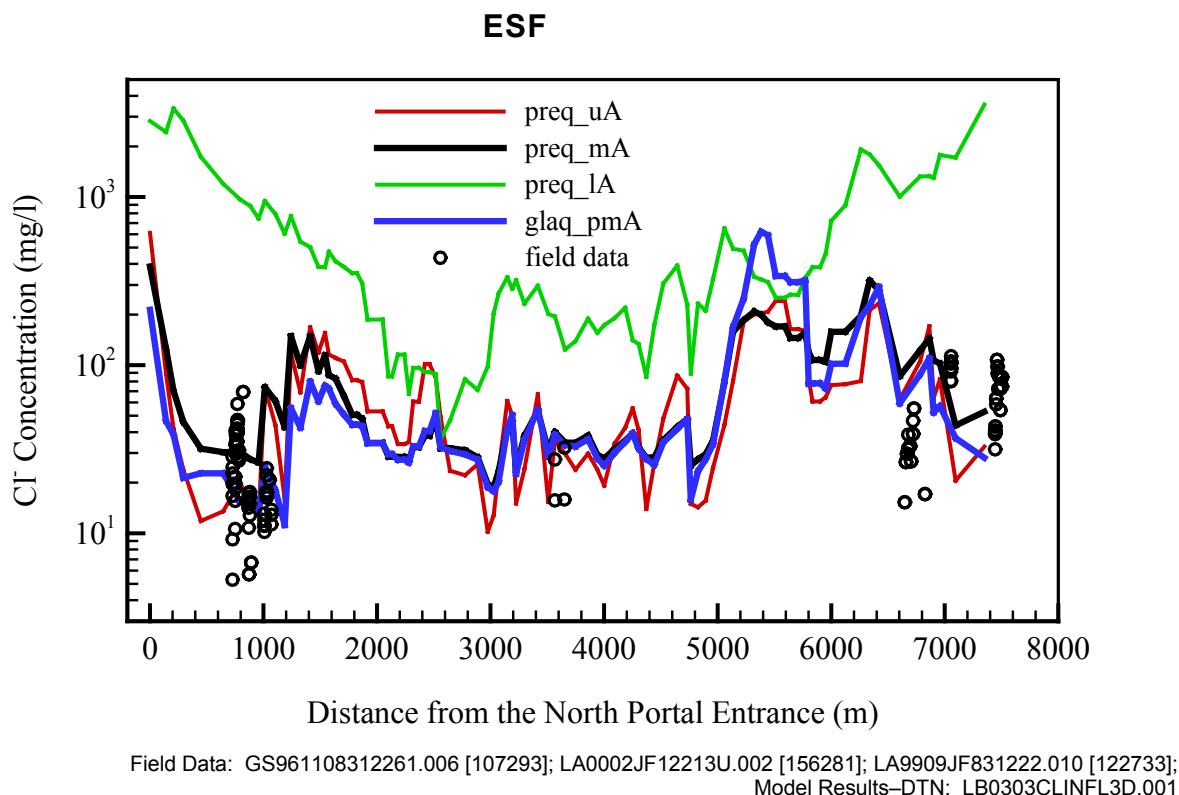


Figure 7.8-1. Comparison of Chloride Concentration (mg/L) Profiles under Present-Day Recharges with Mean, Upper, and Lower Bounds and Glacial Transition Recharge at the ESF

7.9 CALCITE RESULTS

7.9.1 Introduction

The percolation flux in the UZ is an important parameter, because it controls seepage into drifts that may contact waste packages. As shown in Section 6.6, it depends strongly on the infiltration flux, which is a boundary condition of the UZ Model. Observations of precipitated calcite in the UZ constrain the infiltration flux. Therefore, comparing observed hydrogenic calcite deposits to simulations increased confidence in the model's ability to capture this boundary condition. Because direct measurements of infiltration flux is not possible, this confirmation of the boundary condition generally builds confidence in the UZ model. Hydrogenic calcite deposits in fractures and lithophysal cavities at Yucca Mountain have been studied to estimate past

percolation fluxes (Carlos et al. 1995 [162118]; Marshall et al. 1998 [107415]; BSC 2002 [160247]).

One objective of these previous studies was to investigate the relationship between percolation flux and measured calcite abundances. The U.S. Geological Survey (USGS) determined calcite abundances from a deep surface-based borehole (WT-24) (GS021008315215.007 [162127]). Geochronology work performed by the USGS (Neymark et al. 2001 [156889]) indicates that this calcite formed over approximately 10 million years. Hydrogenic mineral coatings in the UZ are nonuniformly distributed and located almost entirely on fracture footwalls and cavity floors—in contrast to saturated environments, in which vein and cavity deposits usually coat all surfaces.

A column corresponding to the location of a deep borehole (WT-24) was chosen for modeling calcite deposition, because measured calcite abundances (GS021008315215.007 [162127]) were available for comparison. Here, the results of a reactive transport numerical model for calcite deposition under different infiltration conditions are presented. The setup and results of the problem are cited from Xu et al. (2003 [162124]). The reactive transport model used here considers the following essential factors affecting calcite precipitation: (1) infiltration, (2) the ambient geothermal gradient, (3) gaseous CO₂ diffusive transport and partitioning in liquid and gas phases, (4) fracture-matrix interaction for water flow and chemical constituents (dual permeability), and (5) water-rock interaction. Any water-rock interaction effects (e.g., pH modification) also affect the calcite solubility hence its abundance in each rock unit. The dual-permeability model allows us to address not only the abundances of calcite with depth, but also its relative abundance in fractures and in the rock matrix as a function of the hydrological/geochemical processes in each medium, as well as the interaction of water flowing between fractures and matrix.

7.9.2 Calcite Precipitation Mechanisms

Along with wind-blown dust, precipitation carries much of the calcium to the surface (Vaniman et al. 2001 [157427]). In the soil zone, strong evapotranspiration, along with some water-rock interaction and root-zone biological processes, leads to saturation with respect to calcite. The depth to reach calcite equilibrium depends on climate and infiltration variations over time, episodic water flow, and near-surface biogeochemical conditions. During more typical smaller infiltration events, calcite may reach equilibrium close to the surface. However, large infiltration pulses of calcite-undersaturated water can dissolve near-surface calcite and reach equilibrium at a greater depth. This model validation activity concerns calcite deposition in a deep geological unit, the TSw, where the repository is located. Uncertainty in the infiltrating water composition near the surface is thus in significant because calcite reaches saturation well above this unit. In addition, the constant infiltration rate and steady-state water flow conditions over geological time used in our simulations are also justified by evidence that the rate of calcite growth in the UZ has remained approximately constant over at least the past 8 million years (Paces et al. 1998 [107408]).

The primary driving force for calcite precipitation from percolating waters in the UZ is its decreasing solubility with increasing temperature; calcite precipitates as water flows downward because of the geothermal gradient. Therefore, consideration of the ambient geothermal gradient is very important for calcite precipitation. The temperature distribution is a function of the crustal heat flow and the effect of infiltration. The modeled temperature distributions in borehole

WT-24 are discussed later in Section 7.9.5.2. Pore waters extracted from deep locations of the Yucca Mountain rock matrix are close to equilibrium with respect to calcite (BSC 2002 [160247]), and no measurements of aqueous concentrations are available from fractures because they generally have low liquid saturations.

The calcium concentration and CO₂ partial pressure in percolating water is a major factor controlling the abundances of calcite and its stability. This is a result of the decreasing solubility of CO₂ gas in water with increasing temperature, which in turn causes the following degassing process: $\text{HCO}_3^- + \text{H}^+ \rightarrow \text{CO}_2 (\text{g}) + \text{H}_2\text{O}$. Gaseous CO₂ is also redistributed by gas-phase diffusive transport. Degassing increases the pH, and then contributes to calcite precipitation: $\text{Ca}^{2+} + \text{HCO}_3^- \rightarrow \text{CaCO}_3 (\text{calcite}) + \text{H}^+$. Water and gas flow between fractures and the adjacent matrix governs the resulting calcite distribution within each medium. Calcite precipitation is also affected by other factors, such as the dissolution and precipitation of aluminosilicate minerals (mainly through modifying the pH and the CO₂ partial pressure).

7.9.3 Reactive-Transport Model

Modeling of calcite deposition in the Yucca Mountain UZ was performed using the reactive transport computer code TOUGHREACT (Xu and Pruess 1998 [117170]; 2001 [156280]). (This version of the code has not been qualified under AP-SI.1Q, but its use for corroboration is appropriate.) The code uses a sequential iteration approach similar to Yeh and Tripathi (1991 [162125]), Walter et al. (1994 [162122]), and Xu et al. (1999 [162123]), which solve the transport and reaction equations separately. Flow and transport are based on space discretization by means of integral finite differences. An implicit time-weighting scheme is used for individual components of the model: flow, transport, and kinetic geochemical reaction. The chemical transport equations are solved independently for each component, whereas the reaction equations are solved on a gridblock basis using Newton-Raphson iteration. Full details of the code are given in Xu and Pruess (1998 [117170]; 2001 [156280]).

In the model, advective and diffusive transport of aqueous chemical species is considered in the liquid phase. Molecular diffusive transport of gaseous species (CO₂) is considered in the gas phase. Aqueous chemical complexation and gas dissolution/exsolution are accounted for under local equilibrium, whereas mineral dissolution/precipitation can proceed at equilibrium and/or can be kinetically controlled. Gas species in the chemical computations are assumed to behave as ideal gases (i.e., fugacity equals partial pressure). Temperature effects are considered for geochemical reaction calculations, because equilibrium and kinetic data are functions of temperature.

Changes in porosity and permeability from mineral dissolution and precipitation of water flow are not considered for the present modeling. This feedback between transport and chemistry can be important, but a rather large computational time penalty has to be paid if this is modeled explicitly. By neglecting porosity and permeability change, modelers obtain quasi-steady flow conditions. This makes it possible to consider geochemistry in great detail for a simulation period of 10 million years.

A dual-permeability approach, in which fractures and matrix are treated as two separate continua, was employed for water flow and chemical transport in the unsaturated fractured tuff. In this approach, interflow (water and chemicals) is allowed between fractures and the adjacent

matrix, and global flow occurs within both fracture and matrix continua. The active fracture model (AFM), developed by Liu et al. (1998 [105729]), was used to describe fracture-matrix interaction and preferential liquid flow in fractures.

7.9.4 Hydrogeological and Geochemical Conditions

7.9.4.1 Hydrogeological Conditions

The Yucca Mountain UZ consists of layers of welded and nonwelded volcanic tuffs. The welded and nonwelded tuffs have vastly different hydrological properties. Welded units are characterized by relatively low porosity, low matrix permeability, and high fracture density, whereas the nonwelded tuffs have higher matrix porosity and permeability, and lower fracture density (Liu et al. 1998 [105729]). Montazer and Wilson (1984 [100161]) developed a conceptual model for the UZ at Yucca Mountain that identified five main hydrogeological units based on the degree of welding and on the associated relationships to fracture intensity. This conceptual model has formed the basis for modeling flow in the UZ at Yucca Mountain. Table 7.9-1 describes each unit, which is further divided into a number of model layers with different hydrogeological and geochemical properties (BSC 2003 [160240]; BSC 2002 [158375]). The Calico Hills nonwelded (CHn) unit is comprised of zeolitic and vitric nonwelded tuffs underlying the basal vitrophyre of the Topopah Spring Tuff. Below the CHn are the Crater Flat undifferentiated (CFu) units, consisting of the lower Bullfrog and Tram Tuffs of the Crater Flat Group. The hydrogeological units below the TSw were not considered in geochemical transport simulations, so details regarding these units are not given in Table 7.9-1. We are primarily interested in calcite deposition within the TSw unit, where the repository is located (tsw4 and tsw5 model layers in Table 7.9-1). The exclusion of the underlying hydrogeological units does not affect the results in the TSw unit because flow is predominantly gravity driven, and upward chemical diffusion is subordinate to downward advective transport.

Table 7.9-1. Hydrogeologic Units, Model Layers, and Hydrogeological Properties for the Yucca Mountain Unsaturated Zone Flow and Transport Model, as Given by the Calibrated Property Model

Hydrogeologic Unit	Description	Model Layer	Fracture		Matrix	
			Permeability (m ²)	Porosity	Permeability (m ²)	Porosity
TCw: Tiva Canyon Welded unit	Moderately to densely welded portions of the Tiva Canyon Tuff of the Paintbrush Group	tcw1	2.41×10^{-12}	3.7×10^{-2}	3.86×10^{-15}	0.253
		tcw2	1.00×10^{-10}	2.6×10^{-2}	2.74×10^{-19}	0.082
		tcw3	5.42×10^{-12}	1.9×10^{-2}	9.23×10^{-17}	0.203
PTn: Paintbrush Nonwelded unit	Variably welded Paintbrush Tuff and its associated bedded tuffs, including those located at the bottom of the Tiva Canyon and top of the Topopah Spring Tuffs	ptn1	1.86×10^{-12}	1.4×10^{-2}	9.90×10^{-13}	0.387
		ptn2	2.00×10^{-11}	1.5×10^{-2}	2.65×10^{-12}	0.439
		ptn3	2.60×10^{-13}	3.2×10^{-3}	1.23×10^{-13}	0.254
		ptn4	4.67×10^{-13}	1.5×10^{-2}	7.86×10^{-14}	0.411
		ptn5	7.03×10^{-13}	7.9×10^{-3}	7.00×10^{-14}	0.499
		ptn6	4.44×10^{-13}	4.6×10^{-3}	2.21×10^{-13}	0.492
TSw: Topopah Spring welded unit	Moderately to densely welded portions of the Topopah Spring Tuff down to and including the densely welded basal vitrophyre	tsw1	3.21×10^{-11}	7.1×10^{-3}	6.32×10^{-17}	0.053
		tsw2	3.56×10^{-11}	1.2×10^{-2}	5.83×10^{-16}	0.157
		tsw3	3.86×10^{-11}	8.5×10^{-3}	3.08×10^{-17}	0.154
		tsw4	1.70×10^{-11}	1.0×10^{-2}	4.07×10^{-18}	0.110
		tsw5	4.51×10^{-11}	1.5×10^{-2}	3.04×10^{-17}	0.131
		tsw6	7.01×10^{-11}	2.0×10^{-2}	5.71×10^{-18}	0.112
		tsw7	7.01×10^{-11}	2.0×10^{-2}	4.49×10^{-18}	0.094
		tsw8	5.92×10^{-13}	1.6×10^{-2}	4.53×10^{-18}	0.037
		tsw9	4.57×10^{-13}	5.9×10^{-3}	5.46×10^{-17}	0.173

DTN: LB997141233129.001 [104055]

7.9.4.2 Geochemical Model

Minerals considered in the simulations are calcite, gypsum, goethite, tridymite, cristobalite- α , quartz, amorphous silica, hematite, fluorite, albite, K-feldspar, anorthite, Ca-smectite, Mg-smectite, Na-smectite, illite, kaolinite, opal-CT, stellerite, heulandite, mordenite, clinoptilolite, and glass (Xu et al. 2003 [162124]). This full assemblage of minerals and the corresponding aqueous species are hereafter termed the “extended-case geochemical system.” This assemblage has complexities and uncertainties in terms of thermodynamics and kinetics of mineral solid solutions (clays, zeolites and feldspars), effects on pH, and the partial pressure of CO₂. A simpler set of minerals and aqueous species (base-case geochemical system) disregards all aluminosilicates, as well as Fe- and Mg-bearing minerals.

Calcite and gypsum dissolution and precipitation were assumed to take place under geochemical equilibrium, whereas dissolution and precipitation of the other minerals were treated under kinetic constraints. Initial mineral abundances were taken from DTN: LB991200DSTTHC.003

[161276]. Potential secondary minerals (i.e., those allowed to precipitate but which may not necessarily form) were determined from field and experimental observations of water-rock interaction and from equilibrium geochemical model calculations. Reactive surface areas of minerals on fracture walls were calculated from the fracture-matrix interface area/volume ratio, the fracture porosity, and the derived mineral volume fractions (DTN: LB0101DSTTHCR1.003 [161278]). These areas were based on the fracture densities, fracture porosities, and mean fracture diameter. Mineral surface areas in the rock matrix were calculated using the geometric area of a cubic array of truncated spheres that make up the framework of the rock and reductions to those areas, owing to the presence of alteration phases such as clays and zeolites.

Initial pore water chemical concentrations were based on analyses of ultracentrifuged water and chemical speciation calculations presented in BSC (2002 [158375]). Except for perched water that lies well below the potential repository horizon, water has not been observed in fractures in the UZ. Therefore, the initial composition of water in the fractures was set to be the same as the matrix pore water (Table 7.9-2). The same water composition, re-equilibrated at the temperature of the top model boundary, was assumed for infiltrating water. Oxidizing conditions were considered for this water, because the fracture permeability of the rock is high and the system is unsaturated (air phase is present everywhere). The CO₂ gas partial pressures used for initial and top boundary conditions of the gas transport are in equilibrium with the corresponding aqueous chemical composition. An elevated gas partial pressure (relative to an atmospheric value of 0.344×10^{-3} bar) at the upper boundary can be attributed to soil-zone CO₂ production.

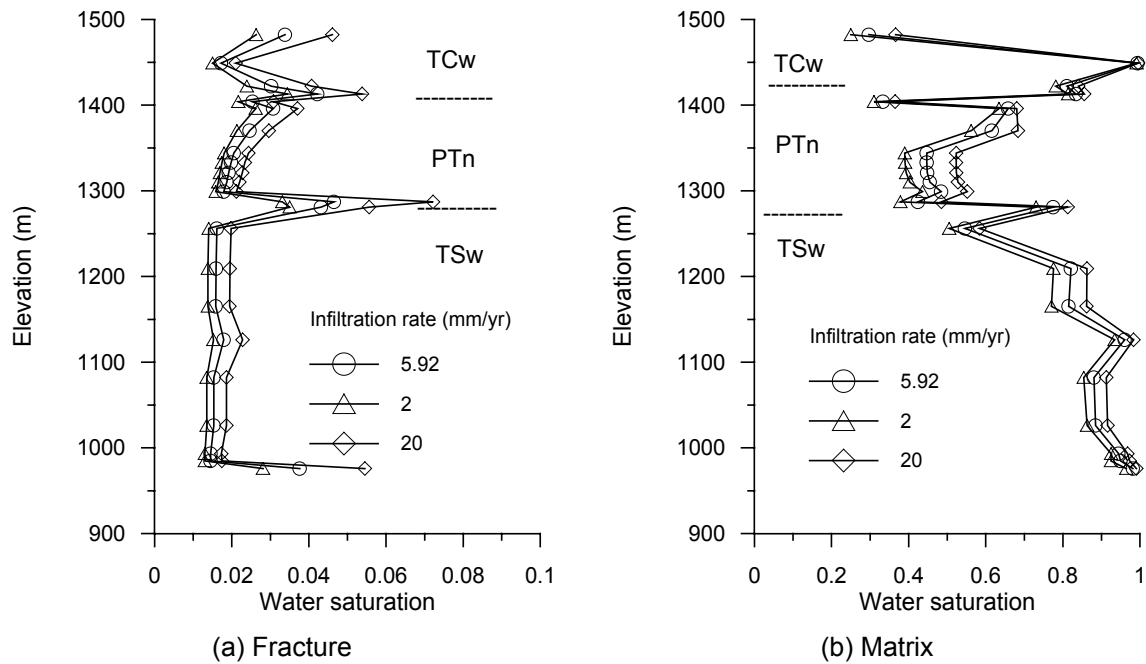
Table 7.9-2. Water and Gas Chemistry Used for Initial and Boundary Conditions of the Reaction-Transport Simulations

Component	Concentration	Unit
Ca	101	mg/L
Mg	17	mg/L
Na	61.3	mg/L
K	8	mg/L
SiO ₂ (aq)	70.5	mg/L
Al	1.67×10^{-5}	mg/L
HCO ₃	200	mg/L
Cl	117	mg/L
SO ₄	116	mg/L
F	0.86	mg/L
Fe	6.46×10^{-8}	mg/L
pH	8.32 (at 25 °C) 7.75 (at 17 °C)	
PCO ₂	2.726×10^{-3} at 17 °C	bar

Source: Xu et al. 2003 [162124])

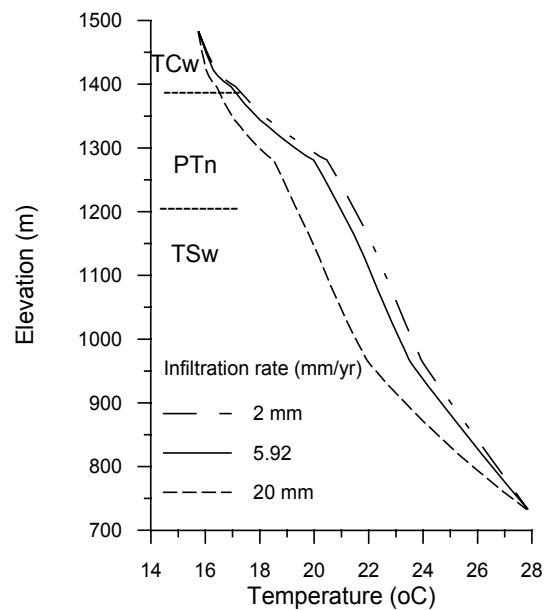
7.9.4.3 Simulation Setup

Simulations were performed using three infiltration rates, a base-case rate of 5.92 mm/yr (BSC 2003 [160240]), and bounding rates of 2 mm/yr and 20 mm/yr. The corresponding (to infiltration rates) steady-state water flow conditions were used for geochemical transport simulations. Steady-state water saturation distribution is presented in Figure 7.9-1. Steady-state temperature distributions corresponding to the same three infiltration rates are shown in Figure 7.9-2. These were obtained using a top temperature of 15.6°C at the land surface and a bottom temperature of 28°C at the water table. For the three infiltration rates, the same water and gas chemistry was used for the top boundary condition. As discussed in Section 7.9.2, the infiltrating water composition applied here is considered to be the water chemistry after transformation by soil-zone processes (evapotranspiration predominantly). Calcite precipitation in the TSw unit is not sensitive to uncertainties in the infiltrating water chemistry, because it is well below the region where calcite becomes saturated. Moreover, episodic flow likely has been strongly dampened by the overlying weakly fractured bedded tuffs in the PTn hydrogeological unit.



Source: Xu et al. 2003 [162124]

Figure 7.9-1. Modeled Steady-State Water Saturations for the WT-24 Column Using Infiltration Rates: 2, 5.92, and 20 mm/yr



Source: Xu et al. 2003 [162124]

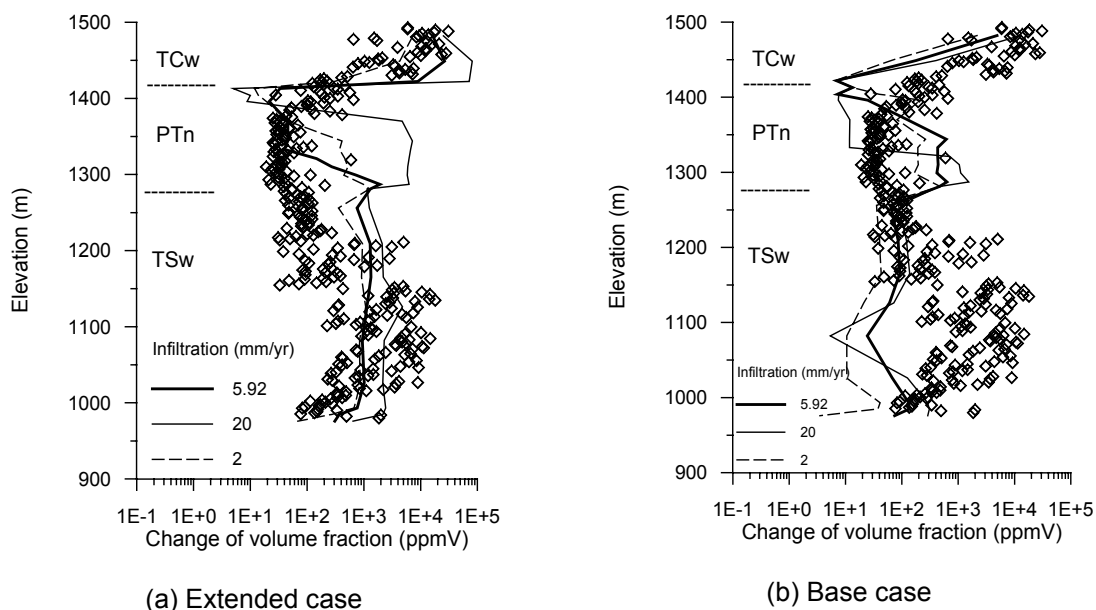
Figure 7.9-2. Modeled Temperature Profiles in Borehole WT-24 as a Function of Depth for Three Infiltration Rates

For the reactive transport simulations of calcite precipitation, a simulation time of 10 million years was selected, because this calcite formed over approximately 10 million years (Neymark et al. 2001 [156889]). Infiltration rates and temperatures were held constant throughout the time of the simulation; therefore, the results reflect the average conditions over this period of time.

7.9.5 Results and Discussion

7.9.5.1 Comparison with Measured Data

The simulated total (fracture plus matrix) calcite abundances in the WT-24 column obtained using the three different infiltration rates are presented together with measured data in Figure 7.9-3a (extended-case geochemical system) and Figure 7.9-3b (base-case geochemical system). Generally, the results obtained using the base-case infiltration rate (5.92 mm/yr) agree better with the measured WT-24 mineral abundances than those obtained using the other infiltration rates, especially for the PTn unit. The extended-case geochemical system gives a better match to the total calcite abundances, especially for the TSw unit, indicating that some contribution of Ca from the rock is required.



NOTE: Diamonds represent bulk rock calcite abundances measured by the U.S. Geological Survey (GS021008315215.007 [162127]). Simulated results are from Xu et al. 2003 [162124].

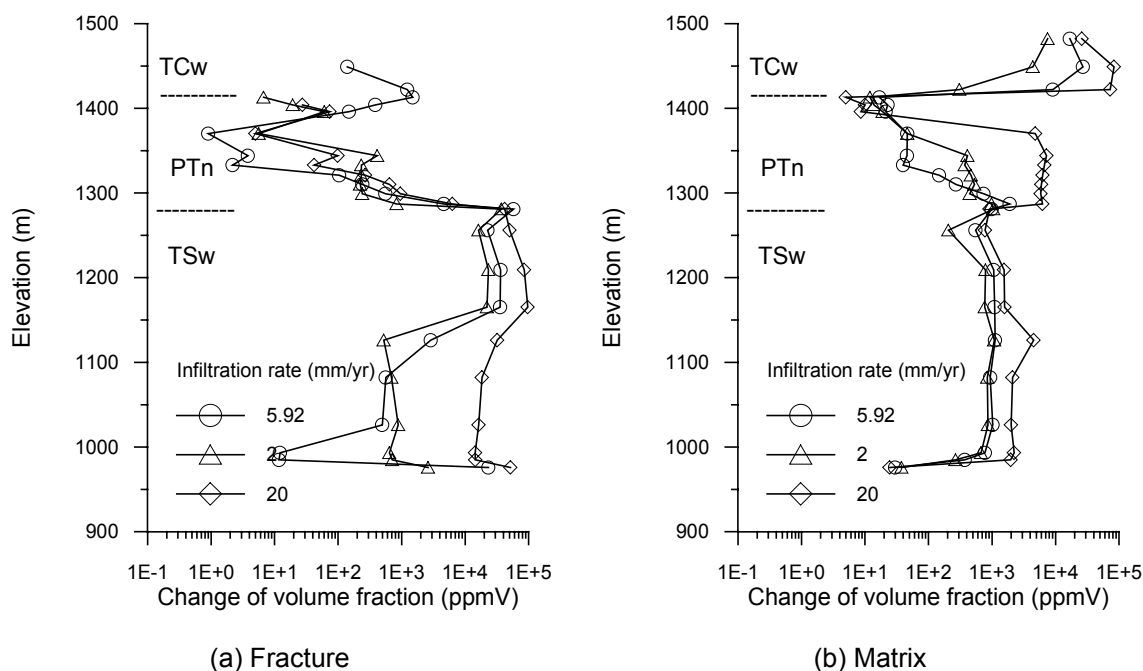
Figure 7.9-3. Simulated Total (Fracture plus Matrix) Calcite Abundances (in ppmV or 10^{-6} Volume Fraction) in the WT-24 Column for Different Infiltration Rates after 10 Million Years: (a) Extended-Case Geochemical System, (b) Base-Case Geochemical System

The simulated calcite abundances in the basal PTn layer for the three infiltration simulations are higher than that measured in WT-24. This results from an increase in the temperature gradient (Figure 7.9-2) resulting in a concomitant decrease in calcite solubility. The relatively larger calcite abundances in the bottom layer of the PTn have been observed at other locations such as in another deep borehole, USW G-2 (Carey et al. 1998 [109051]). The lower measured calcite abundances may also result for lateral flow not captured in the one-dimensional simulations.

Results for the welded TSw unit (of the most interest to the YMP) generally fall in the wide range of measured calcite data. Calcite deposition values obtained from the highest infiltration rate (20 mm/yr) are closer to the high bound of measured values. Those values from the base case (5.92 mm/yr) fall in the middle of the TSw measured data range. This may imply that the 20 mm/yr percolation rate is the high bound for the WT-24 location, whereas the base infiltration (5.92 mm/yr) from the flow property calibration (used for the flow model) may be close to the long-term mean infiltration rate for this location. The extended-case geochemical system provides the closest match to the measured data in the TSw unit, because of the contribution of Ca from feldspars.

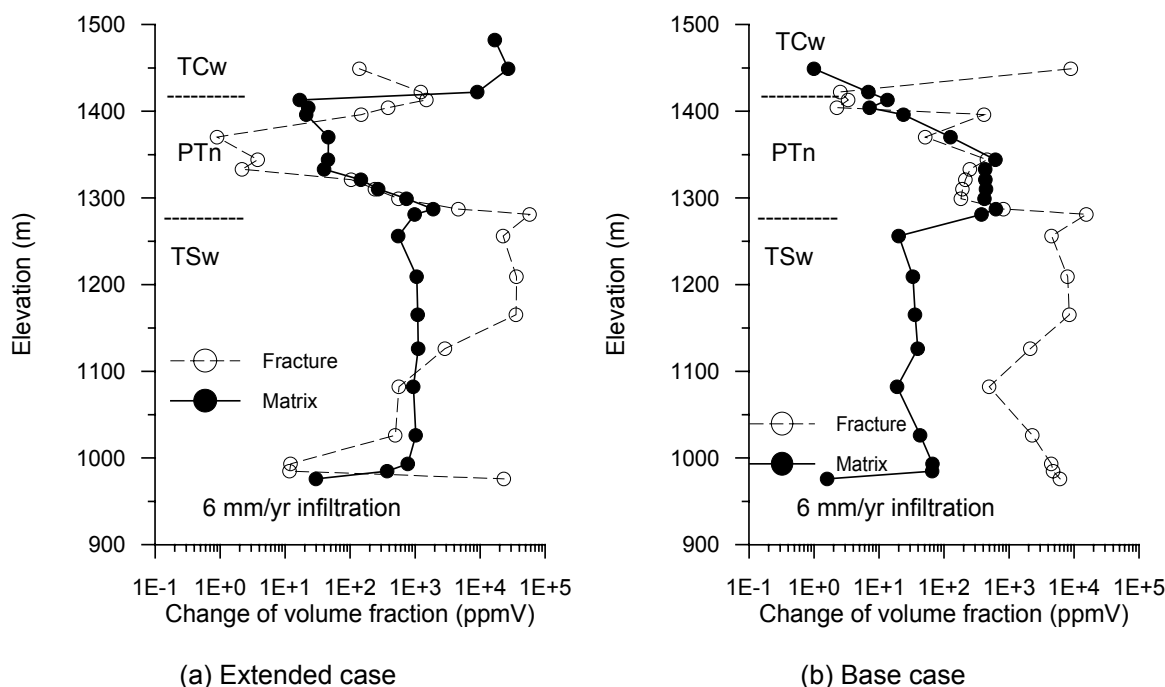
7.9.5.2 Calcite Precipitation in Fractures and Matrix

Modeled calcite abundances in the fracture and matrix continua are very different for the various hydrogeological units (Figures 7.9-4 and 7.9-5). Figure 7.9-4 shows calcite abundances in fractures and matrix for the three infiltration rates with the extended-case geochemical system. In the PTn unit (Figures 7.9-5a and 7.9-5b), the matrix shows a similar or larger proportion of calcite than the fractures, except near the contact with the TSw, where the distribution reverses. In the uppermost part of the TSw unit (just above the repository horizon), calcite precipitation in fractures is dominant, indicating that flow is enhanced in the fractures. Calcite coatings are frequently found in fractures and lithophysal cavities (intersected with fractures) in the TSw tuffs (Paces et al. 1998 [107408]).



Source: Xu et al. 2003 [162124]

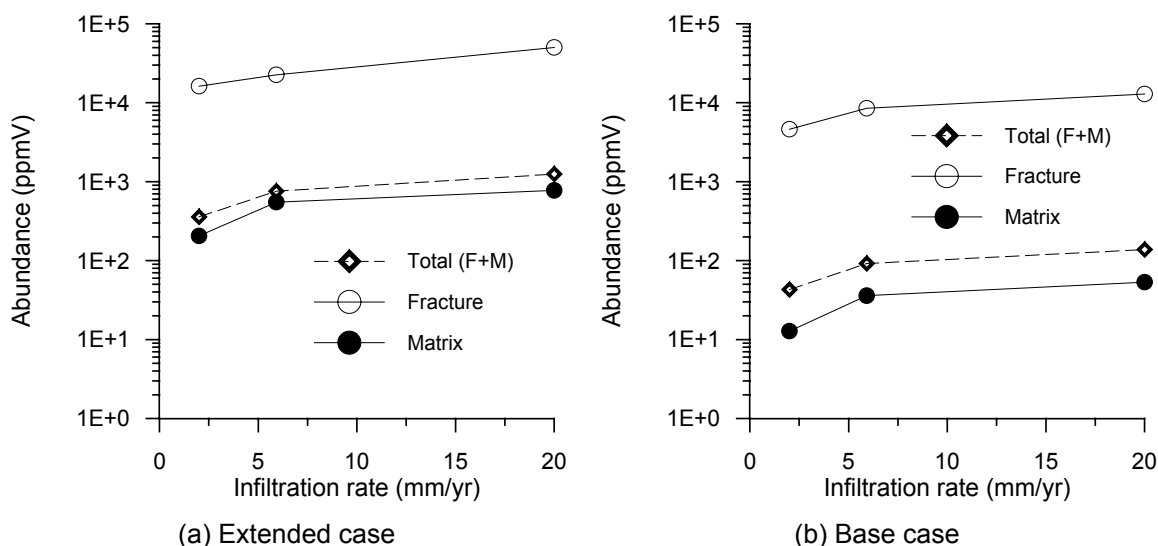
Figure 7.9-4. Modeled Calcite Abundances (in ppmV or 10^{-6} Volume Fraction) in Fractures and in the Matrix after 10 Million Years for Differing Infiltration Rates Using the Extended-Case Geochemical System



Source: Xu et al. 2003 [162124]

Figure 7.9-5. Modeled Calcite Abundances (in ppmV or 10^{-6} Volume Fraction) in Fractures and in the Matrix for (a) the Extended-Case and (b) Base-Case Geochemical Systems

However, the abundances in Figures 7.9-4 and 7.9-5 reflect only the proportion of calcite within the fracture and the matrix volumes individually. Figure 7.9-6 shows changes of calcite volume fraction versus infiltration rate for layer tsw4 (at an elevation of 1,126 m). In the extended case (Figure 7.9-6a), there are about equal total amounts of calcite in the matrix and fractures (the total is about twice that in the matrix, which makes up most of the volume of the rock), even though the fractures show a much larger proportion of calcite (Figure 7.9-5a). For the base-case system (Figure 7.9-6b), calcite in the fractures is about three-fourths of the total calcite in the rock, owing to the limited amount of Ca coming from the rock matrix and forming calcite. Greater simulated calcite abundances in the fractures result from the fractures carrying higher water fluxes in these strongly fractured, densely welded rocks.



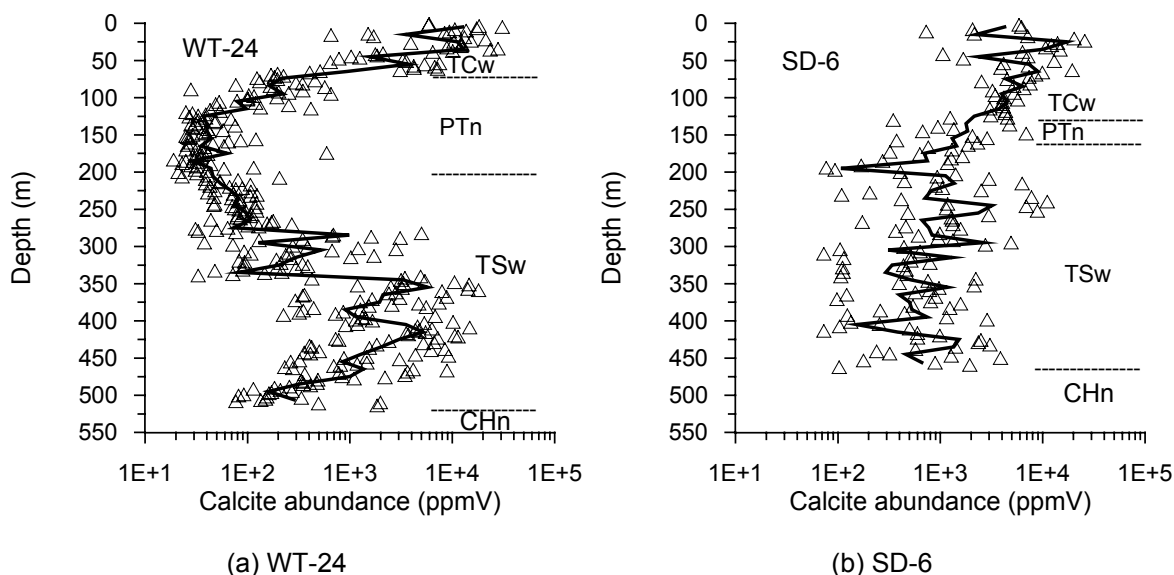
Source: Xu et al. 2003 [162124]

Figure 7.9-6. Changes in Calcite Volume Fraction (ppmV) vs. Infiltration Rates for TSw4 Layer (at an Elevation of 1,126 m) for (a) the Extended-Case and (b) Base-Case Geochemical Systems

The extended-case and base-case simulations also show that from about 2 to 5.92 mm/yr, the amount of calcite precipitated in the welded Topopah Spring tuff is sensitive to the infiltration rate (Figures 7.9-6a and 7.9-6b). This dependence decreases at higher infiltration rates (5.92 mm/yr infiltration rate to 20 mm/yr) owing to a modification of the geothermal gradient from the increased percolation flux (Figure 7.9-2). The decrease in temperature at this level is about 2°C, which resulted in less calcite precipitating in the TSw, and more calcite being transported below the TSw.

7.9.5.3 Spatial Variation in Calcite Deposition

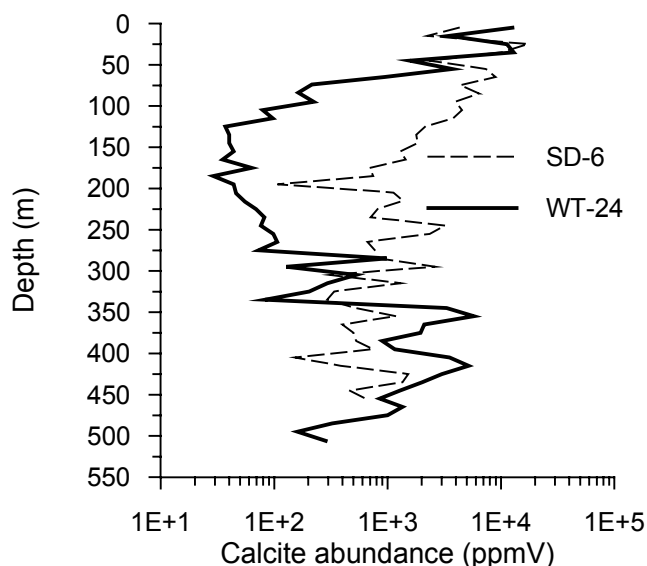
Observed calcite abundances vary significantly in space and as a function of depth. Studies for the WT-24 column can give some general insight into calcite deposition conditions, but cannot represent the entire picture at Yucca Mountain. Calcite abundance data for borehole USW SD-6 were later released by USGS in 2002 (DTN: GS020608315215.002 [162126]), but modeling of calcite deposition for SD-6 has not been performed. Measured calcite data have a wide range of values (orders from 10^2 to 10^4 ppmV). To compare the two columns, which show large variability, the geometric means over a specified depth range were compared. The calcite data were grouped according to (1) every 10 m in depth (if possible) and (2) within one geologic unit. The calculation of calcite geometric means (in Microsoft Excel) are documented in Wang (2003 [162417], SN-LBNL-SCI-160-V1, pp. 89–92). The original measured calcite data and calculated geometric means versus depth are presented in Figure 7.9-7. To better compare WT-24 with SD-6, we plot both geometric means in Figure 7.9-8. For the PTn, SD-6 has much more calcite deposition than WT-24. The thickness of the PTn unit for SD-6 is thinner than that of WT-24. For the TSw, calcite abundances in SD-6 fall in a range similar to those in WT-24. In the 3-D UZ Flow Model, a mean infiltration of 19.6 mm/yr is used in SD-6, which is higher than the 5.9 mm/yr in WT-24. This once again indicates that between a 5.92 and 20 mm/yr infiltration rate, the amount of calcite is not expected to be significantly different in the TSw.



Field Data-DTNs: GS021008315215.007 [162127] for WT-24;
GS020608315215.002 [162126] for SD-6

NOTE: Symbols represent USGS-measured calcite abundances. Solid lines represent geometric means.

Figure 7.9-7. Calcite Abundances (in ppmV or 10^{-6} Volume Fraction) with Depth in Boreholes WT-24 and SD-6



SOURCE: Wang 2003 [162417], SN-LBNL-SCI-160-V1, p. 92

Figure 7.9-8. Geometric Means of Calcite Abundances with Depth for Boreholes WT-24 and SD-6

7.9.6 Concluding Remarks

Modeling calcite deposition provides additional evidence for validation of the UZ Model. Over a range of 2–20 mm/yr infiltration rates, the simulated calcite abundances generally fall within the range of calcite observed in the field, which satisfies the validation criterion. The simulated

calcite distributions capture the U.S. Geological Survey-measured data from the WT-24 well cuttings (GS021008315215.007 [162127]). The 20 mm/yr infiltration rate may be the upper bound for WT-24 location, whereas the base-case infiltration rate (5.92 mm/yr) used for the flow model gives the closest match to the data. The observed calcite precipitation for the top of TSw occurs mostly in the fractures, which is also captured. The modeling results can provide useful insight into process mechanisms such as fracture-matrix interaction, as well as conditions and parameters controlling calcite deposition. The modeled calcite abundances generally increase with increasing infiltration rate, but become less sensitive to infiltration at higher rates as a result of changes to the geothermal gradient. Between a 5.92 and 20 mm/yr infiltration rate, the amount of calcite is not expected to be significantly different in the TSw, a conclusion supported by the similar abundances in WT-24 and SD-6 in the TSw.

One-dimensional simulation is appropriate because both flow and geothermal gradient are primarily vertical. The current observed calcite is formed cumulatively over about 10 million years. A number of uncertainties are involved in the numerical simulation results. The most influential of which are variations of geothermal gradient and infiltration over time. Differences between 1-D and 3-D flow are much less than the differences in geothermal gradient and infiltration over 10 million years. Agreement between simulated and measured calcite abundance could work to establish the validity of the flow field and infiltration rates used.

7.10 MODEL VALIDATION USING STRONTIUM GEOCHEMISTRY AND ISOTOPIC RATIOS

This section describes the use of strontium (Sr) and strontium isotopic ratios ($^{87}\text{Sr}/^{86}\text{Sr}$) for validation of the UZ Model. Validation methodology consists of work presented in peer-reviewed journals, as well as comparison of model results to data collected for pore waters. The criterion for the validation is a qualitative agreement between simulated Sr concentrations and the average of the observations at the same elevation, and an agreement with vertical trends (BSC 2002 [160819], Attachment 1, Section I-1-2-5).

7.10.1 Background

Strontium concentrations and the $^{87}\text{Sr}/^{86}\text{Sr}$ ratio in pore fluids and secondary minerals can provide important constraints on infiltration rates, flow paths, residence times, and degrees of water-rock and fracture-matrix interaction at Yucca Mountain (Stuckless et al. 1991 [106947]; Marshall et al. 1991 [106335]; Peterman et al. 1992 [147110]; Peterman and Stuckless 1993 [101149]; Johnson and DePaolo 1994 [162560]; Vaniman and Chipera 1996 [100089]; Sonnenthal and Bodvarsson 1999 [117127]; Paces et al. 2001 [156507]). Strontium concentrations in pore waters are related to the infiltration rate (through evaporation), the dissolution of minerals in surface deposits, reaction with minerals or glass in the tuffs, precipitation of calcite, and exchange with clays and zeolites (Vaniman et al. 2001 [157427]; Vaniman and Chipera 1996 [100089]; Sonnenthal and Bodvarsson 1999 [117127]). The similarity of Sr to Ca in charge and ionic radius results in Sr incorporation into Ca-bearing minerals such as plagioclase feldspar and secondary minerals such as Ca-zeolites and Ca-rich smectite.

The $^{87}\text{Sr}/^{86}\text{Sr}$ ratio in pore waters depends on its initial ratio and is affected along a flow path by dissolution of Sr-bearing phases (e.g., calcite, feldspars, volcanic glass), exchange with clays or

zeolites, and the mixing of waters having differing isotopic ratios (Johnson and DePaolo 1994 [162560], p. 1571). If such fluids have differing strontium concentrations, mixing will result in hyperbolic curves of $^{87}\text{Sr}/^{86}\text{Sr}$ versus total Sr (Faure 1986 [105559], p. 143), making them more complex chemically, but adding additional constraints to understanding the hydrological system. In nature, almost no fractionation of Sr isotopes occurs; however, fractionation of Rb from Sr leads to variations in $^{87}\text{Sr}/^{86}\text{Sr}$ because of the decay of ^{87}Rb to ^{87}Sr . Because the half-life of ^{87}Rb is about 5×10^{10} years, this decay effect is insignificant over the few hundred thousand years of interest for the UZ flow system.

The effect of the rock on the isotopic composition of water thus depends on the Sr content as well as on its isotopic ratio. The amount of rock dissolution and mineral precipitation depends on the degree to which the mineral assemblage is in disequilibrium with the water. Unaltered volcanic glass is more reactive than minerals, so that the rate of reaction of devitrified tuff with water is lower than that with glass. However, several factors can result in reduced apparent rates of reaction. The development of amorphous silica saturation in the soil zone has been proposed as a strong inhibitor of water-rock reaction in the underlying tuffs at Yucca Mountain (Meijer 2002 [158813], pp. 803–804). Alteration products on the surface of fractures or on mineral grains would also lead to rates limited by diffusion through such films rather than by reaction, retarding the dissolution rate (Sonnenthal and Ortoleva 1994 [117914], p. 407). Incongruent dissolution of volcanic glass has also been proposed as a cause for lower quantities of Sr dissolved into pore fluids in the PTn bedded tuffs (Vaniman and Chipera 1996 [100089], p. 4421).

7.10.2 Validation of Conceptual and Numerical Models of UZ Transport Based on Corroborative Information from Published Works

Based on Cl/Sr ratios in a relatively few number of pore-water samples that were similar to those of an estimated effective precipitation composition, and the lack of a substantial shift in $^{87}\text{Sr}/^{86}\text{Sr}$ ratio in pore salts and calcite, Sonnenthal and Bodvarsson (1999 [117127], pp. 111, 151) suggested that the Sr concentrations in the UZ above the zeolitic units were in large part inherited from surface evapotranspiration processes, with only a minor contribution from water-rock interaction. Three-dimensional UZ transport modeling, including ion exchange, showed relatively high pore-water Sr concentrations in nonzeolitic units and a strong shift to lower concentrations (by a few orders of magnitude) in zeolitic units, which was consistent with pore-water and perched-water compositions in contact with the respective rock units. This comparison of modeled Sr pore water concentrations was good supporting evidence for the approximately 5 mm/yr mean infiltration rate at Yucca Mountain based on Cl concentrations in pore water (Sonnenthal and Bodvarsson 1999 [117127], p. 107). The model also produced Sr compositions at perched-water locations that were high where the perching was on the basal vitrophyre of the Topopah Spring tuff and very low where the perched water contacted zeolitic rocks. The results were consistent with several measurements made in the various boreholes that had intersected perched water bodies.

Extensive exchange of Sr with Ca in clinoptilolite, other Ca-rich zeolites, and clays is well documented in the Yucca Mountain UZ (Vaniman et al. 2001 [157427]; Vaniman and Chipera 1996 [100089], p. 4431). An analysis performed by Vaniman et al. (2001 [157427], p. 3409) showed that the excess Sr in the zeolitic rocks from the UZ-16 borehole, produced by ion exchange, was consistent with 10 million years of infiltration at about 5 mm/year. Therefore, this

published work provides independent corroboration of the results obtained by Sonnenthal and Bodvarsson (1999 [117127], p. 107), based on conceptual and numerical models that form the basis for the UZ Model presented in this report. Support for the 5 mm/yr being a long-term maximum is the observation that the $^{87}\text{Sr}/^{86}\text{Sr}$ ratios in calcite are shifted to slightly higher values in calcite precipitated more recently compared to early-formed calcite, indicating some contribution of Sr from water-rock interaction (Paces et al. 2001 [156507], pp. 75). Therefore, some of the Sr in the zeolitic units must have been derived from dissolution of tuff. An increase in the $^{87}\text{Sr}/^{86}\text{Sr}$ ratio in pore water at lower infiltration rates is a result of the longer residence time that the water has in contact with rock having a much higher $^{87}\text{Sr}/^{86}\text{Sr}$ ratio. This evidence, and the generally high Sr concentrations through the UZ above zeolitic rocks, suggests that although some Sr is lost to precipitating calcite, a comparable amount is gained by tuff dissolution. If some of the Sr in the zeolitic rocks is in excess of that produced by infiltration, then the estimated infiltration rate, based on Sr concentrations in the zeolitic rocks, would be an upper limit.

Another piece of corroborating evidence comes from the compositions of calcite in fracture coatings. An excellent long-term record of the loss of Sr through ion exchange in the zeolites is given by the Sr concentrations in coexisting calcite, which are a few hundred ppm through much of the UZ, and then drop to a few ppm below zeolitic layers in the Calico Hills unit (Vaniman and Chipera 1996 [100089], pp. 4428–4429, Table 3). This corroborates the model results showing flow through the zeolitic units and Sr exchange with Ca in zeolites, resulting in waters having very low Sr concentrations.

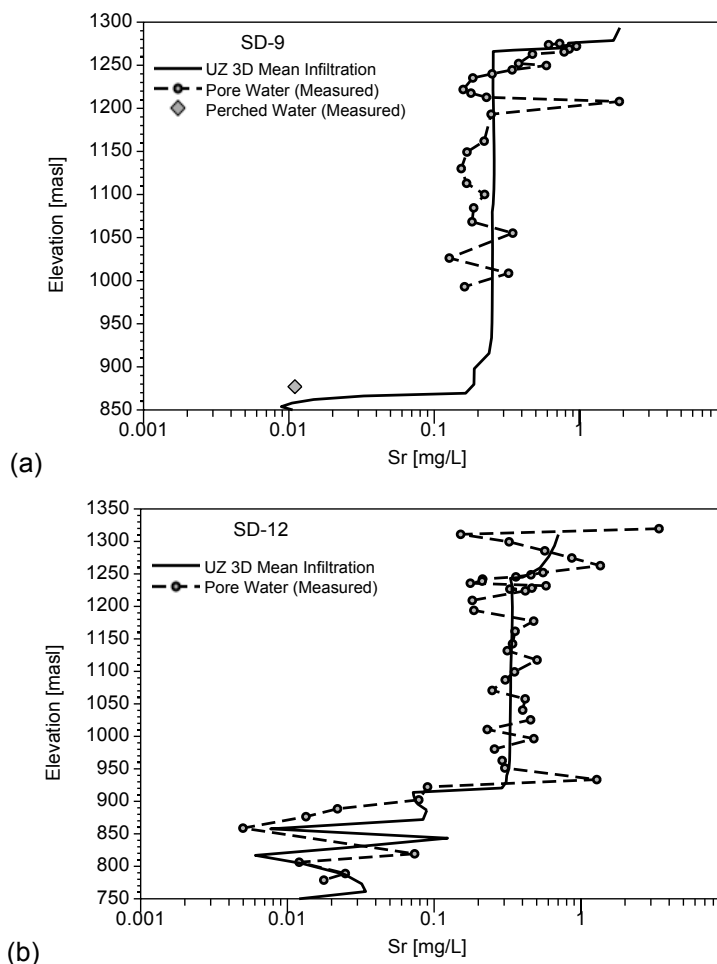
7.10.3 Model for 3-D Sr Concentrations

A first approximation to modeling Sr concentrations in the UZ is to consider Sr as a conservative species in the nonzeolitic units and an exchangeable species in the zeolitic units (Sonnenthal and Bodvarsson 1999 [117127], p. 143). Simulations were run based on the model for Cl used in Section 6.5 employing the base-case present-day infiltration rate (scenario “preq_mA” in Table 6.5-2). The only modifications to this model were for the Sr diffusion coefficient ($7.94 \times 10^{-10} \text{ m}^2/\text{s}$ at 25°C ; Lasaga 1998 [117091], p. 315) and the Sr distribution coefficient (K_d) in zeolitic rocks ($1.0 \text{ m}^3/\text{kg}$; DTN: LA0302AM831341.002 [162575]). The latter value for the K_d is the approximate mean based on a range from 0.05 to $2.0 \text{ m}^3/\text{kg}$ provided in the DTN. Because all the K_d values in this range would result in a moderate to strong shift in pore water Sr concentrations from nonzeolitic to zeolitic rocks, the effect of assuming a uniform K_d only results in uncertainty in the degree to which concentrations within and below the zeolitic units are shifted to lower values.

Strontium input at the surface was assumed to be wholly from precipitation, using an approximate Cl/Sr concentration ratio in precipitation of approximately 100 (Sonnenthal and Bodvarsson 1999 [117127], p. 147). The lower boundary condition (saturated zone) was set to zero concentration. Although this is less than the potential Sr concentrations in the saturated zone, the effect on the UZ would be limited to gridblocks adjacent to the lower boundary only, where few samples have been collected. The simulation was run for 4 million years using T2R3D V1.4 (LBNL 1999 [146654]), which resulted in a steady state concentration distribution. Simulations run for 1 and 2 m.y. showed some deviation from steady-state in low permeability gridblocks near the base of the domain, but not in most of the UZ locations where samples were collected. Although the 4 m.y. simulation may still show slight deviation from steady state in the

bottom gridblocks where concentrations are very low, the differences do not impact the model validation.

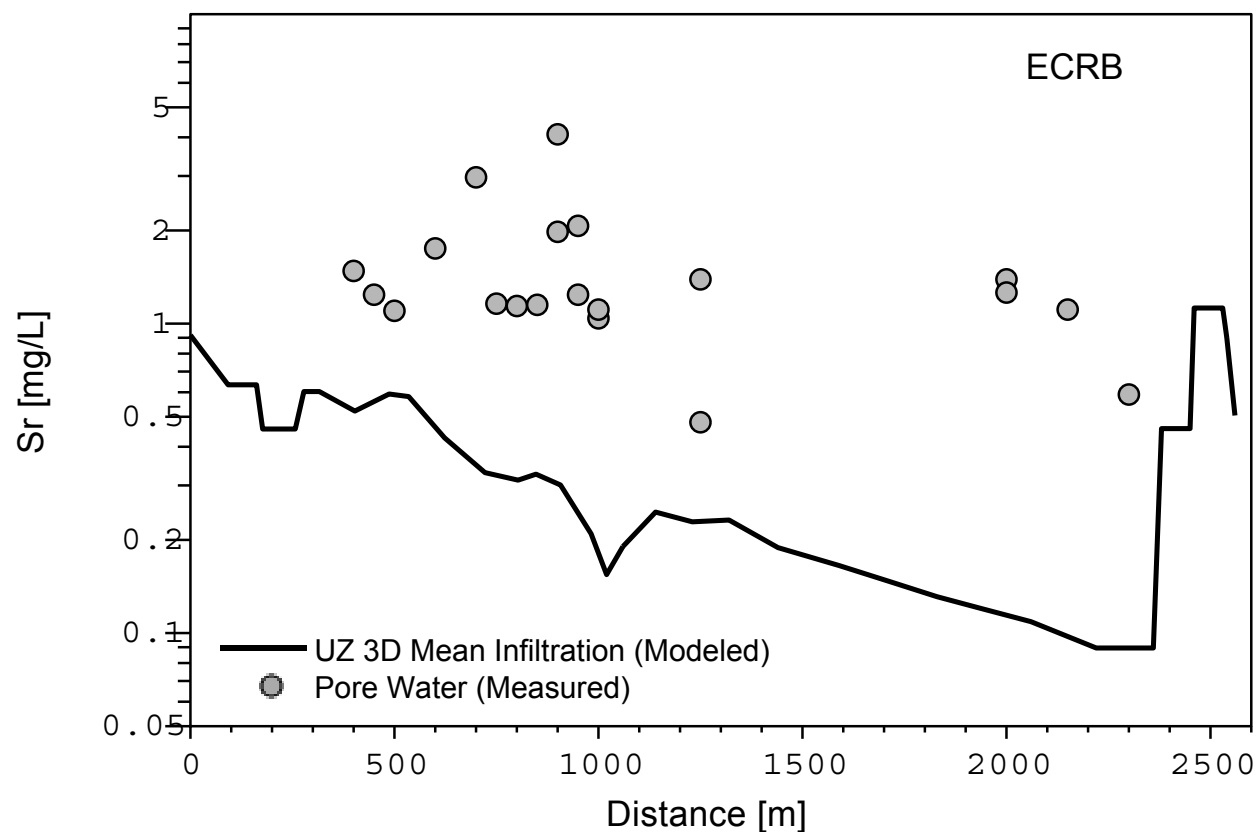
Modeled Sr concentrations are compared to measured values for pore salts extracted (by leaching) from two surface-based boreholes (SD-9 and SD-12; DTN: GS990308315215.004 [145711]), perched waters, and pore waters obtained by ultracentrifugation of core samples from the ECRB (DTN: GS020408312272.003 [160899]). Comparison of measured and modeled Sr concentrations as a function of elevation for the surface-based boreholes is shown in Figure 7.10-1(a and b). Inputs and outputs for the 3-D Sr Model simulations have been submitted to the TDMS under Output-DTN: LB0304UZSRTRAN.001. Measured concentrations in the UZ above the perched water show a range of concentrations from about 0.1 to 2 mg/L, with perched-water concentrations (and pore-water concentrations at a similar depth) closer to 0.01 mg/L. This sharp reduction in Sr concentrations is greater than the equivalent drop in Cl concentrations in the perched-water bodies and is consistent with ion exchange in zeolitic rocks. Strong variations exist in the measured Sr concentrations as a function of depth in the UZ. However, no distinct trends can be discerned. The steady-state modeled concentrations above the perched water are very close to the mean values in boreholes SD-9 and SD-12. Where perched water samples were collected in SD-9, the model results capture the drop in concentration quite closely. In SD-12, the measured and modeled concentrations below 900 meters exhibit a reversal to higher concentrations. This reversal is consistent with lateral flow in the vitric units, rather than simple vertical flow through the zeolitic units that would result in consistently low concentrations below them. The criterion for validation is qualitative agreement between the simulated strontium concentrations and the average of the observations at the same elevation, and agreement with the vertical trends (BSC 2002 [160819], Attachment I-1-2-5). The comparisons shown for the surface-based boreholes meet the validation criteria.



DTN: GS990308315215.004 [145711]
 Model Input and Outputs DTN: LB0304UZSRTRAN.001

Figure 7.10-1. Comparison of Measured and Modeled Sr Concentrations as a Function of Elevation for the Surface-Based Boreholes (a) SD-9 and (b) SD-12

Measured and modeled Sr concentrations in pore waters extracted from cores taken in the ECRB are shown in Figure 7.10-2. Measured concentrations are nearly all between 1 and 2 mg/L, with one sample having a concentration of about 3.6 mg/L. These concentrations are generally much higher than those measured in the surface-based boreholes. It is not clear if the different techniques used (leaching in the surface-based samples and ultracentrifugation in the ECRB) have resulted in any systematic bias in the Sr concentrations. Consistent with the lower Cl concentrations in most ECRB samples, compared to areas to the east where the infiltration rates are expected to be lower, the modeled Sr concentrations are also generally lower. Although the comparison of measured and modeled concentrations generally meet the order-of-magnitude criterion, the deviations are generally greater than that for the surface-based boreholes. Ratios for $^{87}\text{Sr}/^{86}\text{Sr}$ are not available for these samples, and therefore the degree to which Sr concentrations may have been shifted to higher values by water-rock interaction cannot be assessed. Bulk-rock compositions for major and trace elements for tuffs in the ECRB are virtually identical to samples collected elsewhere (Peterman and Cloke 2002 [162576], pp. 696). Consequently, a shift caused by locally greater water-rock interaction (in the welded tuffs) is not likely.



DTN: GS020408312272.003 [160899]
 Model Input and Outputs DTN: LB0304UZSRTRAN.001

Figure 7.10-2. Measured and Modeled Sr Concentrations in Pore Waters Extracted from Cores Taken in the ECRB

The Sr model has been validated sufficiently for the purpose of LA. Additional confidence will be gained by direct incorporation of water-rock interaction and Sr isotopes to constrain the extent of Sr addition/loss to the rock, thus reducing uncertainties.

8. CONCLUSIONS

This Model Report documents the development, results, and analyses of the UZ Flow Model and its submodels in accordance with the requirements of Section 5.4.1(b) of AP-SIII.10Q. These models and modeling analyses include the following:

- 3-D UZ calibration and flow field model for generating nine base-case flow fields
- 3-D UZ alternative flow field model for generating nine alternative flow fields
- Mountain-scale, ambient TH model
- 3-D gas flow model
- Chloride submodel
- Calcite analysis
- Tracer transport analysis
- Modeling analysis of active fracture model
- Model validation activities and results.

The UZ Flow Model and its submodels are developed to simulate past, present, and future hydrogeological, geothermal, and geochemical conditions and processes within the Yucca Mountain UZ to support various TSPA-LA activities. In particular, as part of the output of this Model Report, nine 3-D, base-case steady-state flow fields of the Yucca Mountain UZ system have been generated for TSPA-LA calculations. This Model Report has documented the UZ Flow Model and its submodels in terms of modeling approaches, hydrogeological conceptual models, data source and incorporation, methodology of model calibrations, model parameter estimation and modifications, and model results and analysis of the 18 flow fields (9 base-case + 9 alternative). This report also includes associated analyses on tracer transport with the 18 flow fields. The development and calibration of the mountain-scale ambient TH, gas flow, chloride, calcite, and strontium models are mainly for building confidence in the UZ Flow Model, with the output data and tracking numbers listed in Table 8-1.

Table 8-1. Output Data and Data Tracking Numbers

DTN	Location in this report			Remarks
	Text	Figure	Table	
LB03023DSSCP9I.001*	6.8.1, 6.8.2.1, 7.2, 7.3, 7.5, 9.4	Figures 6.2-2-4, 6.6-1-4, 6.6-6, 6.6-8, 6.6-10, 6.6-12, 6.6-14, 6.6-16, 6.6-18, 6.6-20, 6.6-22, 6.6-23, 7.2-1, 7.3-1	Tables 6.2-10, 6.6-3, 6.7-2	Results of nine flow fields (base case), input/output files, and simulations results to be used by TSPA-LA
LB03033DSSFF9I.001	9.4	Figures 6.6-5, 6.6-7, 6.6-9, 6.6-11, 6.6-13, 6.6-15, 6.6-17, 6.6-19, 6.6-21, 6.6-23	Tables 6.6-2, 6.6-4, 6.7-3	Results of nine flow fields (alternative and supporting files for both base case and alternative flow fields), input/output files, and simulation results
LB03033DUZTRAN.001	9.4	Figures: 6.7-1-6.7-8	Tables: 6.7-2-6.7-5	Tc and Np Transport simulation scenarios, input/output files; using nine base-case and nine alternative flow fields
LB0303THERMSIM.001	9.4	Figures 6.3-2-4, 7.7-1-3		3-D UZ ambient thermal model, Input/output, supporting files, and simulation results
LB0303THERMESH.001	6.3.4, 9.4	Figure 6.3-1	Table 6.3-1	3-D UZ thermal model grid
LB0303GASFLW3D.001	9.4	Figures 6.4-1, 6.4-2, 7.4-1, 7.4-2		3-D gas flow model, input/out, supporting files, and simulation results
LB0303C14INF3D.001	9.4	Figures 7.5-1, 7.5-2		C-14 simulations, input/output files, and simulation results
LB03013DSSCP3I.001	6.3.4, 6.4.1, 7.2, 9.4		Tables 6.2-5-9, 6.6-1, Attachment I Tables I-1 to I-6	3-D site scale model calibrated property sets: Data Summaries
LB0303CLINFL3D.001	9.4	Figures 6.5-1-4, 7.8-1		Cl transport simulation results, input/output files
LB0304RDTRNSNS.001	9.4	Figures 6.8-1-4	Tables 6.8-1, 6.8-2	3-D flow and transport sensitivity analysis with active fracture model parameter, input/output, supporting files, and simulation results
LB0304UZSRTRAN.001	7.10.3, 9.4	Figures 7.10-1, 7.10-2		UZ strontium transport model, input/output files, and simulation results
LB0303A8N3MDLG.001	9.4	Figures 7.6-1, 7.6-4, 7.6-6, 7.6-7, 7.6-8, 7.6-9, 7.6-10	Tables 7.6-2, 7.6-3	Alcove 8/Niche 3 Seepage Modeling: Simulation files and results
LB0305TSPA18FF.001			Table 6.2-11	Eighteen 3-D Site Scale UZ Flow Fields Converted from TOUGH2 to T2FEHM format (See Attachment IV.2)
LB0305PTNNTSW9I.001	Attachment IV IV.1			PTN/TSW Interface Percolation Flux Maps for 9 Alternative Infiltration Scenarios
LB0302PTNNTSW9I.001	Attachment IV IV.1			PTN/TSW Interface Percolation Flux Maps for 9 Alternative Infiltration Scenarios

NOTE: *The nine base-case flow fields will be directly used for TSPA-LA.

8.1 UZ FLOW MODEL CALIBRATION

As a critical step, field-measured saturation, water potential, and perched-water data have been used to calibrate the UZ Flow Model. Such calibrations are part of the important iterative processes of model development to increase confidence in model predictions of site conditions. This Model Report continues this model calibration effort using the 1-D inversions reported in the Model Report (BSC 2002 [160240]) and in the previous 3-D modeling effort (BSC 2001 [158726]). This work focuses particularly on the PTn unit and potential perched-water layers using a 3-D forward calibration approach.

Calibration was conducted using three sets of rock-property parameters (BSC 2002 [160240]), associated with present-day lower, mean, and upper infiltration rates, and the current geological model and numerical grid (BSC 2002 [160109]). Two sets of rock properties were examined for the PTn units, with one set selected to be included in the base case and the other for the alternative set, based on analysis of chloride data. In addition, a permeability-barrier conceptual model was adopted for modeling water-perching occurrences. Under the permeability barrier concept, rock properties were locally modified to better match data in several grid layers near the observed perched zones.

The model calibration efforts conclude that the UZ Flow Model can reproduce moisture conditions in the Yucca Mountain UZ in terms of liquid saturations and water potentials, as verified by observations. In general, the modeled results from all nine base-case flow-field simulations using the perched-water conceptual model are in good agreement with the measured water-perching elevations at seven boreholes for upper-bound and mean present-day infiltration scenarios. However, under the lower-bound present-day infiltration rate, the models did not match the perched-water data very well in boreholes SD-7, SD-9, NRG-7a, and UZ- 14 because of the low percolation fluxes at these locations. This will have little effect on flow fields.

The UZ Flow Model provides results of steady-state fluid and heat flow as well as transient tracer transport. Flow processes for model layers above the TSw and PTn units may be subject to episodic infiltration. Since the model results with these layers may not reflect actual conditions, which are time- and scale-dependent, therefore the results may be directly applicable to studies on a much smaller scale such as the emplacement drift. In this report, the uncertainties in the results owing to input-parameter and model-gridding uncertainties are evaluated by generating a number of flow fields with various parameter sets, infiltration maps, and conceptual models.

8.2 GEOTHERMAL MODEL CALIBRATION

The ambient geothermal model simulates large-scale UZ geothermal and heat flow conditions. The 3-D ambient thermal model was calibrated against qualified temperature data measured from five boreholes, using the base-case present-day infiltration parameter set with a 3-D dual-permeability thermal grid. Simulated temperature results are in good agreement with the observed temperature profiles from the boreholes. Such results provide the ambient temperature distributions that determine boundary and initial conditions for the mountain-scale and drift-scale TH, THC, and THM coupled-process models.

8.3 GAS FLOW MODEL

A 3-D pneumatic simulation has been performed as a part of the UZ Flow Model calibration effort. Results of gas flow simulations are compared to the measured pneumatic data from three boreholes, including SD-7, SD-12, and UZ-7a, for the purposes of calibration and validation. As a result of calibration, fracture permeability in several TSw layers were reduced by a factor of 15, leading to an overall good match between the 3-D model prediction and measurement of pneumatic data under 3-D flow conditions. The gas flow calibration results add confidence that the UZ Flow Model is reliable and appropriate for modeling gas flow in the UZ.

8.4 CHLORIDE SUBMODEL

Chloride is a naturally occurring conservative tracer. It enters the groundwater system as a solute in the infiltration flux. Thus, chloride data can be used to examine the long-term infiltration rate in the Flow Model. The chloride flux to the UZ at Yucca Mountain is calculated based on the precipitation, runoff, and runoff at the ground surface of the mountain.

The chloride transport modeling considered four scenarios of infiltration rates, including present-day (or modern) mean, upper, and lower bounds, as well as glacial transition mean infiltration. Each scenario compares the results of two sets of flow fields with different PTn properties, one set denoted as a base-case flow field and the other as an alternative set, in order to study the effect of potential lateral flow in the PTn unit. The base case incorporates a property set of the PTn that would more likely cause lateral flow diversion, with the alternative less likely. Results show that the chloride transport model with the base case in the present-day, mean infiltration yields the closest and most consistent match with field data. In other words, the property set of the PTn that would favor lateral flow diversion (in the PTn unit) yields more reasonable results in matching the chloride concentration in the field samples. It indicates that lateral diversion may occur in the PTn unit at Yucca Mountain.

8.5 CALCITE SUBMODEL

Calcite precipitation has been modeled in unsaturated fractured rocks, considering several essential factors: (1) infiltration rate, (2) ambient geothermal gradient, (3) gaseous CO₂ diffusive transport and partitioning between liquid and gas phases, and (4) fracture-matrix interaction for water flow and chemical constituents, and (5) water-rock interaction.

Modeling calcite deposition can be used to build some constraints on the infiltration-percolation flux. The modeling also provides additional evidence for validation of the UZ Model. Over a range of 2–20 mm/yr infiltration rates, the simulated calcite distributions capture the measured data from the WT-24 well cuttings. The 20 mm/yr infiltration rate may be the upper bound for the WT-24 location, whereas the base-case infiltration rate (5.92 mm/yr) used for the flow model gives the closest match to the data. The observed calcite precipitation for the top of TSw occurs mostly in the fractures, which is also captured by the modeling. The modeled results can provide useful insight into process mechanisms such as fracture-matrix interaction, as well as conditions and parameters controlling calcite deposition. The modeled calcite abundances generally increase with increasing infiltration rate, but become less sensitive to infiltration at higher rates as a result of its impact to the geothermal gradient. Data from borehole SD-6 are roughly consistent with the relation between infiltration rate and calcite abundances, although a locally higher thermal gradient in the PTn can also be a factor in the calcite distribution.

8.6 TSPA FLOW FIELDS

Eighteen 3-D UZ flow fields (nine for the base case and nine for the alternative ones) were generated for TSPA-LA calculations. The nine base-case flow fields were produced for use by FEHM in the TSPA calculations. These flow fields were based on (1) the TSPA-LA grid (BSC 2002 [160109]), (2) nine infiltration maps representing three climates; (3) the six parameter sets; and (4) the two conceptual models of PTn flow and a perched-water conceptual model with the calibrated perched-water parameters. The purpose of studying a large number of flow fields for various modeling scenarios was to cover all TSPA-LA scenarios and to account for possible current and future site conditions. Alternative parameter sets for the PTn were used to investigate conceptual model uncertainty. The main uncertainties currently considered in the UZ Flow Model included fracture-matrix properties, present-day and future net infiltration rates over the mountain, and conceptual models for perched water occurrence, and the role of PTn for lateral flow.

A detailed analysis of simulated percolation fluxes at the repository level and at the water table was conducted for all simulation scenarios of 18 flow fields. These percolation fluxes and their distributions at the repository level indicated that there exists a certain amount of large-scale lateral flow or diversion by the PTn unit (on the order of several hundreds of meters) for the nine base-case simulations. In comparison, the nine alternative flow fields predict smaller lateral diversion when flowing through the PTn unit. In both models, however, significant flow diversion and redistribution into faults within the PTn unit is predicted. On the other hand, a comparison of simulated percolation fluxes at the repository level with those at the water table indicated that significant lateral flow occurs at perched or zeolitic layers when traveling through the CHn layers.

Fracture-matrix flow components at the repository horizon and at the water table were also analyzed for the 18 simulations. The statistics show that fracture flow is dominant in the welded tuffs, both at the repository horizon and at the water table, in all the 18 flow fields. For three present-day infiltration scenarios—fracture-matrix flow components simulated at the repository level—fracture flow contributes more than 90% of total flow, and at the water table—70–80% of the total flow. Furthermore, faults provide major flow pathways for focused percolation fluxes. Fault flow percentage increases with depth from 30–40% at the repository level to 60% at the water table (Section 6.6.3, Tables 6.6-3 and 6.6-4).

8.7 TRACER TRANSPORT TIMES

A total of 40 tracer transport simulations were conducted to obtain insight into the impacts of infiltration rates, perched-water and PTn conceptual models, and retardation effects on tracer migration from the repository to the water table (Section 6.7). All the 18 TSPA-LA flow fields were incorporated into these 40 transport runs. For each flow field, there were two tracer transport runs, one for conservative (or nonadsorbing) and the other for reactive (or adsorbing) tracer transport, respectively, with tracer release from repository fracture blocks. For the two present-day mean infiltration cases, tracer release from repository matrix blocks was also investigated, resulting in four additional transport runs. These tracer-transport studies indicate that there exist a wide range of tracer transport times associated with different infiltration rates, type of tracers, and PTn water conceptual models. The most important factors for tracer-transport times are found to be (1) surface infiltration rates; (2) adsorption effects in the CHn unit; and (3) release from repository fracture or matrix blocks.

Statistics of tracer transport times at 10% and 50% mass breakthrough at the water table from the 40 simulations show that tracer-transport times are inversely proportional to average surface infiltration. When the average infiltration rate increases from 5 to 35 (mm/yr), average tracer transport (50% breakthrough) times decrease by two to three orders of magnitude. Nonadsorbing tracers migrate one to two orders of magnitude faster than adsorbing tracers when traveling from the repository to the water table under the same infiltration conditions. The base-case flow fields predict a little shorter or more conservative tracer transport times than the alternative ones in general. The simulation results show that the two different PTn models have an insignificant impact on tracer transport at the lower units, i.e., from the repository to the water table.

8.8 SENSITIVITY ANALYSIS OF ACTIVE-FRACTURE-MODEL PARAMETER

The impacts of uncertainty in the active fracture parameter (γ) on the simulated flow and transport were evaluated by sensitivity analyses of flow and transport simulation results (Section 6.8). Two additional 3-D flow simulations, using reduced values of active fracture parameter γ for TSw units and all units below the repository (including the units where the repository is located), respectively, were performed to carry out the analyses. By comparing liquid saturation, water potential, and the percolation flux obtained by these two simulations with those obtained by simulations using unmodified (calibrated) γ values, we found that the changes in liquid saturation, water potential, and percolation flux are rather small. In general, the flow fields are not very sensitive to the active fracture parameter γ . On the other hand, tracer transport times were found to be sensitive to the value.

8.9 MODEL VALIDATION

Model validation efforts have been documented in this Model Report. Validation activities for the UZ Flow Model include corroboration with experimental data and modeling studies, using the following corroboration with experimental data: (1) ECRB observation data; (2) WT-24 perched-water data; (3) gas flow data from boreholes SD-12 and UZ-7a; (4) borehole measured ^{14}C data; and Alcove 8 flow and seepage test results. In addition, validation efforts are also performed for the ambient thermal model, chloride model, calcite model, and strontium model using field observed data from surface-based boreholes or from the ESF.

In all these validation examples, the simulation results of the UZ Flow Model and Submodels are shown to be able to match different types of available observation data, such as water potentials, perched-water locations, tracer and geochemical concentrations, temperatures and pneumatic pressures. The criteria of the model validation of the TWP are in general satisfied. These efforts have provided validation of the UZ Flow Model and its submodels for their accuracy and reliability in describing hydrological, thermal and chemical conditions and predicting flow and transport processes in the UZ system of Yucca Mountain.

8.10 BARRIER CAPABILITY OF THE UZ

The 500-700 m thick UZ consists of surficial soils and the TSw, PTn, TSw and CHn units above and below the repository. The thick UZ formation itself is a natural barrier to downward water percolation and transport. The flow model documented in this Model Report quantitatively describes the barrier capabilities of the UZ. The surficial soils function as a barrier by diverting (as runoff) some of the water that arrives as precipitation and runoff, and by storing the remainder so that some of it is evaporated as evapotranspiration. Substantial amount of water

thus diverted or evaporated cannot percolate as net infiltration (USGS 2001 [160355], p. 23). The surficial soils are shown to be an effective natural barrier to water recharge and surface infiltration, using the statistics of Tables 6.5-2 and 6.1-2 for the present-day climates. Table 8-2 lists the estimated percentage of net infiltration (Table 6.1-2) over net recharge (=precipitation+runon-runoff, Table 6.5-2), indicating that only 0.63%, 1.95%, and 2.5% of net water recharge on the model top boundary penetrates the top soil layer and becomes net infiltration, respectively, for the lower-, mean, and upper-bound infiltration scenarios. More than 97% of net recharge returns to the atmosphere by evapotranspiration.

Table 8-2. Percentage of Net Infiltration over Net Recharge after Evapotranspiration for Present-Day/Modern Climates over the Model Domain)

Present-day/Modern Infiltration Scenarios	Precipitation¹ (mm/year)	Net recharge¹ (mm/year)	Net infiltration² (mm/year)	Net Infiltration %
Low	185.9	198.5	1.25	0.63
Mean	189.5	227.1	4.43	1.95
Upper	267.1	429.9	10.74	2.50

NOTES: ¹ from Table 6.5-2
² from Table 6.1-2

Barrier capability of the UZ below the surficial soils is the subject of the present model report. We first consider UZ tuffs above and below the repository: water not diverted or evaporated by surficial soils and evapotranspiration entering the UZ formation as net infiltration, which is set as the surface boundary recharge condition for the UZ flow model. The UZ formation units above the repository serve as a barrier by storage and diversion. Percolating water flow through the PTn is matrix-dominated flow rather than fracture-dominated flow, which has been shown in Section 6.6-3 to subject to strong capillary barrier effects and lateral diversion. Therefore, the PTn unit buffers the repository from sudden changes in percolation flux and from episodic surface infiltration pulses. Because of predicted climate changes, the Yucca Mountain region as well as the UZ is expected in the future to receive more precipitation and more infiltration than at present, so that percolation flux at the repository horizon will increase. Storage in the UZ above the repository, particularly in the PTn unit, will significantly delay the increase in percolation flux below the PTn. However, the modeling approach adopted here ignores that delay because the flow field is modeled as changing instantly to the long-term steady state. This ignores the lower net infiltration during the transitional period and results in more conservative model predictions.

Lateral flow diversion within the PTn due to the capillary barrier effect is demonstrated in this Model Report by two conceptual models. This lateral diversion diverts a large amount of percolation flux into faults, which becomes fast and focused flow pathways, which may bypass repository drifts. For example, the UZ Model predicts with the present-day mean infiltration that more than 25% of percolation is diverted to faults by the units above the repository, mainly by the PTn. This will, on average, reduce percolation fluxes at the repository horizon, which is the driving force for potential seepage into drifts. Lateral diversion in the PTn thus reduces the amount of water seeping into drifts, which may transport radionuclides to the saturated zone.

Below the repository horizon, the UZ also has a barrier capability of delaying radionuclide transport to the saturation zone. The UZ does this by retarding the water flow and by removing

some of the radionuclides by sorption. The flow in the UZ below the repository horizon is partially through perched water bodies and low-permeability zeolitic zones of the CHn. Flow through perched water bodies or zeolitic zones is slow because of the permeability in these areas. Percolation flux may also be diverted horizontally over perched water bodies caused by permeability barriers. This laterally diverted flow through perched water bodies travels slowly, because of the longer distance and the smaller driving force (gravity gradient). Overall, low-permeability zeolitic zones and perched-water bodies retard downward percolation flux and increase tracer travel times. This increased residence time enhances adsorption and matrix diffusion effects while radionuclides are transported through these regions.

The other portion of the flow below the repository goes through unfractured CHn vitric zones of the Calico Hills formation, and is retarded by low matrix permeability and large pore storage. This will also promote diffusion of radionuclides from fractures to matrix, and delay overall transport times. Furthermore, all UZ tuffs, even in faults, have some adsorptive capacity for radionuclides, regardless of zeolitic or vitric units of the CHn. Adsorbing effect of radionuclides on unsaturated tuffs not only delays its arrival at the water table, but reduces the transported mass by radioactive decay.

8.11 LIMITATIONS

The UZ Flow Model and submodels are appropriate tools for characterizing flow and transport processes in the UZ of Yucca Mountain. The accuracy and reliability of the UZ Flow Model predictions are critically dependent on the accuracy of estimated model properties, other types of input data, and hydrogeological conceptual models. These models are limited mainly by the current understanding of the mountain system, including the geological and conceptual models, the volume-average modeling approach, and the available field and laboratory data.

Past site investigations have shown that large variabilities exists in the flow and transport parameters over the spatial and temporal scales of the mountain. Even though considerable progress has been made in this area, uncertainty associated with the UZ Flow Model input parameters will continue to be a key issue for future studies. The major uncertainties in the UZ Model parameters are: (1) accuracy of estimated current, past, and future net infiltration rates over the mountain; (2) quantitative descriptions of the heterogeneity of welded and nonwelded tuffs, their flow properties, and detailed spatial distributions within the mountain, especially below the repository; (3) fracture properties in zeolitic units and faults from field studies; (4) evidence of lateral diversion caused by zeolites in the CHn units and within the PTn units; and (5) transport properties (e.g., adsorption or K_d coefficients in different rock types, matrix molecular diffusion coefficients in different units for different radionuclides, dispersivities in fracture and matrix systems). These uncertainties exist, but they have been addressed with the modeling studies in this Model Report. In particular, most uncertainties are captured in the range of flow field generated.

This document and its conclusions may be affected by technical product input information. However, the results and conclusions of the UZ flow fields will not be affected by the status of temperature and geochemistry data used in the calibration or validation studies, because these flow fields are based on flow simulations under isothermal and different climate conditions.

8.12 SATISFACTION OF ACCEPTANCE CRITERIA

In section 4.2, seven NRC acceptance criteria were identified. How they are satisfied are discussed as follows.

For criteria from Section 2.2.1.1.3 of YMRP (NRC 2003 [163274])

- AC 1 System Description and Model Integration are adequate: The UZ system is described in Section 6.1. This description is based on data from field and laboratory investigations, and is consistent with standard conceptual models of the UZ at Yucca Mountain. In addition, spatial variability of model parameters are adequately represented by the 3-D model grid, with more than 60 different types of fracture-matrix properties, while spatial variability of model parameters are sufficiently covered by six sets of parameters calibrated to different infiltration rates. The model calibration and validation activities show that the description is adequate for modeling UZ flow and transport
- AC 2 data are sufficient: Data from field and laboratory testing have been synthesized and used to calibrate the model. The model validation shows that these data are sufficient to justify the model for its intended use.
- AC3 Data uncertainty is characterized and propagated: Hydrological properties used in the UZ Flow Model have been calibrated (BSC 2003 [160240]; [161773]) using mean, upper, and lower bound infiltration maps, thus capturing the uncertainty in model parameters. Three flow fields were generated for each future climate condition (present day, monsoon, and glacial transition).
- AC4 Model uncertainty is characterized and propagated: Two property sets for the PTn were used to study the alternative flow model in which lateral flow occurs in the PTn .

For criteria from Section 2.2.1.3.6.3 of YMRP (NRC 2003 [163274]):

- AC1 Identification of barriers is adequate: The model simulates flow and transport in the unsaturated rocks above and below the repository horizon, two natural barriers identified in BSC (2002 [160146]) TDR-WIS-PA-000006. Barrier capability is described in Section 8.10.
- AC 2 Description of barrier capability to isolate waste is acceptable: Barrier capability is determined by the delay in transport of radionuclides to the water table. Simulations of tracer transport time have been validated, showing that the description is acceptable.
- AC3 Technical basis for barrier capability is adequately presented: In Section 6.7, radionuclide transport from repository to the water table is presented in more than forty simulations, incorporating eighteen 3-D flow fields.

INTENTIONALLY LEFT BLANK

9. INPUTS AND REFERENCES

The following is a list of the references cited in this document. Column 1 represents the unique six digit numerical identifier (the Document Input Reference System [DIRS] number), which is placed in the text following the reference callout (e.g., BSC 2002 [160819]). The purpose of these numbers is to assist the reader in locating a specific reference. Within the reference list, multiple sources by the same author (e.g., BSC 2002) are sorted alphabetically by title.

9.1 DOCUMENTS CITED

- 101180 Ahlers, C.F.; Bandurraga, T.M.; Bodvarsson, G.S.; Chen, G.; Finsterle, S.; and Wu, Y-S. 1995. *Summary of Model Calibration and Sensitivity Studies Using the LBNL/USGS Three-Dimensional Unsaturated Zone Site-Scale Model*. Milestone 3GLM107M. Berkeley, California: Lawrence Berkeley National Laboratory. ACC: MOL.19960208.0092.
- 109715 Ahlers, C.F.; Finsterle, S.; and Bodvarsson, G.S. 1999. "Characterization and Prediction of Subsurface Pneumatic Response at Yucca Mountain, Nevada." *Journal of Contaminant Hydrology*, 38, (1-3), 47-68. New York, New York: Elsevier. TIC: 244160.
- 156269 Bear, J. 1972. *Dynamics of Fluids in Porous Media*. Environmental Science Series. Biswas, A.K., ed. New York, New York: Elsevier. TIC: 217356.
- 153427 Benson, C.F. and Bowman, R.S. 1996. "Erratum, Tri- and Tetrafluorobenzoates as Nonreactive Tracers in Soil and Groundwater." *Soil Science Society of America Journal*, 60, 1780. Madison, Wisconsin: Soil Science Society of America. TIC: 246741.
- 105170 Birkholzer, J.; Li, G.; Tsang, C-F.; and Tsang, Y. 1999. "Modeling Studies and Analysis of Seepage into Drifts at Yucca Mountain." *Journal of Contaminant Hydrology*, 38, (1-3), 349-384. New York, New York: Elsevier. TIC: 244160.
- 100103 Bodvarsson, G.S.; Bandurraga, T.M.; and Wu, Y.S., eds. 1997. *The Site-Scale Unsaturated Zone Model of Yucca Mountain, Nevada, for the Viability Assessment*. LBNL-40376. Berkeley, California: Lawrence Berkeley National Laboratory. ACC: MOL.19971014.0232.
- 120055 Bodvarsson, G.S.; Boyle, W.; Patterson, R.; and Williams, D. 1999. "Overview of Scientific Investigations at Yucca Mountain—The Potential Repository for High-Level Nuclear Waste." *Journal of Contaminant Hydrology*, 38, (1-3), 3-24. New York, New York: Elsevier. TIC: 244160.
- 162477 Bodvarsson, G.S.; Kwicklis, E.; Shan, C.; and Wu, Y.S. 2003. "Estimation of Percolation Flux from Borehole Temperature Data at Yucca Mountain, Nevada." *Journal of Contaminant Hydrology*, 62-63, 3-22. New York, New York: Elsevier. TIC: 254205.

- 160133 Bodvarsson, G.S.; Liu, H.H.; Ahlers, C.F.; Wu, Y-S.; and Sonnenthal, S. 2001. "Parameterization and Upscaling in Modeling Flow and Transport in the Unsaturated Zone of Yucca Mountain." Chapter 11 of *Conceptual Models of Flow and Transport in the Fractured Vadose Zone*. Washington, D.C.: National Academy Press. TIC: 252777.
- 155638 BSC (Bechtel SAIC Company) 2001. *EBS Radionuclide Transport Abstraction*. ANL-WIS-PA-000001 REV 00 ICN 03. Las Vegas, Nevada: Bechtel SAIC Company. ACC: MOL.20010806.0076.
- 158463 BSC (Bechtel SAIC Company) 2001. *In Situ Field Testing of Processes*. ANL-NBS-HS-000005 REV 01. Las Vegas, Nevada: Bechtel SAIC Company. ACC: MOL.20020108.0351.
- 158204 BSC (Bechtel SAIC Company) 2001. *Multiscale Thermohydrologic Model*. ANL-EBS-MD-000049 REV 00 ICN 02. Las Vegas, Nevada: Bechtel SAIC Company. ACC: MOL.20020123.0279.
- 161340 BSC (Bechtel SAIC Company) 2001. *Radionuclide Transport Models Under Ambient Conditions*. MDL-NBS-HS-000008 REV 00 ICN 01. Las Vegas, Nevada: Bechtel SAIC Company. ACC: MOL.20020409.0011.
- 160828 BSC (Bechtel SAIC Company) 2001. *Unsaturated Zone and Saturated Zone Transport Properties (U0100)*. ANL-NBS-HS-000019 REV 00 ICN 02. Las Vegas, Nevada: Bechtel SAIC Company. ACC: MOL.20020311.0017.
- 156609 BSC (Bechtel SAIC Company) 2001. *Unsaturated Zone Flow Patterns and Analysis*. MDL-NBS-HS-000012 REV 00. Las Vegas, Nevada: Bechtel SAIC Company. ACC: MOL.20011029.0315.
- 158726 BSC (Bechtel SAIC Company) 2001. *UZ Flow Models and Submodels*. MDL-NBS-HS-000006 REV 00 ICN 01. Las Vegas, Nevada: Bechtel SAIC Company. ACC: MOL.20020417.0382.
- 160247 BSC (Bechtel SAIC Company) 2002. *Analysis of Geochemical Data for the Unsaturated Zone*. ANL-NBS-HS-000017 REV 00 ICN 02. Las Vegas, Nevada: Bechtel SAIC Company. ACC: MOL.20020314.0051.
- 158375 BSC (Bechtel SAIC Company) 2002. *Drift-Scale Coupled Processes (DST and THC Seepage) Models*. MDL-NBS-HS-000001 REV 01 ICN 02. Las Vegas, Nevada: Bechtel SAIC Company. ACC: MOL.20020312.0156.
- 159124 BSC (Bechtel SAIC Company) 2002. *Geologic Framework Model (GFM2000)*. MDL-NBS-GS-000002 REV 01. Las Vegas, Nevada: Bechtel SAIC Company. ACC: MOL.20020530.0078.
- 160819 BSC (Bechtel SAIC Company) 2002. *Technical Work Plan for: Performance Assessment Unsaturated Zone*. TWP-NBS-HS-000003 REV 02. Las Vegas, Nevada: Bechtel SAIC Company. ACC: MOL.20030102.0108.

- 158966 BSC (Bechtel SAIC Company) 2002. *The Enhanced Plan for Features, Events, and Processes (FEPs) at Yucca Mountain*. TDR-WIS-PA-000005 REV 00. Las Vegas, Nevada: Bechtel SAIC Company. ACC: MOL.20020417.0385.
- 160146 BSC (Bechtel SAIC Company) 2002. *Total System Performance Assessment-License Application Methods and Approach*. TDR-WIS-PA-000006 REV 00. Las Vegas, Nevada: Bechtel SAIC Company. ACC: MOL.20020923.0175.
- 162268 BSC (Bechtel SAIC Company) 2003. *Abstraction of Drift Seepage*. MDL-NBS-HS-000019 REV 00C. Las Vegas, Nevada: Bechtel SAIC Company. ACC: MOL.20030728.0198. TBV-5280
- 161773 BSC (Bechtel SAIC Company) 2003. *Analysis of Hydrologic Properties Data*. MDL-NBS-HS-000014 REV 00. Las Vegas, Nevada: Bechtel SAIC Company. ACC: DOC.20030404.0004.
- 160240 BSC (Bechtel SAIC Company) 2003. *Calibrated Properties Model*. MDL-NBS-HS-000003 REV 01. Las Vegas, Nevada: Bechtel SAIC Company. ACC: DOC.20030219.0001.
- 160109 BSC (Bechtel SAIC Company) 2003. *Development of Numerical Grids for UZ Flow and Transport Modeling*. ANL-NBS-HS-000015 REV 01. Las Vegas, Nevada: Bechtel SAIC Company. ACC: DOC.20030404.0005.
- 163938 BSC (Bechtel SAIC Company) 2003. *Drift-Scale Radionuclide Transport*. MDL-NBS-HS-000016 REV 00C. Las Vegas, Nevada: Bechtel SAIC Company. ACC: MOL.20030804.0205.
- 162267 BSC (Bechtel SAIC Company) 2003. *Seepage Calibration Model and Seepage Testing Data*. MDL-NBS-HS-000004 REV 02. Las Vegas, Nevada: Bechtel SAIC Company. ACC: DOC.20030408.0004.
- 164325 BSC (Bechtel SAIC Company) 2003. *Underground Layout Configuration*. 800-P0C-MGR0-00100-000-00D. Las Vegas, Nevada: Bechtel SAIC Company. ACC: ENG.20030716.0002.
- 161770 Canori, G.F. and Leitner, M.M. 2003. *Project Requirements Document*. TER-MGR-MD-000001 REV 01. Las Vegas, Nevada: Bechtel SAIC Company. ACC: DOC.20030404.0003.
- 109051 Carey, J.W.; Chipera, S.J.; Vaniman, D.T.; and Bish, D.L. 1998. *Three-Dimensional Mineralogic Model of Yucca Mountain, Nevada: Rev 2.0*. Deliverable SP32BSM4. Los Alamos, New Mexico: Los Alamos National Laboratory, Earth and Environmental Sciences Division. ACC: MOL.20000110.0159.

- 162118 Carlos, B.A.; Chipera, S.J.; and Bish, D.L. 1995. "Calcite and Zeolite Fracture Coatings in Topopah Spring Tuff Along Drill Hole Wash, Yucca Mountain, Nevada." *High Level Radioactive Waste Management, Proceedings of the Sixth Annual International Conference, Las Vegas, Nevada, April 30-May 5, 1995*. Pages 100-102. La Grange Park, Illinois: American Nuclear Society. TIC: 215781.
- 100719 Codell, R.B. and Murphy, W.M. 1992. "Geochemical Model for 14C Transport in Unsaturated Rock." *High Level Radioactive Waste Management, Proceedings of the Third International Conference, Las Vegas, Nevada, April 12-16, 1992*. 2, 1959-1965. La Grange Park, Illinois: American Nuclear Society. TIC: 204231.
- 124052 CRWMS M&O (Civilian Radioactive Waste Management System Management and Operating Contractor) 1997. *The Site-Scale Unsaturated Zone Transport Model of Yucca Mountain*. Milestone SP25BM3, Rev. 1. Las Vegas, Nevada: CRWMS M&O. ACC: MOL.19980224.0314.
- 100356 CRWMS M&O 1998. "Unsaturated Zone Hydrology Model." Chapter 2 of *Total System Performance Assessment-Viability Assessment (TSPA-VA) Analyses Technical Basis Document*. B00000000-01717-4301-00002 REV 01. Las Vegas, Nevada: CRWMS M&O. ACC: MOL.19981008.0002.
- 123913 CRWMS M&O 2000. *Abstraction of Flow Fields for RIP (ID:U0125)*. ANL-NBS-HS-000023 REV 00. Las Vegas, Nevada: CRWMS M&O. ACC: MOL.20000127.0089.
- 141187 CRWMS M&O 2000. *Conceptual and Numerical Models for UZ Flow and Transport*. MDL-NBS-HS-000005 REV 00. Las Vegas, Nevada: CRWMS M&O. ACC: MOL.19990721.0526.
- 141407 CRWMS M&O 2000. *Natural Analogs for the Unsaturated Zone*. ANL-NBS-HS-000007 REV 00. Las Vegas, Nevada: CRWMS M&O. ACC: MOL.19990721.0524.
- 154291 CRWMS M&O 2001. *Abstraction of Drift Seepage*. ANL-NBS-MD-000005 REV 01. Las Vegas, Nevada: CRWMS M&O. ACC: MOL.20010309.0019.
- 154594 CRWMS M&O 2001. *Abstraction of NFE Drift Thermodynamic Environment and Percolation Flux*. ANL-EBS-HS-000003 REV 00 ICN 02. Las Vegas, Nevada: CRWMS M&O. ACC: MOL.20010221.0160.
- 135997 Doughty, C. 1999. "Investigation of Conceptual and Numerical Approaches for Evaluating Moisture, Gas, Chemical, and Heat Transport in Fractured Unsaturated Rock." *Journal of Contaminant Hydrology*, 38, (1-3), 69-106. New York, New York: Elsevier. TIC: 244160.
- 116801 Driscoll, F.G. 1986. *Groundwater and Wells*. 2nd Edition. St. Paul, Minnesota: Johnson Filtration Systems. TIC: 217555.

- 100145 Fabryka-Martin, J.T.; Wolfsberg, A.V.; Dixon, P.R.; Levy, S.S.; Musgrave, J.A.; and Turin, H.J. 1997. *Summary Report of Chlorine-36 Studies: Sampling, Analysis, and Simulation of Chlorine-36 in the Exploratory Studies Facility*. LA-13352-MS. Los Alamos, New Mexico: Los Alamos National Laboratory. ACC: MOL.19980812.0254.
- 146355 Fabryka-Martin, J.T.; Wolfsberg, A.V.; Roach, J.L.; Winters, S.T.; and Wolfsberg, L.E. 1998. "Using Chloride to Trace Water Movement in the Unsaturated Zone at Yucca Mountain." *High-Level Radioactive Waste Management, Proceedings of the Eighth International Conference, Las Vegas, Nevada, May 11-14, 1998*. Pages 264-268. La Grange Park, Illinois: American Nuclear Society. TIC: 237082.
- 105559 Faure, G. 1986. *Principles of Isotope Geology*. 2nd Edition. New York, New York: John Wiley & Sons. TIC: 237212.
- 103746 Flint, A.L. and Flint, L.E. 1994. "Spatial Distribution of Potential Near Surface Moisture Flux at Yucca Mountain." *High Level Radioactive Waste Management, Proceedings of the Fifth Annual International Conference, Las Vegas, Nevada, May 22-26, 1994*. 4, 2352-2358. La Grange Park, Illinois: American Nuclear Society. TIC: 210984.
- 100147 Flint, A.L.; Hevesi, J.A.; and Flint, L.E. 1996. *Conceptual and Numerical Model of Infiltration for the Yucca Mountain Area, Nevada*. Milestone 3GUI623M. Denver, Colorado: U.S. Geological Survey. ACC: MOL.19970409.0087.
- 100033 Flint, L.E. 1998. *Characterization of Hydrogeologic Units Using Matrix Properties, Yucca Mountain, Nevada*. Water-Resources Investigations Report 97-4243. Denver, Colorado: U.S. Geological Survey. ACC: MOL.19980429.0512.
- 163967 Flint, L.E.; Flint, A.L.; and Selker, J.S. 2003. "Influence of Transitional Volcanic Strata on Lateral Diversion at Yucca Mountain, Nevada" *Water Resources Research*, 39, (4), 4-1 to 4-17. [Washington, D.C.]: American Geophysical Union. TIC: 254439.
- 109425 Forester, R.M.; Bradbury, J.P.; Carter, C.; Elvidge-Tuma, A.B.; Hemphill, M.L.; Lundstrom, S.C.; Mahan, S.A.; Marshall, B.D.; Neymark, L.A.; Paces, J.B.; Sharpe, S.E.; Whelan, J.F.; and Wigand, P.E. 1999. *The Climatic and Hydrologic History of Southern Nevada During the Late Quaternary*. Open-File Report 98-635. Denver, Colorado: U.S. Geological Survey. TIC: 245717.
- 164178 Freeze, G. 2003. *KTI Letter Report, Response to Additional Information Needs on TSPAI 2.05 and TSPAI 2.06*. REG-WIS-PA-000003 REV 00 ICN 02. Las Vegas, Nevada: Bechtel SAIC Company. ACC: DOC.20030423.0004.
- 100575 Fridrich, C.J.; Dudley, W.W., Jr.; and Stuckless, J.S. 1994. "Hydrogeologic Analysis of the Saturated-Zone Ground-Water System, Under Yucca Mountain, Nevada." *Journal of Hydrology*, 154, 133-168. Amsterdam, The Netherlands: Elsevier. TIC: 224606.

- 162573 Goode, D.J. 1996. "Direct Simulation of Groundwater Age." *Water Resources Research*, 32, (2), 289-296. Washington, D.C.: American Geophysical Union. TIC: 252291.
- 141512 Grathwohl, P. 2000. *Diffusion in Natural Porous Media: Contaminant Transport, Sorption/Desorption and Dissolution Kinetics*. Boston, Massachusetts: Kluwer Academic Publishers. TIC: 247983.
- 116809 Hevesi, J.A.; Flint, A.L.; and Istok, J.D. 1992. "Precipitation Estimation in Mountainous Terrain Using Multivariate Geostatistics. Part II: Isohyetal Maps." *Journal of Applied Meteorology*, 31, (7), 677-688. Boston, Massachusetts: American Meteorological Society. TIC: 225248.
- 162560 Johnson, T.M. and DePaolo, D.J. 1994. "Interpretation of Isotopic Data in Groundwater-Rock Systems: Model Development and Application to Sr Isotope Data from Yucca Mountain." *Water Resources Research*, 30, (5), 1571-1587. Washington, D.C.: American Geophysical Union. TIC: 252320.
- 117091 Lasaga, A.C. 1998. *Kinetic Theory in the Earth Sciences*. Princeton, New Jersey: Princeton University Press. TIC: 246279.
- 160832 Lide, D.R., ed. 2002. *CRC Handbook of Chemistry and Physics*. 83rd Edition. Boca Raton, Florida: CRC Press. TIC: 253582.
- 160230 Liu, H.H.; Bodvarsson, G.S.; and Finsterle, S. 2002. "A Note on Unsaturated Flow in Two-Dimensional Fracture Networks." *Water Resources Research*, 38, (9), 15-1 to 15-9. [Washington, D.C.]: American Geophysical Union. TIC: 253307.
- 105729 Liu, H.H.; Doughty, C.; and Bodvarsson, G.S. 1998. "An Active Fracture Model for Unsaturated Flow and Transport in Fractured Rocks." *Water Resources Research*, 34, (10), 2633-2646. Washington, D.C.: American Geophysical Union. TIC: 243012.
- 162478 Liu, J.; Sonnenthal, E.L.; and Bodvarsson, G.S. 2003. "Calibration of Yucca Mountain Unsaturated Zone Flow and Transport Model Using Porewater Chloride Data." *Journal of Contaminant Hydrology*, 62-63, 213-235. New York, New York: Elsevier. TIC: 254205.
- 107415 Marshall, B.D.; Paces, J.B.; Neymark, L.A.; Whelan, J.F.; and Peterman, Z.E. 1998. "Secondary Minerals Record Past Percolation Flux at Yucca Mountain, Nevada." *High-Level Radioactive Waste Management, Proceedings of the Eighth International Conference, Las Vegas, Nevada, May 11-14, 1998*. Pages 127-129. La Grange Park, Illinois: American Nuclear Society. TIC: 237082.
- 106335 Marshall, B.D.; Peterman, Z.E.; Futa, K.; and Stuckless, J.S. 1991. "Strontium Isotopes in Carbonate Deposits at Crater Flat, Nevada." *High Level Radioactive Waste Management, Proceedings of the Second Annual International Conference, Las Vegas, Nevada, April 28-May 3, 1991*. 2, 1423-1428. La Grange Park, Illinois: American Nuclear Society. TIC: 204272.

- 158813 Meijer, A. 2002. "Conceptual Model of the Controls on Natural Water Chemistry at Yucca Mountain, Nevada." *Applied Geochemistry*, 17, ([6]), 793-805. [New York, New York]: Elsevier. TIC: 252808.
- 100161 Montazer, P. and Wilson, W.E. 1984. *Conceptual Hydrologic Model of Flow in the Unsaturated Zone, Yucca Mountain, Nevada*. Water-Resources Investigations Report 84-4345. Lakewood, Colorado: U.S. Geological Survey. ACC: NNA.19890327.0051.
- 161902 Moridis, G.J.; Hu, Q.; Wu, Y-S.; and Bodvarsson, G.S. 2003. "Preliminary 3-D Site-Scale Studies of Radioactive Colloid Transport in the Unsaturated Zone at Yucca Mountain, Nevada." *Journal of Contaminant Hydrology*, 60, ([3-4]), 251-286. New York, New York: Elsevier. TIC: 253921.
- 139151 National Research Council. 1996. *Rock Fractures and Fluid Flow, Contemporary Understanding and Applications*. Washington, D.C.: National Academy Press. TIC: 235913.
- 162140 Neretnieks, I. 2002. "A Stochastic Multi-Channel Model for Solute Transport—Analysis of Tracer Tests in Fractured Rock." *Journal of Contaminant Hydrology*, 55, ([3-4]), 175-211. New York, New York: Elsevier. TIC: 253977.
- 156889 Neymark, L.A.; Amelin, Y.V.; Paces, J.B.; Peterman, Z.E.; and Whelan, J.F. 2001. "Age Constraints on Fluid Inclusions in Calcite at Yucca Mountain." "Back to the Future - Managing the Back End of the Nuclear Fuel Cycle to Create a More Secure Energy Future," *Proceedings of the 9th International High-Level Radioactive Waste Management Conference (IHLRWM), Las Vegas, Nevada, April 29, May 3, 2001*. La Grange Park, Illinois: American Nuclear Society. TIC: 247873.
- 163274 NRC (U.S. Nuclear Regulatory Commission) 2003. *Yucca Mountain Review Plan, Final Report*. NUREG-1804, Rev. 2. Washington, D.C.: U.S. Nuclear Regulatory Commission, Office of Nuclear Material Safety and Safeguards. TIC: 254568.
- 107408 Paces, J.B.; Neymark, L.A.; Marshall, B.D.; Whelan, J.F.; and Peterman, Z.E. 1998. "Inferences for Yucca Mountain Unsaturated-Zone Hydrology from Secondary Minerals." *High-Level Radioactive Waste Management, Proceedings of the Eighth International Conference, Las Vegas, Nevada, May 11-14, 1998*. Pages 36-39. La Grange Park, Illinois: American Nuclear Society. TIC: 237082.
- 156507 Paces, J.B.; Neymark, L.A.; Marshall, B.D.; Whelan, J.F.; and Peterman, Z.E. 2001. *Ages and Origins of Calcite and Opal in the Exploratory Studies Facility Tunnel, Yucca Mountain, Nevada*. Water-Resources Investigations Report 01-4049. Denver, Colorado: U.S. Geological Survey. TIC: 251284.
- 164181 Pan, L.; Warrick, A.W.; and Wierenga, P.J. 1997. "Downward Water Flow Through Sloping Layers in the Vadose Zone: Time-Dependence and Effect of Slope Length." *Journal of Hydrology*, 199, ([1-2]), 36-52. [New York, New York]: Elsevier. TIC: 254555.

- 162576 Peterman, Z.E. and Cloke, P.L. 2002. "Geochemistry of Rock Units at the Potential Repository Level, Yucca Mountain, Nevada (includes Erratum)." *Applied Geochemistry*, 17, ([6, 7]), 683-698, 955-958. New York, New York: Pergamon. TIC: 252516; 252517.
- 101149 Peterman, Z.E. and Stuckless, J.S. 1993. "Isotopic Evidence of Complex Ground-Water Flow at Yucca Mountain, Nevada, USA." *High Level Radioactive Waste Management, Proceedings of the Fourth Annual International Conference, Las Vegas, Nevada, April 26-30, 1993*. 2, 1559-1566. La Grange Park, Illinois: American Nuclear Society. TIC: 208542.
- 147110 Peterman, Z.E.; Stuckless, J.S.; Marshall, B.D.; Mahan, S.A.; and Futa, K. 1992. "Strontium Isotope Geochemistry of Calcite Fracture Fillings in Deep Core, Yucca Mountain, Nevada -- A Progress Report." *High Level Radioactive Waste Management, Proceedings of the Third International Conference, Las Vegas, Nevada, April 12-16, 1992*. 2, 1582-1586. La Grange Park, Illinois: American Nuclear Society. TIC: 204231.
- 105743 Philip, J.R.; Knight, J.H.; and Waechter, R.T. 1989. "Unsaturated Seepage and Subterranean Holes: Conspectus, and Exclusion Problem for Circular Cylindrical Cavities." *Water Resources Research*, 25, (1), 16-28. Washington, D.C.: American Geophysical Union. TIC: 239117.
- 101707 Pruess, K. and Narasimhan, T.N. 1985. "A Practical Method for Modeling Fluid and Heat Flow in Fractured Porous Media." *Society of Petroleum Engineers Journal*, 25, (1), 14-26. Dallas, Texas: Society of Petroleum Engineers. TIC: 221917.
- 160778 Pruess, K.; Oldenburg, C.; and Moridis, G. 1999. *TOUGH2 User's Guide, Version 2.0*. LBNL-43134. Berkeley, California: Lawrence Berkeley National Laboratory. TIC: 253038.
- 104252 Richards, L.A. 1931. "Capillary Conduction of Liquids Through Porous Mediums." *Physics*, 1, 318-333. [New York, New York: American Physical Society]. TIC: 225383.
- 102097 Rousseau, J.P.; Kwicklis, E.M.; and Gillies, D.C., eds. 1999. *Hydrogeology of the Unsaturated Zone, North Ramp Area of the Exploratory Studies Facility, Yucca Mountain, Nevada*. Water-Resources Investigations Report 98-4050. Denver, Colorado: U.S. Geological Survey. ACC: MOL.19990419.0335.
- 100178 Rousseau, J.P.; Loskot, C.L.; Thamir, F.; and Lu, N. 1997. *Results of Borehole Monitoring in the Unsaturated Zone Within the Main Drift Area of the Exploratory Studies Facility, Yucca Mountain, Nevada*. Milestone SPH22M3. Denver, Colorado: U.S. Geological Survey. ACC: MOL.19970626.0351.

- 100644 Sass, J.H.; Lachenbruch, A.H.; Dudley, W.W., Jr.; Priest, S.S.; and Munroe, R.J. 1988. *Temperature, Thermal Conductivity, and Heat Flow Near Yucca Mountain, Nevada: Some Tectonic and Hydrologic Implications*. Open-File Report 87-649. [Denver, Colorado]: U.S. Geological Survey. TIC: 203195.
- 162132 Shapiro, A.M. 2001. "Effective Matrix Diffusion in Kilometer-Scale Transport in Fractured Crystalline Rock." *Water Resources Research*, 37, (3), 507-522. [Washington, D.C.]: American Geophysical Union. TIC: 253979.
- 161591 Sharpe, S. 2003. *Future Climate Analysis—10,000 Years to 1,000,000 Years After Present*. MOD-01-001 REV 01. [Reno, Nevada: Desert Research Institute]. ACC: MOL.20030407.0055.
- 117914 Sonnenthal, E. and Ortoleva, P.J. 1994. "Numerical Simulations of Overpressured Compartments in Sedimentary Basins." *Basin Compartments and Seals*. Ortoleva, P.J., ed. AAPG Memoir 61. 403-416. Tulsa, Oklahoma: American Association of Petroleum Geologists. TIC: 235940.
- 117127 Sonnenthal, E.L. and Bodvarsson, G.S. 1999. "Constraints on the Hydrology of the Unsaturated Zone at Yucca Mountain, NV from Three-Dimensional Models of Chloride and Strontium Geochemistry." *Journal of Contaminant Hydrology*, 38, (1-3), 107-156. New York, New York: Elsevier. TIC: 244160.
- 106947 Stuckless, J.S.; Peterman, Z.E.; and Muhs, D.R. 1991. "U and Sr Isotopes in Ground Water and Calcite, Yucca Mountain, Nevada: Evidence Against Upwelling Water." *Science*, 254, 551-554. Washington, D.C.: American Association for the Advancement of Science. TIC: 224423.
- 139195 Tokunaga, T.K. and Wan, J. 1997. "Water Film Flow Along Fracture Surfaces of Porous Rock." *Water Resources Research*, 33, (6), 1287-1295. Washington, D.C.: American Geophysical Union. TIC: 242739.
- 101014 Triay, I.R.; Meijer, A.; Conca, J.L.; Kung, K.S.; Rundberg, R.S.; and Strietelmeier, B.A. 1996. *Summary and Synthesis Report on Radionuclide Retardation for the Yucca Mountain Site Characterization Project*. Milestone 3784. Los Alamos, New Mexico: Los Alamos National Laboratory. ACC: MOL.19961231.0099.
- 108774 Tyler, S.W.; Chapman, J.B.; Conrad, S.H.; Hammermeister, D.P.; Blout, D.O.; Miller, J.J.; Sully, M.J.; and Ginanni, J.M. 1996. "Soil-Water Flux in the Southern Great Basin, United States: Temporal and Spatial Variations Over the Last 120,000 Years." *Water Resources Research*, 32, (6), 1481-1499. Washington, D.C.: American Geophysical Union. TIC: 235938.
- 158378 USGS (U.S. Geological Survey) 2001. *Future Climate Analysis*. ANL-NBS-GS-000008 REV 00 ICN 01. Denver, Colorado: U.S. Geological Survey. ACC: MOL.20011107.0004.

- 160355 USGS (U.S. Geological Survey) 2001. *Simulation of Net Infiltration for Modern and Potential Future Climates*. ANL-NBS-HS-000032 REV 00 ICN 02. Denver, Colorado: U.S. Geological Survey. ACC: MOL.20011119.0334.
- 100610 van Genuchten, M.T. 1980. "A Closed-Form Equation for Predicting the Hydraulic Conductivity of Unsaturated Soils." *Soil Science Society of America Journal*, 44, (5), 892-898. Madison, Wisconsin: Soil Science Society of America. TIC: 217327.
- 100089 Vaniman, D.T. and Chipera, S.J. 1996. "Paleotransport of Lanthanides and Strontium Recorded in Calcite Compositions from Tuffs at Yucca Mountain, Nevada, USA." *Geochimica et Cosmochimica Acta*, 60, (22), 4417-4433. New York, New York: Pergamon Press. TIC: 231351.
- 157427 Vaniman, D.T.; Chipera, S.J.; Bish, D.L.; Carey, J.W.; and Levy, S.S. 2001. "Quantification of Unsaturated-Zone Alteration and Cation Exchange in Zeolitized Tuffs at Yucca Mountain, Nevada, USA." *Geochimica et Cosmochimica Acta*, 65, (20), 3409-3433. [New York, New York]: Elsevier. TIC: 251574.
- 162122 Walter, A.L.; Frind, E.O.; Blowes, D.W.; Ptacek, C.J.; and Molson, J.W. 1994. "Modeling of Multicomponent Reactive Transport in Groundwater. 1. Model Development and Evaluation." *Water Resources Research*, 30, (11), 3137-3148. Washington, D.C.: American Geophysical Union. TIC: 252320.
- 162417 Wang, J.S. 2003. "Scientific Notebooks Referenced in Model Report U0050, UZ Flow Models and Submodels, MDL-NBS-HS-000006 REV 01." Memorandum from J.S. Wang (BSC) to File, June 6, 2003, with attachments. ACC: MOL.20030611.0227.
- 108835 Wang, J.S.Y. and Narasimhan, T.N. 1985. "Hydrologic Mechanisms Governing Fluid Flow in a Partially Saturated, Fractured, Porous Medium." *Water Resources Research*, 21, (12), 1861-1874. Washington, D.C.: American Geophysical Union. TIC: 225290.
- 106793 Wang, J.S.Y. and Narasimhan, T.N. 1993. "Unsaturated Flow in Fractured Porous Media." Chapter 7 of *Flow and Contaminant Transport in Fractured Rock*. Bear, J.; Tsang, C-F.; and de Marsily, G., eds. San Diego, California: Academic Press. TIC: 235461.
- 100094 Winograd, I.J.; Coplen, T.B.; Landwehr, J.M.; Riggs, A.C.; Ludwig, K.R.; Szabo, B.J.; Kolesar, P.T.; and Revesz, K.M. 1992. "Continuous 500,000-Year Climate Record from Vein Calcite in Devils Hole, Nevada." *Science*, 258, 255-260. Washington, D.C.: American Association for the Advancement of Science. TIC: 237563.
- 153972 Wu, Y-S. and Pruess, K. 2000. "Numerical Simulation of Non-Isothermal Multiphase Tracer Transport in Heterogeneous Fractured Porous Media." *Advances in Water Resources*, 23, (7), 699-723. New York, New York: Elsevier. TIC: 249626.

- 117161 Wu, Y-S.; Haukwa, C.; and Bodvarsson, G.S. 1999. "A Site-Scale Model for Fluid and Heat Flow in the Unsaturated Zone of Yucca Mountain, Nevada." *Journal of Contaminant Hydrology*, 38, (1-3), 185-215. New York, New York: Elsevier. TIC: 244160.
- 160195 Wu, Y-S.; Pan, L.; Zhang, W.; and Bodvarsson, G.S. 2002. "Characterization of Flow and Transport Processes within the Unsaturated Zone of Yucca Mountain, Nevada, Under Current and Future Climates." *Journal of Contaminant Hydrology*, 54, ([3-4]), 215-247. [New York, New York]: Elsevier. TIC: 253316.
- 154918 Wu, Y-S.; Zhang, W.; Pan, L.; Hinds, J.; and Bodvarsson, G.S. 2000. *Capillary Barriers in Unsaturated Fractured Rocks of Yucca Mountain, Nevada*. LBNL-46876. Berkeley, California: Lawrence Berkeley National Laboratory. TIC: 249912.
- 161058 Wu, Y-S.; Zhang, W.; Pan, L.; Hinds, J.; and Bodvarsson, G.S. 2002. "Modeling Capillary Barriers in Unsaturated Fractured Rock." *Water Resources Research*, 38, (11), 35-1 through 35-12. [Washington, D.C.]: American Geophysical Union. TIC: 253854.
- 117167 Wu, Y.S.; Ritcey, A.C.; and Bodvarsson, G.S. 1999. "A Modeling Study of Perched Water Phenomena in the Unsaturated Zone at Yucca Mountain." *Journal of Contaminant Hydrology*, 38, (1-3), 157-184. New York, New York: Elsevier. TIC: 244160.
- 117170 Xu, T. and Pruess, K. 1998. *Coupled Modeling of Non-Isothermal Multi-Phase Flow, Solute Transport and Reactive Chemistry in Porous and Fractured Media: 1. Model Development and Validation*. LBNL-42050. Berkeley, California: Lawrence Berkeley National Laboratory. TIC: 243735.
- 156280 Xu, T. and Pruess, K. 2001. "Modeling Multiphase Non-Isothermal Fluid Flow and Reactive Geochemical Transport in Variably Saturated Fractured Rocks: 1. Methodology." *American Journal of Science*, 301, 16-33. [New Haven, Connecticut: Yale University, Kline Geology Laboratory]. TIC: 251482.
- 162123 Xu, T.; Samper, J.; Ayora, C.; Manzano, M.; and Custodio, E. 1999. "Modeling of Non-isothermal Multi-component Reactive Transport in Field Scale Porous Media Flow Systems." *Journal of Hydrology*, 214, ([1-4]), 144-164. [New York, New York]: Elsevier. TIC: 254290.
- 162124 Xu, T.; Sonnenthal, E.; and Bodvarsson, G. 2003. "A Reaction-Transport Model for Calcite Precipitation and Evaluation of Infiltration Fluxes in Unsaturated Fractured Rock." *Journal of Contaminant Hydrology*, 64, ([1-2]), 113-127. New York, New York: Elsevier. TIC: 254008.
- 160839 Yang, I.C. 2002. "Percolation Flux and Transport Velocity in the Unsaturated Zone, Yucca Mountain, Nevada." *Applied Geochemistry*, 17, ([6]), 807-817. [New York, New York]: Elsevier. TIC: 253605.

- 162125 Yeh, G-T. and Tripathi, V.S. 1991. "A Model for Simulating Transport of Reactive Multispecies Components: Model Development and Demonstration." *Water Resources Research*, 27, (12), 3075-3094. Washington, D.C.: American Geophysical Union. TIC: 236255.
- 162133 Zhou, Q.; Liu, H-H.; Bodvarsson, G.S.; and Oldenburg, C.M. 2003. "Flow and Transport in Unsaturated Fractured Rock: Effects of Multiscale Heterogeneity of Hydrogeologic Properties." *Journal of Contaminant Hydrology*, 60, ([1-2]), 1-30. New York, New York: Elsevier. TIC: 253978.

Software Cited

- 139918 LBNL (Lawrence Berkeley National Laboratory) 09/16/1999. *Software Code: iTOUGH2*. V4.0. SUN, DEC. 10003-4.0-00.
- 134754 LBNL (Lawrence Berkeley National Laboratory) 1999. *Software Code: infil2grid*. V1.6. PC with Windows/95 or 98. Sun or DEC Workstation with Unix OS. 10077-1.6-00.
- 146654 LBNL (Lawrence Berkeley National Laboratory) 1999. *Software Code: T2R3D*. V1.4. FORTRAN 77, SUN, DEC / ALPHA. 10006-1.4-00.
- 146496 LBNL (Lawrence Berkeley National Laboratory) 2000. *Software Code: TOUGH2*. V1.4. Sun Workstation and DEC/ALPHA. 10007-1.4-01.
- 153471 LBNL (Lawrence Berkeley National Laboratory) 2000. *Software Routine: bot_sum.f*. V1.0. SUN AND DEC. 10349-1.0-00.
- 147023 LBNL (Lawrence Berkeley National Laboratory) 2000. *Software Routine: genincon-v0.f*. V1.0. Sun workstation w/Unix OS. 10220-1.0-00.
- 147027 LBNL (Lawrence Berkeley National Laboratory) 2000. *Software Routine: get_temp_v0.f*. V1.0. Sun workstation w/Unix OS. 10222-1.0-00.
- 147030 LBNL (Lawrence Berkeley National Laboratory) 2000. *Software Routine: toptemp_v0.f*. V1.0. Sun workstation w/Unix OS. 10224-1.0-00.
- 154345 LBNL (Lawrence Berkeley National Laboratory) 2001. *Software Routine: vf_con.for*. V1.0. PC w/Windows. 10466-1.0-00.
- 162143 LBNL (Lawrence Berkeley National Laboratory) 2002. *Software Code: Bkread.f*. V1.0. SunOS 5.5.1. 10894-1.0-00.
- 154793 LBNL (Lawrence Berkeley National Laboratory) 2002. *Software Code: infil2grid*. V1.7. DEC-Alpha, PC. 10077-1.7-00.
- 160107 LBNL (Lawrence Berkeley National Laboratory) 2002. *Software Code: TBgas3D*. V2.0. SUN UltraSparc. 10882-2.0-00.

- 161256 LBNL (Lawrence Berkeley National Laboratory) 2002. *Software Code: TOUGHREACT*. V3.0. DEC-Alpha with Unix OSF1 V5.1 and OSF1 V5.0, Sun Solaris 5.5.1, Linux Redhat 7.2. 10396-3.0-00.
- 154785 LBNL (Lawrence Berkeley National Laboratory) 2002. *Software Code: WINGRIDDER*. V2.0. PC. 10024-2.0-00.
- 162142 LBNL (Lawrence Berkeley National Laboratory) 2002. *Software Code: Smesh.f*. V1.0. SunOS 5.5.1. 10896-1.0-00.
- 154787 LBNL (Lawrence Berkeley National Laboratory) 2002. *Software Routine: 2kgrid8.for*. V1.0. DEC-Alpha, PC. 10503-1.0-00.
- 161491 LBNL (Lawrence Berkeley National Laboratory) 2003. *Software Code: TOUGH2*. V1.6. PC/MS-DOS under Windows 98, Sun UltraSparc OS 5.5.1, DEC-Alpha OSF1 V4.0. 10007-1.6-01.
- 163453 LBNL (Lawrence Berkeley National Laboratory) 2003. *Software Code: WTRISE*. V2.0. PC/WINDOWS 2000/98; DEC ALPHA/OSF1 V5.1. 10537-2.0-00.
- 163162 LBNL (Lawrence Berkeley National Laboratory) 2003. *Software Code: flow-con*. V1.0. PC/ WINDOWS 95/98(MS-DOS emulation); DEC ALPHA/OSF1 V5.1. 10993-1.0-00.
- 163161 LBNL (Lawrence Berkeley National Laboratory) 2003. *Software Code: T2FEHM*. V4.0. DEC ALPHA / OSF1 V4.0/ V5.1. 10997-4.0-00.

9.2 CODES, STANDARDS, REGULATIONS, AND PROCEDURES

- 156605 10 CFR 63. Energy: Disposal of High-Level Radioactive Wastes in a Geologic Repository at Yucca Mountain, Nevada. Readily available.

AP-2.22Q, Rev. 0, ICN 1. *Classification Criteria and Maintenance of the Monitored Geologic Repository Q-List*. Washington, D.C.: U.S. Department of Energy, Office of Civilian Radioactive Waste Management. ACC: DOC.20030422.0009.

AP-SI.1Q, Rev. 5, Mod 1. *Software Management*. Washington, D.C.: U.S. Department of Energy, Office of Civilian Radioactive Waste Management. ACC: DOC.20030708.0001.

AP-SIII.10Q, Rev. 1, ICN 2. *Models*. Washington, D.C.: U.S. Department of Energy, Office of Civilian Radioactive Waste Management. ACC: DOC.20030627.0003.

9.3 SOURCE DATA, LISTED BY DATA TRACKING NUMBER

- 147613 GS000308311221.005. Net Infiltration Modeling Results for 3 Climate Scenarios for FY99. Submittal date: 03/01/2000.

- 153407 GS000608312271.001. Pore-Water Hydrochemistry and Isotopic Data for Boreholes USW NRG-6, USW NRG-7A, USW SD-7, USW SD-9, USW SD-12, USW UZ-14 and UE-25 UZ#16 from 10/1/96 to 1/31/97. Submittal date: 06/23/2000.
- 156375 GS010708312272.002. Chemical Data for Pore Water from Tuff Cores of USW NRG-6, USW NRG-7/7A, USW UZ-14, USW UZ-N55 and UE-25 UZ#16. Submittal date: 09/05/2001.
- 160899 GS020408312272.003. Collection and Analysis of Pore Water Samples for the Period from April 2001 to February 2002. Submittal date: 04/24/2002.
- 162129 GS020508312242.001. Trench Fault Infiltration in Alcove 8 Using Permeameters from March 5, 2001 to June 1, 2001. Submittal date: 05/22/2002.
- 162126 GS020608315215.002. Carbon Dioxide Abundances, Carbon Dioxide Concentrations, and Normative Calcite Concentrations for Cuttings from Borehole USW SD-6, USW WT-24, and ECRB Cross Drift Boreholes, Determined by Carbon Dioxide Evolution, May 25, 2000 and September 8, 2000. Submittal date: 06/26/2002.
- 162141 GS020908312242.002. Trenched Fault Infiltration in Alcove 8 Using Permeameters from June 1, 2001 to March 26, 2002. Submittal date: 09/17/2002.
- 162127 GS021008315215.007. Carbon Dioxide and Normative Calcite Concentrations in Powdered Cuttings from Borehole USW WT-24 Determined by CO₂ Evolution between July 1998 and August 1999. Submittal date: 11/07/2002.
- 162131 GS030108314224.001. Geotechnical Data for Alcove 8 (ECRB) and Niche 3 (ESF): Full Periphery Geologic Map (Drawing OA-46-356). Submittal date: 02/05/2003.
- 105572 GS950208312232.003. Data, Including Water Potential, Pressure and Temperature, Collected from Boreholes USW NRG-6 and USW NRG-7A from Instrumentation through March 31, 1995. Submittal date: 02/13/1995.
- 107244 GS950408318523.001. Temperature, Thermal Conductivity, and Heat Flow Near Yucca Mountain, Nevada. Submittal date: 04/21/1995.
- 106756 GS951108312232.008. Data, Including Water Potential, Pressure and Temperature, Collected from Boreholes UE-25 UZ#4 & UZ#5 from Instrumentation through September 30, 1995, and from USW NRG-6 & NRG-7A from April 1 through September 30, 1995. Submittal date: 11/21/1995.
- 105573 GS960308312232.001. Deep Unsaturated Zone Surface-Based Borehole Instrumentation Program Data from Boreholes USW NRG-7A, USW NRG-6, UE-25 UZ#4, UE-25 UZ#5, USW UZ-7A, and USW SD-12 for the Time Period 10/01/95 through 3/31/96. Submittal date: 04/04/1996.

- 107230 GS960308312312.005. Water-Level, Discharge Rate and Related Data from the Pump Tests Conducted at Well USW UZ-14, August 17 through August 30, 1993. Submittal date: 03/15/1996.
- 105974 GS960808312232.004. Deep Unsaturated Zone Surface-Based Borehole Instrumentation Program Data for Boreholes USW NRG-7A, USW NRG-6, UE-25 UZ#4, UE-25 UZ#5, USW UZ-7A and USW SD-12 for the Time Period 4/1/96 through 8/15/96. Submittal date: 08/30/1996.
- 106784 GS960908312261.004. Shut-in Pressure Test Data from UE-25 NRG#5 and USW SD-7 from November, 1995 to July, 1996. Submittal date: 09/24/1996.
- 107293 GS961108312261.006. Gas Chemistry, ESF Alcoves 2 and 3, 11/95 - 4/96; Water Chemistry, Alcove 2 (Tritium), Alcove 3, and ESF Tunnel; and Pneumatic Pressure Response from Boreholes in Exploratory Studies Facility Alcoves 2 and 3, 10/95 - 5/96. Submittal date: 11/12/1996.
- 121708 GS961108312271.002. Chemical and Isotopic Composition of Pore Water and Pore Gas, 1994–96, from Boreholes USW UZ-1, USW UZ-14, UE-25 UZ#16, USW NRG-6, USW NRG-7A, USW SD-7, USW SD-9, ESF-AL#3-RBT#1, and ESF-AL#3-RBT#4, and ESF Rubble. Submittal date: 12/04/1996.
- 105975 GS970108312232.002. Deep Unsaturated Zone, Surface-Based Borehole Instrumentation Program - Raw Data Submittal for Boreholes USW NRG-7A, USW NRG-6, UE-25 UZ#4, UE-25 UZ#5, USW UZ-7A, and USW SD-12, for the Period 8/16/96 through 12/31/96. Submittal date: 01/22/1997.
- 105978 GS970808312232.005. Deep Unsaturated Zone Surface-Based Borehole Instrumentation Program Data from Boreholes USW NRG-7A, UE-25 UZ#4, UE-25 UZ#5, USW UZ-7A and USW SD-12 for the Time Period 1/1/97 - 6/30/97. Submittal date: 08/28/1997.
- 111467 GS970908312271.003. Unsaturated Zone Hydrochemistry Data, 2-1-97 to 8-31-97, Including Chemical Composition and Carbon, Oxygen, and Hydrogen Isotopic Composition: Porewater from USW NRG-7A, SD-7, SD-9, SD-12 and UZ-14; and Gas from USW UZ-14. Submittal date: 09/08/1997.
- 105980 GS971108312232.007. Deep Unsaturated Zone Surface-Based Borehole Instrumentation Program Data from Boreholes USW NRG-7A, UE-25 UZ #4, UE-25 UZ #5, USW UZ-7A and USW SD-12 for the Time Period 7/1/97 - 9/30/97. Submittal date: 11/18/1997.
- 105982 GS980408312232.001. Deep Unsaturated Zone Surface-Based Borehole Instrumentation Program Data from Boreholes USW NRG-7A, UE-25 UZ #4, USW NRG-6, UE-25 UZ #5, USW UZ-7A and USW SD-12 for the Time Period 10/01/97 - 03/31/98. Submittal date: 04/16/1998.

- 109746 GS980508312313.001. Water-Level and Related Data Collected in Support of Perched-Water Testing in Borehole USW WT-24, September 10, 1997 through February 3, 1998. Submittal date: 05/07/1998.
- 106752 GS980708312242.010. Physical Properties of Borehole Core Samples, and Water Potential Measurements Using the Filter Paper Technique, for Borehole Samples from USW WT-24. Submittal date: 07/27/1998.
- 106748 GS980808312242.014. Physical Properties of Borehole Core Samples and Water Potential Measurements Using the Filter Paper Technique for Borehole Samples from USW SD-6. Submittal date: 08/11/1998.
- 119820 GS980908312242.036. Water Potentials Measured with Heat Dissipation Probes in ECRB Holes from 4/23/98 to 7/31/98. Submittal date: 09/22/1998.
- 153677 GS981008312272.004. Analysis for Chemical Composition of Pore Water from Boreholes USW UZ-7A, USW WT-24, USW SD-6, USW SD-7, and USW SD-12 During FY 1997 and 1998. Submittal date: 10/28/1998.
- 146134 GS990208312272.001. Analysis for Chemical Composition of Pore Water from Borehole USW UZ-14 and UE-25 UZ#16 and Groundwater from UE-25 UZ#16. Submittal date: 02/23/1999.
- 145711 GS990308315215.004. Strontium Isotope Ratios and Strontium Concentrations in Rock Core Samples and Leachates from USW SD-9 and USW SD-12. Submittal date: 03/25/1999.
- 148603 LA000000000034.002. Diffusion of Sorbing and Non-Sorbing Radionuclides. Submittal date: 06/22/1993.
- 154760 LA0002JF12213U.001. Chemistry Data for Porewater Extracted from Drillcore from Surface-Based Boreholes USW NRG-6, USW NRG-7A, USW UZ-7A, USW UZ-14, UE-25 UZ#16, USW UZ-N55, USW SD-6, USW SD-7, USW SD-9, USW SD-12, and USW WT-24. Submittal date: 02/15/2000.
- 156281 LA0002JF12213U.002. Chemistry Data for Porewater Extracted from ESF, Cross Drift and Busted Butte Drill Core. Submittal date: 02/15/2000.
- 149557 LA0003JC831362.001. Preliminary Matrix Diffusion Coefficients for Yucca Mountain Tuffs. Submittal date: 4/10/2000.
- 162476 LA0010JC831341.001. Radionuclide Retardation Measurements of Sorption Distribution Coefficients for Barium. Submittal date: 10/19/2000.
- 153321 LA0010JC831341.002. Radionuclide Retardation Measurements of Sorption Distribution Coefficients for Cesium. Submittal date: 10/19/2000.
- 153322 LA0010JC831341.003. Radionuclide Retardation Measurements of Sorption Distribution Coefficients for Strontium. Submittal date: 10/19/2000.

- 153323 LA0010JC831341.004. Radionuclide Retardation Measurements of Sorption Distribution Coefficients for Selenium. Submittal date: 10/19/2000.
- 153320 LA0010JC831341.005. Radionuclide Retardation Measurements of Sorption Distribution Coefficients for Uranium. Submittal date: 10/19/2000.
- 153318 LA0010JC831341.006. Radionuclide Retardation Measurements of Sorption Distribution Coefficients for Plutonium. Submittal date: 10/19/2000.
- 153319 LA0010JC831341.007. Radionuclide Retardation Measurements of Sorption Distribution Coefficients for Neptunium. Submittal date: 10/19/2000.
- 162575 LA0302AM831341.002. Unsaturated Zone Distribution Coefficients (KDS) for U, NP, PU, AM, PA, CS, SR, RA, and TH. Submittal date: 02/04/2003.
- 145598 LA9909JF831222.004. Chloride, Bromide, and Sulfate Analyses of Busted Butte and Cross Drift Tunnel Porewaters in FY99. Submittal date: 09/29/1999.
- 122733 LA9909JF831222.010. Chloride, Bromide, Sulfate, and Chlorine-36 Analyses of ESF Porewaters. Submittal date: 09/29/1999.
- 145402 LAJF831222AQ98.011. Chloride, Bromide, Sulfate and Chlorine-36 Analyses of Springs, Groundwater, Porewater, Perched Water and Surface Runoff. Submittal date: 09/10/1998.
- 161278 LB0101DSTTHCR1.003. Attachment III - Mineral Reactive Surface Areas: TPTPMN and DST THC Models for AMR N0120/U0110 REV01, "Drift-Scale Coupled Processes (Drift-Scale Test and THC Seepage) Models.". Submittal date: 01/26/2001.
- 159525 LB0205REVUZPRP.001. Fracture Properties for UZ Model Layers Developed from Field Data. Submittal date: 05/14/2002.
- 161285 LB0208UZDSCPMI.001. Drift-Scale Calibrated Property Sets: Mean Infiltration Supporting Files. Submittal date: 08/27/2002.
- 161243 LB0208UZDSCPMI.002. Drift-Scale Calibrated Property Sets: Mean Infiltration Data Summary. Submittal date: 08/26/2002.
- 161433 LB02091DSSCP3I.002. 1-D Site Scale Calibrated Properties: Data Summary. Submittal date: 09/18/2002.
- 162422 LB02092DSSCFPR.001. 2-D Site Scale Calibrated Fault Properties: Supporting Files. Submittal date: 09/18/2002.
- 162128 LB02092DSSCFPR.002. 2-D Site Scale Calibrated Fault Properties: Data Summary. Submittal date: 09/18/2002.

- 160799 LB0210THRMLPRP.001. Thermal Properties of UZ Model Layers: Data Summary. Submittal date: 10/25/2002.
- 162130 LB0301N3SURDAT.001. Niche 3107 Measurements and Elevations Used for Grid Generation. Submittal date: 01/29/2003.
- 162354 LB03023DKMGRID.001. UZ 3-D Site Scale Model Grids. Submittal date: 02/26/2003.
- 162378 LB0302AMRU0035.001. Model Validation and Parameter Uncertainty: Supporting Files. Submittal date: 02/07/2003.
- 162570 LB0303A8N3LIQR.001. Alcove 8 - Niche 3 Seepage Data Compilation. Submittal date: 03/19/2003.
- 136593 LB980901233124.101. Pneumatic Pressure and Air Permeability Data from Niche 3107 and Niche 4788 in the ESF from Chapter 2 of Report SP33PBM4: Fracture Flow and Seepage Testing in the ESF, FY98. Submittal date: 11/23/1999.
- 106787 LB990501233129.001. Fracture Properties for the UZ Model Grids and Uncalibrated Fracture and Matrix Properties for the UZ Model Layers for AMR U0090, "Analysis of Hydrologic Properties Data". Submittal date: 08/25/1999.
- 110226 LB990861233129.001. Drift Scale Calibrated 1-D Property Set, FY99. Submittal date: 08/06/1999.
- 125868 LB991091233129.001. One-Dimensional, Mountain-Scale Calibration for AMR U0035, "Calibrated Properties Model". Submittal date: 10/22/1999.
- 147328 LB991121233129.001. Calibrated Parameters for the Present-Day, Mean Infiltration Scenario, Used for Simulations With Perched Water Conceptual Model #1 (Flow Through) for the Mean Infiltration Scenarios of the Present-Day, Monsoon and Glacial Transition Climates. Submittal date: 03/11/2000.
- 147335 LB991121233129.003. Calibrated Parameters for the Present-Day, Upper-Bound Infiltration Scenario, Used for Simulations with Perched Water Conceptual Model #1 for the Upper-Bound Infiltration Scenarios of the Present-Day, Monsoon and Glacial Transition Climates. Submittal date: 03/11/2000.
- 147346 LB991121233129.005. Calibrated Parameters for the Present-Day, Lower-Bound Infiltration Scenario, Used for Simulations with Perched Water Conceptual Model #1 for the Lower-Bound Infiltration Scenarios of the Present-Day, Monsoon and Glacial Transition Climates. Submittal date: 03/11/2000.
- 161276 LB991200DSTTHC.003. Mineral Initial Volume Fractions: Attachment II of AMR N0120/U0110, "Drift-Scale Coupled Processes (Drift-Scale Test and THC Seepage) Models." Submittal date: 03/11/2000.

- 104055 LB997141233129.001. Calibrated Basecase Infiltration 1-D Parameter Set for the UZ Flow and Transport Model, FY99. Submittal date: 07/21/1999.
- 152554 MO0004QGFMPIK.000. Lithostratigraphic Contacts from MO9811MWDGFM03.000 to be Qualified Under the Data Qualification Plan, TDP-NBS-GS-000001. Submittal date: 04/04/2000.
- 153398 MO0012CARB1314.000. Water - Carbon 13 and Carbon 14 Abundance. Submittal date: 12/01/2000.
- 153777 MO0012MWDGFM02.002. Geologic Framework Model (GFM2000). Submittal date: 12/18/2000.
- 155989 MO0109HYMXPROP.001. Matrix Hydrologic Properties Data. Submittal date: 09/17/2001.
- 161496 MO0301SEPFEPS1.000. LA FEP List. Submittal date: 01/21/2003.
- 105067 SNT02110894001.002. Geologic Core Logs for USW SD-7. Submittal date:

9.4 OUTPUT DATA, LISTED BY DATA TRACKING NUMBER

LB03013DSSCP3I.001. 3-D Site Scale Calibrated Properties: Data Summaries. Submittal date: 01/27/2003.

LB03023DSSCP9I.001. 3-D Site Scale UZ Flow Field Simulations for 9 Infiltration Scenarios. Submittal date: 02/28/2003.

LB0302PTNTSW9I.001. PTn/TSw Interface Percolation Flux Maps for 9 Infiltration Scenarios. Submittal date: 02/28/2003.

LB03033DSSFF9I.001. 3-D Site Scale UZ Flow Fields for 9 Infiltration Scenarios: Simulations. Submittal date: 03/28/2003.

LB03033DUZTRAN.001. Tc and Np distributions/transport in UZ flow-fields. Submittal date: 03/28/2003.

LB0303A8N3MDLG.001. Alcove 8 - Niche 3 Seepage Modeling: Simulations. Submittal date: 03/31/2003.

LB0303C14INF3D.001. Carbon-14 isotope distributions in UZ flow-fields. Submittal date: 03/28/2003.

LB0303CLINFL3D.001. Chloride ion distributions in UZ flow-fields. Submittal date: 03/28/2003.

LB0303GASFLW3D.001. Time-dependent gas pressure distributions in UZ flow-fields. Submittal date: 03/28/2003.

LB0303THERMESH.001. Thermal Model Mesh. Submittal date: 03/28/2003.

LB0303THERMSIM.001. UZ Thermal Modeling: Simulations. Submittal date: 03/28/2003.

LB030432DGRIDS.001. Three 2-D Cross-section Grids. Submittal date: 04/29/2003.

LB0304GASFLW3D.001. Time-dependent gas pressure distributions in UZ flow-fields (using a 5-character element thermal mesh). Submittal date: 04/29/2003.

LB0304RDTRNSNS.001. Supporting Files of 3D Flow and Transport Sensitivity Analyses. Submittal date: 04/29/2003.

LB0304UZSRTRAN.001. UZ strontium transport modeling: Simulations. Submittal date: 04/29/2003.

LB0305PTNTSW9I.001. PTn/TSw Interface Percolation Flux Maps for 9 Alternative Infiltration Scenarios. Submittal date: 05/12/2003.

LB0305TSPA18FF.001. Eighteen 3-D Site Scale UZ Flow Fields Converted from TOUGH2 to T2FEHM format. Submittal date: 05/09/2003.

ATTACHMENT I
Calibrated Parameter Sets, Combining One-Dimensional Inversions and Three-Dimensional Perched-Water and Chloride-Transport Modeling, Used in Generating the Nine Flow Fields, and Tracer Transport Times

Table I-1. Calibrated Parameters for the Present-Day, Mean Infiltration Scenario, Used for Simulations with the Mean Infiltration Scenarios of the Present-Day, Monsoon, and Glacial Transition Climates

Model Layer	K_M (m ²)	α_M (1/Pa)	m_M (-)	K_F (m ²)	α_F (1/Pa)	m_F (-)	γ (-)
tcw11	3.74E-15	1.01E-5	0.388	4.24E-11	5.27E-3	0.633	0.587
tcw12	5.52E-20	3.11E-6	0.280	9.53E-11	1.57E-3	0.633	0.587
tcw13	5.65E-17	3.26E-6	0.259	1.32E-11	1.24E-3	0.633	0.587
ptn21	9.90E-13	1.01E-5	0.176	1.86E-12	1.68E-3	0.580	0.09
ptn22	2.65E-12	1.60E-4	0.326	2.00E-11	7.68E-4	0.580	0.09
ptn23	1.23E-13	5.58E-6	0.397	2.60E-13	9.23E-4	0.610	0.09
ptn24	7.86E-14	1.53E-4	0.225	4.67E-13	3.37E-3	0.623	0.09
ptn25	7.00E-14	5.27E-5	0.323	7.03E-13	6.33E-4	0.644	0.09
ptn26	2.21E-13	2.49E-4	0.285	4.44E-13	2.79E-4	0.552	0.09
tsw31	2.95E-17	8.70E-5	0.218	5.42E-12	1.00E-4	0.633	0.129
tsw32	2.23E-16	1.14E-5	0.290	4.72E-12	1.00E-4	0.633	0.600
tsw33	6.57E-18	6.17E-6	0.283	5.18E-12	1.59E-3	0.633	0.600
tsw34	1.77E-19	8.45E-6	0.317	2.21E-12	1.04E-4	0.633	0.569
tsw35	4.48E-18	1.08E-5	0.216	6.08E-12	1.02E-4	0.633	0.569
tsw36	2.00E-19	8.32E-6	0.442	8.99E-12	7.44E-4	0.633	0.569
Tsw37	2.00E-19	8.32E-6	0.442	8.99E-12	7.44E-4	0.633	0.569
Tsw38	2.00E-18	6.23E-6	0.286	8.10E-13	2.12E-3	0.633	0.569
Tswz (zeolitic portion of tsw39)	3.50E-17	4.61E-6	0.059	8.10E-13	1.50E-3	0.633	0.370
Tswv (vitric portion of tsw39)	1.49E-13	4.86E-5	0.293	a	a	a	a
ch1z	3.50E-17	2.12E-7	0.349	2.50E-14	1.40E-3	0.633	0.370
ch1v	6.65E-13	8.73E-5	0.240	a	a	a	a
ch2v	2.97E-11	2.59E-4	0.158	a	a	a	a
ch3v	2.97E-11	2.59E-4	0.158	a	a	a	a
ch4v	2.97E-11	2.59E-4	0.158	a	a	a	a
ch5v	2.97E-11	2.59E-4	0.158	a	a	a	a
ch6v	2.35E-13	1.57E-5	0.147	a	a	a	a
ch2z	5.20E-18	2.25E-6	0.257	2.50E-14	8.90E-4	0.633	0.370
ch3z	5.20E-18	2.25E-6	0.257	2.50E-14	8.90E-4	0.633	0.370
ch4z	5.20E-18	2.25E-6	0.257	2.50E-14	8.90E-4	0.633	0.370
ch5z	5.20E-18	2.25E-6	0.257	2.50E-14	8.90E-4	0.633	0.370
ch6z	8.20E-19	1.56E-7	0.499	2.50E-14	1.40E-3	0.633	0.370
pp4	8.77E-17	4.49E-7	0.474	2.50E-14	1.83E-3	0.633	0.370
pp3	7.14E-14	8.83E-6	0.407	2.20E-13	2.47E-3	0.633	0.199

Table I-1. Calibrated Parameters for the Present-Day, Mean Infiltration Scenario, Used for Simulations with the Mean Infiltration Scenarios of the Present-Day, Monsoon, and Glacial Transition Climates (continued)

Model Layer	K_M (m ²)	α_M (1/Pa)	m_M (-)	K_F (m ²)	α_F (1/Pa)	m_F (-)	γ (-)
pp2	1.68E-15	2.39E-6	0.309	2.20E-13	3.17E-3	0.633	0.199
pp1	2.35E-15	9.19E-7	0.272	2.50E-14	1.83E-3	0.633	0.370
bf3	4.34E-13	1.26E-5	0.193	2.20E-13	2.93E-3	0.633	0.199
bf2	8.10E-17	1.18E-7	0.617	2.50E-14	8.90E-4	0.633	0.370
pcM38/ pcF38	3.00E-19	6.23E-6	0.286	3.00E-18	6.23E-6	0.286	0.00
pcM39/ pcF39	6.20E-18	4.61E-6	0.059	6.20E-17	4.61E-6	0.059	0.00
pcM1z/ pcF1z	9.30E-20	2.12E-7	0.349	9.30E-19	2.12E-7	0.349	0.00
pcM2z/ pcF2z	2.40E-18	2.25E-6	0.257	2.40E-17	2.25E-6	0.257	0.00
pcM5z/ pcF5z	2.40E-18	2.25E-6	0.257	2.40E-18	2.25E-6	0.257	0.00
pcM6z/ pcF6z	1.10E-19	1.56E-7	0.499	1.10E-19	1.56E-7	0.499	0.00
pcM4p/ pcF4p	7.70E-19	4.49E-7	0.474	7.70E-19	4.49E-7	0.474	0.00

NOTE: These data have been developed as documented in this Model Report and submitted under Output-DTN: LB03013DSSCP3I.001

a = Conceptual model for Calibrated Properties Model does not include fractures in these model layers

Table I-2. Calibrated Parameters for the Present-Day, Upper-Bound Infiltration Scenario, Used for Simulations with the Upper-Bound Infiltration Scenarios of the Present-Day, Monsoon, and Glacial Transition Climates

Model Layer	K_M (m ²)	α_M (1/Pa)	m_M (-)	K_F (m ²)	α_F (1/Pa)	m_F (-)	γ (-)
Tcw11	3.90E-15	1.23E-5	0.388	3.16E-12	5.01E-3	0.633	0.500
Tcw12	1.16E-19	3.39E-6	0.280	1.00E-10	2.19E-3	0.633	0.500
Tcw13	4.41E-16	3.25E-6	0.259	9.67E-13	1.86E-3	0.633	0.500
ptn21	1.26E-13	1.84E-4	0.199	1.00E-11	2.38E-3	0.611	0.08
ptn22	5.98E-12	2.42E-5	0.473	1.00E-11	1.26E-3	0.665	0.08
ptn23	3.43E-13	4.06E-6	0.407	1.96E-13	1.25E-3	0.627	0.08
ptn24	3.93E-13	5.27E-5	0.271	4.38E-13	2.25E-3	0.631	0.08
ptn25	1.85E-13	2.95E-5	0.378	6.14E-13	1.00E-3	0.637	0.08
ptn26	6.39E-13	3.54E-4	0.265	3.48E-13	3.98E-4	0.367	0.08
Tsw31	1.77E-17	4.85E-5	0.218	6.46E-11	1.00E-4	0.633	0.100
Tsw32	2.13E-16	1.96E-5	0.290	5.62E-11	1.00E-4	0.633	0.561
Tsw33	2.39E-17	5.22E-6	0.283	6.17E-11	1.58E-3	0.633	0.561
Tsw34	2.96E-19	1.65E-6	0.317	2.63E-11	1.00E-4	0.633	0.570
Tsw35	8.55E-18	5.03E-6	0.216	7.24E-11	5.78E-4	0.633	0.570
Tsw36	7.41E-19	1.08E-6	0.442	1.07E-10	1.10E-3	0.633	0.570
Tsw37	7.41E-19	1.08E-6	0.442	1.07E-10	1.10E-3	0.633	0.570
Tsw38	7.40E-18	5.58E-6	0.286	8.10E-13	8.91E-4	0.633	0.570
Tswz (zeolitic portion of tsw39)	3.50E-17	4.61E-6	0.059	8.10E-13	1.50E-3	0.633	0.500
Tswv (vitric portion of tsw39)	2.24E-13	4.86E-5	0.293	a	a	a	a
ch1z	3.50E-17	2.12E-7	0.349	2.50E-14	1.40E-3	0.633	0.500
ch1v	1.39E-12	8.82E-5	0.240	a	a	a	a
ch2v	4.90E-11	2.73E-4	0.158	a	a	a	a
ch3v	4.90E-11	2.73E-4	0.158	a	a	a	a
ch4v	4.90E-11	2.73E-4	0.158	a	a	a	a
ch5v	4.90E-11	2.73E-4	0.158	a	a	a	a
ch6v	2.72E-13	1.67E-5	0.147	a	a	a	a
ch2z	5.20E-18	2.25E-6	0.257	2.50E-14	8.90E-4	0.633	0.500
ch3z	5.20E-18	2.25E-6	0.257	2.50E-14	8.90E-4	0.633	0.500
ch4z	5.20E-18	2.25E-6	0.257	2.50E-14	8.90E-4	0.633	0.500
ch5z	5.20E-18	2.25E-6	0.257	2.50E-14	8.90E-4	0.633	0.500
ch6z	8.20E-19	1.56E-7	0.499	2.50E-14	1.40E-3	0.633	0.500
pp4	1.02E-15	4.57E-7	0.474	2.50E-12	8.91E-4	0.633	0.500
pp3	1.26E-13	9.50E-6	0.407	2.20E-12	1.66E-3	0.633	0.500
pp2	1.70E-15	2.25E-6	0.309	2.20E-13	1.66E-3	0.633	0.500
pp1	2.57E-15	8.77E-7	0.272	2.50E-14	8.91E-4	0.633	0.500
bf3	3.55E-14	3.48E-5	0.193	2.20E-13	1.66E-3	0.633	0.500

Table I-2. Calibrated Parameters for the Present-Day, Upper-Bound Infiltration Scenario, Used for Simulations with the Upper-Bound Infiltration Scenarios of the Present-Day, Monsoon, and Glacial Transition Climates (continued)

Model Layer	K_M (m ²)	α_M (1/Pa)	m_M (-)	K_F (m ²)	α_F (1/Pa)	m_F (-)	γ (-)
bf2	8.10E-17	1.18E-7	0.617	2.50E-14	8.90E-4	0.633	0.500
pcM38/ pcF38	3.00E-19	5.58E-6	0.286	3.00E-18	5.58E-6	0.286	0.00
pcM39/ pcF39	6.20E-18	4.61E-6	0.059	6.20E-17	4.61E-6	0.059	0.00
pcM1z/ pcF1z	9.30E-20	2.12E-7	0.349	9.30E-19	2.12E-7	0.349	0.00
pcM2z/ pcF2z	2.40E-18	2.25E-6	0.257	2.40E-17	2.25E-6	0.257	0.00
pcM5z/ pcF5z	2.40E-18	2.25E-6	0.257	2.40E-18	2.25E-6	0.257	0.00
pcM6z/ pcF6z	1.10E-19	1.56E-7	0.499	1.10E-19	1.56E-7	0.499	0.00
pcM4p/ pcF4p	7.70E-19	4.57E-7	0.474	7.70E-19	4.57E-7	0.474	0.00

NOTE: These data have been developed as documented in this Model Report and submitted under Output-DTN: LB03013DSSCP3I.001

a = Conceptual model for Calibrated Properties Model does not include fractures in these model layers

Table I-3. Calibrated Parameters for the Present-Day, Lower-Bound Infiltration Scenario, Used for Simulations with the Lower-Bound Infiltration Scenarios of the Present-Day, Monsoon, and Glacial Transition Climates

Model Layer	K_M (m ²)	α_M (1/Pa)	M_M (-)	K_F (m ²)	α_F (1/Pa)	m_F (-)	γ (-)
tcw11	3.44E-15	1.16E-5	0.388	3.16E-12	4.68E-3	0.633	0.483
tcw12	3.00E-20	2.67E-6	0.280	9.73E-11	3.20E-3	0.633	0.483
tcw13	3.96E-17	1.64E-6	0.259	9.47E-13	2.13E-3	0.633	0.483
ptn21	1.86E-13	6.13E-5	0.165	1.00E-11	1.66E-3	0.503	0.01
ptn22	3.27E-12	1.51E-5	0.390	1.00E-11	9.39E-4	0.651	0.01
ptn23	4.20E-13	2.04E-6	0.388	1.84E-13	1.28E-3	0.518	0.01
ptn24	3.94E-13	2.32E-5	0.210	4.31E-13	2.02E-3	0.594	0.01
ptn25	2.22E-13	2.04E-5	0.296	7.12E-13	7.42E-4	0.555	0.01
ptn26	5.43E-13	1.82E-4	0.264	3.08E-13	2.00E-4	0.401	0.01
tsw31	1.42E-17	8.02E-5	0.218	5.13E-11	1.00E-4	0.633	0.037
tsw32	3.96E-16	9.46E-6	0.290	4.47E-11	1.31E-4	0.633	0.528
tsw33	1.60E-18	4.25E-6	0.283	4.90E-11	1.94E-3	0.633	0.528
tsw34	1.38E-19	1.19E-6	0.317	2.09E-11	6.55E-4	0.633	0.476
tsw35	2.33E-18	1.97E-6	0.216	5.75E-11	1.35E-3	0.633	0.476
tsw36	5.58E-19	4.22E-7	0.442	8.51E-11	1.31E-3	0.633	0.476
tsw37	5.58E-19	4.22E-7	0.442	8.51E-11	1.31E-3	0.633	0.476
tsw38	2.93E-18	1.43E-6	0.286	8.10E-13	1.75E-3	0.633	0.476
tswz (zeolitic portion of tsw39)	3.50E-17	4.61E-6	0.059	8.10E-13	1.50E-3	0.633	0.276
tswv (vitric portion of tsw39)	3.15E-13	1.86E-5	0.293	a	a	a	a
ch1z	3.50E-17	2.12E-7	0.349	2.50E-14	1.40E-3	0.633	0.276
ch1v	3.15E-14	4.50E-5	0.240	a	a	a	a
ch2v	1.13E-11	1.22E-4	0.158	a	a	a	a
ch3v	1.13E-11	1.22E-4	0.158	a	a	a	a
ch4v	1.13E-11	1.22E-4	0.158	a	a	a	a
ch5v	1.13E-11	1.22E-4	0.158	a	a	a	a
ch6v	2.54E-13	9.05E-6	0.147	a	a	a	a
ch2z	5.20E-18	2.25E-6	0.257	2.50E-14	8.90E-4	0.633	0.276
ch3z	5.20E-18	2.25E-6	0.257	2.50E-14	8.90E-4	0.633	0.276
ch4z	5.20E-18	2.25E-6	0.257	2.50E-14	8.90E-4	0.633	0.276
ch5z	5.20E-18	2.25E-6	0.257	2.50E-14	8.90E-4	0.633	0.276
ch6z	8.20E-19	1.56E-7	0.499	2.50E-14	1.40E-3	0.633	0.276
pp4	2.98E-16	2.88E-7	0.474	2.50E-14	1.88E-3	0.633	0.276

Table I-3. Calibrated Parameters for the Present-Day, Lower-Bound Infiltration Scenario, Used for Simulations with the Lower-Bound Infiltration Scenarios of the Present-Day, Monsoon, and Glacial Transition Climates (continued)

Model Layer	K_M (m ²)	α_M (1/Pa)	M_M (-)	K_F (m ²)	α_F (1/Pa)	m_F (-)	γ (-)
pp3	5.37E-14	7.97E-6	0.407	2.20E-13	1.32E-3	0.633	0.248
pp2	4.24E-16	2.41E-6	0.309	2.20E-13	2.80E-3	0.633	0.248
pp1	7.02E-16	1.36E-6	0.272	2.50E-14	6.39E-4	0.633	0.276
bf3	2.97E-14	1.32E-5	0.193	2.20E-13	1.92E-3	0.633	0.248
bf2	8.1E-17	1.18E-7	0.617	2.50E-14	8.9E-4	0.633	0.276
pcM38/ pcF38	3.00E-19	1.43E-6	0.286	3.00E-19	1.43E-6	0.286	0.00
pcM39/ pcF39	6.20E-18	4.61E-6	0.059	6.20E-18	4.61E-6	0.059	0.00
pcM1z/ pcF1z	9.30E-20	2.12E-7	0.349	9.30E-20	2.12E-7	0.349	0.00
pcM2z/ pcF2z	2.40E-18	2.25E-6	0.257	2.40E-18	2.25E-6	0.257	0.00
pcM5z/ pcF5z	2.40E-18	2.25E-6	0.257	2.40E-18	2.25E-6	0.257	0.00
pcM6z/ pcF6z	1.10E-19	1.56E-7	0.499	1.10E-19	1.56E-7	0.499	0.00
pcM4p/ pcF4p	7.70E-19	2.88E-7	0.474	7.70E-19	2.88E-7	0.474	0.00

NOTE: These data have been developed as documented in this Model Report and submitted under Output-DTN: LB03013DSSCP3I.001

a = Conceptual model for Calibrated Properties Model does not include fractures in these model layers (Section 5).

Table I-4. Calibrated Parameters for the Alternative Modeling Studies of the Present-Day, Mean Infiltration Scenario, Used for Simulations with the Mean Infiltration Scenarios of the Present-Day, Monsoon, and Glacial Transition Climates

Model Layer	K_M (m ²)	α_M (1/Pa)	m_M (-)	K_F (m ²)	α_F (1/Pa)	m_F (-)	γ (-)
tcw11	3.74E-15	1.01E-5	0.388	4.24E-11	5.27E-3	0.633	0.587
tcw12	5.52E-20	3.11E-6	0.280	9.53E-11	1.57E-3	0.633	0.587
tcw13	5.65E-17	3.26E-6	0.259	1.32E-11	1.24E-3	0.633	0.587
ptn21	4.60E-15	1.62E-4	0.245	2.11E-12	8.70E-4	0.633	0.232
ptn22	4.43E-12	1.46E-4	0.219	9.41E-12	1.57E-3	0.633	0.232
ptn23	9.20E-15	2.47E-5	0.247	5.35E-13	5.18E-3	0.633	0.232
ptn24	2.35E-12	7.90E-4	0.182	1.00E-11	1.86E-3	0.633	0.232
ptn25	2.15E-13	1.04E-4	0.300	1.24E-12	1.33E-3	0.633	0.232
ptn26	1.00E-11	9.83E-4	0.126	3.17E-13	1.34E-3	0.633	0.232
tsw31	2.95E-17	8.70E-5	0.218	5.42E-12	1.00E-4	0.633	0.129
tsw32	2.23E-16	1.14E-5	0.290	4.72E-12	1.00E-4	0.633	0.600
tsw33	6.57E-18	6.17E-6	0.283	5.18E-12	1.59E-3	0.633	0.600
tsw34	1.77E-19	8.45E-6	0.317	2.21E-12	1.04E-4	0.633	0.569
tsw35	4.48E-18	1.08E-5	0.216	6.08E-12	1.02E-4	0.633	0.569
tsw36	2.00E-19	8.32E-6	0.442	8.99E-12	7.44E-4	0.633	0.569
Tsw37	2.00E-19	8.32E-6	0.442	8.99E-12	7.44E-4	0.633	0.569
Tsw38	2.00E-18	6.23E-6	0.286	8.10E-13	2.12E-3	0.633	0.569
Tswz (zeolitic portion of tsw39)	3.50E-17	4.61E-6	0.059	8.10E-13	1.5E-3	0.633	0.370
Tswv (vitric portion of tsw39)	1.49E-13	4.86E-5	0.293	a	a	a	a
Ch1z	3.50E-17	2.12E-7	0.349	2.50E-14	1.4E-3	0.633	0.370
Ch1v	6.65E-13	8.73E-5	0.240	a	a	a	a
Ch2v	2.97E-11	2.59E-4	0.158	a	a	a	a
Ch3v	2.97E-11	2.59E-4	0.158	a	a	a	a
Ch4v	2.97E-11	2.59E-4	0.158	a	a	a	a
Ch5v	2.97E-11	2.59E-4	0.158	a	a	a	a
Ch6v	2.35E-13	1.57E-5	0.147	a	a	a	a
Ch2z	5.20E-18	2.25E-6	0.257	2.50E-14	8.90E-4	0.633	0.370
Ch3z	5.20E-18	2.25E-6	0.257	2.50E-14	8.90E-4	0.633	0.370
Ch4z	5.20E-18	2.25E-6	0.257	2.50E-14	8.90E-4	0.633	0.370
Ch5z	5.20E-18	2.25E-6	0.257	2.50E-14	8.90E-4	0.633	0.370
Ch6z	8.20E-19	1.56E-7	0.499	2.50E-14	1.40E-3	0.633	0.370
Pp4	8.77E-17	4.49E-7	0.474	2.50E-14	1.83E-3	0.633	0.370
Pp3	7.14E-14	8.83E-6	0.407	2.20E-13	2.47E-3	0.633	0.199
Pp2	1.68E-15	2.39E-6	0.309	2.20E-13	3.17E-3	0.633	0.199
Pp1	2.35E-15	9.19E-7	0.272	2.50E-14	1.83E-3	0.633	0.370
Bf3	4.34E-13	1.26E-5	0.193	2.20E-13	2.93E-3	0.633	0.199
Bf2	8.10E-17	1.18E-7	0.617	2.50E-14	8.90E-4	0.633	0.370

Table I-4. Calibrated Parameters for the Alternative Modeling Studies of the Present-Day, Mean Infiltration Scenario, Used for Simulations with the Mean Infiltration Scenarios of the Present-Day, Monsoon, and Glacial Transition Climates (continued)

Model Layer	K_M (m ²)	α_M (1/Pa)	m_M (-)	K_F (m ²)	α_F (1/Pa)	m_F (-)	γ (-)
PcM38/ pcF38	3.00E-19	6.23E-6	0.286	3.00E-18	6.23E-6	0.286	0.00
pcM39/ pcF39	6.20E-18	4.61E-6	0.059	6.20E-17	4.61E-6	0.059	0.00
pcM1z/ pcF1z	9.30E-20	2.12E-7	0.349	9.30E-19	2.12E-7	0.349	0.00
pcM2z/ pcF2z	2.40E-18	2.25E-6	0.257	2.40E-17	2.25E-6	0.257	0.00
pcM5z/ pcF5z	2.40E-18	2.25E-6	0.257	2.40E-18	2.25E-6	0.257	0.00
pcM6z/ pcF6z	1.10E-19	1.56E-7	0.499	1.10E-19	1.56E-7	0.499	0.00
pcM4p/ pcF4p	7.70E-19	4.49E-7	0.474	7.70E-19	4.49E-7	0.474	0.00

NOTE: These data have been developed as documented in this Model Report and submitted under Output-DTN: LB03013DSSCP3I.001

a = Conceptual model for Calibrated Properties Model does not include fractures in these model layers

Table I-5. Calibrated Parameters for the Alternative Modeling Studies of the Present-Day, Upper-Bound Infiltration Scenario, Used for Simulations with the Upper-Bound Infiltration Scenarios of the Present-Day, Monsoon, and Glacial Transition Climates

Model Layer	K_M (m ²)	α_M (1/Pa)	m_M (-)	K_F (m ²)	α_F (1/Pa)	m_F (-)	γ (-)
tcw11	3.90E-15	1.23E-5	0.388	3.16E-12	5.01E-3	0.633	0.500
tcw12	1.16E-19	3.39E-6	0.280	1.00E-10	2.19E-3	0.633	0.500
tcw13	4.41E-16	3.25E-6	0.259	9.67E-13	1.86E-3	0.633	0.500
ptn21	2.14E-14	1.56E-4	0.245	1.00E-11	2.69E-3	0.633	0.100
ptn22	1.29E-11	1.33E-4	0.219	3.85E-13	1.38E-3	0.633	0.100
ptn23	4.07E-14	2.39E-5	0.247	9.04E-14	1.23E-3	0.633	0.100
ptn24	4.27E-12	5.62E-4	0.182	3.16E-13	2.95E-3	0.633	0.100
ptn25	1.01E-12	9.48E-5	0.300	1.59E-13	1.10E-3	0.633	0.100
ptn26	1.00E-11	5.23E-4	0.126	9.23E-13	9.55E-4	0.633	0.100
tsw31	1.77E-17	4.85E-5	0.218	6.46E-11	1.00E-4	0.633	0.100
tsw32	2.13E-16	1.96E-5	0.290	5.62E-11	1.00E-4	0.633	0.561
tsw33	2.39E-17	5.22E-6	0.283	6.17E-11	1.58E-3	0.633	0.561
tsw34	2.96E-19	1.65E-6	0.317	2.63E-11	1.00E-4	0.633	0.570
tsw35	8.55E-18	5.03E-6	0.216	7.24E-11	5.78E-4	0.633	0.570
tsw36	7.41E-19	1.08E-6	0.442	1.07E-10	1.10E-3	0.633	0.570
tsw37	7.41E-19	1.08E-6	0.442	1.07E-10	1.10E-3	0.633	0.570
tsw38	7.40E-18	5.58E-6	0.286	8.10E-13	8.91E-4	0.633	0.570
tswz (zeolitic portion of tsw39)	3.50E-17	4.61E-6	0.059	8.10E-13	1.50E-3	0.633	0.500
tswv (vitric portion of tsw39)	2.24E-13	4.86E-5	0.293	a	a	a	a
ch1z	3.50E-17	2.12E-7	0.349	2.50E-14	1.40E-3	0.633	0.500
ch1v	1.39E-12	8.82E-5	0.240	a	a	a	a
ch2v	4.90E-11	2.73E-4	0.158	a	a	a	a
ch3v	4.90E-11	2.73E-4	0.158	a	a	a	a
ch4v	4.90E-11	2.73E-4	0.158	a	a	a	a
ch5v	4.90E-11	2.73E-4	0.158	a	a	a	a
ch6v	2.72E-13	1.67E-5	0.147	a	a	a	a
ch2z	5.20E-18	2.25E-6	0.257	2.50E-14	8.90E-4	0.633	0.500
ch3z	5.20E-18	2.25E-6	0.257	2.50E-14	8.90E-4	0.633	0.500
ch4z	5.20E-18	2.25E-6	0.257	2.50E-14	8.90E-4	0.633	0.500
ch5z	5.20E-18	2.25E-6	0.257	2.50E-14	8.90E-4	0.633	0.500
ch6z	8.20E-19	1.56E-7	0.499	2.50E-14	1.40E-3	0.633	0.500
pp4	1.02E-15	4.57E-7	0.474	2.50E-12	8.91E-4	0.633	0.500
pp3	1.26E-13	9.50E-6	0.407	2.20E-12	1.66E-3	0.633	0.500
pp2	1.70E-15	2.25E-6	0.309	2.20E-13	1.66E-3	0.633	0.500
pp1	2.57E-15	8.77E-7	0.272	2.50E-14	8.91E-4	0.633	0.500
bf3	3.55E-14	3.48E-5	0.193	2.20E-13	1.66E-3	0.633	0.500

Table I-5. Calibrated Parameters for the Alternative Modeling Studies of the Present-Day, Upper-Bound Infiltration Scenario, Used for Simulations with the Upper-Bound Infiltration Scenarios of the Present-Day, Monsoon, and Glacial Transition Climates (continued)

Model Layer	K_M (m ²)	α_M (1/Pa)	m_M (-)	K_F (m ²)	α_F (1/Pa)	m_F (-)	γ (-)
bf2	8.10E-17	1.18E-7	0.617	2.50E-14	8.90E-4	0.633	0.500
pcM38/ pcF38	3.00E-19	5.58E-6	0.286	3.00E-18	5.58E-6	0.286	0.00
pcM39/ pcF39	6.20E-18	4.61E-6	0.059	6.20E-17	4.61E-6	0.059	0.00
pcM1z/ pcF1z	9.30E-20	2.12E-7	0.349	9.30E-19	2.12E-7	0.349	0.00
pcM2z/ pcF2z	2.40E-18	2.25E-6	0.257	2.40E-17	2.25E-6	0.257	0.00
pcM5z/ pcF5z	2.40E-18	2.25E-6	0.257	2.40E-18	2.25E-6	0.257	0.00
pcM6z/ pcF6z	1.10E-19	1.56E-7	0.499	1.10E-19	1.56E-7	0.499	0.00
pcM4p/ pcF4p	7.70E-19	4.57E-7	0.474	7.70E-19	4.57E-7	0.474	0.00

NOTE: These data have been developed as documented in this Model Report and submitted under Output-DTN: LB03013DSSCP3I.001

a = Conceptual model for Calibrated Properties Model does not include fractures in these model layers

Table I-6. Calibrated Parameters for the Alternative Modeling Studies of the Present-Day, Lower-Bound Infiltration Scenario, Used for Simulations with the Lower-Bound Infiltration Scenarios of the Present-Day, Monsoon, and Glacial Transition Climates

Model Layer	K_M (m ²)	α_M (1/Pa)	m_M (-)	K_F (m ²)	α_F (1/Pa)	m_F (-)	γ (-)
tcw11	3.44E-15	1.16E-5	0.388	3.16E-12	4.68E-3	0.633	0.483
tcw12	3.00E-20	2.67E-6	0.280	9.73E-11	3.20E-3	0.633	0.483
tcw13	3.96E-17	1.64E-6	0.259	9.47E-13	2.13E-3	0.633	0.483
ptn21	5.55E-15	6.38E-5	0.245	1.00E-11	2.93E-3	0.633	0.065
ptn22	8.40E-12	1.67E-4	0.219	1.00E-11	6.76E-4	0.633	0.065
ptn23	1.92E-14	4.51E-5	0.247	1.16E-13	3.96E-3	0.633	0.065
ptn24	6.66E-13	2.52E-3	0.182	1.00E-11	2.51E-3	0.633	0.065
ptn25	1.96E-14	1.24E-4	0.300	4.37E-13	1.53E-3	0.633	0.065
ptn26	1.00E-11	1.63E-3	0.126	8.29E-14	1.52E-3	0.633	0.065
tsw31	1.42E-17	8.02E-5	0.218	5.13E-11	1.00E-4	0.633	0.037
tsw32	3.96E-16	9.46E-6	0.290	4.47E-11	1.31E-4	0.633	0.528
tsw33	1.60E-18	4.25E-6	0.283	4.90E-11	1.94E-3	0.633	0.528
tsw34	1.38E-19	1.19E-6	0.317	2.09E-11	6.55E-4	0.633	0.476
tsw35	2.33E-18	1.97E-6	0.216	5.75E-11	1.35E-3	0.633	0.476
tsw36	5.58E-19	4.22E-7	0.442	8.51E-11	1.31E-3	0.633	0.476
tsw37	5.58E-19	4.22E-7	0.442	8.51E-11	1.31E-3	0.633	0.476
tsw38	2.93E-18	1.43E-6	0.286	8.10E-13	1.75E-3	0.633	0.476
tswz (zeolitic portion of tsw39)	3.50E-17	4.61E-6	0.059	8.10E-13	1.50E-3	0.633	0.276
tswv (vitric portion of tsw39)	3.15E-13	1.86E-5	0.293	a	a	a	a
ch1z	3.50E-17	2.12E-7	0.349	2.50E-14	1.40E-3	0.633	0.276
ch1v	3.15E-14	4.50E-5	0.240	a	a	a	a
ch2v	1.13E-11	1.22E-4	0.158	a	a	a	a
ch3v	1.13E-11	1.22E-4	0.158	a	a	a	a
ch4v	1.13E-11	1.22E-4	0.158	a	a	a	a
ch5v	1.13E-11	1.22E-4	0.158	a	a	a	a
ch6v	2.54E-13	9.05E-6	0.147	a	a	a	a
ch2z	5.20E-18	2.25E-6	0.257	2.50E-14	8.90E-4	0.633	0.276
ch3z	5.20E-18	2.25E-6	0.257	2.50E-14	8.90E-4	0.633	0.276
ch4z	5.20E-18	2.25E-6	0.257	2.50E-14	8.90E-4	0.633	0.276
ch5z	5.20E-18	2.25E-6	0.257	2.50E-14	8.90E-4	0.633	0.276
ch6z	8.20E-19	1.56E-7	0.499	2.50E-14	1.40E-3	0.633	0.276
pp4	2.98E-16	2.88E-7	0.474	2.50E-14	1.88E-3	0.633	0.276
pp3	5.37E-14	7.97E-6	0.407	2.20E-13	1.32E-3	0.633	0.248
pp2	4.24E-16	2.41E-6	0.309	2.20E-13	2.80E-3	0.633	0.248
pp1	7.02E-16	1.36E-6	0.272	2.50E-14	6.39E-4	0.633	0.276

Table I-6. Calibrated Parameters for the Alternative Modeling Studies of the Present-Day, Lower-Bound Infiltration Scenario, Used for Simulations with the Lower-Bound Infiltration Scenarios of the Present-Day, Monsoon, and Glacial Transition Climates (continued)

Model Layer	K_M (m ²)	α_M (1/Pa)	m_M (-)	K_F (m ²)	α_F (1/Pa)	m_F (-)	γ (-)
bf3	2.97E-14	1.32E-5	0.193	2.20E-13	1.92E-3	0.633	0.248
bf2	8.10E-17	1.18E-7	0.617	2.50E-14	8.90E-4	0.633	0.276
pcM38/ pcF38	3.00E-19	1.43E-6	0.286	3.00E-19	1.43E-6	0.286	0.00
pcM39/ pcF39	6.20E-18	4.61E-6	0.059	6.20E-18	4.61E-6	0.059	0.00
pcM1z/ pcF1z	9.30E-20	2.12E-7	0.349	9.30E-20	2.12E-7	0.349	0.00
pcM2z/ pcF2z	2.40E-18	2.25E-6	0.257	2.40E-18	2.25E-6	0.257	0.00
pcM5z/ pcF5z	2.40E-18	2.25E-6	0.257	2.40E-18	2.25E-6	0.257	0.00
pcM6z/ pcF6z	1.10E-19	1.56E-7	0.499	1.10E-19	1.56E-7	0.499	0.00
pcM4p/ pcF4p	7.70E-19	2.88E-7	0.474	7.70E-19	2.88E-7	0.474	0.00

NOTE: These data have been developed as documented in this Model Report and submitted under Output-DTN: LB03013DSSCP3I.001.

a = Conceptual model for Calibrated Properties Model does not include fractures in these model layers (Section 5).

ATTACHMENT II—LOCATION COORDINATES AND SURFACE ELEVATIONS OF SELECTED BOREHOLES USED IN MODEL CALIBRATION AND STUDIES

Table II-1. Coordinates and Surface Elevations of Selected Boreholes

Borehole	Easting (ft)	Northing (ft)	Elevation (ft)	Easting (m)	Northing (m)	Elevation (m)
NRG-6	564187	766726	4093	171964.198	233698.0848	1247.5464
NRG-7A	562984	768880	4209	171597.523	234354.624	1282.9032
SD-6	558608	762421	4906	170263.718	232385.9208	1495.3488
SD-7	561240	758950	4475	171065.952	231327.96	1363.98
SD-9	561818	767998	4275	171242.126	234085.7904	1303.02
SD-12	561606	761957	4343	171177.509	232244.4936	1323.7464
UZ#4	566140	768716	3941	172559.472	234304.6368	1201.2168
UZ#5	566136	768593	3954	172558.253	234267.1464	1205.1792
UZ-7a	562270	760693	4230	171379.896	231859.2264	1289.304
UZ-14	560142	771310	4427	170731.282	235095.288	1349.3496
UZ#16	564857	760535	4002	172168.414	231811.068	1219.8096
H-5	558908	766634	4852	170355.158	233670.0432	1478.8896
G-2	560504	778826	5098	170841.619	237386.1648	1553.8704
G-3	558483	752780	4858	170225.618	229447.344	1480.7184
WT#24	562329	776703	4900	171397.879	236739.0744	1493.52

Source: From: DTN: MO0012MWDGFM02.002 [153777], file contacts00el.dat

INTENTIONALLY LEFT BLANK

ATTACHMENT III—COMPUTATIONS IN INPUT DATA PREPARATIONS AND SIMULATION RESULT ANALYSES

This attachment presents the details of calculations in postprocessing of the simulation results and data analyses of Sections 6.5, 6.6, and 6.8. The working files are saved in the attached CD labeled as: Files of Attachments III for Model Report, MDL-NBS-HS-000006 REV01.

III.1 Calculating the Chloride Flux of Section 6.5

III.1.1 Formulation

The chloride flux is calculated using the following formulation:

$$F_{Cl} = C_{Cl,p} \times 10^{-6} (F_{prec} + F_{runon} - F_{runoff}) \quad (\text{Eq. III.1.1-1})$$

where F_{Cl} is chloride flux (kg Cl⁻/second); F_{prec} is precipitation flux (kg water/second); F_{runon} is runon (kg water/second); F_{runoff} is runoff flux (kg water/second). $C_{Cl,p}$ is chloride concentration in precipitation, and was assumed to 0.55 mg/l Cl⁻ (Sonnenthal and Bodvarsson 1999 [117127], p. 148). These flux terms are generated using software routine infil2grid V1.7 (LBNL 2002 [154793]), using the net infiltration data listed below:

Table III.1.1-1 Infiltration Data Files

modern upper bound infiltration	modernu.dat
modern mean infiltration	modernm.dat
modern low bound infiltration	modernl.dat
glacial mean infiltration	glacialm.dat

DTN: GS000308311221.005 [147613]

NOTE: Attached CD (Files of Attachments III for Model Report,
MDL-NBS-HS-000006 REV01): III.1/files in Table III.1.1-1/

III.1.2 Input and Output Files Used in the Calculations

All the input files for the calculations are in the GENER format of the TOUGH2 code. Chloride (Cl) fluxes to be calculated are defined as mass recharge rates on the surface with infiltration and are represented also in terms of GENER. The input file uses the following format:

Line 1: NGENER (an integer for the total number of GENER terms)
Line 2: Notation giving mean flux
Lines from 3 to NGENER:

Format (A8, 28x, A5, F10.4, F10.4)

ELEMENT, COMPONENT, FLUX, ENTHALPY.

The input and output files used in the calculation are listed in Tables III.1.2-1 – III.1.2-4 for the three present-day infiltration scenarios and one glacial transition infiltration scenario, respectively.

Table III.1.2-1. CI Flux Calculation for Present-Day, Upper-Bound Infiltration

Input files (GENER files)	Precipitation flux	modernugenprec.dat
	Runon flux	modernugenrunon.dat
	Runoff flux	modernugenrunoff.dat
Output file (CI flux)		modernu_GENER_CI

NOTE: Attached CD (Files of Attachments III for Model Report, MDL-NBS-HS-000006 REV01): III.1/files in Table III.1.2-1/

Table III.1.2-2. CI Flux Calculation for Present-Day, Mean Infiltration

Input files (GENER files)	Precipitation flux	genmmprec
	Runon flux	genmmrunon
	Runoff flux	genmmrunoff
Output file (CI flux)		Gen_mm_CI

NOTE: Attached CD (Files of Attachments III for Model Report, MDL-NBS-HS-000006 REV01): III.1/files in table III.1.2-2/

Table III.1.2-3. CI Flux Calculation for Present-Day Lower-Bound Infiltration

Input files (GENER files)	Precipitation flux	modernlgenprec
	Runon flux	modernlgenrunon
	Runoff flux	modernlgenrunoff
Output file (CI flux)		modernl_GENER_CI

NOTE: Attached CD (Files of Attachments III for Model Report, MDL-NBS-HS-000006 REV01): III.1/files in table III.1.2-3/

Table III.1.2-4. CI Flux Calculation for Glacial Infiltration

Input files (GENER files)	Precipitation flux	glacmgenprec
	Runon flux	glacmgenrunon
	Runoff flux	glacmgenrunoff
Output file (CI flux)		glacm_GENER_CI

NOTE: Attached CD (Files of Attachments III for Model Report, MDL-NBS-HS-000006 REV01): III.1/files in table III.1.2-4/

III.1.3 Calculation Procedures

CI flux is calculated by taking the following steps:

Step 1: Open three input files using EXCEL. Then copy/paste them into one worksheet in the order of precipitation, runon, and runoff.

Step 2: Identify columns representing precipitation (column C), runon (column G), and runoff (column K).

Step 3: Use Equation (III.1.1-1) to calculate CI flux by typing:

- $= 0.55 \times 10^{-6} \times (C3 + E3 - K3)$ in Column M, Row 3. Then press <ENTER> key to get CI flux for the cell of Column M and Row 3.
- Calculate CI fluxes for the rest of the elements by highlighting and dragging down the cursor from the lower right-hand corner until Row (NGENER+2) appears.

Details of the calculation are documented in a Scientific Notebook (see Wang 2003 [162417], SN-LBNL-SCI-219-V1, pp. 122, 135–140).

III.2 Calculating Vertical Fluxes, Distribution, and Percentage of Fracture-Matrix Flow for Section 6.6

III.2.1 Extraction of Vertical Flux at the PTn Bottom

Extracting vertical fluxes at the PTn bottom or the TSw top requires two files: (1) model mesh file of the 3-D TSPA-LA model grid (“MESH_2KN.V1”, Output-DTN:LB03023DSSCP9I.001), and an output file of the base-case flow fields or any other cases of interest (e.g. “preq_mA.out”, Output-DTN: LB03023DSSCP9I.001).

In addition, the following are the four mesh-related files of identifying gridblocks, element coordinates and connection areas of the PTn bottom and TSw top layers. They have the names “PTN_BOT.XY”, “PTN.BOT”, and “TSW.TOP”, and “CONN.area”, respectively.

“PTN_BOT.XY” contains three columns and 2,042 rows. The three columns are gridblock name, x coordinate, and y coordinate. Each row corresponds to one gridblock located at the bottom layer of the PTn unit.

“PTN.BOT”: this file contains 2042 columns and only one row containing the names of the gridblocks located at the bottom layer of the PTn unit.

“TSW.TOP”: this file also contains 2042 columns and only one row containing the names of the gridblocks located at the top layer of the TSw unit.

“CONN.area”: contains connection areas for all PTn bottom/TSw top vertical connections.

These four files will be used for extracting all vertical fluxes at the PTn bottom for different infiltration scenarios and flow fields. The extracting steps are as follows:

Step 1: Extracting flow components:

Find vertical fracture-fracture (F-F) flux, matrix-matrix (M-M) flux and fracture-matrix (F-M) flux using UNIX commands (with flow field of “preq_mA.out” as an example):

```
fgrep—f TSW.TOP preq_mA.out> tsw_top.conn  
fgrep—f PTN.BOT tsw_top.conn>ptn-tsw.conn  
grep—v ' F0' ptn-tsw.conn>ptn-tsw_M.conn
```

The nonvertical connections (data rows 1,993–2,377) are then deleted from the file “ptn-tsw_M.conn”. Now, file “ptn-tsw_M.conn” contains only vertical matrix-matrix flux at the PTn bottom.

The vertical fracture-fracture flux at the PTn bottom is obtained in the following form:

```
grep -v ' M0' ptn-tsw.conn>ptn-tsw_F.conn
```

Delete data rows 1,993–2,377 from “ptn-tsw_F.conn” to exclude nonvertical connections.

The vertical fracture–matrix flux at the PTn bottom is obtained as:

```
grep ' M0' ptn-tsw.conn>tem.conn  
grep ' F0' tem.conn>ptn-tsw_FM.conn
```

Step 2: Importing flow components to the spreadsheet

Use Microsoft Excel to sum the vertical fluxes from the three types of vertical connections as follows:

Open file “ptn-tsw_M.conn”, “ptn-tsw_F.conn”, and “ptn-tsw_FM.conn”.

Copy the columns for the gridblock name of connected pairs and the fluxes in these files to a working spreadsheet (“total_ptn_flux.xls”). Note that the connections in above three files are written in the same sequence.

Step 3: Handling PTn absence:

In the UZ Flow Model grid, TCw and PTn units are absent in a number of grid columns. For these columns, infiltration rates are directly added to the top layers of the TSw. Therefore, these infiltration rates are considered as bottom PTn fluxes.

Use command “fgrep –f TSW.TOP GENER>preq_m.inf” to extract infiltration data, and then edit “preq_m.inf” using a PC MS DOS editor. File “preq_m.inf” consists of two columns. Column 1 is the name of gridblocks that are directly connected to the model top boundary; the second column is its corresponding infiltration rate (in kg/s). Note the “GENER” file is different for different infiltration scenarios.

There are a total of 110 direct connections to the top boundary from the TSw unit.

Step 4: Incorporation of additional files and summation

Import preq_m.inf to the working spreadsheet (“total_ptn_flux.xls”).

Import “PTN_BOT.XY” to the working spreadsheet.

Import “CONN.area” to the spreadsheet (Note that all connections in different files should be in the same sequence).

Sum fluxes along fracture-fracture (F-F), matrix-matrix (M-M), and fracture-matrix (F-M) connections for the same column and infiltration corrections.

Transform the unit of total vertical flux from kg/s to mm/y by performing $q_n = q_o * 31557600.0 / \text{area}$, where q_n is the vertical flux in mm/year, q_o is the vertical flux in kg/s, and area is the corresponding connection area.

The calculations are all done using the Excel standard formula function.

Export the columns of x and y coordinates and total fluxes (mm/y) to a text file, “preq_mA_ptn.q”.

Use Tecplot to plot the vertical flux distribution map at the PTn bottom using the data file “preq_mA_ptn.q”.

Table III 2.1-1 lists the files used to extract vertical fluxes at the PTn bottom.

Table III.2.1-1. Files Used in Extracting Vertical Flux at the PTn Bottom

Input Files	Mesh file	MESH_2KN.V1
	Model output	preq_mA.out
	Processing used files	PTN_BOT.XY, PTN.BOT, TSW.TOP CONN.area, GENER
Working Files		tsw_top.conn, ptn_tsw.conn, ptn_tsw_F.conn, ptn_tsw_M.conn, ptn_tsw_FM.conn, preq_m.inf, tem.conn
Working Spreadsheet and Output Files		total_ptn_flux.xls, preq_mA_ptn.q

Attached CD (Files of Attachments III for Model Report, MDL-NBS-HS-000006 REV01):
III.2/files in Table III.2.1-1/

III.2.2 Extraction of Vertical Flux at the Repository Layer

Extracting vertical fluxes at the repository layer requires the 3-D TSPA-LA model grid (“MESH_2KN.V1”, Output-DTN: LB03023DSSCP9I.001) and an output file of the base-case

flow fields or any other case of interest (e.g., “preq_mA.out”, Output-DTN: LB03023DSSCP9I.001).

In addition, we need the following four mesh-related files of identifying gridblocks, their coordinates and connection areas: “REPO.XY”, “REPO.DAT”, “REPO+1.DAT”, and “CONN_rep.area”, respectively:

“REPO.XY”: this file contains three columns: grid block name, x and y. There are a total of 2,042 rows for all the grid blocks located at the entire repository horizon.

“REPO.DAT”: this file contains 2042 rows and only one column listing the names of the gridblocks located at the entire repository horizon.

“REPO+1.DAT”: this file contains 2042 rows and only one column listing the names of the gridblocks located at the layer just above the repository horizon.

“CONN_rep.area”: this file contains connection areas for all vertical connections at the repository layer.

These four files will be used to extract all vertical fluxes through the repository horizon with different infiltration scenarios.

Step 1: Find vertical fracture-fracture flux, matrix-matrix flux and fracture-matrix flux,

using the following Unix commands:

- `fgrep -f REPO+1.DAT preq_mA.out>repo+1.conn`
- `fgrep -f REPO.DAT repo+1.conn>repo.conn`
- `grep -v 'F0' repo.conn>repo_M.conn`
- `grep -v 'M' repo.conn>repo_F.conn`
- `grep 'M' repo.conn>tem.conn`
- `grep 'F0' tem.conn>repo_FM.conn`

Step 2: Remove data rows of nonvertical connections

Using a text editor, remove rows of nonvertical connections from “repo_F.conn” and “repo_M.conn”. For vertical connections, the last three characters in the block names of two connected blocks are the same. Actually, the vertical connections are the first 2,042 connections in “repo_M.conn” and “repo_F.conn”.

Step 3: Import flow components to spreadsheet:

Open three files: “repo_M.conn”, “repo_F.conn”, and “repo_FM.conn” in Excel, and then copy the columns for gridblock name of connected cells and flux in these files to a working spreadsheet (“total_rep_flux.xls”). Make sure all connections are in the same sequence.

Step 4: Incorporate additional files and summation

- Import “CONN_rep.area” and “REPO.XY” to the spreadsheet.
- Transform unit of flux from kg/s to mm/y by performing

$$q_n = q_o * 31557600.0 / \text{area}$$
 where q_n is vertical flux in mm/year, q_o is vertical flux in kg/s, and area is corresponding connection area.

The above calculations are all performed using the Excel formulas function.

- Export the columns of x and y coordinates and total flux (mm/y) to a text file “preq_mA_rep.q”
- Use Tecplot to plot the vertical flux distribution map at repository horizon, using the data file “preq_mA_rep.q”.

Table III 2.2-1 lists the files used to extract vertical fluxes at the repository layer:

Table III.2.2-1. Files Used to Extract Vertical Fluxes at the Repository Layer

Input Files	Mesh file	MESH_2KN.V1
	Model output	preq_mA.out
	Processing used files	REPO.XY, REPO.DAT, REPO+1.DAT CONN_rep.area
Working Files		repo+1.conn, repo.conn, repo_M.conn, repo_F.conn, repo_FM.conn, tem.conn
Working Spreadsheet and Output Files		total_rep_flux.xls, preq_mA_rep.q

NOTE: Attached CD (Files of Attachments III for Model Report, MDL-NBS-HS-000006 REV01): III.2/files in Table III.2.2-1/

III.2.3 Extraction of Vertical Flux at the Domain Bottom

In addition to the UZ grid mesh file and a TOUGH2 output file of the flow field of interest, we also need two files containing the bottom grid coordinates and vertical connection area: “BT.XY” and “CONN_bt.area”, respectively. “BT.XY” contains three columns: grid block name, x, and y. There are a total of 2,042 rows for all the gridblocks located at the domain bottom. “CONN_bt.area” contains connection areas along all vertical connections at the domain bottom.

These two files will be used to extract all vertical fluxes through the bottom of different infiltration scenarios.

Step 1: Find vertical fracture-fracture flux and matrix-matrix flux, using the following Unix commands:

- `grep 'BT' preq_mA.out > bt.conn`
- `grep 'F0' bt.conn > bt_F.conn`

- `grep 'M0' bt.conn>bt_M.conn`

Setp 2: Sum the F-F and M-M vertical fluxes.

Use Microsoft Excel to open files “bt_M.conn” and “bt_F.conn”, and then copy the columns for gridblock name of connected cells and flux in the two files to a working spreadsheet (“total_bt_flux.xls”). Note that both “bt_M.conn” contains 2042 M-M connections and “bt_F.conn” has 2,042 F-F connections.

- Import “CONN_bt.area” and “BT.XY” to the spreadsheet.
- Transform unit of flux from kg/s to mm/y by performing $q_n = q_o * 31557600.0 / \text{area}$, where q_n is vertical flux in mm/year, q_o is vertical flux in kg/s, and area is the corresponding connection area.

All above calculations are done using the Excel standard formula function.

- Export the columns of X, Y and total flux (mm/y) to a text file “preq_mA_bt.q”.
- Use Tecplot to plot the vertical flux distribution map at domain bottom using the data file “preq_mA_bt.q”.

Table III 2.3-1 lists the files used in extracting the vertical fluxes at the domain bottom:

Table III.2.3-1. Files Used to Extract Vertical Fluxes at the Domain Bottom

Input Files	Mesh file	MESH_2KN.V1
	Model output	preq_mA.out
	Processing used files	BT.XY, CONN_bt.area
Working Files		bt.conn, bt_F.conn, bt_M.conn
Working Spreadsheet and Output Files		total_bt_flux.xls, preq_mA_bt.q

NOTE: Attached CD (Files of Attachments III for Model Report, MDL-NBS-HS-000006 REV01): III.2/files in table III.2.3-1/

III.2.4 Calculation of Percentage of Flux in Fractures, Matrix, and Faults

Step 1: Calculate the total flux in fractures at the entire repository horizon as follows:

- Copy the columns of F-F flux, F-M flux, and total flux and paste them onto a working spreadsheet (“compu_frac_q_percentage.xls”) from “total_rep_flux.xls” (see Section III.2.2 of this attachment for more information about this file).
- In accounting for F-M flux, note that some connections are F-M and others are M-F (matrix-fracture). Delete F-M connections from this column (i.e., F-M flux is not treated as fracture flux).

- Sum the cells in columns of F-F flux and M-F flux, and total fracture flux is obtained (qf).
- Sum the cells in the column of total flux, and total vertical flux at the repository horizon is obtained (q).
- Percentage is computed by $qf/q*100\%$.

Step 2: Calculate total flux in the matrix at the repository layer:

- Total matrix flux (qm), $q_m = q - q_f$. Its percentage is $q_m/q*100\%$.

Step 3: Calculate total flux in faults at the repository layer

- Export the columns of the connected gridblock names and total flux to a text file (“fault_rep_q.dat”) from “total_rep_flux.xls”.
- Edit the “fault_rep_q.dat” by deleting characters at column 1–5 and column 7–8 from data column of gridblock names. Those gridblocks with upper-case letter at column 6 in their names are fault blocks.
- Import “fault_rep_q.dat” to a working spreadsheet (“compu_fault_q.xls”). Use the Excel sort function to sort the data by the sixth character of the gridblock name.
- Delete the lines with lower-case letters at column 6 of the gridblock names.
- Sum the column of total flux. Total fault flux is obtained as (qfa).
- Its percentage is calculated by $q_{fa}/q*100\%$.

Step 4: Calculate the total vertical flux in fractures and the matrix at water table

- Sum the columns of F-F flux and total flux in working file “total_bt_flux.xls” (Section III.2.3, Step 2). Total F-F flux (qf) and total flux (q) are obtained.
- Fracture flux percentage is computed by $qf/q*100\%$.
- Matrix flux percentage is computed by $(1-qf/q)*100\%$.

Step 5: Calculate the total flux in faults at the water table

Total flux in faults at the water table is calculated in the same way as for calculation of total flux in faults at repository horizon, except the flux data is from “total_bt_flux.xls”. See the working file “compu_bt_fault_q.xls” and “fault_bt_q.dat”.

Table III 2.4-1 lists all the files used in this section (III.2.4)

Table III.2.4-1. Files Used in Calculation of Percentage of Flux in Fractures, Matrix, and Faults

Input Files	total_rep_flux.xls, total_bt_flux.xls
Working Spreadsheet and Output Files	compu_frac_q_percentage.xls, fault_rep_q.dat, compu_fault_q.xls, compu_bt_fault_q.xls, fault_bt_q.dat

NOTE: Attached CD (Files of Attachments III for Model Report, MDL-NBS-HS-000006 REV01): III.2/files in table III.2.4-1/

III.2.5 Extraction of Vertical Flux within the Repository for Cumulative Flux Distribution

The list of gridblock names is needed for extracting the vertical flux through the repository zone from file “total_rep_q.dat”. There are a total of 469 blocks within the repository zone, their names are listed in file “REPO_Z”.

- Export flux data at repository horizon from the spreadsheet “total_rep_flux.xls” (III.2.2, Step 3) to a text file “total_rep_q.dat”.
- Use Unix command:

```
fgrep -f REPO_Z total_rep_q.dat > rep_zone_q.dat
```

to extract fluxes through gridblocks within the repository zone.

- Import “rep_zone_q.dat” to a spreadsheet and copy the columns of fluxes to a working spreadsheet “preq_ma_rep.xls”.
- Calculate flux frequency using the histogram function under the Data Analysis menu of Excel, and plot the frequency distribution using the Graph function.

Table III 2.5-1 lists all the files used in this section (III.2.4)

Table III.2.5-1. Files Used in Extracting Vertical Flux at the Repository Zone:

Input Files	REPO_Z, total_rep_flux.xls
Working Files and Output Files	total_rep_q.dat, rep_zone_q.dat, preq_ma_rep.xls

NOTE: Attached CD (Files of Attachments III for Model Report, MDL-NBS-HS-000006 REV01): III.2/files in table III.2.5-1/

III.2.6 Cumulative Flux Distribution

- Copy all cumulative flux distribution frequency data to a working spreadsheet (“cumu_flux.xls”, see Attached CD, Files of Attachments III for Model Report, MDL-NBS-HS-000006 REV01: III.2/files in Section III.2.6) from the flux data of different climate scenario (e.g., “preq_ma_rep.xls”).
- Plot the cumulative flux distribution curve using the Excel graph function.

III.3 Postprocessing Flow Fields In Sensitivity Analyses Of Section 6.8

III.3.1 Formulation

The equation for calculating the relative changes of percolation flux is

$$R_c = \frac{F_c - F_0}{F_0} \quad (\text{Eq. III.3.1-1})$$

where R_c is the relative change, F_c is the percolation flux calculated in the sensitivity simulations, F_0 is the base-case percolation flux.

III.3.2 Input/output Files

The percolation fluxes through the gridblocks within the repository area and the entire repository horizon are extracted from TOUGH 2 output files (Table III.3.2-1):

Table III.3.2-1 Postprocessing Input Files (Simulation Output Files)

File name	Description	DTN
flow9.dat_preq_mA.dat	Base-case flow field output	LB0304RDTRNSNS.001
flow9.dat_TSw	Flow-field output for the case with reduced gamma for TSw units	LB0304RDTRNSNS.001
flow9.dat_Urepo	Flow-field output for the case with reduced gamma for units below the repository (including units at where the repository is located)	LB0304RDTRNSNS.001
REPO_ZONE.cell	Names of gridblock within the repository area	LB03033DSSFF9I.001
REPO_layer.cell	Names of gridblock within the entire repository horizon.	LB03033DSSFF9I.001

File REPO_ZONE.cell and REPO_layer.cell list the names of the gridblocks within the repository zone and within the entire repository horizon, respectively.

Data extraction and calculation produce the following final results and intermediate data files in which the matrix and fracture percolation flux through gridblocks within the repository area and the entire repository horizon are saved (Table III.3.2-2):

Table III 3.2-2. Working Files of Percolation Flux Data Extraction

File name	Description
FLOW9_BM.out	Repository area matrix percolation flux, base-case.
FLOW9_BF.out	Repository area fracture percolation flux, base-case.
FLOW9BM.out	Matrix percolation flux of the entire repository horizon, base-case.
FLOW9BF.out	Fracture percolation flux of the entire repository horizon, base-case.
FLOW9_TM.out	Matrix percolation flux of the repository area, the case with reduced gamma for tsw units.
FLOW9_TF.out	Fracture percolation flux of the repository area, the case with reduced gamma for TSw units.
FLOW9TM.out	Matrix percolation flux of the entire repository horizon, the case with reduced gamma for TSw units.
FLOW9TF.out	Fracture percolation flux of the entire repository horizon, the case with reduced gamma for TSw units.
FLOW9_UM.out	Matrix percolation flux of the repository area, the case reduced gamma for units below the repository (including units at where the repository is located).
FLOW9_UF.out	Fracture percolation flux of the repository area, the case reduced gamma for units below the repository (including units at where the repository is located).
FLOW9UM.out	Matrix percolation flux of entire repository horizon, the case reduced gamma for units below the repository (including units at where the repository is located).
FLOW9UF.out	Fracture percolation flux of the entire repository horizon, the case reduced gamma for units below the repository (including units at where the repository is located).
Relative_changes_of_flux_in_repo.dat	Matrix, fracture and total percolation flux of the repository area, for base case, the case reduced gamma for TSw units and the case reduced gamma for units below the repository (including units at where the repository is located) and, the relative changes of the flux due to gamma change.
Relative_changes_of_flux_repo_layer.dat	Matrix, fracture and total percolation flux of the entire repository horizon, for base case, the case reduced gamma for TSw units and the case reduced gamma for units below the repository (including units at where the repository is located) and, the relative changes of the flux due to gamma change.

NOTE: Attached CD (Files of Attachments III for Model Report, MDL-NBS-HS-000006 REV01): III.3/files in table III.3.2-2/

III.3.3 Procedure for Extracting and Calculating the Relative Changes in Percolation Flux

The matrix and fracture percolation flux data are extracted by the following steps:

Step 1: Use the following Unix commands to extract the data related to the gridblocks listed in REPO_ZONE.cell and REPO_layer.cell, respectively:

```
fgrep -f REPO_ZONE.cell flow9.dat_preq_mA.dat >a1
fgrep -f REPO_layer.cell flow9.dat_preq_mA.dat >a2
fgrep -f REPO_ZONE.cell flow9.dat_TSw.dat >a3
fgrep -f REPO_layer.cell flow9.dat_TSw.dat >a4
fgrep -f REPO_ZONE.cell flow9.dat_Urepo.dat >a5
fgrep -f REPO_layer.cell flow9.dat_Urepo.dat >a6
```

Before applying these commands, make sure that the first column (before the block names) in REPO_ZONE.cell and REPO_layer.cell is deleted, if it is blank.

Step 2: Split the matrix data and fracture data as follows:

```
grep 'M0' a1> FLOW9_BM.out
grep 'F0' a1> FLOW9_BF.out
grep 'M0' a2> FLOW9BM.out
grep 'F0' a2> FLOW9BF.out
grep 'M0' a3> FLOW9_TM.out
grep 'F0' a3> FLOW9_TF.out
grep 'M0' a4> FLOW9TM.out
grep 'F0' a4> FLOW9TF.out
grep 'M0' a5> FLOW9_UM.out
grep 'F0' a5> FLOW9_UF.out
grep 'M0' a6> FLOW9UM.out
grep 'F0' a6> FLOW9UF.out
```

Step 3: Extract the connection data by manually deleting the gridblock data rows:

Manually delete the gridblock data rows (should be the first 469 rows) from FLOW9_BM.out, FLOW9_BF.out, FLOW9_TM.out, FLOW9_TF.out, FLOW9_UM.out, FLOW9_UF.out.

Manually delete the gridblock data rows (should be the first 2,042 rows) from FLOW9BM.out, FLOW9BF.out, FLOW9TM.out, FLOW9TF.out, FLOW9UM.out, and FLOW9UF.out. Then save the files.

Step 4: Manually delete data rows related to the fracture–matrix connections:

Manually delete data rows related to fracture–matrix and matrix–fracture connection data from files FLOW9_BM.out, FLOW9_BF.out, FLOW9_TM.out, FLOW9_TF.out, FLOW9_UM.out, FLOW9_UF.out (should be data rows 939–the end), and from data files: FLOW9BM.out, FLOW9BF.out, FLOW9TM.out, FLOW9TF.out, FLOW9UM.out and FLOW9UF.out (should be data rows 4095–the end).

Step 5: Manually select one vertical connection related to each gridblock:

Manually select one vertical connection related to each gridblock by deleting the other connections related to the gridblock from files FLOW9_BM.out, FLOW9_BF.out, FLOW9BM.out, FLOW9BF.out, FLOW9_TM.out, FLOW9_TF.out, FLOW9TM.out, FLOW9TF.out, FLOW9_UM.out, FLOW9_UF.out, FLOW9UM.out and FLOW9UF.out.

The selected vertical connections are constantly in the same direction (upward or downward).

Step 6: Combine the fracture and matrix percolation flux and calculate the relative changes of the percolation flux:

Copy the third data column from FLOW9_BM.out and FLOW9_BF.out, and paste them onto column A and column B in an Excel spread sheet. Using the standard function, column C=column A + column B, to combine the matrix and fracture percolation flux for gridblocks within the repository area (base case), where Column C is the total percolation flux of the gridblocks, column A is the fracture flux of the gridblocks, and column B is the matrix flux of the gridblocks.

The same operation is also applied to the following couples of files:

FLOW9BM.out and FLOW9BF.out
 FLOW9_TM.out and FLOW9_TF.out
 FLOW9TM.out and FLOW9TF.out
 FLOW9_UM.out and FLOW9_UF.out
 FLOW9UM.out and FLOW9UF.out

Doing this yields the percolation fluxes through the gridblocks within the repository area and the gridblocks within the entire repository horizon, in the base case, the case with reduced gamma for TSw units and the case with reduced gamma for units below the repository (including the repository units).

The data columns for percolation flux of gridblocks within the repository area are stored in the file called: Relative_changes_of_flux_in_repo.dat. Data columns in the file are described in Table III.3.3-1.

Table III.3.3-1. Definition of Data Columns in the File Called Relative_changes_of_flux_in_repo.dat
 Relative_changes_of_flux_repo_layer.dat

Column Name	Simulation	Content
Column A: base_F	Base case	Fracture fluxes
Column B: base_M	Base case	Matrix fluxes
Column C: base_total	Base case	Total fluxes
Column D: TSw_F	Reduced gamma for TSw units	Fracture fluxes
Column E: TSw_M	Reduced gamma for TSw units	Matrix fluxes
Column F: Tsw_total	Reduced gamma for TSw units	Total fluxes
Column G: TSw_re_change	Reduced gamma for TSw units	Relative flux changes
Column H: Urepo_F	Reduced gamma for units below the repository including the repository units	Fracture fluxes
Column I: Urepo_M	Reduced gamma for units below the repository including the repository units	Matrix fluxes
Column J: Urepo_total	Reduced gamma for units below the repository including the repository units	Total fluxes
Column K: Urepo_re_change	Reduced gamma for units below the repository including the repository units	Relative flux changes

The relative changes of each gridblock within the repository area are calculated as follows:

$$\text{column G} = (\text{column F} - \text{column C}) / \text{column C}$$

where column G is the relative change in the percolation flux caused by the changes of gamma value for TSw units, and

$$\text{column K} = (\text{column J} - \text{column C}) / \text{column C}$$

where column K is the relative change in the percolation flux caused by the changes of gamma value for units below the repository (including the unit where the repository is located).

The same operation is also applied to the extracted percolation flux of the gridblocks within the entire repository horizon, and the data are saved in file called `Relative_changes_of_flux_repo_layer.dat`

Step 7: Calculate the average changes as follows:

Use a standard function to calculate: $A = \frac{\sum \text{column G}}{469}$ where column G, in file `Relative_changes_of_flux_in_repo.dat`, contains the relative changes in the percolation flux of every gridblock within the repository area (due to changes of gamma for TSw units), A is the average relative change of the percolation flux, and 469 is the total number of repository blocks.

The same operation is also applied to column K. This yields the average of the relative changes in the percolation fluxes of the gridblocks within the repository area (in response to the gamma changes of units below the repository, including units where the repository is located).

The same operation is also applied to column G and column K, in the file called `Relative_changes_of_flux_repo_layer.dat`. Note that the number of the gridblocks within the entire repository horizon is 2042. The average of the relative changes in the percolation-fluxes through the gridblocks within the entire repository horizon (in response to the gamma changes of TSw units and units below the repository, including the units at where the repository is located) are then obtained (Table III.3.3-4, file name `table_relative_flux_change.doc`):

Table III.3.3-2 (Table 6.8-2). Relative Changes of Percolation Flux in Response to the Changes of γ

Simulation ID	Within the Repository Area	The whole Repository Layer
TSw	-4.478E-3	-1.450E-2
UnderRepo	-5.655E-3	-0.016

III.4. ATTACHED DATA FILES (CD: FILES OF ATTACHMENTS III FOR MODEL REPORT, MDL-NBS-HS-000006 REV01)

This CD has been submitted to the Records Processing Center with the report and can be accessed through the Records Processing Center. All files mentioned above except for the files from the TDMS (submitted with DTN) are attached in the CD called “Files of Attachments III for Model Report, MDL-NBS-HS-000006 REV01.” The files are organized in the CD in the order in which they appeared above and are described below:

CD label:

Files of Attachments III for Model Report, MDL-NBS-HS-000006 REV01

List of the Contents:

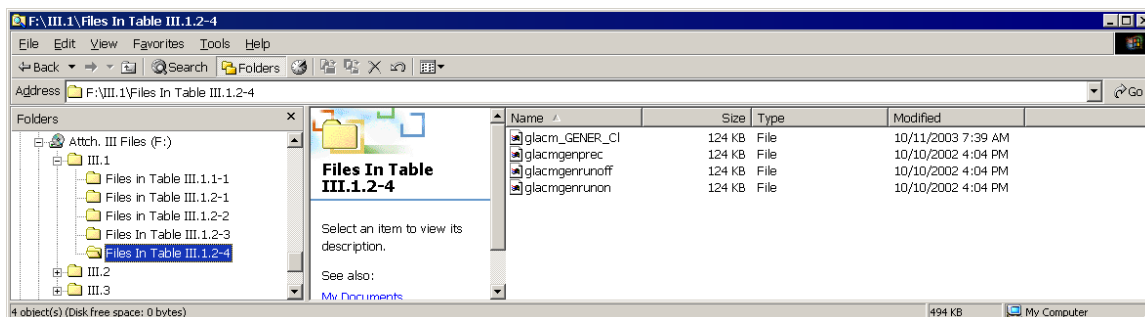
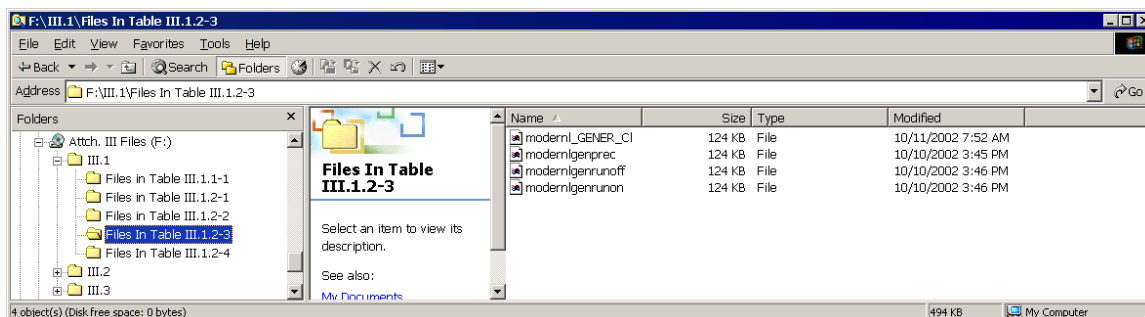
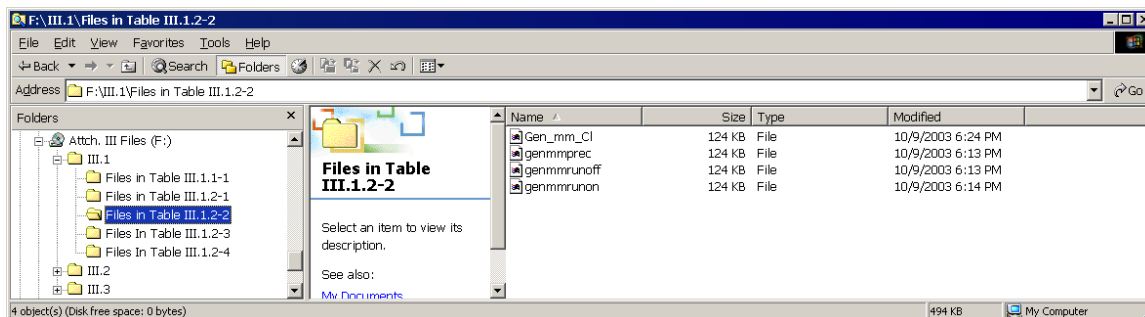
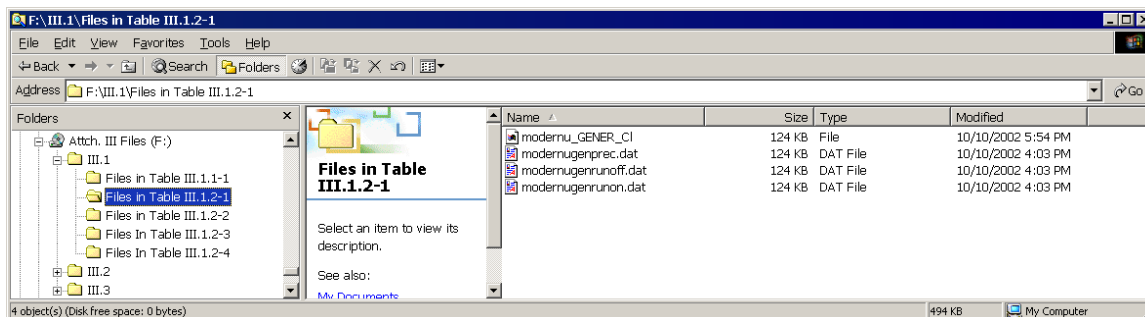
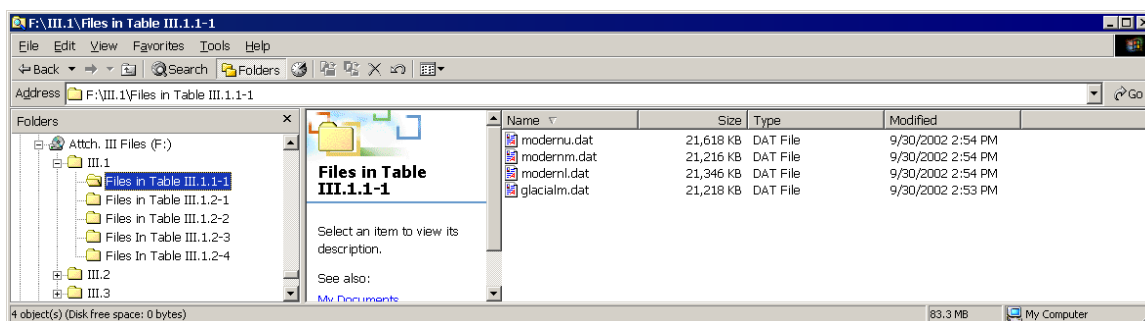
The folder structure, file names, file size, and dates stored in the subfolders of the CD are described in the following table (Table III.4-1) and screen captures.

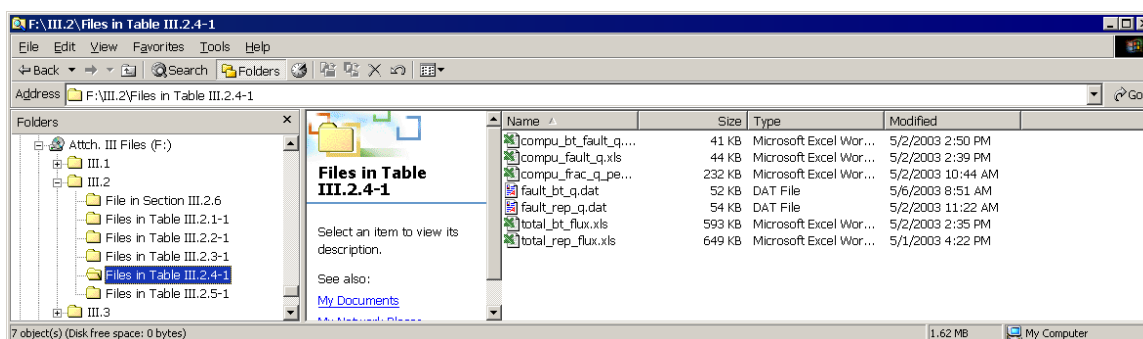
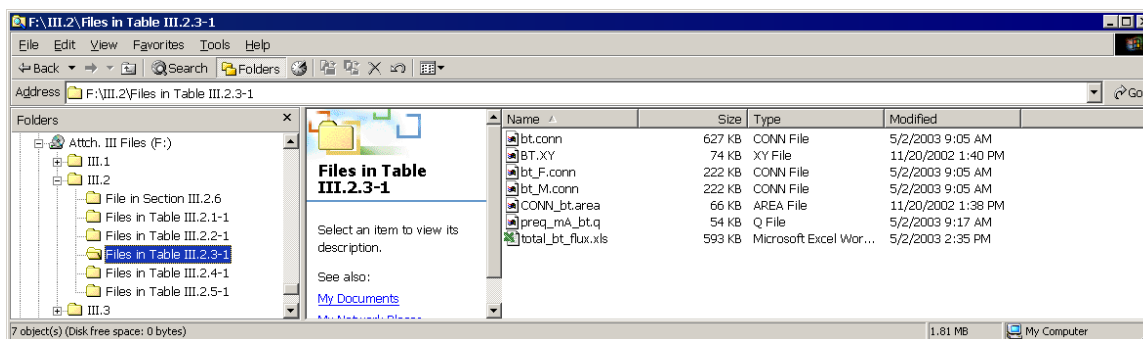
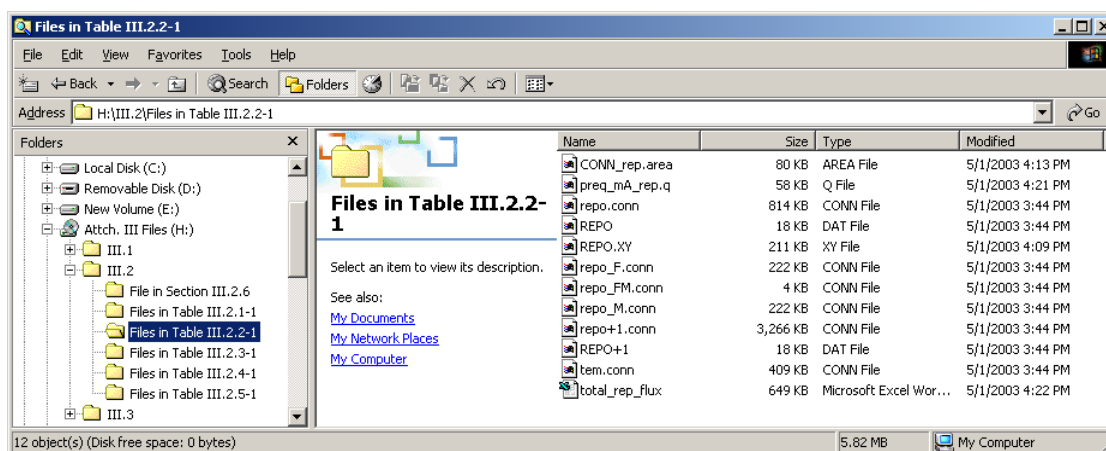
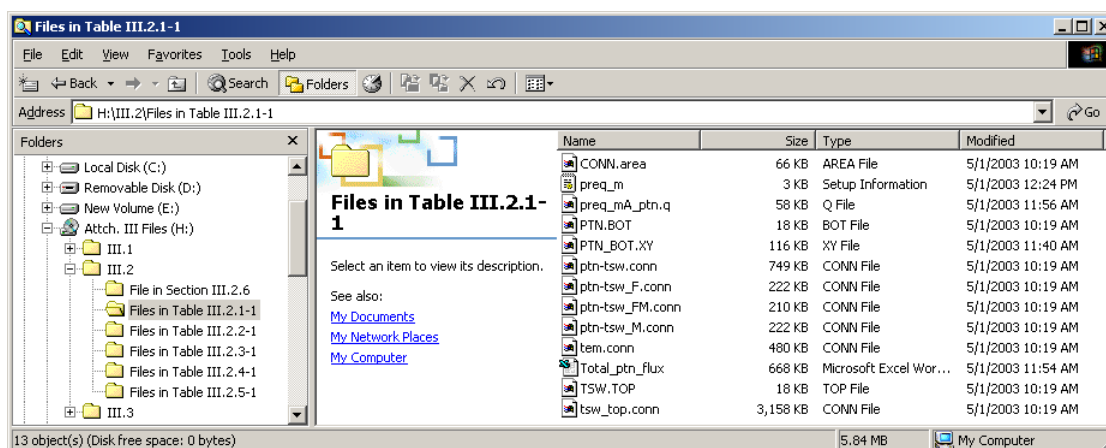
Table III.4-1. List of the File Contents of the Attached CD, Files of Attachments III for Model Report, MDL-NBS-HS-000006 REV01

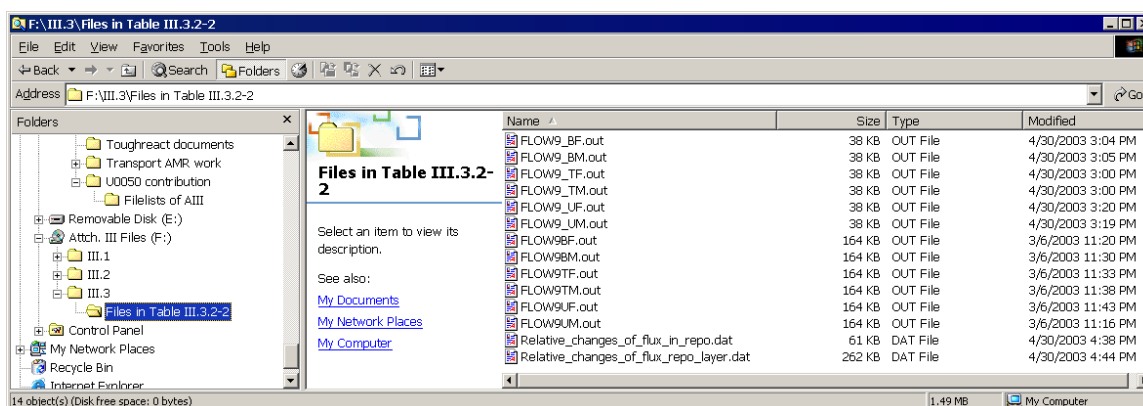
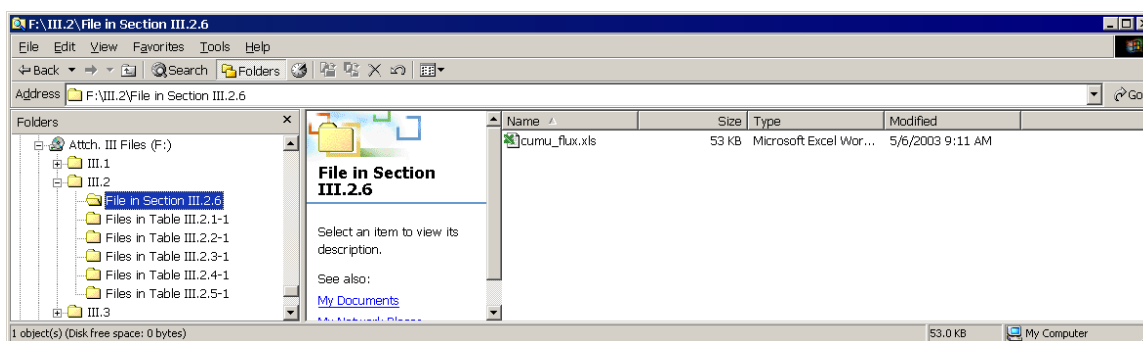
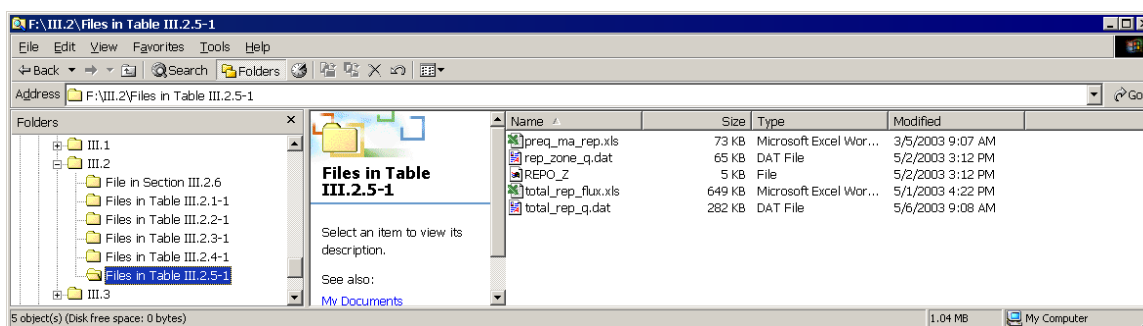
Folder	Subfolder	Files
III.1	Files in Table III.1.1-1	modernu.dat modernm.dat modernl.dat glacialm.dat
	Files in Table III.1.2-1	modernugenprec.dat modernugenrunon.dat modernugenrunoff.dat modernu_GENER_CI
	Files in Table III.1.2-2	genmmmprec genmmrunon genmmrunoff Gen_mm_CI
	Files In Table III.1.2-3	modernlgenprec modernlgenrunon modernlgenrunoff modernl_GENER_CI
III.1	Files In Table III.1.2-4	glacmgenprec glacmgenrunon glacmgenrunoff glacm_GENER_CI
III.2	Files in Table III.2.1-1	PTN_BOT.XY PTN.BOT TSW.TOP CONN.area tsw_top.conn ptn_tsw.conn, ptn_tsw_F.conn ptn_tsw_M.conn ptn_tsw_FM.conn preq_m.inf total_ptn_flux.xls preq_mA_ptn.q tem.conn

Table III.4.1. List of the Contents of the Attached CD, Files of Attachments III for Model Report, MDL-NBS-HS-000006 REV01 (Continued)

Folder	Subfolder	Files
III.2	Files in Table III.2.2-1	REPO.XY REPO.DAT REPO+1.DAT CONN_rep.area repo+1.conn repo.conn repo_M.conn repo_F.conn repo_FM.conn tem.conn total_rep_flux.xls preg_ma_rep.q
	Files in Table III.2.3-1	BT.XY CONN_bt.area bt.conn bt_F.conn bt_M.conn total_bt_flux.xls preg_ma_bt.q
	Files in Table III.2.4-1	total_rep_flux.xls total_bt_flux.xls compu_frac_q_percentage.xls fault_rep_q.dat compu_fault_q.xls compu_bt_falut_q.xls fault_bt_q.dat
	Files in Table III.2.5-1	REPO_Z total_rep_flux.xls total_rep_q.dat rep_zone_q.dat preg_ma_rep.xls
	File in Section III.2.6	cumu_flux.xls
III.3	Files in Table III.3.2-2	FLOW9_BM.out FLOW9_BF.out FLOW9BM.out FLOW9BF.out FLOW9_TM.out FLOW9_TF.out FLOW9TM.out FLOW9TF.out FLOW9_UM.out FLOW9_UF.out FLOW9UM.out FLOW9UF.out Relative_changes_of_flux_in_repo.dat Relative_changes_of_flux_repo_layer.dat







ATTACHMENT IV—PTN/TSW FLUX AND FLOW-FIELD CONVERSION

IV.1 PTN/TSW PERCOLATION FLUX DATA

To use the simulated 3-D UZ percolation fluxes for other modeling studies, vertical percolation fluxes at PTn/TSw interfaces are extracted (procedures given in Attachment III.2.1) for the 18 flow fields of nine base cases and nine alternatives. The PTn/TSw percolation data for the nine base case flow fields are submitted to the TDMS with DTN: LB0302PTNTSW9I.001, while the PTn/TSw percolation data for the nine alternative flow fields are submitted with DTN: LB0305PTNTSW9I.001.

IV.2 FLOW FIELD CONVERSION

The 18 3-D UZ flow fields are generated using a dual-permeability model with extra global fracture-matrix connections, which cannot be directly used by the FEHM code in TSPA calculations. Therefore, the 18 TOUGH2 flow fields need to be converted, using the routine flow-con V1.0 (STN: 10993-1.0-00; LBNL 2003 [163162]), into flow fields on the dual-permeability mesh (mesh_2kb.dkm), which does not have the extra fracture-matrix connections. The output-flow field files of flow-con V1.0 (LBNL 2003 [163162]) are then used as input files to the routine: T2FEHM V4.0 (STN: 10997-4.0-00, LBNL 2003 [163161]), which converts TOUGH2 files in the format of "flow9.dat" into files readable to FEHM.

These converted 18 flow fields are submitted to the TDMS for the use of the TSPA with DTN: LB0305TSPA18FF.001.

INTENTIONALLY LEFT BLANK

ATTACHMENT V

Mathematical Equations

This attachment lists the equations used in this UZ Flow Model for unsaturated liquid flow under isothermal conditions. They include Darcy's law (Bear 1972 [156269]), Richard's equation (Richards 1931 [104252], van Genuchten model (1980 [100610]), and active fracture model (Liu et al. 1998 [105729]).

For fracture continuum or matrix continuum in the dual continuum system, the basic mass balance equations solved by TOUGH2 can be written in the following form:

$$\frac{d}{dt} \int_{V_n} M_f dV_n = \int_{\Gamma_n} \mathbf{F}_f \cdot \mathbf{n} d\Gamma_n + \int_{V_n} (q_f + q_{fm}) dV_n \quad (\text{Eq.V-1})$$

$$\frac{d}{dt} \int_{V_n} M_m dV_n = \int_{\Gamma_n} \mathbf{F}_m \cdot \mathbf{n} d\Gamma_n + \int_{V_n} (q_m - q_{fm}) dV_n \quad (\text{Eq.V-2})$$

where subscripts f , m stand for fracture continuum and matrix continuum, respectively. (We denote $p = f$ or m in the following discussion). The integration is over an arbitrary subdomain V_n of the flow system under study, which is bounded by the closed surface Γ_n . \mathbf{F} denotes mass flux. \mathbf{n} is a normal vector on surface element Γ_n , pointing inward into V_n . The quantity M represents mass per volume with $M_p = \phi_p S_p \rho$ (where ϕ_p is porosity, S_p is saturation, and ρ is liquid density). q_p denotes sinks and sources per unit volume. q_{fm} is fracture-matrix exchange flux per unit volume, a coupling term for describing fluid flow between the fracture and the matrix continuum. The q_{fm} takes positive values if the exchange flux is from matrix to fracture, and negative if from fracture to matrix; see Equation V-13.

Darcy's law is expressed as:

$$\mathbf{F}_p = \rho \mathbf{u}_p = -k_p \frac{k_{rp} \rho}{\mu} (\nabla P_p - \rho \mathbf{g}) \quad (\text{Eq.V-3})$$

where \mathbf{u}_p is the Darcy velocity (volume flux), k_p is absolute permeability, k_{rp} is relative permeability, μ is viscosity, \mathbf{g} is gravity acceleration constant, and P_p is capillary pressure. In the Darcy's law written in this form, the variation of gas pressure is neglected. The capillary pressure is related to the gas pressure by the following equation:

$$P_p = -P_{pg} + P_{pl} \quad (\text{Eq.V-4})$$

where P_{pl} is water phase pressure and P_{pg} is the gas pressure.

By combining mass balance equations (Equations V-1–V-2) with Darcy's law (Equation V-3), we have Richard's equation (Richards 1931 [104252]; Pruess et al. 1999 [160778], Equation A.17, p. 147) for both the fracture and matrix continuum described as:

$$\frac{\partial}{\partial t}\theta_f = \text{div}[K_f \nabla \psi_f] + q_f + q_{fm} \quad (\text{Eq.V-5})$$

$$\frac{\partial}{\partial t}\theta_m = \text{div}[K_m \nabla \psi_m] + q_m - q_{fm} \quad (\text{Eq.V-6})$$

where $K_p = k_p k_{rp} \rho g / \mu$ is hydraulic conductivity, $\psi_p = z + P_p / (\rho g)$ is the total water potential, z is elevation, and $\theta_p = \phi_p S_p$ is specific volumetric moisture content for fracture or matrix.

The water capillary pressure for the matrix continuum is described by the well-known van Genuchten relation (van Genuchten 1980 [100610]), described as:

$$P_m(S_{em}) = \frac{1}{\alpha_m} [S_{em}^{-1/m_m} - 1]^{1/n_m} \quad (\text{Eq.V-7})$$

where P_m is matrix capillary pressure, α_m (Pa^{-1}), and n_m and $m_m = 1 - 1/n_m$ are van Genuchten parameters for the matrix continuum, S_{em} is the effective matrix water saturation, together with effective fracture water saturation S_{ef} discussed below:

$$S_{ep} = \frac{S_p - S_{rp}}{1 - S_{rp}} \quad (\text{Eq.V-8})$$

where S_p is the water saturation of fracture or matrix and S_{rp} is the residual fracture or matrix saturation.

The relative permeability k_{rm} for the matrix continuum is given as:

$$k_{rm} = S_{em}^{1/2} [1 - \{1 - S_{em}^{1/m}\}^m]^2 \quad (\text{Eq.V-9})$$

The water capillary pressure P_f for the fracture continuum is determined by:

$$P_f(S_{ef}) = \frac{1}{\alpha_f} [S_{ef}^{(\gamma-1)/m_f} - 1]^{1/n_f} \quad (\text{Eq.V-10})$$

where S_{ef} is the effective water saturation of all connected fractures (defined in Equation V-8), α_f (Pa^{-1}), n_f , and $m_f=1-1/n_f$ are van Genuchten parameters for the fracture continuum, γ is the active fracture parameter (Liu et al. 1998 [105729]).

The relative permeability k_{rf} for the fracture continuum is given as:

$$k_{rf} = S_{ef}^{(1+\gamma)/2} [1 - \{1 - S_{ef}^{(1-\gamma)/m_f}\}^{m_f}]^2 \quad (\text{Eq.V-11})$$

In an unsaturated fracture network, the ratio of the interface area contributing to flow and transport between fractures and the matrix, to the total interface area determined geometrically from the fracture network, is called the fracture-matrix interface area reduction factor. The reduction factor R is introduced by Liu et al. (1998 [105729]) with the following expression:

$$R \cong S_{ef}^{1+\gamma} \quad (\text{Eq.V-12})$$

The interface area between fracture continuum and matrix continuum, used to calculate q_{fm} , is multiplied by the factor R in the active fracture model (Liu et al. 1998 [105729]).

The fracture-matrix exchange flux introduced in Equations V-1–V-2 can be approximated as quasi-steady, with rate of matrix-fracture flux proportional to the difference in (local) average pressure:

$$q_{fm} \propto R A \frac{\psi_m - \psi_f}{l_f} \quad (\text{Eq.V-13})$$

where A is the total interface area between fracture-matrix (area/volume), and l_f is the fracture spacing (BSC 2003 [160109]).

INTENTIONALLY LEFT BLANK